

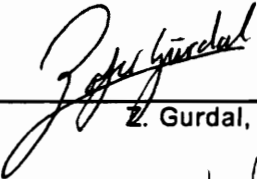
222
68

**A Method for the
Geometrically Nonlinear Analysis of
Compressively Loaded Prismatic Composite Structures**

by
Frederick Stoll

Dissertation submitted to the Faculty of the
Virginia Polytechnic Institute and State University
in partial fulfillment of the requirements for the degree of
DOCTOR OF PHILOSOPHY
in
Engineering Mechanics

APPROVED:



Z. Gurdal, Chairperson



O. H. Griffin, Jr.



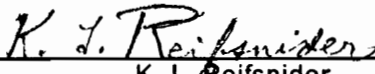
R. T. Haftka



M. W. Hyer



E. R. Johnson



K. L. Reifsnider

January, 1991
Blacksburg, Virginia

**A Method for the
Geometrically Nonlinear Analysis of
Compressively Loaded Prismatic Composite Structures**

by

Frederick Stoll

Z. Gurdal, Chairperson

Engineering Mechanics

(ABSTRACT)

A method was developed for the geometrically nonlinear analysis of the static response of thin-walled stiffened composite structures loaded in uniaxial or biaxial compression. The method is applicable to arbitrary prismatic configurations composed of linked plate strips, such as stiffened panels and thin-walled columns. The longitudinal ends of the structure are assumed to be simply supported, and geometric shape imperfections can be modelled. The method can predict the nonlinear phenomena of postbuckling strength and imperfection sensitivity which are exhibited by some buckling-dominated structures. The method is computer-based and is semi-analytic in nature, making it computationally economical in comparison to finite element methods.

The method uses a perturbation approach based on the use of a series of buckling mode shapes to represent displacement contributions associated with nonlinear response. Displacement contributions which are of second order in the modal amplitudes are incorporated in addition to the buckling mode shapes. The principle of virtual work is applied using a finite basis of buckling modes, and terms through the third order in the modal amplitudes are retained. A set of cubic nonlinear algebraic equations are obtained, from which approximate equilibrium solutions are determined. Buckling mode shapes for the general class of structure are obtained using the VIPASA analysis code within the PASCO stiffened-panel design code. Thus, subject to some additional restrictions in loading and plate anisotropy, structures which can be modelled with respect to buckling behavior by VIPASA can be analyzed with respect to nonlinear response using the new method.

Results obtained using the method are compared with both experimental and analytical results in the literature. The configurations investigated include several different unstiffened and blade-stiffened panel configurations, featuring both homogeneous, isotropic materials and laminated composite material. Results for the local-postbuckling response of stiffened and unstiffened panels agree well with results in the literature for moderate postbuckling load levels. In flat blade-stiffened panels which exhibit significant interaction of the local and Euler buckling modes, the method is successful in predicting the consequent imperfection sensitivity, but the method loses accuracy as imperfection amplitudes are increased.

Acknowledgements

The work reported here was performed under the NASA-Virginia Tech Composites Program, which was funded by NASA Langley Research Center Grant number NAG-1-343. I wish to thank my advisor, Prof. Zafer Gurdal, for his help, patience, and encouragement, and Dr. James H. Starnes Jr. of NASA LaRC for his help, and for the opportunity to work on this project. I also thank Dr. Gaylen A. Thurston of NASA LaRC for his time spent in helpful discussions. I thank each of my committee members for their time spent on my behalf.

Finally, I thank for her support and encouragement my friend and wife, Dr. Collen A. Finegan-Stoll, who, in the midst of my efforts, managed to work ten months a year, write her own PhD dissertation, and give birth to our two wonderful children, Erick and Tyler.

Table of Contents

1.0 Introduction	1
2.0 Review of Literature	6
2.1 Postbuckled Plate Literature	7
2.1.1 Experimental Observations of Postbuckled Plates	7
2.1.2 Analysis of Postbuckled Plates	8
2.2 Postbuckled Stiffened-Panel Literature	10
2.2.1 Experimental Observations of Postbuckled Stiffened-Panels	10
2.2.2 Analysis of Postbuckled Stiffened-Panels	13
2.2.2.1 General comments	13
2.2.2.2 Analysis of global postbuckling	15
2.2.2.3 Analysis of local postbuckling	16
2.2.2.4 Analysis of modal interaction	17
2.2.2.5 General methods of analysis	21
2.2.3 Current Research Effort	24
3.0 Method of Analysis	27
3.1 Equilibrium Condition and Boundary-Value Problem	27
3.1.1 Plate Strips	28
3.1.1.1 Strain-displacement equations	28
3.1.1.2 Conditions for equilibrium	30
3.1.1.3 Side-edge conditions	32
3.1.1.4 Plate constitutive equations	33

3.1.2	Linked-Plate Structures	34
3.1.2.1	Specification of geometry	34
3.1.2.2	Generalized displacements and forces at a node line	37
3.1.2.3	Panel loading	40
3.1.2.4	Boundary conditions at the node lines	41
3.1.2.5	Boundary conditions at the panel ends	43
3.1.2.6	Equilibrium condition for the panel	45
3.2	Form of the Solution	48
3.2.1	Expression of Displacements	48
3.2.2	Expansion of the Strains, Curvatures, and Stress Resultants	49
3.2.3	Expansion of the Plate Euler Equations	51
3.3	Linear Solutions	52
3.3.1	Formulae for Determining the Prebuckling Solutions	54
3.3.1.1	Boundary condition options for a panel with a continuous, planar skin	58
3.3.1.2	Boundary-condition options for a configuration with no continuous, planar skin	59
3.4	Buckling Eigensolutions:	59
3.5	Second-Order Displacement Fields	64
3.5.1	First-Order Fields in terms of Separated Variables	66
3.5.2	Second-Order Fields in terms of Separated Variables	67
3.5.3	Governing Equations in terms of Separated Variables	69
3.5.4	Generalized Displacements and Generalized Force-Resultants Along Boundaries:	72
3.5.5	Boundary Conditions Along the Node Lines	75
3.5.6	Solution of the Boundary Value Problem for $\{\xi_{*ij}(y)\}$	76
3.5.7	Symmetry of Second-Order Displacement Fields with respect to i and j	76
3.5.8	Discussion of the Load-Dependence of the Second-Order Fields:	78
3.6	Enforcement of the Load Ratio	79
3.7	Final Determination of Equilibrium Solutions	83
3.7.1	Original Approach	83

3.7.2 Final Approach	84
4.0 Results and Discussion	92
4.1 Postbuckling of Square Unstiffened Panels	92
4.1.1 Isotropic Plates with Simple Edge Support	92
4.1.2 Composite Panel with Simple Edge Support	95
4.1.3 Square Isotropic Plates with Various Boundary Conditions	97
4.2 Postbuckling of a Rectangular Unstiffened Composite Panel	99
4.3 Postbuckling of a Three Bay Blade-Stiffened Panel	108
4.3.1 Full (Symmetric) Representation of the Panel	110
4.3.2 Panel Representation Using a Stiffener-Unit	121
4.4 Modal Interaction in Wide, Blade Stiffened Panels	129
4.4.1 Test Configurations	129
4.4.2 Displacement Shape Functions for the Thin-Stiffener Panel	133
4.4.3 Displacement Shape Functions for a Stocky-Stiffener Panel	136
4.4.4 Analysis with NLPAN	142
4.4.5 NLPAN Results for the Thin-Stiffener Panel	144
4.4.6 NLPAN Results for the Stocky-Stiffener Panels	148
4.4.7 Additional Comments on the NLPAN Results for Imperfection Sensitive Panels	148
4.5 Computational Expense of NLPAN	153
5.0 Conclusions and Recommendations	154
5.1 Conclusions	154
5.2 Recommendations for Future Work	157
References	159
Appendix A. Nonlinear Plate Theory	164

A.1.1	Strain-Displacement Relations	164
A.1.2	Equilibrium Equations in Terms of Stress Resultants:	169
A.1.3	Plate Constitutive Equations:	175
Appendix B. Y-Dependence of Buckling Eigensolutions		177
B.1.1	Complex Representation	177
B.1.2	Out-of-Plane Displacements	179
B.1.3	In-Plane Displacements	182
B.1.4	Final Expression of the Eigensolutions	187
Appendix C. Finite-Difference Solution for the Second-Order Displacement Fields		189
C.1.1	Finite-Difference Expressions for the Governing Equations	189
C.1.2	Finite-Difference Expressions for the Generalized Edge Force-Resultants	192
C.1.3	System of Equations for a Plate Strip	197
C.1.4	Global System of Equations	204
Vita		206

List of Symbols

Symbol	Description	Section where defined
A	Load parameter used in controlling the ratio of the biaxial load components N_{yG} and N_{xG} -or- Planform area of a plate strip	3.2.1
b	Width of a plate strip (in the local y -direction)	3.1.1.1
B	Reference width of a panel or other structure (global y -direction)	3.1.2.1
cl	Indicates "clamped" boundary condition for a plate edge	
e	Index number of the side edge of a plate strip: $y = 0$ for $e = 1$; $y = b$ for $e = 2$	3.1.1.3
e_y, e_z	Measures of the eccentricity of a node line relative to an associated plate-strip edge	3.1.2.2
E	Young's modulus	
$\{f_e\}$	Generalized force resultants at side edge no. e of a plate strip, defined w.r.t. local coordinate axes: $[f_{x_e} f_{y_e} f_{z_e} m_e]^T$	3.1.1.3
$\{f^n\}$	Same as $\{f_e\}$ except referred to the associated node line and global coordinate axes: $[f_x^n f_y^n f_z^n m^n]^T$	3.1.2.2
$\{F^n\}$	Generalized force resultants along a node line: $[F_x^n F_y^n F_z^n M^n]^T$	3.1.2.2
h	Plate thickness	
I	Bending moment of inertia	
L	Length of a structure in the longitudinal (x) direction	3.1.2.1
m	Number of longitudinal halfwaves for buckling mode no. i	3.4
\hat{m}	Number of longitudinal halfwaves of contribution no. α ($\alpha = 1, 2$) of second-order displacement field no. ij : $\hat{m} = m \pm n$	3.5
M	Number of buckling modes used in an analysis	3.7.2
$\{M\}$	Bending moment resultants in a plate strip: $[M_x M_y M_{xy}]^T$	App. A

n	Index number of a node line -or- Number of longitudinal halfwaves for buckling mode no. j	3.1.2.1 3.5
n_1, n_2	Index numbers of the two boundary node-lines of a structure	3.1.2.4
\hat{n}	The in-plane unit vector normal to the edge of a plate: $\hat{n} = n_x \hat{i} + n_y \hat{j}$	App. A
N	Total number of node lines in a structure	3.1.2.1
$\{N\}$	In-plane stress resultants in a plate strip: $[N_x \ N_y \ N_{xy}]^T$	App. A
N_{xG} or \bar{N}_x	Axial load on a panel or other structure (the mean tensile load in the x-direction per unit width, based on B)	3.1.2.3
N_{yG} or \bar{N}_y	Edge-normal transverse load on a panel (the mean tensile load in the global y-direction per unit length, based on L)	3.1.2.3
\hat{N}_{xG}	Unit load value specified for N_{xG}	3.1.2.3
\hat{N}_{yG}	Unit load value specified for N_{yG}	3.1.2.3
\hat{N}_{yG}^A	Unit load value for N_{yG} used in association with load parameter A	3.3
p	Index number of a plate strip	3.1.2.1
P	Total number of plate strips in a structure	3.1.2.1
q_i	Modal amplitude for the i^{th} buckling mode	3.2.1
q_i^o	Modal imperfection amplitude for an imperfection in the shape of the i^{th} buckling mode	3.2.1
\hat{R}	Ratio of the specified unit load components: $\hat{R} = \hat{N}_{yG}/\hat{N}_{xG}$	3.1.2.4
s_α	Sign used in association with contribution no. α ($\alpha = 1, 2$) of a second-order displacement field: $s_\alpha = \pm 1$	3.5
ss	Indicates "simple support" boundary condition for a plate edge	
$\{u\}$	Displacement components for the mid-surface of a plate strip w.r.t. the local coordinate axes: $[u(x, y) \ v(x, y) \ w(x, y)]^T$	3.1.1.1
$\{u^o\}$	Values for $\{u\}$ describing geometric shape imperfections	3.1.1.1
$\{u_e\}$	Generalized displacements along side-edge no. e of a plate strip, defined w.r.t. local coordinate axes: $[u_e \ v_e \ w_e \ \psi_e]^T$	3.1.1.3
$\{u_i\}$	Buckling eigenfunctions (or buckling "modes"): $[u_i \ v_i \ w_i]^T$	3.2.1
$\{u_{ij}\}$	Second-order displacement fields: $[u_{ij} \ v_{ij} \ w_{ij}]^T$	3.2.1
$\{u_L\}$	Displacements associated with unit loads \hat{N}_{xG} and \hat{N}_{yG} : $[u_L \ v_L \ 0]^T$	3.2.1

$\{U^t\}$	Displacements associated with unit load $\hat{N}_{\lambda_0}^t$ for $\varepsilon_x = 0$: $[0 \ v^t \ 0]^T$	3.2.1
$\{U^n\}$	Generalized displacements along a node line: $[U^n \ V^n \ W^n \ \Psi^n]^T$	3.1.2.2
y_e	The local y -coordinate value at edge no. e of a plate strip: $y_e = 0$ for $e = 1$; $y_e = b$ for $e = 2$	3.1.1.3
α	Index number for the two contributions to $\{u_{ij}\}$: $\alpha = 1, 2$	3.5
$\{\varepsilon\}$	In-plane strain components: $[\varepsilon_x \ \varepsilon_y \ \gamma_{xy}]^T$	3.1.1.1
$\{\varepsilon^c\}$	Nominal in-plane strain components at the mid-surface of a plate	3.1.1.1
$\{\varepsilon^m\}$	Mechanical (load-related) in-plane strain components at the mid-surface of a plate	3.1.1.1
$\{\kappa^c\}$	Nominal curvature components of the mid-surface of a plate: $[\kappa_x^c \ \kappa_y^c \ \kappa_{xy}^c]^T$	3.1.1.1
$\{\kappa^m\}$	Mechanical (load-related) curvature components of the mid-surface of a plate strip	3.1.1.1
λ	Generalized axial-load parameter: controls end shortening	3.2.1
λ_b	Reference value of λ used when computing $\{u_{ij}\}$	3.5
μ	Rotational offset between the local y - z coordinate axes and the global y - z coordinate axes	3.1.2.2
ν	Poisson's ratio	
ψ_e	The rotation angle of edge no. e of a plate strip (the gradient of w at the edge, in the local y -direction)	3.1.1.3
Ψ^n	The rotation angle of node-line no. n	3.1.2.2
$\{\xi_i\}$	The y -dependent portion of buckling eigenfunction no. i : $[\xi_i(y) \ \eta_i(y) \ \phi_i(y)]^T$	3.4
$\{\xi_{\alpha ij}\}$	The y -dependent portion of contribution no. α ($\alpha = 1, 2$) of the second-order displacement field no. ij : $[\xi_{\alpha ij}(y) \ \eta_{\alpha ij}(y) \ \phi_{\alpha ij}(y)]^T$	3.5

Subscripts and superscripts

$f(x) _{x=0, L}$	$f(0) + f(L)$
$f(x) _{x=0}^L$	$f(L) - f(0)$
$(-)_e$	Expression associated with side-edge no. e of a plate strip
$(-)_i$	Expression appearing with the factor q_i

- (-)_{ij} Expression appearing with the factor $(q_i q_j)$
- (-)_{ijk} Expression appearing with the factor $(q_i q_j q_k)$
- (-)_{ijke} Expression appearing with the factor $(q_i q_j q_k q_e)$
- (-)_L Expression corresponding to the linear response of a perfect structure to unit global loads \hat{N}_{xG} and \hat{N}_{yG}
- (-)_{L^A} Expression corresponding to the linear response of a perfect structure to unit global load \hat{N}_{xG}^A with $\varepsilon_x \equiv 0$
- (-)_n Expression corresponding to node line no. n
- (-)_p or (-)^p Expression corresponding to plate strip no. p
- [-]^T Transform of a matrix
- (-)_α Expression corresponding to contribution no. α ($\alpha = 1, 2$) of a second-order displacement field
- ([^]-) Expression associated with the response to the unit load system \hat{N}_{xG} and \hat{N}_{yG}
- ([·]-) A scalar amplitude associated with harmonic contributions to the generalized displacements or generalized force-resultants along a node line or along the side edge of a plate strip

List of Illustrations

Figure 1.	Examples of compressively loaded prismatic linked-plate structures.	2
Figure 2.	Generalized displacements and generalized force-resultants at the side edges of a plate strip.	29
Figure 3.	Stiffened panel showing plate-strip numbers, node-line numbers, and labeling conventions	36
Figure 4.	Eccentricity measures e_y and e_x , and the local-to-global orientation angle μ	38
Figure 5.	End load versus center deflection for simply supported square plates	94
Figure 6.	Convergence of results with respect to the finite-difference interval width	96
Figure 7.	End shortening versus center deflection for a simply supported square unstiffened graphite/epoxy composite panel.	98
Figure 8.	Labeling key for the boundary conditions considered for square isotropic plates with uniaxial loading.	100
Figure 9.	End load versus center deflection for square plates having a variety of boundary conditions on the unloaded edges	101
Figure 10.	End load versus end shortening for square plates having a variety of boundary conditions on the unloaded edges	102
Figure 11.	Unstiffened quasi-isotropic composite panel with uniaxial loading	104
Figure 12.	End load versus end shortening for a uniaxially loaded quasi-isotropic composite panel	107
Figure 13.	Longitudinal strains at the surface of a uniaxially loaded quasi-isotropic composite panel	109
Figure 14.	Three bay blade-stiffened panel configuration used for the study of local-postbuckling behavior	111
Figure 15.	Transverse profiles for the first five symmetric buckling modes having five longitudinal halfwaves.	113
Figure 16.	Profiles of the contributions to a second-order displacement field $\{u_{ii}\}$	115
Figure 17.	Profiles of the contributions to a second-order displacement field $\{u_{ij}\}$	116
Figure 18.	Profiles of the contributions to a second order-displacement field $\{u_{ij}\}$	117
Figure 19.	Example of the modification used for x -independent contributions to the second-order displacement fields.	119

Figure 20. Analytical results for the local-postbuckling response of a three-bay blade-stiffened panel 120

Figure 21. Stiffener-unit representation of a three bay blade-stiffened panel. 123

Figure 22. Analytical results from NLPAN using a stiffener-unit representation of a three bay panel 125

Figure 23. Longitudinal surface strains in the skin at the center of a three bay panel (location 1) 126

Figure 24. Transverse surface strains in the skin adjoining a stiffener for a three bay panel (location 2) 127

Figure 25. Blade stiffened panel configurations used in experiments investigating modal interaction 131

Figure 26. Profiles of the displacement fields of a thin-stiffener panel 134

Figure 27. The mixed second-order displacement field at the stiffener tip for a thin-stiffener panel ($\lambda_b = 0$). 137

Figure 28. Demonstration of the singularities in the contributions to the mixed second-order displacement field 138

Figure 29. Profiles of the mixed second-order field contributions as affected by the reference value of the load parameter 139

Figure 30. Profiles of the displacement fields of stocky-stiffener panel # 2 140

Figure 31. Results for the thin-stiffener panel, NLPAN Approach 1. 145

Figure 32. Results for the thin-stiffener panel comparing NLPAN Approaches 1 and 2. . 147

Figure 33. Results for stocky-stiffener panel # 1 comparing NLPAN Approaches 1 and 2. 149

Figure 34. Results for stocky-stiffener panel # 2 comparing NLPAN Approaches 1 and 2. 150

Figure 35. Results for stocky-stiffener panel # 3 comparing NLPAN Approaches 1 and 2. 151

Figure 36. Conventions for plate stress-resultants and coordinate axes. 166

Figure 37. Measures of the loads acting on a plate edge. 171

List of Tables

Table 1. Options Available for Specifying Conditions Along the Boundary Node-Lines .	42
Table 2. Graphite/Epoxy Lamina Properties [64]	97
Table 3. Graphite/Epoxy Lamina Properties [9]	103
Table 4. PASCO-Computed Buckling Loads for an Unstiffened Composite Panel	105
Table 5. Values of Length Computed for Three Stocky Stiffener Panels	133
Table 6. Functional Forms Used for VIPASA Out-of-Plane Case (b)	181
Table 7. Functional Forms Used for VIPASA Out-of-Plane Case (c)	181
Table 8. Functional Forms Used for VIPASA Out-of-Plane Case (d)	182
Table 9. Functional Forms Used for VIPASA In-Plane Case (a)	185
Table 10. Functional Forms Used for VIPASA In-Plane Case (b)	186

1.0 Introduction

Thin-walled compression members are found in a large variety of structural applications. These include stiffened panels found in, for example, the skins and ribs of aircraft wings, the bulkheads of ships, and thin-walled open- and closed-section columns used in buildings and bridges. Most existing structural components of this type are fabricated of metallic materials; however the same need for strength, stiffness, and reduced weight which makes thin-walled stiffened structures attractive has stimulated interest in the potential benefits of using fiber-reinforced composite materials.

The specific class of thin-walled compression members considered here are compressively loaded prismatic configurations, some examples of which are shown in Figure 1. These are structures (or structural components) which can be modelled as prismatic assemblages of finite-length plate strips, where each strip is linked at one or both longitudinal edges to other plate strips and is subjected primarily to in-plane loading as a result of the global loads imposed on the structure. These configurations are generally modelled with regard to classical buckling response, where the lowest eigenvalue provided by a buckling analysis is assumed to represent the maximum load sustainable by the structure, provided that material failure has not occurred at a lower load level.

There are often geometrically nonlinear effects which cause an actual structure to possess strength significantly greater than or less than the strength predicted based on a buckling analysis. When the primary buckling mode is a "local" mode (where the buckling halfwave length in the longitudinal direction is of the same order of magnitude as a representative width between plate junctures in the stiffened structure, and the junctures between plate components rotate but do not translate), then often the structure can support considerable additional load beyond the buckling load. Such a structure is said to have postbuckling strength. When

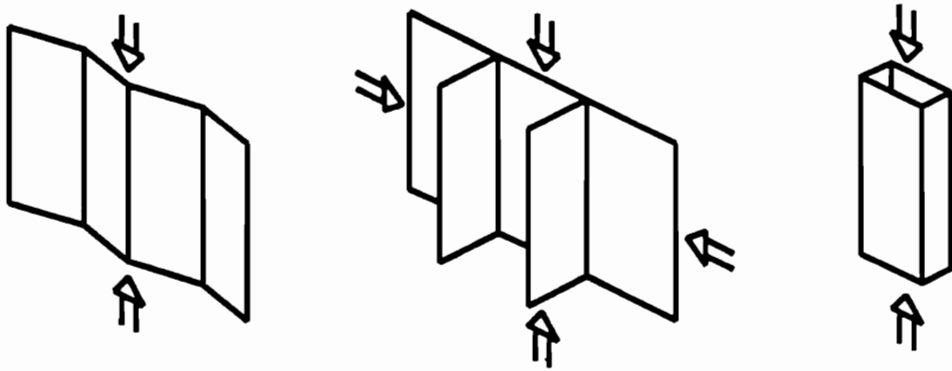


Figure 1. Examples of compressively loaded prismatic linked-plate structures.

the primary buckling mode is the "global" (or "Euler") mode (characterized by the deflection of the structure in a single halfwave over the length), the structure may have some postbuckling strength, or may be neutrally stable.

When the global and local buckling modes have associated theoretical buckling eigenvalues which are equal, the mathematically idealized structure is highly unstable in postbuckling. This is due to the phenomenon called "modal interaction;" the overall bending stiffness which resists global postbuckling motion is reduced by local postbuckling deformations. When an unstable postbuckling path exists for an idealized structure, a physical structure generally exhibits elastic limit-load behavior, where the limit load is less than the theoretical buckling load. This is because imperfections and secondary loads which are inevitably present (material and geometric imperfections, load eccentricity, lateral pressure, structural weight, and inertial forces) make the structural response nonlinear from the onset of load application, causing the load-response path to shift away from the theoretical prebuckling path toward the unstable postbuckling path without achieving the theoretical buckling load. Structures exhibiting this type of modal interaction are thus said to be imperfection sensitive with regard to elastic strength. Because a structure may exhibit this type of imperfection sensitivity, or may exhibit postbuckling strength, the accurate prediction of the strength requires an analysis which includes both the effects of geometric nonlinearities, and the effects of imperfections.

A great deal of emphasis is placed on mass minimization of stiffened structures, partly for the purpose of minimizing material usage, but more importantly for transportation vehicles, to minimize fuel consumption with a concern for life-cycle costs and environmental impact. In aeronautical and space applications, weight minimization receives great emphasis, so that specified safety factors for strength are often relatively small. Based on the failure criteria used during the optimization process, a minimum-mass design may satisfy safety factors without any additional margins, and thus, inaccuracies in the prediction of failure can result in unacceptable strength or performance characteristics, or conversely, in undesirable weight penalties. An optimal stiffened-panel design which is based on buckling constraints is

particularly suspect with regard to adequacy of strength, because such a design is prone to have simultaneous buckling eigenvalues for the local and global buckling modes [1]; such a design is often termed a "naive" optimum design, because the possibility exists that a significantly different design is truly optimal if the effects of imperfections are taken into account. Thus, it is desirable to replace or augment the classical buckling analysis with a corresponding geometrically nonlinear analysis.

Finite element analysis techniques exist which can compute the elastic behavior of the described structures to practically any desired degree of accuracy, but these techniques are computationally expensive, particularly when nonlinear effects are modelled, and thus are poorly suited for applications in optimization or preliminary design. Several stiffened-panel design codes have been developed which use analytical or semi-analytical approaches to obtain more economical methods of geometrically nonlinear analysis. These include PASCO (Panel Analysis and Sizing Code) [2], POSTOP (Postbuckled Open-Stiffener Optimum Panels) [3], and PANDA2 [4], each of which attempts to account for some or all of the nonlinear phenomena discussed above. However, each of these methods has limitations with regard to the configurations which can be accurately modelled.

As the subject of this dissertation, a new method has been developed for the geometrically nonlinear analysis of the equilibrium response of the class of compressively loaded prismatic composite structures which can be modeled as a set of linked plate strips. The structures are assumed to have simple support at the longitudinal ends, and may have any of a variety of support conditions specified at the side boundaries. The component plate strips may have anisotropic material properties suitable for modelling a variety of composite laminates of practical interest. Loading of the structure may be uniaxial or, for some panel-like configurations, biaxial, and the method can be used with or without geometric shape imperfections. The method employs buckling eigenfunctions, obtained from the VIPASA buckling and vibration analysis program [5] (which is incorporated in the PASCO design code), as shape functions for modelling geometrically nonlinear response; thus, subject to some additional restrictions in loading and plate anisotropy, structures which can be modelled with

regard to buckling response by VIPASA can be analyzed with regard to geometrically nonlinear response using the method presented here. The method is encoded in a FORTRAN program named NLPAN, which has been implemented on a digital computer.

In the following section, literature pertaining to the postbuckling and nonlinear response of compressively loaded plates and linked-plate type structures is reviewed. Next, the theory for the new method is presented in detail. Finally the method is applied to several flat stiffened and unstiffened panel configurations in order to explore certain options in the analytical approach and to assess the performance of the method.

2.0 Review of Literature

The review of literature here will be limited to a consideration of flat stiffened and unstiffened panels to which only axial or biaxial in-plane loading is applied. Structures with unsymmetric laminates will not be considered. While curved panels and shells can be modelled approximately as assemblages of plate strips, the literature for such configurations will not be reviewed. The focus on the literature of flat panels does not reflect a limitation in the method of analysis presented here, but rather limits the scope of the literature review to problems of the type investigated in the verification test cases discussed in Chapter 4. The review is additionally limited to a consideration of structural response associated with elastic material behavior.

There are three survey and summary papers in the literature which provide a good overview of issues relating to the response and analysis of compressively loaded flat panels. The buckling and postbuckling behavior of composite plates, and to a lesser degree, stiffened composite panels, is discussed in [6]. The buckling and postbuckling of stiffened panels (and shells) are discussed in [7] and [1], with an emphasis on the prediction of imperfection sensitivity associated with modal interaction.

Some literature on postbuckled plates is first considered, because it helps to provide a perspective on the response and analysis of postbuckled stiffened panels and thin-walled columns. Observations from experimental investigations of postbuckled plates will be discussed, followed by a consideration of some methods which have been used to analyze them. Next, literature will be reviewed which covers experimental investigations of the nonlinear behavior of compressively loaded stiffened panels and thin-walled columns, followed by a review of existing methods of analysis for those structures.

2.1 Postbuckled Plate Literature

2.1.1 Experimental Observations of Postbuckled Plates

Compressively loaded rectangular plates with supported edges have postbuckling strength which is generally limited only by material yielding or failure. This fact has been known at least since the early days of aluminum airframe construction, and motivated the often-cited study of von Karman and associates [8] concerning the strength of postbuckled metallic plates. Simply supported composite plates can display significant postbuckling strength, as reported in, for example, [9] and [10]. Uniaxially loaded composite plates with one side edge simply supported and one side edge free also demonstrate postbuckling strength [11].

For a simply supported rectangular plate with orthotropic material properties, buckling mode shapes are sinusoidal in the directions of both of the reference axes. During progressive loading into the postbuckling regime, the postbuckled shape usually retains the same qualitative shape as the buckling mode. In some circumstances, however, uniaxially loaded plates (particularly those which are longer in the direction of the load axis than they are wide) exhibit a sudden increase in the number of halfwaves in the direction of the load axis [10,12]. The same type of mode change has been observed in one-edge-free plates [11]. In two nominally identical one-edge-free postbuckling specimens tested in [11], one exhibited a mode change, whereas the other did not. This suggests that imperfections in the plates or test fixtures may play a role in producing the mode change phenomenon. The phenomenon of mode change in postbuckled plates appears to be benign in that it did not, in the cited experiments, cause detectable material failure, nor did it coincide with a limit in elastic postbuckling strength. However, the sudden snap observed in the experiments may cause subtle material damage which accumulates with repetitive snapping due to load cycling, resulting in fatigue

failure. Thus, the prediction of mode-change during postbuckling response may be important in structural applications where plates or stiffened panels are designed to operate in postbuckling.

2.1.2 Analysis of Postbuckled Plates

Levy [13] and Coan [14] provide postbuckling solutions for simply supported square plates which are loaded uniaxially with uniform end shortening. The form of the displacements used to represent solutions in [13] and [14] serves as a reference form, to which the form of the displacement solutions used in the current method (see Section 3.2.1) are compared. Thus, the solutions of [13] and [14] are examined here in some detail. The von Karman nonlinear plate equations are assumed to apply. In Levy's study, the unloaded side edges are constrained to remain straight with no net normal in-plane loads, whereas in Coan's study, the unloaded side edges are uniformly free of in-plane loads, and thus they may experience in-plane distortion. Both studies express out-of-plane deflections w as a double Fourier sine series (where the notation of [14] has been converted to the notation of [13]):

$$w = \sum_{m=1}^{\infty} \sum_{n=1}^{\infty} w_{mn} \sin(m\pi x/L) \sin(n\pi y/b) \quad (1)$$

where w_{mn} is a load-dependent scalar, x and y are the reference coordinates in the plane of the plate, L is the dimension in the x -direction (the load axis), and b is the plate dimension in the y -direction. Renaming the mn^{th} load-dependent constant, $w_{mn} = q_i$, and shape function $\sin(m\pi x/L) \sin(n\pi y/b) = w_i(x, y)$, the complete displacement field for the postbuckled solutions of both [13] and [14] can be expressed in the form

$$\begin{aligned}
u(x, y) &= \lambda u_L(x) + \sum_{i=1}^{\infty} \sum_{j=1}^{\infty} q_i q_j u_{ij}(x, y) \\
v(x, y) &= \lambda v_L(y) + \sum_{i=1}^{\infty} \sum_{j=1}^{\infty} q_i q_j v_{ij}(x, y) \\
w(x, y) &= \sum_{i=1}^{\infty} q_i w_i(x, y)
\end{aligned} \tag{2}$$

where u and v are the in-plane displacements in the x - and y -directions, respectively, λ is the parameter controlling end shortening, λu_L and λv_L give the displacements for the unbuckled solution, and $u_{ij}(x, y)$ and $v_{ij}(x, y)$ are load-independent shape functions.

There are several points worth noting regarding the solution form shown above. First, each function w_i represents a buckling eigenfunction for the plate, and thus, the load-dependent scalars q_i represent "modal amplitudes" for the participating buckling mode shapes. Second, when the above form is used to express the nonlinear equilibrium equations for the plate, each ij^{th} pair of in-plane shape functions, u_{ij} and v_{ij} , can be determined independently to identically satisfy the in-plane equilibrium equations and the homogeneous form of the boundary conditions; thus, in truncating the infinite series expression for w in order to make the problem tractable, the in-plane equilibrium equations are always satisfied. The third point noted here is that retention of only a few terms in the series for w (approximately four to six) provides results for displacements which are fairly accurate up to loads of several times the buckling load [13]. The primary buckling mode provides the dominant contribution to the out-of-plane displacements in postbuckling. It is also interesting to note that while the difference in the in-plane boundary conditions used by Levy versus those used by Coan does not affect the buckling load or mode shape, there are significant differences in the postbuckling response (see Section 4.1). This indicates a sensitivity of postbuckling response to variations in the boundary conditions at the side edges.

The literature contains many additional works dealing with the postbuckling analysis of plates; a large variety of plate shapes, anisotropic properties, and boundary conditions are

considered. Many of these works are summarized in [15]. The great variety of analyses in the literature are not discussed further here, except for the topic of predicting mode changes in postbuckling. Mode-change is investigated in [16], where out-of-plane displacements are represented in terms of only two buckling modes; it was found necessary to include the effects of shape imperfections in order to model the mode-change phenomenon. Direct minimization of the total potential energy is used in [17] to compute equilibrium solutions and predict the mode-change phenomenon. Mode change is assumed to be consistent with the assumption that the plate seeks the absolute lowest total potential energy level. This method does not rigorously model the response of a plate to a monotonically varied generalized load. A stable equilibrium state can exist at any *local* minimum in the total potential energy, so that the change in mode shape actually occurs when the active local minimum disappears with increasing load. This discrepancy is avoided in the theoretical approach of Thurston [18], which is capable of tracing the load-response path through limit points and secondary bifurcation points.

2.2 *Postbuckled Stiffened-Panel Literature*

2.2.1 Experimental Observations of Postbuckled Stiffened-Panels

As was the case for simple plates with supported edges, compressively loaded stiffened panels can exhibit considerable postbuckling strength. This has been observed in, for example, blade-stiffened composite panels [19], I-stiffened composite panels [20], hat-stiffened composite panels [19,21], and in simple one-edge-free, channel, hat, I, and Z composite stiffener sections [11,22]. The significant postbuckling strength observed for the structures listed above is primarily associated with buckling and postbuckling response which occurs in

a "local" mode shape, i.e. one in which the buckling mode shape is generally characterized by rotation of plate-strip junctures without translation, and by a buckling halfwave length in the longitudinal direction which is of the same order of magnitude as a representative width between plate junctures in the stiffened structure.

A set of three J-stiffened composite panels were tested for buckling response in [23]. The panels were of a variety of lengths, but each had two stiffeners and unsupported side-edges, and the loaded ends of each panel were potted. All three of the panels buckled in a "torsional" (or "twisting") mode, characterized by rotation of the stiffener sections about the lines of attachment to the panel skin, with compatible rotation of the skin at the joint line. The modes occur in halfwave lengths much greater than what would be expected for a pure local buckling mode in the sense described previously. Two of the three panels tested did exhibit postbuckling strength (the third suffered material failure upon buckling), but for each panel, the observed buckling load was significantly less than the theoretical buckling load. It was hypothesized that the panels are imperfection sensitive with regard to the onset of the twisting buckling mode [23].

The global (also called Euler or wide-column) buckling/postbuckling mode is characterized by a bowing type of response occurring over the length of the panel with little distortion of the cross-section, assuming that the side-edges are unsupported. If the side edges are supported, then the panel will bow in two coordinate directions in the manner of a simply-supported plate. The global mode of response is not investigated much in the recent literature, because it can be analyzed rather easily using wide-column theory or plate theory in conjunction with the extensional and bending stiffnesses of the panel cross-section. Some experimental results are presented by Tulk and Walker [24] for a wide blade-stiffened panel of homogeneous, isotropic material with simple end supports and unsupported side-edges, subjected to uniform end-shortening. For cases where no local buckling is induced, the postbuckling response is seen to be essentially neutral, meaning that for end-shortening values beyond the critical value, the load carried by the panel remains at about the critical value.

As is the case for rectangular plates, sudden changes in the mode shape during local postbuckling are observed for stiffened structures. A sudden increase in the number of halfwaves in the direction of the load axis is observed for locally postbuckled composite channels in [11]. Two nominally identical channel specimens were tested in compression in [11]. One specimen exhibited a mode change, whereas the other did not, again suggesting that imperfections in the specimens or test fixtures may play a role in producing the local-mode-change phenomenon.

The phenomenon of mode-change discussed above is often referred to as a manifestation of "modal interaction," because the two different displacement patterns observed are similar to two of the buckling mode shapes. While this form of modal interaction involves a sudden switching between two dominant shapes, there is a second type of modal interaction exhibited by stiffened panels which has received considerable attention since the mid-1960's. This second type of modal interaction occurs between local buckling and global buckling modes having critical loads which are relatively close in value. This type of modal interaction can cause the elastic strength of the structure to be highly sensitive to geometric imperfections.

In order to study the interaction of local and global buckling modes, a series of tests were performed on wide blade-stiffened panels of homogeneous isotropic material [24-27]. All panels had simply supported ends and unsupported side-edges. Panels with two different cross-section types were considered. The first type had stocky stiffeners which deformed little during local buckling and postbuckling, and the second type had thin stiffeners which participated significantly in local buckling and postbuckling. Panels of a wide variety of lengths were tested, and the effects of imperfections in the shapes of both the local and global buckling modes were studied. Imperfection sensitivity was demonstrated to be severe in some cases, causing as much as a 44% reduction in the elastic limit load compared to the theoretical buckling load. The sensitivity was found to be most extreme for configurations in which the local and global buckling eigenvalues were approximately the same, but significant imperfection sensitivity was observed in panels for which the two buckling eigenvalues differed by as much as a factor of two.

2.2.2 Analysis of Postbuckled Stiffened-Panels

2.2.2.1 General comments

The computer code STAGSC-1 [28,29] appears to be one of the most powerful tools available for the general nonlinear analysis of shell-type structures (including stiffened and unstiffened panels). It can use a variety of structural models, including finite elements, and its greatest strength is its implementation of strategies for dealing with complicated nonlinear phenomena. For example, limit points can be traversed using the constant-arc-length method of Riks [30], and the method of Thurston [31] is available in the code in order to navigate bifurcation off of a nonlinear load/response path, including the case where multiple bifurcation paths coincide [32]. STAGSC-1 represents a superior analytical method for assessing results obtained using simplified nonlinear analyses, but it is extremely expensive when used to simulate the nonlinear behavior of complicated structural configurations. The approaches to analysis reviewed in this section attempt to model nonlinear phenomena by more economical means. While the issues of traversing limit points and bifurcation points are important in performing a general nonlinear analysis, the emphasis in this review of analysis techniques is on the formulation of the solution to the governing equations as it affects the accuracy of the solutions obtained.

In 1945 Koiter [33] presented a general theory of the stability of equilibrium for elastic systems with conservative loading, and his work has served as the basis for a majority of work done since. Although Koiter addresses "stability," he addresses also the effects of geometric imperfections and the phenomena of postbuckling strength and imperfection sensitivity, all of which are demonstrated to have important practical consequences in structures for which stability is an issue. Koiter used a perturbation approach to study the equilibrium behavior of perfect and imperfect structures in the vicinity of the theoretical bifurcation point. While the approach of [33] has the strength of facilitating the analytical determination of parameters

which characterize the initial postbuckling response, the method is limited to a consideration of structural response in the neighborhood of the critical bifurcation point. Nonetheless the following important conclusions are drawn from [33]: i) buckling eigenfunctions can serve as useful shape functions in the nonlinear analysis of buckling-dominated structures, by helping to minimize the number of independent variables in an analysis, ii) the phenomenon of postbuckling strength is associated with a stable secondary equilibrium paths, iii) the phenomenon of imperfection sensitivity is associated with an unstable secondary equilibrium path, and iv) the degradation of load-carrying capability in imperfection-sensitive structures is dependent on the amplitude, and sometimes the sense (positive or negative), of shape imperfections. Regarding the third point above, it has been demonstrated analytically that for blade-stiffened panels with coincident critical loads for local and global buckling, a highly unstable postbuckling equilibrium path exists [34]. This confirms a theoretical basis for the possibility of imperfection sensitivity in stiffened panels.

The greater role played by transverse (out-of-plane) shear deformation in the buckling of composite plates compared to metal plates is well established [35], and thus, some authors include transverse shear deformation effects in buckling and postbuckling analyses [35-37]. Similarly, the nonlinear material behavior exhibited by some composites is emphasized by some authors in the analysis of composite structures [36]. Nonetheless, both transverse shear deformation and nonlinear material behavior produce higher-order effects which it seems reasonable to ignore for the sake of simplicity in developing a new method such as the one presented here.

One aspect shared by nearly all analytic or semi-analytic (mixed analytic and numerical) methods of analysis for postbuckling is the assumption that buckling mode shapes have harmonic forms along the length of the component plates. This assumption reduces the partial differential equations governing buckling to ordinary differential equations in terms of the transverse in-plane coordinate [5]. Similar simplifications can be made at many other steps in the mathematical derivations which lead to a method of nonlinear analysis, as will be shown

in Chapter 3. The sacrifice in obtaining these simplifications is a restriction in the type of support conditions which can be simulated at the longitudinal ends of a panel.

Based on the different elastic response modes observed in experiments, the analyses found in the literature can be discussed in terms of three distinct classes of behavior: global postbuckling, local postbuckling, and modal interaction. These classes are each considered in following sections.

2.2.2.2 *Analysis of global postbuckling*

In the analysis of global buckling and postbuckling, many researchers use the Bernoulli kinematic assumptions in performing wide-column analyses of stiffened panels [3,4,38]. The Bernoulli assumptions for thin-walled prismatic structures are analogous to the Kirchhoff assumptions for beams. According to the Bernoulli assumptions, cross-sections of a member remain flat and perpendicular to a longitudinal reference axis which deforms with the member in global buckling. These kinematic assumption, while valid for some configurations, will be unconservative for others because in-plane shearing of stiffeners and webs is not accounted for, and are not applicable to panels which are of finite width with supported side edges, for which the cross-sections must deform during global buckling deflection.

Giles and Anderson [39] established beam-column relationships for application to wide columns, which relate the mid-length bending moment to the axial load, pressure loading, initial bowing imperfection, and axial load eccentricity. In the PANDA2 design code [4], two options for a global buckling analysis are available. The first option is to represent a finite-width stiffened panel as a finite-width unstiffened panel with smeared stiffener properties, allowing the use of plate theory. The second option is a wide-column buckling analysis for a representative stiffener/skin unit of the panel. Bushnell [4] and Anderson and Stroud [40] simulate wide, clamped-end panels by modelling reduced-length panels with simply supported

ends. Bushnell uses a panel length reduced by the divisor $\sqrt{3.85}$; Anderson and Stroud select a divisor value of 2.

2.2.2.3 Analysis of local postbuckling

Local buckling analyses often use methods along the lines of plate buckling analyses, with the added complication that displacement compatibility and equilibrium must be satisfied where plates join. This has the consequence that the load multiplier is no longer separable as an isolated factor in the eigenvalue problem [5], so that a search technique must be used to locate the buckling eigenvalues. Assuming that displacements in a nonlinear analysis are represented as a perturbation expansion in the buckling modal amplitudes, the higher-order displacement contributions associated with nonlinear response are also more difficult to determine when compared to simple plate problems. For simple plates, the displacement contributions which are of second order in the modal amplitudes involve only in-plane displacements (see equations (2)), but for linked-plate problems, the in-plane displacements of one plate strip induce out-of-plane displacements in (noncoplanar) adjoining plate strips.

To reduce these complications, some authors use what Sridharan and Peng [41] refer to as the "classical assumptions" of local postbuckling deformations. These are [41]: "1) at a corner of the plate structure where two plates meet at an angle, the normal displacement w for each plate vanishes; 2) the normal stress resultant N_y in the transverse direction vanishes for each plate at the corner." A quantitative justification for the assumptions was given in [42]. For a case such as a blade-stiffened panel where one plate (the stiffener) joins at an angle to a second plate which is locally continuous (the panel skin), the "classical assumption" as stated can be modified to improve the physical accuracy of the assumptions. In the modified form, the stiffener introduces no *discontinuity* in the normal stress resultant N_y in the panel skin. This allows for a nonzero value of N_y in the skin at the line of attachment of the stiffener. In certain circumstances the "classical assumptions" discussed above are fundamentally in-

correct or inaccurate, such as when three plate strips with a common joint lie in three different planes, or when two adjoining plate strips lie in planes which are nearly, but not exactly, parallel.

2.2.2.4 Analysis of modal interaction

The analysis of modal interaction and imperfection sensitivity usually involves the use of modal amplitudes as generalized coordinates. Imperfection shapes are also expressed in terms of modal imperfection amplitudes corresponding to the buckling mode-shapes included in the analysis. In other words, the modal imperfection amplitudes are the Fourier coefficients of a series expression for the imperfection shape in terms of buckling eigenfunctions.

The first study directed at analyzing the imperfection sensitivity of compressively loaded linked-plate structures is generally attributed to van der Neut [43]. He modelled an idealized thin-walled column with a rectangular cross-section. The two flanges are assumed to carry the entire axial load, and they are held in relative position, with simple support at the side edges, by two webs which are infinitely stiff in shear but which support no axial load. A local/global division is used in the analysis, in which the global buckling/postbuckling behavior is based on the tangent extensional and bending stiffnesses of the idealized cross-section, which in turn depend on the curvature due to global bending. The local postbuckling analysis uses analytical results for the postbuckling response of long, simply supported rectangular plates strips, in order to compute the axial stiffness of each postbuckled flange. The axial and bending stiffnesses of the column cross-section are thus easily determined. Imperfections in the shape of local and global buckling modes are accounted for. Van der Neut's results predict imperfection sensitivity in the idealized column, particularly when the theoretical global buckling load is equal to or somewhat greater than the load for local buckling. Imperfections in the shape of the local buckling mode lead to global buckling at loads below the theoretical local buckling load. In [44], van der Neut applied a similar idealized approach to the analysis

of hat-stiffened panels, in which the panel skin and the cap of the hat are assumed to carry all of the axial load. Imperfection sensitivity was found to be less severe than in the thin-walled column. Crawford and Hedgepath [45] use a similar approach to the analysis of a truss-core sandwich panel. A certain degree of imperfection sensitivity was predicted. The general approach of a local/global division in the analysis is adopted in many later studies.

Around the same time as van der Neut's study, Graves-Smith [46] performed a detailed analysis of the interaction of local and global buckling in thin-walled metallic columns of rectangular section. Plastic deformation of the material was also accounted for. The results predicted imperfection sensitivity in the elastic regime, due to interaction of the local and global buckling modes. Graves-Smith computed the deflection fields which were quadratic in the modal amplitudes (as were shown to play a role in postbuckled plates), of which one is bilinear in the local and global modal amplitudes. This latter displacement field, which was observed experimentally by Bijlaard and Fisher in 1953 [41], has the same approximate cross-sectional shape as one of the secondary (higher in eigenvalue) local buckling modes with the same number of halfwaves along the length of the column as the primary local buckling mode. This observation has led to approaches in which the secondary local buckling mode is included in the analysis as another interacting buckling mode [38,47-49]. This approach offers certain advantages which are discussed in later sections.

A blade-stiffened panel configuration studied by Tvergaard [50,51] has subsequently been studied by several other researchers [4,38,52-54]. The Tvergaard panel is a wide panel with uniformly spaced blade stiffeners (without flanges) on one side of the panel. The panel is subjected to uniform end-shortening at simply supported ends (loaded along the neutral bending axis). The configuration is classified as singly symmetric in the two dominant buckling modes. This means that the local buckling mode is symmetric with regard to positive or negative sense, whereas the global mode is not symmetric; global buckling deflections of one sense will increase the compression on the skin and decrease the compression near the stiffener tips, whereas global deflections of the other sense will have the opposite effect. In reference [50], Tvergaard used Koiter's perturbation approach of [33] to analyze a configura-

tion with coincidental buckling eigenvalues for the local and global buckling modes. The contributions to deflection fields were limited to the linear in-plane displacements, and out-of-plane displacements in the shapes of the two buckling modes. Total potential energy terms through the third order were retained. An often-cited result of Tvergaard's (Figure 4 of [50]) is the fall-off in the limit load with increasing imperfection amplitudes in the shapes of the local and global buckling modes. For the test case reported, imperfection amplitudes which are on the order of the plate thickness cause a reduction in load capacity of over fifty percent.

Subsequent, more accurate analyses by Tvergaard [51], Koiter and Pignataro [52], and others have led to the conclusion that while the results in [50] are asymptotically correct as the imperfection amplitudes go to zero, the results are overly pessimistic for imperfection amplitudes of practical significance. The analyses of [51] and [52] both feature the following significant differences from the original analysis of Tvergaard: potential energy terms are retained through the fourth order in the modal amplitudes rather than the third order, and displacement contributions which are quadratic in the modal amplitudes are included. This implies that for solutions of reasonable accuracy, it may be necessary for one or both of the above-mentioned elements to be present in the analysis.

Amplitude modulation: Koiter and associates [47,52,53,55] used a concept called "amplitude modulation" in order to provide simple, relatively accurate analyses for thin-walled columns, and wide panels with evenly spaced stiffeners. Its use was inspired by the fact that the interaction of the local buckling mode (which features multiple halfwaves of uniform amplitude along the length) and the global buckling mode (which introduces a bending curvature that varies as a simple half sine-wave over the length) cause the local buckling waveform to be modulated, meaning that the amplitudes of the wave peaks are caused to vary along the length of the member. Similarly, the waveforms of all additional displacements induced by the interaction of the two mentioned modes exhibit amplitude modulation. The representation of an amplitude-modulated local buckling mode using unaltered buckling modes requires several modes of similar transverse profile, but with different halfwave lengths.

In order to model the phenomenon of amplitude modulation without resorting to the use of a large number of buckling modes, Koiter and Kuiken [55] introduced the "amplitude modulation function," which is used as a multiplying factor for local buckling mode shapes. To illustrate this concept, assume that x is the longitudinal coordinate axis, and that the x -dependence of a local buckling mode is given by $\sin(m\pi x/L)$ where m is the integer halfwave number and L is the length of the structure. Using the modulation function $f(x)$, the modulated local buckling waveform will have an x -dependence given by $f(x) \sin(m\pi x/L)$. If more than one local buckling mode is used as a shape function, then each mode has its own amplitude modulation function. The modulating functions are initially unknown and are determined as a part of the solution procedure. A benefit to the use of the amplitude modulation concept is that each of the participating modes represents a distinct type of structural deformation. This contributes to an intuitive understanding of the structural response. A drawback of the amplitude modulation concept as used in the noted references is that it involves the assumption that the global buckling response is one-dimensional, as is the case for columns or wide columns (wide panels with unsupported side edges). It is not clear whether the concept can be meaningfully applied to configurations for which the global buckling deformations are highly two-dimensional, such as would be the case for a panel with supported side-edges.

While the early studies of Koiter et al which employed amplitude modulation concepts [52,53,55] made use of only the global buckling mode and the primary local buckling mode, it is shown in [47] that when significant local buckling deflections occur on both sides of the neutral axis, the method must include a second local buckling mode. The second local buckling mode is one which has the same longitudinal halfwave number as the primary local buckling mode, but which has a transverse profile similar to that of the so-called mixed second-order field associated with the interaction of the global mode and the primary local mode. The second local buckling mode is represented in conjunction with an amplitude modulation function.

Doubly symmetric structures: In the earlier discussion of the Tvergaard panel, it was noted that the structure is singly symmetric. It is shown in [56] that for structures which are

doubly symmetric with regard to buckling (such as a thin-walled rectangular column, or a panel stiffened symmetrically on both sides), the omission of total potential energy terms which are of order greater than three in the modal amplitudes (as is done in many applications of Koiter's general theory) precludes the prediction of modal interaction. Thus, a general method of analysis must consider the equivalent of total potential energy terms through the fourth order.

2.2.2.5 General methods of analysis

Probably the most highly developed methods for the study of imperfection sensitivity and modal interaction in compressively loaded linked-plate structures are those of Sridharan and his associates, late versions of which are described in [38,49]. The methods make use of many approximation concepts developed by Koiter et al [47,52,53,55]. The methods are restricted to columns of general cross-section or to wide panels with evenly spaced stiffeners, with homogeneous, isotropic material properties. The Bernoulli kinematic assumptions (Section 2.2.2.2) are used to describe global buckling mode-shapes, and amplitude modulation functions (Section 2.2.2.4) are employed. The methods thus require the use of only three or four buckling eigenfunctions to obtain accurate predictions of elastic limit loads for imperfect structures featuring modal interaction. A finite strip method is used for determining local buckling mode-shapes and second-order displacement contributions, and a finite element method is used to discretize the amplitude modulation functions along the longitudinal axis of the structure. The "classical assumptions" of local postbuckling analysis, discussed in Section 2.2.2.3, are used in appropriate steps of the analysis. A drawback of this general method is the limitation imposed by the Bernoulli assumptions, namely that the global buckling response is one-dimensional.

The PASCO design code for stiffened panels [2] has the capability to account for some geometrically nonlinear effects. The heart of the PASCO design code is the VIPASA computer

code [5] for the analysis of the buckling and vibration of stiffened composite panels, so the method of VIPASA merits attention here. VIPASA computes buckling (and vibration) eigensolutions for prismatic linked-plate structures subjected to in-plane loads, using a finite strip method. The displacement functions used on each plate strip satisfy the buckling equations exactly, and along the lines where plate strips join, the conditions of equilibrium and displacement compatibility are satisfied. Thus, the solutions are considered to be exact within the context of non-shear-deformable plate theory, and within the limitations of the boundary conditions at the panel ends. An important feature of VIPASA is its ability to obtain, with certainty, any specified number of eigensolutions at a given longitudinal halfwave-length, beginning with the one corresponding to the critical eigenvalue, and continuing with solutions corresponding to the ascending sequence of eigenvalues.

The panel sizing code PASCO [2] which uses the VIPASA analysis makes use of the beam-column relationships derived in [39] to determine a uniform bending moment which is applied to a panel to account for the effects of bowing imperfections, pressure loading, and eccentricity of the end load. The uniform bending moment has the effect of redistributing the compressive stresses in the panel section, so that the local buckling mode-shape and the local buckling load will be modified. The global buckling analysis is not affected. While this simple correction is a first step toward accounting for imperfections, the effects of imperfections in the shapes of local buckling modes are not modelled. An additional limitation is that the beam-column relationships apply only for configurations for which the global buckling response is one-dimensional.

The two panel sizing codes POSTOP [3] and PANDA2 [4] use analyses with some similarities of approach. Both use a local/global split of the analysis. A panel is assumed to have many evenly spaced stiffeners, thus permitting use of a representative unit-width panel cell when analyzing local buckling and postbuckling. The local postbuckling deformation is dependent on the value of curvature at the mid-length due to global postbuckling (overall bowing). Deformation in the shape of the global buckling mode is based on the beam-column relationships mentioned earlier and depends on the tangent extensional and bending stiffness

properties of the panel, as determined by the local postbuckling state. Thus, the solution process iterates between the local and global levels. Both codes are limited to panels which consist of a continuous skin with attached stiffeners (or, in the case of PANDA2, truss-core sandwich panels [57]), with POSTOP additionally limited to configurations with open-section stiffeners. The two design codes use different approaches to the analysis of the unit cell, but these approaches are not discussed here. There are other significant differences in the modelling capabilities of the two codes. POSTOP can model only flat stiffened panels, and can not model the effects of an imperfection in the shape of the local buckling mode. PANDA2 can model cylindrical stiffened panels, and can treat imperfections in the shape of the local buckling mode. Because they use the unit cell concept, both POSTOP and PANDA2 are unable to consider the effects of support at the side boundaries, although in the absence of modal interaction PANDA2 can perform a smeared-stiffener analysis of a panel with supported side boundaries. PANDA2 makes available a large number of simple models for analyzing stiffened panels, giving the analyst many options, but requiring careful judgement as to which, if any, of the models are valid for computing the response of a given configuration.

A procedure for the postbuckling analysis of laminated composite stiffened panels is presented by Sheinman and Frostig [58]. Blade, T, and L shaped stiffeners are accommodated in the procedure. The method is mixed analytic and numerical, using beam eigenfunctions to describe the longitudinal variation of out-of-plane displacements, and using a finite-difference representation to describe the distribution of the beam eigenfunctions on the cross-section of the panel. It is difficult to make a general assessment of the method based on the limited results presented in [58].

Analytically determined buckling mode-shapes for a stiffened panel with a rather complicated cross-sectional shape are presented in Figure 1 of [59]. Some of the mode shapes, obtained at a variety of longitudinal halfwave lengths, are unusual and defy obvious classification as local, global or twisting modes. Some of the general methods of analysis that were discussed in this section rely on the classification of buckling mode-shapes into the specified

categories, and thus can not be used to predict certain types of behavior which are exhibited by structures with complicated cross-sections.

2.2.3 Current Research Effort

A number of general methods of analysis have been developed which can analyze in economical fashion (compared to finite element analysis) the nonlinear response of compressively loaded prismatic structures (Section 2.2.2.5). Each of these methods places various limitations on the range of structural configurations and material anisotropy that can be modelled, and two of the methods lack the ability to model local-mode shape imperfections. The new method described in this dissertation offers analysis capabilities which duplicate many capabilities of existing methods, but the new method should also add new capabilities, and perhaps offer a more economical alternative to some of the existing methods.

In the current method, it is assumed that nonlinear plate theory governs the behavior of each plate strip in the linked-plate structure. At the heart of the theoretical approach used here is the expression of postbuckling displacements as an expansion in terms of buckling eigenfunctions. This general approach has similarities to both the series solution approach of Levy [13] for postbuckled plates, and the general approach to stability analysis of Koiter [33]. Unlike the plate problem considered by Levy, the class of structures considered here do not, in general, admit exact series solutions in postbuckling, so a perturbation approach is suggested. Unlike the perturbation approach of Koiter, it is desired here to allow for the incorporation of an arbitrary number of buckling mode shapes having associated critical buckling loads not necessarily in the proximity of the primary buckling load. The perturbation approach used here has the following features:

1. The set of perturbation parameters is the set of "modal amplitudes" corresponding to a set of buckling mode shapes.

2. In the perturbation expansion of displacements, contributions through the second order in the modal amplitudes are retained.
3. A perturbation expansion of the plate Euler equations is used to obtain both the equations governing the buckling eigensolutions and the equations governing the second-order displacement fields.
4. Any selected number of buckling mode shapes may be incorporated in an analysis.
5. The virtual work statement for the structure is used to form a set of nonlinear algebraic equations governing approximate equilibrium solutions; terms are retained in the equations consistent with total potential energy contributions through the fourth order in the modal amplitudes.

The importance of incorporating second-order displacement contributions was discussed in Sections 2.1.2 and 2.2.2.4, and the importance of fourth-order total potential energy contributions was discussed in Section 2.2.2.4. Indeed, the features described above are sufficient to obtain exact series solutions for the postbuckling behavior of simple rectangular plates, such as the solutions given in [13,14]. While the current method is technically a perturbation method, it is hoped that with the features described, the current method will be able to provide accurate solutions well into the postbuckled regime, for arbitrary configurations from the general class under consideration.

A major foundation for implementing the method outlined above, and a major inspiration for the overall effort documented here, is the VIPASA computer code [5], which is capable of determining the buckling eigensolutions for the general class of structures under consideration. The method of VIPASA can account for the elastic properties of some classes of laminated composite plates, and has great flexibility with regard to the configurations which can be modelled. Some aspects of the VIPASA analysis are discussed in later sections. A goal here was to develop a nonlinear analysis capability which retains the flexibility of the VIPASA

method; however, some additional restrictions were adopted here beyond those of VIPASA. While VIPASA is capable of modelling both panels with applied shear loading and panels whose component plates feature bending-twisting coupling, these two capabilities are not included in the current method. When modelled with VIPASA, both shear loading and bending-twisting coupling cause the buckling nodal lines to be skewed relative to the specified boundaries at the longitudinal ends of a rectangular panel. This brings into question the validity of the buckling results. The computer code VICON (Vipasa with CONstraints) [60] has been developed to rectify the shortcomings of VIPASA with regard to the skewing of nodal lines, but the buckling eigensolutions take on a much more complicated mathematical form than those used in the current effort. It was judged to be prudent to adopt the restrictions mentioned above for a first attempt at developing a general nonlinear analysis capability. The family of configurations which can be modelled by the current method is described in detail in the next chapter.

3.0 Method of Analysis

This chapter begins with a specification of the defining characteristics of the stiffened structures to be considered, and a development of the equations which govern the equilibrium of the structure. The method of solution is a perturbation approach. A general form is assumed for the expression of displacements, and three different boundary-value problems are established which govern the shape functions used in the displacement expressions. The procedures used to solve the three boundary-value problem types are discussed in detail. The theorem of virtual work is used to obtain a set of nonlinear algebraic equations from which approximate equilibrium solutions are obtained. In this chapter, the term "structure" is used to refer to arbitrary configurations from the class of structures for which the method is intended. The term "panel" is used when a particular concept under discussion, such as biaxial loading, is most applicable to nominally flat stiffened- or unstiffened-panel configurations.

3.1 Equilibrium Condition and Boundary-Value Problem

Geometrically nonlinear plate theory is assumed to govern the equilibrium behavior of each plate strip within a linked-plate structure, and thus this section begins with a discussion of the geometrically nonlinear plate theory. Next, the characteristics of a general linked-plate structure are discussed. Finally, equations governing the equilibrium of the structure are de-

veloped, both in the form of a boundary value problem, and in the form of a virtual work statement.

3.1.1 Plate Strips

The development of the equations governing the equilibrium of the individual plate strips is presented in detail in Appendix A. The guiding philosophy for the plate theory is presented in this section, and the governing equations are summarized.

3.1.1.1 Strain-displacement equations

A component plate strip of a linked-plate structure is shown in Figure 2. The plate strip is rectangular in planform, and has an associated x - y - z coordinate system, where the x - y plane lies at the mid-surface of the undisplaced plate. The three displacement components of the mid-surface are denoted by $\{u\} = [u(x,y) \ v(x,y) \ w(x,y)]^T$, corresponding to the x -, y -, and z -directions, respectively. The plate strip has dimensions of length L and width b in the x - and y -directions, respectively, with the origin of the coordinate axes located at one corner of the strip. Initial shape imperfections are represented using the convention that for an unloaded imperfect plate-strip the displacements degenerate to the imperfection shape $\{u\} = \{u^o\} = [u^o \ v^o \ w^o]^T$, and all stress resultants are zero.

The in-plane strain components, $\{\epsilon\} = [\epsilon_x \ \epsilon_y \ \gamma_{xy}]^T$, are restricted to be small compared to unity, but rotation amplitudes are permitted to be moderately large, including in-plane rotations. (Unlike plates with more conventional boundary conditions, a plate strip in a linked-plate configuration can undergo significant in-plane rotation if, for example, it has the role of a stiffener web which is participating in the global buckling of a stiffened panel.) The plate strip is assumed to have a uniform thickness which is sufficiently small relative to the width

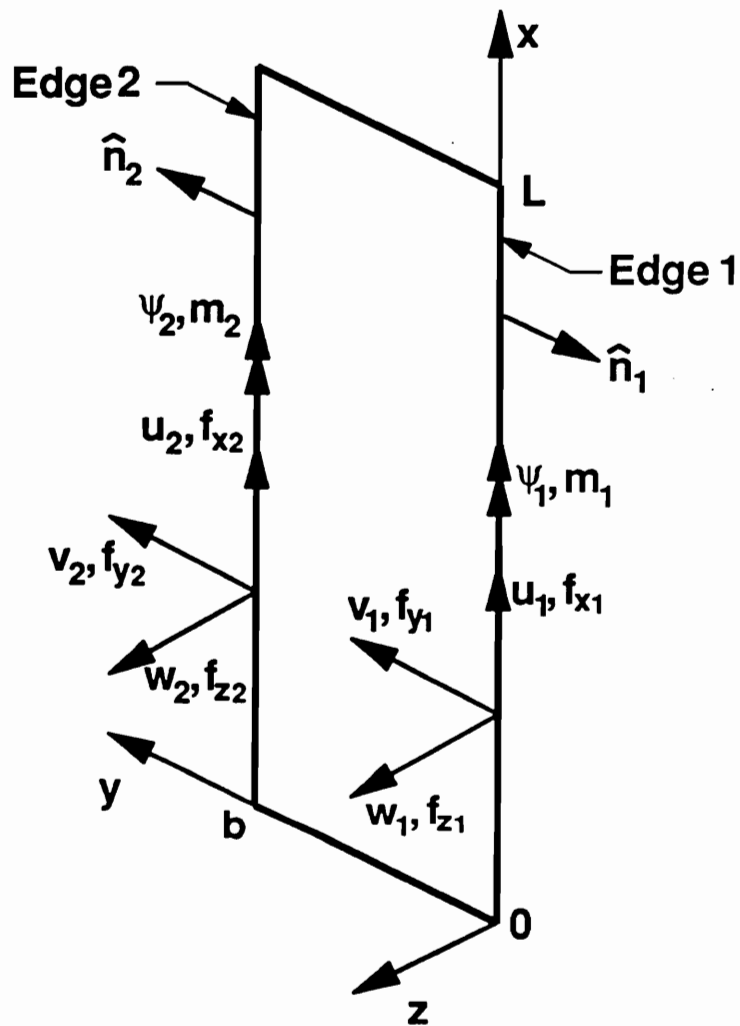


Figure 2. Generalized displacements and generalized force-resultants at the side edges of a plate strip.

and length such that the Kirchhoff-Love kinematic assumptions accurately describe the distribution of the in-plane strain components through the thickness of the plate. Given the above assumptions, the expression for the distribution of in-plane strains in a perfect plate strip is given by (equations (A5))

$$\{\varepsilon(x, y, z)\} = \{\varepsilon^c(x, y)\} + z\{\kappa^c(x, y)\} \quad (3)$$

where the mid-surface strains, $\{\varepsilon^c\} = [\varepsilon_x^c \ \varepsilon_y^c \ \gamma_{xy}^c]^T$, and the mid-surface curvatures, $\{\kappa^c\} = [\kappa_x^c \ \kappa_y^c \ \kappa_{xy}^c]^T$, are given by (equations (A3) and (A6))

$$\{\varepsilon^c\} = \begin{Bmatrix} u_{,x} + .5(v_{,x}^2 + w_{,x}^2) \\ v_{,y} + .5(u_{,y}^2 + w_{,y}^2) \\ u_{,y} + v_{,x} + w_{,x}w_{,y} \end{Bmatrix} \quad \{\kappa^c\} = - \begin{Bmatrix} w_{,xx} \\ w_{,yy} \\ 2w_{,xy} \end{Bmatrix} \quad (4)$$

where, for example, $u_{,x}$ denotes the partial derivative of u with respect to x .

In order to account for geometric shape imperfections, define mechanical strains and curvatures of the mid-surface, $\{\varepsilon^m\}$ and $\{\kappa^m\}$, respectively, to be strains and curvatures which go to zero with the removal of all loads. They are given by the expressions

$$\{\varepsilon^m\} = \begin{Bmatrix} [u_{,x} + .5(v_{,x}^2 + w_{,x}^2)] - [u_{,x}^0 + .5(v_{,x}^{0^2} + w_{,x}^{0^2})] \\ [v_{,y} + .5(u_{,y}^2 + w_{,y}^2)] - [v_{,y}^0 + .5(u_{,y}^{0^2} + w_{,y}^{0^2})] \\ [u_{,y} + v_{,x} + w_{,x}w_{,y}] - [u_{,y}^0 + v_{,x}^0 + w_{,x}^0w_{,y}^0] \end{Bmatrix} \quad (5)$$

$$\{\kappa^m\} = - \begin{Bmatrix} w_{,xx} - w_{,xx}^0 \\ w_{,yy} - w_{,yy}^0 \\ 2w_{,xy} - 2w_{,xy}^0 \end{Bmatrix}$$

The mid-surface mechanical strains and curvatures are those to which the stress resultants are proportional.

3.1.1.2 Conditions for equilibrium

The plate material is assumed to be linearly elastic, and all loads are assumed to be applied at the plate edges. The transverse shear strains γ_{xz} and γ_{yx} are neglected, consistent

with the Kirchhoff-Love assumptions, and the transverse normal stress σ_z is neglected. The theorem of virtual work for the plate strip is (equation (A15) of Appendix A evaluated for a rectangular plate)

$$\begin{aligned}
 \delta W_p &= \int_A (N_x \delta \epsilon_x^c + N_y \delta \epsilon_y^c + N_{xy} \delta \gamma_{xy}^c + M_x \delta \kappa_x^c + M_y \delta \kappa_y^c + M_{xy} \delta \kappa_{xy}^c) dA \\
 &\quad - \int_0^b [\hat{f}_x \delta u + \hat{f}_y \delta v + \hat{f}_z \delta w - \hat{M}_x \delta w_{,x}] \Big|_{x=0, L} dy \\
 &\quad - \int_0^L [\hat{f}_x \delta u + \hat{f}_y \delta v + \hat{f}_z \delta w - \hat{M}_y \delta w_{,y}] \Big|_{y=0, b} dx \\
 &= 0
 \end{aligned} \tag{6}$$

where A is the planform area of the plate strip, and where p denotes the plate strip index number. Stress resultants $\{N\} = [N_x, N_y, N_{xy}]^T$ and $\{M\} = [M_x, M_y, M_{xy}]^T$ introduced above follow standard definitions, provided in Appendix A (equations (A16)). The edge force-resultants f_x , f_y , and f_z are given along x -normal edges by

$$\begin{aligned}
 f_x &= n_x N_x \\
 f_y &= n_x (N_{xy} + N_x v_{,x}) \\
 f_z &= n_x (M_{x,x} + 2M_{xy,y} + N_x w_{,x} + N_{xy} w_{,y})
 \end{aligned} \tag{7}$$

where $n_x = \pm 1$, and along y -normal edges by

$$\begin{aligned}
 f_x &= n_y (N_{xy} + N_y u_{,y}) \\
 f_y &= n_y N_y \\
 f_z &= n_y (2M_{xy,x} + M_{y,y} + N_{xy} w_{,x} + N_y w_{,y})
 \end{aligned} \tag{8}$$

where $n_y = \pm 1$.

The theorem of virtual work is also expressed here in an alternate form, derived through the application of Green's theorem (see Appendix A equations (A24), (A27)-(A29)):

$$\begin{aligned}
\delta W_p = & - \int_A \{ [N_{x,x} + N_{xy,y} + (N_y u_{,y})_{,y}] \delta u + [N_{xy,x} + N_{y,y} + (N_x v_{,x})_{,x}] \delta v \\
& + [M_{x,xx} + 2M_{xy,xy} + M_{y,yy} + (N_x w_{,x} + N_{xy} w_{,y})_{,x} + (N_{xy} w_{,x} + N_y w_{,y})_{,y}] \delta w \} dA \\
& + \int_0^b [(f_x - \hat{f}_x) \delta u + (f_y - \hat{f}_y) \delta v + (f_z - \hat{f}_z) \delta w - (M_x - \hat{M}_x) \delta w_{,x}] |_{x=0, L} dy \\
& + \int_0^L [(f_x - \hat{f}_x) \delta u + (f_y - \hat{f}_y) \delta v + (f_z - \hat{f}_z) \delta w - (M_y - \hat{M}_y) \delta w_{,y}] |_{y=0, b} dx \\
= & 0
\end{aligned} \tag{9}$$

The above expression is used in establishing the plate Euler equations, and the boundary-value problem for the linked-plate structure.

The Euler equations determined from the above equations are (Appendix A equations (A25))

$$N_{x,x} + N_{xy,y} + (N_y u_{,y})_{,y} = 0 \tag{10a}$$

$$N_{xy,x} + N_{y,y} + (N_x v_{,x})_{,x} = 0 \tag{10b}$$

$$M_{x,xx} + 2M_{xy,xy} + M_{y,yy} + (N_x w_{,x} + N_{xy} w_{,y})_{,x} + (N_{xy} w_{,x} + N_y w_{,y})_{,y} = 0 \tag{10c}$$

The associated boundary conditions are given in equations (A26) of Appendix A, but they require modification for application to linked-plate problems, an issue discussed in a later section.

3.1.1.3 Side-edge conditions

The structural configurations under consideration are composed of plate strips linked together along mutual side-edges, so the generalized displacements and generalized force-resultants along the side edges are given special notation to facilitate their usage at various steps in the analysis. The unit normal vector at a side edge is given by $\hat{n} = n_y \hat{j}$, where

$n_y = 1$ or -1 . Each side edge of the strip is given an index number, e , $e = 1, 2$, and the associated y -coordinate, y_e , and y -normal unit vector component, n_y , are given by

$$[y_e, n_y] = \begin{cases} [0, -1] & \text{for } e = 1 \\ [b, 1] & \text{for } e = 2 \end{cases} \quad (11)$$

The generalized displacements and generalized force-resultants along edge e are denoted by $\{u_e\} = [u_e, v_e, w_e, \psi_e]^T$, and $\{f_e\} = [f_{xe}, f_{ye}, f_{ze}, m_e]^T$, respectively, and follow the conventions shown in Figure 2. The edge rotation angle, ψ_e , is the gradient of w in the y -direction, evaluated at the appropriate edge:

$$\psi_e = (w, y) \Big|_{y_e} \quad (12)$$

Force resultants f_{xe} , f_{ye} , and f_{ze} are forces per unit edge-length acting in the x -, y -, and z -directions, respectively, and m_e is the edge bending moment per unit edge-length. The generalized force-resultants at the side edges are expressed in terms of the plate stress resultants as follows:

$$\begin{aligned} f_{xe} &= n_y(N_{xy} + N_y u, y) \\ f_{ye} &= n_y N_y \\ f_{ze} &= n_y(2M_{xy, x} + M_{y, y} + N_{xy} w, x + N_y w, y) \\ m_e &= -n_y M_y \end{aligned} \quad (13)$$

3.1.1.4 Plate constitutive equations

The elastic properties of each plate strip are assumed to be those of a balanced, symmetric laminated composite plate, where in addition the bending-twisting coupling stiffness terms D_{16} and D_{26} are neglected. For this class of materials, the relationships between the stress resultants and the mid-surface mechanical strains and curvatures have the following form:

$$\{N\} = [A]\{\varepsilon^m\} \quad \{M\} = [D]\{\kappa^m\} \quad (14)$$

where

$$[A] = \begin{bmatrix} A_{11} & A_{12} & 0 \\ A_{12} & A_{22} & 0 \\ 0 & 0 & A_{66} \end{bmatrix} \quad [D] = \begin{bmatrix} D_{11} & D_{12} & 0 \\ D_{12} & D_{22} & 0 \\ 0 & 0 & D_{66} \end{bmatrix} \quad (15)$$

The above equations are a reduced form of the relationships given for general laminates in Appendix A equation (A30). configurations. The stiffness terms in the matrices above follow conventional definitions given by, for example, Jones [61]. The matrices $[A]$ and $[D]$ may be different for different plate-strips within the linked-plate structure.

3.1.2 Linked-Plate Structures

In this section, the equations which govern the equilibrium and determine the side-edge conditions for each plate strip are used to specify a boundary value problem for the linked-plate structure. First, parameters which define the structural configuration are discussed. Equations are introduced for transforming quantities between the global coordinate system and the local coordinate systems of each plate. Conventions are given for the specification of panel loading and for the boundary conditions along the side boundaries of the structure. The nature of the boundary conditions along the longitudinal ends of the panel are discussed, and the conditions for equilibrium of the structure are established.

3.1.2.1 Specification of geometry

The linked-plate structure has an associated global x-y-z coordinate system, where the global axes share a common x-scale with the local coordinate systems of the plate strips. If

the linked-plate structure is a nominally flat panel, then it is assumed that the global y -axis extends in the direction of the panel width. The overall dimensions are L in the x -direction, and B in the y -direction. A set of "node lines," corresponding to the free edges of plate strips and the joints between connected plate strips, run parallel to the x -axis. Node lines are so named because of the analogy with nodes in a finite element model, and are not to be confused with the node lines of a buckling mode shape. The generalized displacements at the side edge of a plate strip are rigidly linked to the generalized displacements of a node line. While each node line represents a boundary of sorts, it will be assumed in the present treatment that only two of the node lines in a configuration are designated as boundary node-lines upon which displacement boundary conditions or nonhomogeneous load boundary conditions are imposed. It is also assumed that the boundary node-lines coincide with the limits of the global y -domain of the panel. Some of these features and labeling conventions are shown for a sample configuration in Figure 3.

Several vectors and matrices are used to establish the geometry of the linked-plate structure. Each plate strip is assigned an index number, p , $p = 1, 2, \dots, P$, where P is the total number of plate strips. Each node line is assigned an index number, n , $n = 1, 2, \dots, N$, where N is the total number of node lines. A vector $\{R_n\}$, of length N , is defined such that the number of plate strips which join at node-line n is given by R_n . Let Q be the maximum number of plate strips joining at any node line, i.e. let Q be the largest element in the vector $\{R_n\}$. Then two matrices, $[S_{nr}]$ and $[E_{nr}]$, each having dimensions N by Q , define the connectivity of the configuration, as follows: if p is the index number of the r^{th} plate strip connecting to node line number n , and the index number of the edge through which the plate strip connects is e (see equations (11)), then $S_{nr} = p$ and $E_{nr} = e$. For those nodes where fewer than Q plate strips join, i.e. where $R_n < Q$, the corresponding elements in the matrices $[S_{nr}]$ and $[E_{nr}]$ are unused.

As an example of the preceding notation, consider the stiffened panel shown in Figure 3, where the plate index numbers and the node line numbers are shown. The panel has three plate strips ($P = 3$) and four node lines ($N = 4$), with up to three plate strips joining at any node line ($Q = 3$). The vector $\{R_n\}$ and the matrices $[S_{nr}]$ and $[E_{nr}]$ are given by

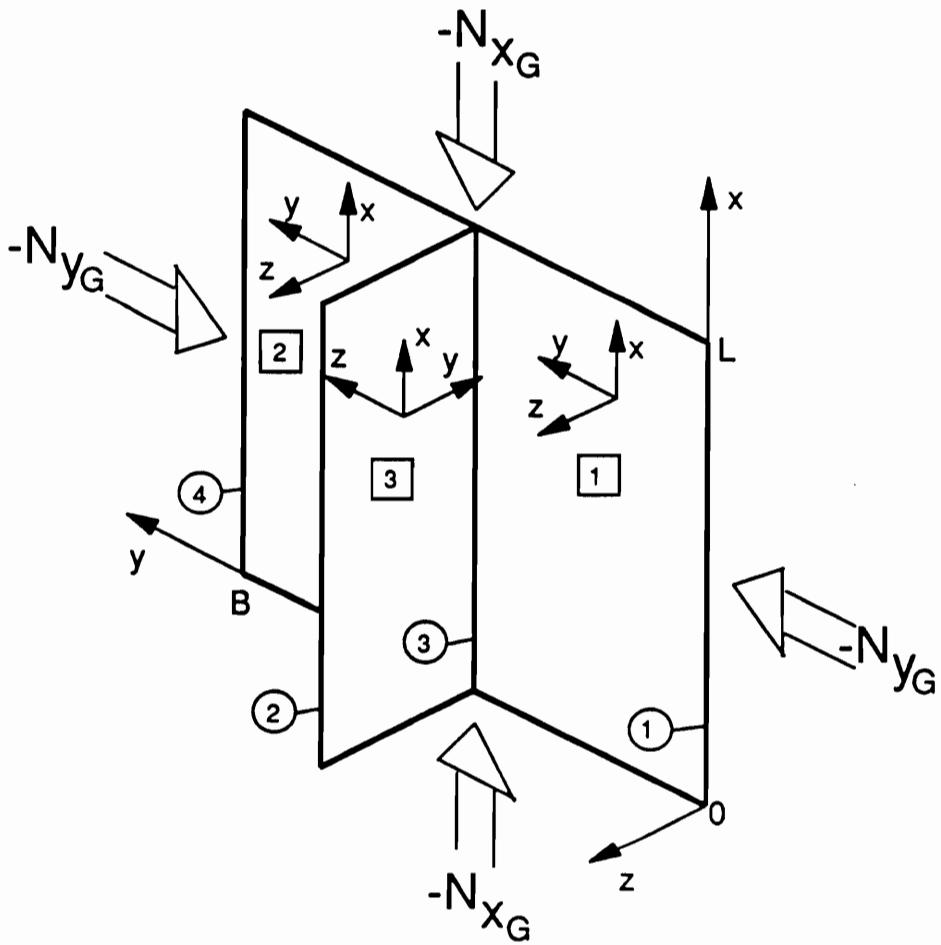


Figure 3. Stiffened panel showing plate-strip numbers, node-line numbers, and labeling conventions: The local plate-strip axes shown don't reflect actual locations of the origins.

$$\{R_n\} = \begin{Bmatrix} 1 \\ 1 \\ 3 \\ 1 \end{Bmatrix} \quad (16)$$

$$[S_{nr}] = \begin{bmatrix} 1 & 0 & 0 \\ 3 & 0 & 0 \\ 1 & 2 & 3 \\ 2 & 0 & 0 \end{bmatrix} \quad (17)$$

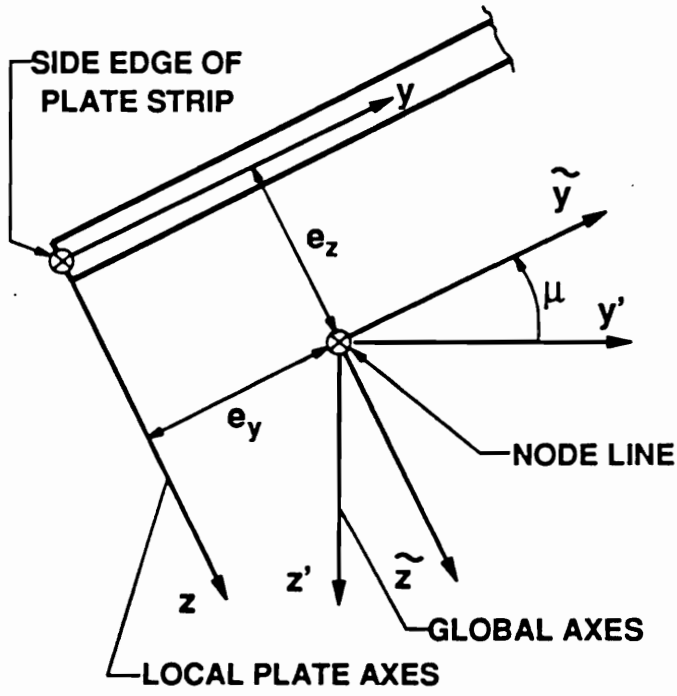
$$[E_{nr}] = \begin{bmatrix} 1 & 0 & 0 \\ 1 & 0 & 0 \\ 2 & 1 & 2 \\ 2 & 0 & 0 \end{bmatrix} \quad (18)$$

where zeroes denote unused array positions.

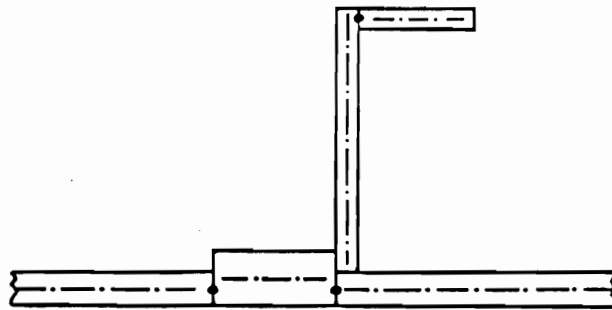
3.1.2.2 Generalized displacements and forces at a node line

In general, there is an angular displacement μ between the local y - z axes of a plate strip and the global y - z axes. In order to model some joint geometries more accurately, a small eccentricity is allowed between the side-edge of a plate strip and the associated node line. The eccentricity has measures e_y and e_z . The configuration measures are depicted along with the angle μ in Figure 4(a), and the cross-section of an idealized configuration having nonzero eccentricities is shown as an example in Figure 4(b).

The generalized displacements and generalized force-resultants along a node line, denoted $\{U^n\} = [U^n \ V^n \ W^n \ \Psi^n]^T$, and $\{F^n\} = [F_x^n \ F_y^n \ F_z^n \ M^n]^T$, respectively, are defined with respect to the global coordinate system, and follow the same conventions as the corresponding measures at the edges of a plate strip, $\{u_e\}$ and $\{f_e\}$ (see Figure 2). In order to establish transformation rules relating $\{u_e\}$ with $\{U^n\}$, consider a third coordinate system, $(\tilde{x} \ \tilde{y} \ \tilde{z})$, which is parallel to the local coordinate system of the plate strip, but which has its origin located on the node line, as shown in Figure 4. The following transformation rules relating the gen-



a) Definitions



b) Example of a configuration with nonzero eccentricities (from [5]).

Figure 4. Eccentricity measures e_y and e_z , and the local-to-global orientation angle μ .

eralized edge displacements in the three coordinate systems were established by Wittrick and Williams [5]:

$$\begin{aligned}
 \tilde{u}_e &= U^n \\
 \tilde{v}_e &= V^n \cos \mu - W^n \sin \mu \\
 \tilde{w}_e &= V^n \sin \mu + W^n \cos \mu \\
 \tilde{\psi}_e &= \Psi^n
 \end{aligned} \tag{19}$$

$$\begin{aligned}
 u_e &= \tilde{u}_e + e_z \tilde{w}_{e,x} + e_y \tilde{v}_{e,x} \\
 v_e &= \tilde{v}_e + e_z \tilde{\psi}_e \\
 w_e &= \tilde{w}_e - e_y \tilde{\psi}_e \\
 \psi_e &= \tilde{\psi}_e
 \end{aligned} \tag{20}$$

As discussed in [5], the eccentricity transformation of equation (20) is not exact, but is sufficiently accurate if the eccentricity measures e_y and e_z are small compared to the characteristic wavelengths of the displacements in the x-direction.

To fully evaluate the second of the above transformations, the x-dependence of the generalized displacements must be known. Thus, the details of the second transformation will be discussed in later sections after the functional forms of the displacements have been introduced. The generalized force-resultants along the side edge of a plate strip, $\{f_e\}$, can be transformed to statically equivalent values which act at along a node line and are defined with respect to the global coordinate system. The transformed generalized force-resultants are denoted $\{f^n\} = [f_x^n f_y^n f_z^n m^n]^T$, where n is the index number of the node line corresponding to edge number e of the plate strip under consideration. The relationships governing the transformation between $\{f_e\}$ and $\{f^n\}$ will be discussed in later sections.

For each node line, the generalized force-resultants $\{F^n\}$ are simply the sum of the contributions $\{f^n\}$ from all plate-strip edges which terminate at the node line. This relationship is expressed symbolically as

$$\{F^n\} = \sum_{r=1}^{R_n} \{f^n\}_r \quad n = 1, 2, \dots, N \tag{21}$$

where $p = S_{nr}$ and $e = E_{nr}$ (S_{nr} and E_{nr} are defined in Section 3.1.2.1), and subscript p indicates the index number of the plate strip to which the generalized force-resultants applies.

3.1.2.3 Panel loading

The primary global load component applied to the configuration is the mean x-normal force per unit width, N_{xG} , defined as the total (tensile) end load divided by the reference width B . A second nonzero global load component, N_{yG} , may be applied if the configuration is a panel configuration which features a continuous, initially flat skin. Component N_{yG} is the mean force per unit length (based on L) acting in the global y-direction normal to the boundary node-lines of the panel. In the analytical approach presented here, panel configurations featuring two or more skins could be treated by specifying the split of N_{yG} between the multiple skins; for simplicity, the present discussion treats only a single skin. In conventional plate theory, the in-plane normal stress resultants, N_x and N_y , are positive for tension; following this convention, N_{xG} and N_{yG} are both negative for compressive loads, as shown in Figure 3.

For configurations to which biaxial loading is applicable (both N_{xG} and N_{yG} are nonzero) two different options are considered for control of the load ratio. The first option is to maintain the load ratio N_{yG}/N_{xG} at a constant value. The second option is to maintain the ratio of width-shortening to end-shortening, $\Delta v/\Delta u$, at a constant value. Both N_{yG} and Δv are assumed to act across the two boundary node-lines.

In discussing the specification of panel loading, a distinction is made between two regimes of response: 1) linear, unbuckled response of the structure ignoring shape imperfections, and 2) nonlinear response of the perfect or imperfect structure. In the first regime of response, it is assumed that only uniform in-plane normal strains and stress resultants are induced in the component plate strips. (Whether or not this assumption is accurate must be judged by the analyst - see the discussion in Section 3.3.) Thus, all plate strips remain free of out-of-plane displacements, and all displacements, strains, and stress resultants

are proportional to a load parameter λ . In the second (nonlinear) regime of response, the load parameter λ determines the panel end-shortening, and the global load components are no longer proportional to λ , but must instead be computed after an equilibrium solution has been obtained.

To initiate an analysis, a unit load \hat{N}_{xG} or a unit end shortening $\Delta\hat{u}$ is specified, and if applicable, a unit load \hat{N}_{yG} or a unit width-shortening $\Delta\hat{v}$ is specified. If the configuration does not feature a continuous, initially flat skin, then $\Delta\hat{v}$ may still be specified, but N_{yG} is assumed to be zero for the prebuckling analysis. The specific values selected for the unit loads are unimportant; only the ratio of the two load components is important, and then only for the case of biaxial loading. Using the strategies to be presented in Section 3.3.1, any combination of unit input values can be used to establish equivalent unit global loads \hat{N}_{xG} and \hat{N}_{yG} . In the linear regime of response the global loads are related to the unit loads through the load multiplier λ :

$$\begin{aligned} N_{xG} &= \lambda \hat{N}_{xG} \\ N_{yG} &= \lambda \hat{N}_{yG} \end{aligned} \tag{22}$$

Equations (22) establish the prebuckling load state used in the buckling analysis performed by VIPASA.

3.1.2.4 Boundary conditions at the node lines

Along each of the two designated boundary node-lines, with index numbers n_1 and n_2 , four boundary conditions are specified corresponding to the four degrees of freedom along a node line. Table 1 identifies two or three boundary-condition options for each of the four degrees of freedom.

Table 1. Options Available for Specifying Conditions Along the Boundary Node-Lines

Option/ Component	1	2	3
U^n, F_x^n	$U^n = \lambda U_L^n$	$F_x^n = 0$	-
V^n, F_y^n	$V^n = \lambda V_L^n$	$F_y^n = n_y N_{yG}$	$V_{,x}^n = 0$ $\bar{F}_y^n = n_y N_{yG}$
W^n, F_z^n	$W^n = 0$	$F_z^n = 0$	-
Ψ^n, M^n	$\Psi^n = 0$	$M^n = 0$	-

In Table 1, symbol $n_y (= \pm 1)$ reflects the unit normal vector direction at the side edges of the panel with respect to the global coordinate axes. Terms U_L^n and V_L^n represent the node-line displacements associated with the linear response of the perfect structure to the unit load system. The term U_L^n is linear in x , corresponding to uniform axial strain. The term V_L^n is independent of x and corresponds to uniform displacement of the side edges (in the global y -direction). In option 3 for component V^n , symbol \bar{F}_y^n is the mean value of the force resultant F_y^n over the length L . This boundary condition option is useful in modelling symmetry conditions or in modelling a reinforced edge.

To model proportional displacement between Δv and Δu , option 1 is chosen for component V^n , whereas to model proportional loading between N_{yG} and N_{xG} , either option 2 or option 3 is chosen for component V^n . If the latter option is desired, then the load N_{yG} will be maintained in proportion to N_{xG} using the following condition:

$$N_{yG}/N_{xG} = \hat{R} = \hat{N}_{yG}/\hat{N}_{xG} \tag{23}$$

where \hat{R} is the constant of proportionality.

Node lines which are not designated as boundary node-lines ($n \neq n_1, n_2$) nonetheless represent boundaries with respect to the domains of the plate strips which comprise the linked-plate configuration. Each internal node line corresponds to either a joint line between

multiple plate strips, or the free edge of a plate strip. For the internal node-lines to be in equilibrium, the generalized force-resultants must vanish:

$$\{F^n\} = \{0\} \quad \begin{array}{l} n = 1, 2, \dots, N \\ n \neq n_1, n_2 \end{array} \quad (24)$$

3.1.2.5 *Boundary conditions at the panel ends*

Because buckling eigenfunctions provided by the VIPASA analysis [5] serve as the primary shape functions in the proposed method of analysis, the assumptions of the VIPASA buckling analysis must be examined in order to understand the nature of the boundary support simulated at the longitudinal ends of the panel. The VIPASA buckling analysis computes “exact” buckling eigensolutions using a linear prebuckling solution in conjunction with assumed forms for the buckling eigenfunctions which permit the buckling equations to be satisfied exactly. The compromise associated with this approach is that the nature of the loading and support boundary conditions at the x -normal ends is predetermined by the assumed form of the buckling eigenfunctions. Consequently, the nonlinear analysis presented here has similar limitations with respect to the boundary conditions which can be modelled at the longitudinal ends of the panel.

Corresponding to a unit solution for the prebuckling displacements $[u_L v_L 0]$, there are unit uniform displacement gradients, $u_{L,x}$ and $v_{L,y}$, within each plate strip, where in addition, $u_{L,x}$ is constant throughout the structure, consistent with the requirement of uniform end-shortening. The buckling eigenfunctions, $\{u_i\} = [u_i v_i w_i]^T$, have the following forms on each plate strip (a trivial phase shift has been applied relative to the conventions of [5]):

$$\{u_i(x,y)\} = \begin{cases} \xi_i(y) \cos m\pi x/L \\ \eta_i(y) \sin m\pi x/L \\ \phi_i(y) \sin m\pi x/L \end{cases} \quad (25)$$

where m is a positive integer, and $\xi_i(y)$, $\eta_i(y)$, and $\phi_i(y)$ are known analytic functions. It can be seen that, in the most accurate sense, the boundary value problem is that of an infinite-length, uniformly compressed linked-plate structure, where the buckling displacements in the y - z plane (v_i, w_i) and the associated bending curvatures κ_{xi} and κ_{yi} are zero at $x = nL$, $n = 0, \pm 1, \pm 2, \dots$. Since $x = 0$ and $x = L$ are included in these stations, then it can be considered that the eigenfunctions satisfy some form of simply supported boundary condition at the ends of a panel of finite length.

The eigenfunction component u_i has an x -dependence of $\cos m\pi x/L$, and thus is not generally zero at $x = 0$ and $x = L$. Consequently, cross-sections of the structure at $x = 0$ or L which initially lie in a plane may rotate or warp during buckling. This raises the question as to what boundary conditions are simulated for the u component of displacement at the ends of a panel of finite length. If the total displacement component u is expressed as the sum of the unbuckled solution and the buckling eigensolution ($u = \lambda u_L + \xi_i(y) \cos m\pi x/L$), then it can be seen that over the wave length $2L/m$ any net shortening in x is due only to λu_L . It can similarly be argued that over the model length L , the effective end-shortening is due only to λu_L , despite the fact that for odd values of m the model length is not an integer multiple of the buckling wavelength, $2L/m$. Considering that any constant- x station carries the net end load, and that incipient buckling occurs at a constant applied end load with no addition of energy, there are effective axial displacements at $x = 0$ and L associated with energy input into the bounded segment of panel, and these effective end displacements do not change during incipient buckling. Thus, loading mechanisms can be imagined to exist at the ends of the finite length panel which duplicate the support provided by the infinite-length panel discussed, and the axial displacements of these imaginary loading mechanisms are governed by λu_L .

3.1.2.6 Equilibrium condition for the panel

To form the virtual work statement for the complete panel, the virtual work is summed over all plate strips in the panel and set to zero. Stated symbolically, the virtual work statement is

$$\sum_{p=1}^P \delta W_p = 0 \quad (26)$$

where δW_p is given in equation (6). Substituting equations (6) into the above expression the virtual work statement can be expressed as

$$\begin{aligned} \delta W &= \sum_{p=1}^P \left[\int_A (\{N\}^T \{\delta \epsilon^c\} + \{M\}^T \{\delta \kappa^c\}) dA - \int_0^b (\hat{f}_x \delta u + \hat{f}_y \delta v + \hat{f}_z \delta w - \hat{M}_x \delta w_{,x}) \Big|_{x=0, L} dy \right]_p \\ &\quad - \sum_{n=1}^N \int_0^L \{\hat{F}^n\}^T \{\delta U^n\} dx \\ &= 0 \end{aligned} \quad (27)$$

where the generalized force-resultants and generalized displacements along the node lines, $\{F^n\} = [F_x^n F_y^n F_z^n M^n]^T$ and $\{U^n\} = [U^n V^n W^n \Psi^n]^T$ respectively, are now used to express the contributions associated with the side (y -normal) edges of the plate strips. The hats symbolize externally applied load components which are nonzero at points on the boundary where displacements are not specified.

The virtual work statement is also presented in an alternate form derived by expressing equation (26) using equation (9):

$$\begin{aligned}
\delta W = & \sum_{p=1}^P \left[- \int_A \{ [N_{x,x} + N_{xy,y} + (N_y u_{,y})_{,y}] \delta u + [N_{xy,x} + N_{y,y} + (N_x v_{,x})_{,x}] \delta v \right. \\
& + [M_{x,xx} + 2M_{xy,xy} + M_{y,yy} + (N_x w_{,x} + N_{xy} w_{,y})_{,x} + (N_{xy} w_{,x} + N_y w_{,y})_{,y}] \delta w \} dA \\
& + \left. \int_0^b [(f_x - \hat{f}_x) \delta u + (f_y - \hat{f}_y) \delta v + (f_z - \hat{f}_z) \delta w - (M_x - \hat{M}_x) \delta w_{,x}] \Big|_{x=0, L} dy \right] \quad (28) \\
& + \sum_{n=1}^N \int_0^L (\{F^n\} - \{\hat{F}^n\})^T \{\delta U^n\} dx \\
= & 0
\end{aligned}$$

This alternate form of the virtual work statement is used for reference in later sections.

The Euler equations associated with the above form of the virtual work statement were given in equations (10), and they cause the area integral in the above equation to be identically zero. The associated boundary conditions are obtained by considering the boundary integrals in the above equation along with the form of simple support at the panel ends which is suggested by the buckling eigenfunctions of equation (25). The boundary conditions established for the panel ends ($x = 0, L$) are

$$\begin{aligned}
f_x &= \hat{f}_x \\
\delta v &= 0 \\
\delta w &= 0 \\
M_x &= \hat{M}_x \equiv 0
\end{aligned} \quad (29)$$

where the expression for f_x is given in equation (7). The second and third conditions above allow for nonzero displacements associated with the linear, unbuckled solution.

At the boundary node-lines (the side-edges of the panel), the following boundary conditions are established, where consistency with Table 1 has been imposed:

$$\begin{aligned}
F_x^n = \hat{F}_x^n = 0 \quad \text{or} \quad U^n = \lambda U_L^n \\
F_y^n = \hat{F}_y^n = n_y N_{yG} \quad \text{or} \quad V^n = \lambda V_L^n \quad \text{or} \quad \frac{1}{L} \int_0^L F_y^n dx = \hat{F}_y^n = n_y N_{yG}, \quad V_{,x}^n = 0 \\
F_z^n = \hat{F}_z^n = 0 \quad \text{or} \quad W^n = 0 \\
M^n = \hat{M}^n = 0 \quad \text{or} \quad \Psi^n = 0
\end{aligned} \tag{30}$$

where the notation is consistent with that used in Table 1. At the nonboundary node-lines, there are no nonzero loads $\{\hat{F}^n\}$ imposed, so, repeating the statement of equation (24),

$$\begin{aligned}
\{F^n\} = \{0\} \quad n = 1, 2, \dots, N \\
n \neq n_1, n_2
\end{aligned} \tag{31}$$

Based on the boundary conditions established above, the virtual work statement of equation (27) can be rewritten as

$$\begin{aligned}
\delta W = \sum_{p=1}^P \left[\int_A (\{N\}^T \{\delta \varepsilon^c\} + \{M\}^T \{\delta \kappa^c\}) dA - \int_0^b (\hat{r}_x \delta u) |_{x=0, L} dy \right]_p - \int_0^L N_{yG} \delta V^n |_{n_1}^{n_2} dx \\
= 0
\end{aligned} \tag{32}$$

where the displacements are assumed to satisfy the kinematic boundary conditions given in equations (29) and selected from (30). In the above equation, n_1 and n_2 are the node-line numbers for the two boundary node lines, having edge-normal vectors in the negative and positive global y -directions, respectively.

A few comments are made here regarding the contribution to the virtual work from the boundary integral at the longitudinal ends of the panel. The longitudinal load is imposed through controlled end shortening. In the solution procedure, the imposed end shortening is represented by the axial displacement term $\lambda u_L(x)$, where λ is the amplitude of the imposed end shortening, and $u_L(x)$ is the axial displacement distribution corresponding to the linear, unbuckled response to an imposed unit end shortening. The primary axial displacements at the longitudinal ends of the panel are associated with the axial displacement term $\lambda u_L(x)$, which does not contribute to δu . However the rotation and/or warping of the panel ends which

can occur during buckling and nonlinear response reflect the fact that δu is not uniformly zero at the panel ends. If it is assumed for example, that the end-shortening is applied through a knife-edge positioned along a neutral bending axis, then the boundary integral under consideration would contribute nothing. The boundary integral could serve as a point of introduction of the effects of elastic rotational restraint along the panel ends. In the present treatment the boundary integral under discussion will be considered to have no role.

3.2 Form of the Solution

3.2.1 Expression of Displacements

Displacements are represented as the sum of linear, unbuckled contributions, and a truncated perturbation expansion in terms of "modal amplitudes," a modal amplitude being the amplitude multiplier for a buckling mode which is being used to represent displacements in the nonlinear regime of response. The modal amplitudes thus serve as the generalized coordinates associated with nonlinear response. Displacement contributions of second order in the modal amplitudes are retained. These contributions are deemed important (see Section 2.2.2.4) in order to achieve solutions of useful accuracy for a variety of geometric configurations. Displacement contributions of third and higher order are neglected.

The displacements, then, have the assumed form

$$\{u\} = \lambda\{u_L\} + A\{u_L^A\} + q_i\{u_i\} + q_i q_j\{u_{ij}\} \quad i, j = 1, 2, 3, \dots \quad (33)$$

where summation over i and j is implied, and the notation $\{u\} = [u \ v \ w]^T$ is used to refer to a set of compatible displacement fields, one field corresponding to each plate strip, where the three components of each displacement field are defined with respect to the local reference

frame of the strip. In the general expression of the approach, the indices i and j both vary from 1 to ∞ , but in practice a finite number of terms are used.

In equation (33), λ is the load parameter controlling end-shortening, and A is a load parameter which, along with λ , determines the shortening of a panel across the width. Parameter A is required only in some circumstances, where it serves to control the ratio of the global load components, N_{yG}/N_{xG} , in panels which admit biaxial loading (see Section 3.1.2.3). Shape function $\{u_L\} = [u_L \ v_L \ 0]^T$ describes the linear unbuckled response to the prescribed unit loads \hat{N}_{xG} and \hat{N}_{yG} , which are distributed so as to produce uniform displacements of the ends and side edges. (Ultimately, the parameter A is replaced by an expression involving the variable parameters q_i ($i = 1, 2, \dots$) - see Section 3.6.) Shape function $\{u_L^A\} = [0 \ v_L^A \ 0]^T$, when used, describes the linear, unbuckled response to a specified unit load $N_{yG} = \hat{N}_{yG}^A$, where the end shortening held to zero. The generalized coordinate q_i is the i^{th} modal amplitude, associated with the i^{th} buckling eigenfunction, $\{u_i\} = [u_i \ v_i \ w_i]^T$. The second-order displacement fields are denoted as $\{u_{ij}\} = [u_{ij} \ v_{ij} \ w_{ij}]^T$.

For an unloaded panel ($\lambda = 0$), the displacements degenerate to the imperfection shape of the panel:

$$\{u_{\lambda=0}\} = \{u^0\} = A^0 \{u_L^A\} + q_i^0 \{u_i\} + q_i^0 q_j^0 \{u_{ij}\} \quad i, j = 1, 2, 3, \dots \quad (34)$$

where q_i^0 are the modal imperfection amplitudes. The form of equation (34) is selected to be consistent with the form of equation (33).

3.2.2 Expansion of the Strains, Curvatures, and Stress Resultants

The assumed forms for the displacements and the imperfection shape are used in the expressions for the mid-surface mechanical strains and curvatures of equations (5) to obtain the following expansions:

$$\begin{aligned} \{\varepsilon^m\} = & \lambda\{\varepsilon_L\} + (A - A^o)\{\varepsilon_L^A\} + (q_i - q_i^o)\{\varepsilon_i\} + (q_i q_j - q_i^o q_j^o)\{\varepsilon_{ij}\} \\ & + (q_i q_j q_k - q_i^o q_j^o q_k^o)\{\varepsilon_{ijk}\} + (q_i q_j q_k q_\ell - q_i^o q_j^o q_k^o q_\ell^o)\{\varepsilon_{ijk\ell}\} \end{aligned} \quad (35)$$

$$\{\kappa^m\} = (q_i - q_i^o)\{\kappa_i\} + (q_i q_j - q_i^o q_j^o)\{\kappa_{ij}\} \quad (36)$$

where summation over repeated indices is implied, and the curvature and strain shape functions introduced above are given by

$$\begin{aligned} \{\varepsilon_L\} = \begin{Bmatrix} u_{L,x} \\ v_{L,y} \\ 0 \end{Bmatrix} \quad \{\varepsilon_L^A\} = \begin{Bmatrix} 0 \\ v_{L,y}^A \\ 0 \end{Bmatrix} \quad \{\varepsilon_i\} = \begin{Bmatrix} u_{i,x} \\ v_{i,y} \\ u_{i,y} + v_{i,x} \end{Bmatrix} \\ \{\varepsilon_{ij}\} = \begin{Bmatrix} u_{ij,x} + .5(v_{i,x}v_{j,x} + w_{i,x}w_{j,x}) \\ v_{ij,y} + .5(u_{i,y}u_{j,y} + w_{i,y}w_{j,y}) \\ u_{ij,y} + v_{ij,x} + .5(w_{i,x}w_{j,y} + w_{i,y}w_{j,x}) \end{Bmatrix} \end{aligned} \quad (37)$$

$$\{\varepsilon_{ijk}\} = \begin{Bmatrix} v_{i,x}v_{jk,x} + w_{i,x}w_{jk,x} \\ u_{i,y}u_{jk,y} + w_{i,y}w_{jk,y} \\ w_{i,x}w_{jk,y} + w_{i,y}w_{jk,x} \end{Bmatrix} \quad \{\varepsilon_{ijk\ell}\} = \begin{Bmatrix} .5(v_{ij,x}v_{kl,x} + w_{ij,x}w_{kl,x}) \\ .5(u_{ij,y}u_{kl,y} + w_{ij,y}w_{kl,y}) \\ .5(w_{ij,x}w_{kl,y} + w_{ij,y}w_{kl,x}) \end{Bmatrix}$$

$$\{\kappa_i\} = - \begin{Bmatrix} w_{i,xx} \\ w_{i,yy} \\ 2w_{i,xy} \end{Bmatrix} \quad \{\kappa_{ij}\} = - \begin{Bmatrix} w_{ij,xx} \\ w_{ij,yy} \\ 2w_{ij,xy} \end{Bmatrix} \quad (38)$$

In the above equations, terms have been grouped to permit the following symmetry to be imposed: $\{u_{ij}\} = \{u_{ji}\}$, and $\{\varepsilon_{ij}\} = \{\varepsilon_{ji}\}$. This symmetry is ultimately used to reduce the computational effort of determining the set of shape functions $\{u_{ij}\}$ ($i, j = 1, 2, \dots$). Using the above expansions along with the plate constitutive equations (14), the stress resultants can be similarly expanded:

$$\begin{aligned} \{N\} = & \lambda\{N_L\} + (A - A^o)\{N_L^A\} + (q_i - q_i^o)\{N_i\} + (q_i q_j - q_i^o q_j^o)\{N_{ij}\} \\ & + (q_i q_j q_k - q_i^o q_j^o q_k^o)\{N_{ijk}\} + (q_i q_j q_k q_\ell - q_i^o q_j^o q_k^o q_\ell^o)\{N_{ijk\ell}\} \end{aligned} \quad (39)$$

$$\{M\} = (q_i - q_i^o)\{M_i\} + (q_i q_j - q_i^o q_j^o)\{M_{ij}\} \quad (40)$$

where, for example,

$$\begin{aligned} \{N_i\} &= [A]\{\varepsilon_i\} \quad , \\ \{M_i\} &= [A]\{\kappa_i\} \end{aligned} \quad (41)$$

and so forth, where $[A]$ and $[D]$ are the plate in-plane and bending stiffness matrices, respectively, with nonzero elements as shown in equations (15). The first two unit in-plane stress resultants are given by $\{N_L\} = [N_{xL} \ N_{yL} \ 0]^T$ and $\{N_L^A\} = [N_{xL}^A \ N_{yL}^A \ 0]^T$. The absence of the component N_{xy} in these expressions, and the absence of γ_{xy} in the corresponding strain expressions of equations (37), are consequences of the biaxial load state and the absence of extension/shear coupling in the plate strips.

3.2.3 Expansion of the Plate Euler Equations

In order to obtain the equations which govern the various displacement shape functions that appear in equation (33), the plate equilibrium equations (10) are expressed using the expanded forms for displacements and stress resultants given in equations (33), (39), and (40). Before performing the expansion, a couple of preliminary items are discussed. First, as will be discussed in Section 3.3, because of the geometry of the configurations, the load-application details, and the elastic properties of the plate strips, the strain and stress-resultant expressions ε_{xL} , N_{xL} , ε_{yL} , N_{yL} , N_{xL}^A , ε_{yL}^A and N_{yL}^A are all constant over the domain of each plate strip, and the expressions γ_{xyL} , N_{xyL} , ε_{xL}^A , γ_{xyL}^A , N_{xyL}^A are all zero over the domain of each plate strip. Consequently, some displacement contributions or their gradients are zero:

$$u_{L,y} = v_{L,x} = u_L^A = v_L^A \equiv 0 \quad (42)$$

Second, as will be discussed in Section 3.6, the load parameter A can be expressed as a geometric expansion in terms of the modal amplitudes:

$$A = q_i A_i + q_i q_j A_{ij} + \dots \quad (43)$$

where the subscripted coefficients A_i, A_{ij} , etc. are constants.

The plate equilibrium equations (10) are expanded and terms are grouped based their order in the modal amplitudes. Some resulting terms are identically zero, consistent with the discussion in the preceding paragraph, and are consequently deleted. For the case in which the imperfection amplitudes are zero ($q_i = 0, i = 1, 2, 3, \dots$) the following equations are obtained:

$$\begin{aligned}
 & q_i [N_{x_i, x} + N_{xy_i, y} + \lambda N_{y_L} u_{i, yy}] \\
 & + q_i q_j [N_{x_{ij}, x} + N_{xy_{ij}, y} + (N_{y_j} u_{i, y})_{, y} + \lambda N_{y_L} u_{ij, yy} + A_j N_{y_L}^A u_{i, yy}] + O(q_i^3) = 0 \\
 \\
 & q_i [N_{xy_i, x} + N_{y_i, y} + \lambda N_{x_L} v_{i, xx}] \\
 & + q_i q_j [N_{xy_{ij}, x} + N_{y_{ij}, y} + (N_{x_j} v_{i, x})_{, x} + \lambda N_{x_L} v_{ij, xx} + A_j N_{x_L}^A v_{i, xx}] + O(q_i^3) = 0 \tag{44} \\
 \\
 & q_i [M_{x_i, xx} + 2M_{xy_i, xy} + M_{y_i, yy} + \lambda (N_{x_L} w_{i, xx} + N_{y_L} w_{i, yy})] \\
 & + q_i q_j [M_{x_{ij}, xx} + 2M_{xy_{ij}, xy} + M_{y_{ij}, yy} + (N_{x_j} w_{i, x} + N_{xy_j} w_{i, y})_{, x} + (N_{xy_j} w_{i, x} + N_{y_j} w_{i, y})_{, y} \\
 & \quad + \lambda (N_{x_L} w_{ij, xx} + N_{y_L} w_{ij, yy}) + A_j (N_{x_L}^A w_{i, xx} + N_{y_L}^A w_{i, yy})] + O(q_i^3) = 0
 \end{aligned}$$

Bracketed expressions in the above expansions set the grounds for determination of the buckling eigensolutions and the second-order displacement fields. In the following three sections, details are given for the methods of determining the linear unbuckled solutions, the buckling eigensolutions, and the second-order displacement fields, respectively.

3.3 Linear Solutions

There are two different displacement shape-functions associated with linear unbuckled response of the perfect structure. The first, $\{u_L\} = [u_L \ v_L \ 0]$, describes the response to the specified global unit loads \hat{N}_{xG} and \hat{N}_{yG} , where the longitudinal strain ϵ_x is required to be uniform throughout the structure. As discussed in Section 3.1.2.3, loading \hat{N}_{yG} may be specified as nonzero only in structures in which it will not induce initial bending in any of the plate

strips. The second shape function, $\{u_L^A\} = [0 \ v_L^A \ 0]$, describes response to the specified global unit loading \hat{N}_{yG} , where the longitudinal strain ε_x is maintained at zero throughout the structure. \hat{N}_{yG} may be selected to be any nonzero value. Displacement contribution $A\{u_L^A\}$ of equation (33) is used for configurations which have a continuous, initially flat skin, in cases where the ratio of the transverse to axial load is specified to remain constant. It is noted that the two shape functions $\{u_L\}$ and $\{u_L^A\}$ are solutions to similar boundary-value problems which differ only by the specification of N_{xG} in the former and of ε_x in the latter. Thus only the solution for $\{u_L\}$ will be discussed, except where differences exist between the two solution procedures.

Because of the nature of the structural geometry, the loading, and the in-plane constitutive equations for the plate strips (equation (15)), the unit load system \hat{N}_{xG} and \hat{N}_{yG} induces uniform stress resultants on each plate strip, expressed as

$$\begin{aligned} N_{xL} &= \text{constant} \\ N_{yL} &= \text{constant} \\ N_{xyL} &\equiv 0 \end{aligned} \tag{45}$$

The above equations satisfy the equilibrium equations (10), and through consideration of the plate constitutive equations (14), the strain-displacement relationships (5), and the pertinent boundary conditions, it can be shown that the associated displacements satisfy

$$\begin{aligned} u_{L,x} = \hat{\varepsilon}_{xL} &= \text{constant} \\ v_{L,y} = \hat{\varepsilon}_{yL} &= \text{constant} \\ u_{L,y} = u_{L,xx} = v_{L,x} = v_{L,yy} &= 0 \end{aligned} \tag{46}$$

The VIPASA buckling analysis uses the unit strains $\hat{\varepsilon}_{xL}$ and $\hat{\varepsilon}_{yL}$, but does not require the displacements u_L and v_L . The determination of the unit strains is straightforward following, for example, the procedure used in PASCO [2]. Where plate strips join, the issue of joint equilibrium boils down to the requirement that all plate strips comprising a continuous initially flat skin carry the same value of N_{yL} , and all other strips carry no N_y loading. Compatibility of displacements in the x -direction is assured by the uniformity of ε_x within the entire panel.

Compatibility of the y - and z -directed displacement components at the joints is not necessarily assured by the procedure used in PASCO. The distribution of N_{yL} among the plate strips within a panel is determined in PASCO with the assumptions that the distribution is statically determinant, and that global loads do not induce any bending of plate strips within the structure. In order to make these assumptions, the PASCO procedure ignores the issue of displacement compatibility at the joints in the y - z plane. This is acceptable for singly connected structures, but, for multiply connected structures (for example, panels with hat-shaped stiffeners), compatibility of the displacements at the joints will not be satisfied exactly. If displacement compatibility were properly accounted for in such structures, even a perfect structure could exhibit slightly nonlinear behavior from the onset of load application. This discrepancy is noted here, but for practical structures the discrepancy may be insignificant. Along the same vein, if N_{yL} loading is imposed on a panel skin which incorporates joint-line eccentricities (as would be the case if stiffener flanges were being modelled) or is imposed on the skin of an unsymmetrically stiffened panel, then bending-extension coupling would exist in the physical structure which would not be simulated in the prebuckling analysis. Some of this nonlinear behavior can ultimately be captured by the nonlinear analysis.

3.3.1 Formulae for Determining the Prebuckling Solutions

The specific formulae for determination of the two linear, unbuckled response states are presented here. They are compatible with the equations used in PASCO [2] but are redeveloped here for completeness in the documentation, using notation consistent with the present development. As stated before, biaxial loading is permitted only if there is a continuous planar skin connecting the boundary node lines; otherwise only loading N_{x0} is permitted. Despite the limitation on the permissibility of a second load component, it is convenient to develop the solution assuming that a planar skin exists and that biaxial loading is imposed. Once this

solution is obtained, various simplifications can be made to handle special cases of geometry, loading, and boundary conditions.

A vector $\{k\}$ of length P is used to specify which plates are part of the panel skin. The elements k_p of vector $\{k\}$ are defined such that

$$k_p = \begin{cases} 1 & \text{if plate strip } p \text{ is part of the panel skin} \\ 0 & \text{otherwise} \end{cases} \quad p = 1, 2, \dots, P \quad (47)$$

The unit global load \hat{N}_{xG} is the mean unit axial load in the longitudinal direction per unit width of the panel, and can be expressed as

$$\hat{N}_{xG} = \frac{1}{B} \sum_{p=1}^P (N_{xL}^p b_p) \quad (48)$$

where B is the width of the panel between the boundary node lines, N_{xL} is the unit value of N_x on plate strip p , and b_p is the width of plate strip p . (In the above equation and in the following equations, the superscript p is not intended as an exponent.) The unit global load \hat{N}_{yG} is the unit normal load per unit length of the panel, and it acts on the panel skin at the boundary node lines. This load is carried by all plate strips in the panel skin, so that the unit y -normal stress resultant in plate strip p is given by

$$N_{yL}^p = k_p \hat{N}_{yG} \quad (49)$$

The unit normal stress resultants within each plate strip are related to the unit normal mid-surface strains of the plate strip through the plate constitutive equations (14):

$$N_{xL}^p = A_{11}^p \hat{\varepsilon}_{xL} + A_{12}^p \hat{\varepsilon}_{yL} \quad (50a)$$

$$N_{yL}^p = A_{12}^p \hat{\varepsilon}_{xL} + A_{22}^p \hat{\varepsilon}_{yL} \quad (50b)$$

where $\hat{\varepsilon}_{xL}$, the unit normal strain in the longitudinal direction, is uniform throughout the panel.

Using equation (49) and the equation (50b), the y-normal mid-surface strain in each plate strip can be expressed in terms of the unit longitudinal strain and the unit load \hat{N}_{yG} :

$$\hat{\varepsilon}_{yL}^p = \frac{\hat{N}_{yG} k_p - \hat{\varepsilon}_{xL} A_{12}^p}{A_{22}^p} \quad (51)$$

The unit longitudinal strain associated with the specified global load components can be determined by using equation (50a) and equation (51) in equation (48) to obtain the following expression:

$$\hat{\varepsilon}_{xL} = \frac{\hat{N}_{xG} B - \hat{N}_{yG} S_2}{S_1} \quad (52)$$

where the constants S_1 and S_2 are given by

$$S_1 = \sum_{p=1}^P b_p \left(A_{11} - \frac{A_{12}^2}{A_{22}} \right)_p \quad (53)$$

$$S_2 = \sum_{p=1}^P b_p k_p \left(\frac{A_{12}}{A_{22}} \right)_p \quad (54)$$

With the unit axial strain now known, equation (51) is used to determine the unit y-normal strain within each plate strip. Equations (50) are then applied to determine the unit normal in-plane stress resultants within each plate strip.

On occasion, it is of interest to know the change in the width of the panel, which is the change of dimension between the two boundary node lines. The change in width, denoted by Δv_L , is simply the sum of the changes in width of the plate strips comprising the panel skin, and this can be expressed mathematically as

$$\Delta v_L = \sum_{p=1}^P k_p b_p \hat{\varepsilon}_{y_L}^p \quad (55)$$

Define the mean y-normal strain of the panel skin to be

$$\hat{\varepsilon}_{y_G} = \frac{\Delta v_L}{B} \quad (56)$$

Using equations (51) and (55) to re-express equation (56), the mean y-normal strain in the skin can be expressed in terms of known values:

$$\hat{\varepsilon}_{y_G} = \frac{1}{B} (\hat{N}_{y_G} S_3 - \hat{\varepsilon}_{x_L} S_4) \quad (57)$$

where constants S_3 and S_4 are given by

$$S_3 = \sum_{p=1}^P k_p b_p \frac{1}{A_{22}^p} \quad (58)$$

$$S_4 = \sum_{p=1}^P k_p b_p \left(\frac{A_{12}}{A_{22}} \right)_p \quad (59)$$

At this point, all of the desired values associated with the linear unbuckled solution are known, but a few additional relationships are developed here for use when the boundary conditions are specified in different ways. By using equation (52) in equation (57), the normal unit load on the side boundaries can be expressed as

$$\hat{N}_{y_G} = \left(\hat{\varepsilon}_{y_G} + \hat{N}_{x_G} \frac{S_4}{S_1} \right) \left(\frac{B S_1}{S_1 S_3 + S_2 S_4} \right) \quad (60)$$

From equation (52) it can be determined that

$$\hat{N}_{yG} = \frac{\hat{N}_{xG}B - \hat{\varepsilon}_{xL}S_1}{S_2} \quad (61)$$

Equating the above two expressions for \hat{N}_{yG} , the following expression for \hat{N}_{xG} can be obtained:

$$\hat{N}_{xG} = \hat{\varepsilon}_{xL} \left(\frac{S_1S_3 + S_2S_4}{BS_3} \right) + \hat{\varepsilon}_{yG} \frac{S_2}{S_3} \quad (62)$$

For configurations having no continuous planar skin, equation (62) reduces to

$$\hat{N}_{xG} = \hat{\varepsilon}_{xL} \frac{S_1}{B} \quad (63)$$

3.3.1.1 *Boundary condition options for a panel with a continuous, planar skin*

There are four different cases identified for sets of parameters which may be used to specify boundary conditions for the unbuckled panel. The first three cases accommodate the various options for specifying boundary conditions which are to be in effect in the regime of nonlinear response (see Table 1 on page 42). The fourth case is for the additional prebuckling solution used to adjust the ratio of the global load components. The four cases are discussed individually below.

Case 1a) \hat{N}_{xG} and \hat{N}_{yG} specified: For this case, equations (49) through (59) provide the solution. The sequence of application of the equations is (53), (54), (52), (51), (50a), (49), (58), (59), and (57).

Case 1b) \hat{N}_{xG} specified and $\hat{\varepsilon}_{yG} = 0$: For this case, equation (60) is used to determine the effective unit load \hat{N}_{yG} . Next, the sequence given for Case (1a) above will provide the complete solution.

Case 1c) $\hat{\epsilon}_{xL}$ and $\hat{\epsilon}_{yG}$ specified: First, equation (62) is used to determine the effective unit load \hat{N}_{xG} , then equation (60) is used to compute the effective unit load \hat{N}_{yG} . Next, the sequence given for Case 1a) above will provide the complete solution.

Case 1d) $\hat{\epsilon}_{xL} \equiv 0$, \hat{N}_{yG}^A specified: This solution is required only in conjunction with Case 1a). The equations which have already been presented are applied, noting that they now apply to strain and stress-resultant measures having the superscript A. With constants S_1 through S_4 already determined, the sequence of application of equations is (57), (51), (62), (50a), and (51).

3.3.1.2 *Boundary-condition options for a configuration with no continuous, planar skin*

These configurations are assumed to be unable to withstand a nonzero value of the applied load \hat{N}_{yG} , as such loading would induce initial bending in the plate strips which is not accounted for in the current method. Indicator k_p of equation (47) is zero for all plate strips. Only one case is identified for specification of the prebuckling load state.

Case 2a) \hat{N}_{xG} specified, $\hat{N}_{yG} \equiv 0$: The sequence of application of equations for this case is basically the same as for Case (1a) for a panel with a skin, except that there are some omissions. Constants S_2 , S_3 , and S_4 of equations (54), (58), and (59), respectively, are all zero. The sequence of application of the equations is (53), (52), (51), (50a), and (49).

3.4 *Buckling Eigensolutions:*

The equations which determine the buckling eigenfunctions are obtained by setting to zero the terms of the expanded equilibrium equations (44) which are of first order in the modal amplitudes. A set of equation trios results, one trio corresponding to each coefficient q_i . The

i^{th} eigenfunction satisfies the trio of equations corresponding to q_i , with λ_i (the i^{th} buckling eigenvalue) substituted for λ :

$$N_{x_i,x} + N_{xy_i,y} + \lambda_i N_{y_L} u_{i,yy} = 0 \quad (64a)$$

$$N_{xy_i,x} + N_{y_i,y} + \lambda_i N_{x_L} v_{i,xx} = 0 \quad (64b)$$

$$M_{x_i,xx} + 2M_{xy_i,xy} + M_{y_i,yy} + \lambda_i (N_{x_L} w_{i,xx} + N_{y_L} w_{i,yy}) = 0 \quad (64c)$$

In general λ_i will be negative, corresponding to a compressive end loading. An infinite number of eigensolutions exists for the eigenvalue problem, and it is assumed here that eigensolutions are ordered according to increasing negative magnitude of the eigenvalues:

$$\lambda_1 \geq \lambda_2 \geq \lambda_3 \geq \dots \quad (65)$$

It is noted that equations (64a) differs from the corresponding equation used in the VIPASA analysis [5], the latter equation being

$$N_{x_i,x} + N_{xy_i,y} + \lambda_i N_{x_L} u_{i,xx} = 0 \quad (66)$$

The term $N_{x_L} u_{i,xx}$ in the above equation was obtained through the use of a nonlinear theory of elasticity in which N_x is considered to be the primary loading in each plate strip. It is argued here that the third left-hand-side term of both equation (66) and equation (64a) can be neglected in the current application. The term $N_{x_L} u_{i,xx}$ in the VIPASA equation is felt to be of negligible importance, based on the consideration of the effects of moderately large in-plane rotations which gave rise to the plate theory used here (see Appendix A). Buckling analyses of stiffened panels were performed using VIPASA both with and without the last left-hand-side term of equation (66) (involving the alteration of a single line of VIPASA source code), and the resulting differences in the computed buckling eigenvalues were on the order of one tenth of one percent. The term $N_{y_L} u_{i,yy}$ of equation (64a) is considered to be of negligible importance, because for a plate strip in the skin of a panel, in-plane rotations will remain small, making

the nonlinear plate theory of von Karman valid, thus eliminating the term, whereas for a plate strip not lying in the skin of a panel, N_{yL} will be zero. The VIPASA buckling solutions can thus be assumed to closely satisfy the buckling equations (64) for the configurations under consideration, whether or not the term $N_{xL}\xi_{i,xx}$ is present in the VIPASA analysis. In the present application, the term $N_{xL}\xi_{i,xx}$ will be omitted from equation (66) during applications of VIPASA, and the stress resultant contributions N_{yL} and N_{yL}^A will be omitted in evaluating the term $(N_y u_{,y})_{,y}$ in the first of the equilibrium equations (10).

The procedure used in VIPASA for determining the eigensolutions is described in detail by Wittrick and Williams [5]. Only the details of the VIPASA procedure which are pertinent to the present method are discussed here. It is noted that VIPASA is capable of determining with certainty the fundamental buckling eigenvalue for a given longitudinal halfwave number, and any desired number of additional eigenvalues in sequential order (increasingly negative value, for the conventions used here).

The i^{th} eigenfunction has the following assumed form on each plate strip (where a phase shift in the x -direction has been applied relative to the conventions of VIPASA in order to locate the x -domain of the panel in the interval $[0, L]$):

$$\{u_i\} = \begin{Bmatrix} u_i \\ v_i \\ w_i \end{Bmatrix} = \begin{Bmatrix} \xi_i(y) \cos m\pi x/L \\ \eta_i(y) \sin m\pi x/L \\ \phi_i(y) \sin m\pi x/L \end{Bmatrix} \quad (67)$$

where m is the number of halfwaves along the length of the panel for the i^{th} eigensolution. When the above displacement forms are inserted into the buckling equations, there result two coupled homogeneous linear second order ordinary differential equations in the functions $\xi_i(y)$ and $\eta_i(y)$, and one homogeneous linear fourth order ordinary differential equation in the function $\phi_i(y)$. These ordinary differential equations are presented in Appendix B in equations (B21) and (B9).

The solutions $\{\xi_i\} = [\xi_i \ \eta_i \ \phi_i]^T$ to the ordinary differential equations presented in Appendix B have the following general form:

$$\{\xi_i(y)\} = \sum_{j=1}^4 \begin{Bmatrix} E_j f_j(y) \\ G_j f_j(y) \\ C_j g_j(y) \end{Bmatrix} \quad (68)$$

where there is, in addition, a compatibility condition between ξ_i and η_i , expressed as

$$\{E_j\} = [R_{jk}] \{G_k\} \quad (69)$$

where $[R_{jk}]$ is a matrix of constants, and C_j , E_j , and G_j are arbitrary constants. The values of the constants R_{jk} and the forms of the functions $f_j(y)$ and $g_j(y)$ all depend on λ_i and m , and are tabulated in Appendix B. There are eight independent arbitrary constants, which take on specific values with the specification of the eight generalized side-edge displacement amplitudes, $\{\dot{\xi}_{ie}\}$ ($e = 1, 2$), defined by

$$\{\dot{\xi}_{ie}\} = \begin{Bmatrix} \dot{\xi}_{ie} \\ \dot{\eta}_{ie} \\ \dot{\phi}_{ie} \\ \dot{\psi}_{ie} \end{Bmatrix} = \begin{Bmatrix} \xi_i(y_e) \\ \eta_i(y_e) \\ \phi_i(y_e) \\ \phi_i'(y_e) \end{Bmatrix} \quad (70)$$

The generalized displacement amplitudes $\{\dot{\xi}_{ie}\}$ at the side edge of a plate strip, when referred to the associated node-line number n and the global coordinate axes (see Section 3.1.2.2), are denoted by $\{\dot{U}^n\} = [\dot{U}^n \dot{V}^n \dot{W}^n \dot{\psi}^n]^T$. In returning a computed eigensolution, VIPASA returns the set of amplitudes $\{\dot{U}^n\}$ corresponding to each node line. (Actually, as a result of the use of complex variables, VIPASA returns the vector $[-\dot{U}^n \dot{V}^n \dot{W}^n \dot{\psi}^n]^T$.) With the x -dependence of the displacement shape functions known, the eccentricity transformation of equations (20) can be evaluated, and a transformation can be specified relating $\{\dot{\xi}_{ie}\}$ and $\{\dot{U}^n\}$ [5]:

$$\{\dot{\xi}_{ie}\} = [T_{ecc}]_e [T_r] \{\dot{U}^n\} \quad (71)$$

where n is the node line number corresponding to edge e of the plate strip under consideration. $[T_r]$ is the rotation-transformation matrix given by

$$[T_r] = \begin{bmatrix} 1 & 0 & 0 & 0 \\ 0 & \cos \mu & -\sin \mu & 0 \\ 0 & \sin \mu & \cos \mu & 0 \\ 0 & 0 & 0 & 1 \end{bmatrix} \quad (72)$$

and $[T_{ecc}]_e$ is the eccentricity-transformation matrix for the buckling eigensolution, given by

$$[T_{ecc}]_e = \begin{bmatrix} 1 & \frac{m\pi}{L} e_{y0} & \frac{m\pi}{L} e_{z0} & 0 \\ 0 & 1 & 0 & e_{z0} \\ 0 & 0 & 1 & -e_{y0} \\ 0 & 0 & 0 & 1 \end{bmatrix} \quad (73)$$

In order to assure that the buckling eigensolutions satisfy side-edge boundary conditions and equilibrium of the node-lines (the plate free edges and side-edge joint lines), a transformation of the type just presented for the generalized edge displacements must be available for transforming the generalized force-resultants at the edge. The generalized force-resultants of equations (13), $\{f_e\} = [f_{x0} \ f_{y0} \ f_{z0} \ m_e]^T$, are expanded in the same manner as was done for the equilibrium equations, to get the portion of $\{f_e\}$ associated with the i^{th} buckling eigensolution. The portion is denoted $\{f_{ie}\}$, and is given by

$$\{f_{ie}\} = \left\{ \begin{array}{l} n_y N_{xy_i} |_{y_e} \\ n_y N_{y_i} |_{y_e} \\ n_y (2M_{xy_i,x} + M_{y_i,y} + \lambda_i N_{y_L} \phi_{i,y}) |_{y_e} \\ -n_y M_{y_i} |_{y_e} \end{array} \right\} \quad (74)$$

These can also be expressed in terms of separated variables:

$$\{f_{ie}\} = \left\{ \begin{array}{l} \dot{f}_{x_{ie}} \cos \frac{m\pi x}{L} \\ \dot{f}_{y_{ie}} \sin \frac{m\pi x}{L} \\ \dot{f}_{z_{ie}} \sin \frac{m\pi x}{L} \\ \dot{m}_{ie} \sin \frac{m\pi x}{L} \end{array} \right\} \quad (75)$$

where the amplitudes $\{\dot{f}_{ie}\}$ are scalars which depend on the functions $\{\xi_i(y)\}$. When the amplitudes $\{\dot{f}_{ie}\}$ are referred to the node line and global coordinate axes, they are denoted $\{\dot{f}_i^n\}$, and the x-dependence associated with the latter quantities is the same as for the former quantities (equations (75)). For $\{f_i^n\}$ to be statically equivalent to $\{f_{ie}\}$, the virtual work of $\{f_{ie}\}$ acting through virtual displacements $\{\delta u_{ie}\}$ will be equal to the virtual work of $\{f_i^n\}$ acting through virtual displacements $\{\delta U_i^n\}$. This condition is met by requiring that [5]

$$\{\dot{f}_i^n\} = [T_r]^T [T_{ecc}]_e^T \{\dot{f}_{ie}\} \quad (76)$$

The associated generalized node-line force-resultant amplitudes, $\{\dot{F}_i^n\}$, are equal to the sum of the contributions $\{\dot{f}_i^n\}$ from all plate strips terminating at a node-line, as expressed in equation (24). The values $\{\dot{F}_i^n\}$ are zero at all nonboundary node-lines (equation (21)). At boundary node-lines, $\{\dot{U}_i^n\}$ and $\{\dot{F}_i^n\}$ satisfy the homogeneous forms of the boundary conditions selected from Table 1 on page 42.

3.5 Second-Order Displacement Fields

The equations used to determine the functions $\{u_{ij}\} = [u_{ij} \ v_{ij} \ w_{ij}]^T$ for each plate strip are obtained by setting to zero the terms of the expanded equilibrium equations (44) which are of second order in the modal amplitudes, excluding the terms which contain the parameter A_{ij} . (The excluded terms have a different characteristic waveform in the longitudinal direction than is used for the shape function $\{u_{ij}\}$.) Each resulting ij^{th} trio of partial differential equations is to be satisfied independently, and these are given by

$$N_{x_{ij},x} + N_{xy_{ij},y} + \frac{1}{2} [(N_{y_i} u_{j,y})_{,y} + (N_{y_j} u_{i,y})_{,y}] = 0 \quad (77a)$$

$$N_{xy_{ij},x} + N_{y_{ij},y} + \lambda_b N_{x_L} v_{ij,xx} + \frac{1}{2} [(N_{x_i} v_{j,x})_{,x} + (N_{x_j} v_{i,x})_{,x}] = 0 \quad (77b)$$

$$\begin{aligned} M_{x_{ij},xx} + 2M_{xy_{ij},xy} + M_{y_{ij},yy} + \lambda_b (N_{x_L} w_{ij,xx} + N_{y_L} w_{ij,yy}) \\ + \frac{1}{2} [(N_{x_i} w_{j,x} + N_{xy_i} w_{j,y})_{,x} + (N_{xy_i} w_{j,x} + N_{y_i} w_{j,y})_{,y} \\ + (N_{x_j} w_{i,x} + N_{xy_j} w_{i,y})_{,x} + (N_{xy_j} w_{i,x} + N_{y_j} w_{i,y})_{,y}] = 0 \end{aligned} \quad (77c)$$

where the second-order contributions in equations (44) were regrouped so as to obtain equations which are symmetric with respect to the subscripts i and j . The term $\lambda_b N_{y_L} u_{ij,yy}$ has been omitted in the first equation above, consistent with the discussion in the Section 3.4 . The parameter λ_b is a reference value of λ , not necessarily the exact value of λ at which an equilibrium solution is sought. The selection of the value for λ_b will be discussed in Section 3.7 . The above equations involve known eigenfunctions $\{u_i\}$ and $\{u_j\}$, and the unknown shape-function $\{u_{ij}\}$. Let m and n denote the number of halfwaves in the x -direction for eigenfunctions $\{u_i\}$ and $\{u_j\}$, respectively. Separation of variables can be used to convert the trio of partial differential equations (77) into two trios of ordinary differential equations in the variable y , by assuming the following form for $\{u_{ij}\}$ [56]:

$$\{u_{ij}\} = \sum_{\alpha=1}^2 \left\{ \begin{array}{l} \xi_{\alpha_{ij}}(y) \sin \hat{m}\pi x/L \\ \eta_{\alpha_{ij}}(y) \cos \hat{m}\pi x/L \\ \phi_{\alpha_{ij}}(y) \cos \hat{m}\pi x/L \end{array} \right\} \quad (78)$$

where

$$\hat{m} = \begin{cases} m+n & \alpha=1 \\ m-n & \alpha=2 \end{cases} \quad (79)$$

The ordinary differential equations which result are derived in the following sections, along with various other expressions which must be known for a full determination of the second-order displacement fields. First the generalized strain measures and the stress resultants will

be expressed in terms of separated variables, and then the governing equations will be expressed in terms of the unknown displacement shape functions, again with separated variables. The generalized force-resultants at the side edges will be expressed in the same fashion, as needed for the imposition of boundary conditions.

3.5.1 First-Order Fields in terms of Separated Variables

The first-order displacement fields (the buckling eigenfunctions) have the following form, copied from equation (67):

$$\{u_i\} = \begin{Bmatrix} u_i \\ v_i \\ w_i \end{Bmatrix} = \begin{Bmatrix} \xi_i(y) \cos m\pi x/L \\ \eta_i(y) \sin m\pi x/L \\ \phi_i(y) \sin m\pi x/L \end{Bmatrix} \quad (80)$$

where the functions $\{\xi_i\} = [\xi_i \ \eta_i \ \phi_i]^T$ are known based on results from a buckling analysis. The first-order mid-surface strain and curvature fields are given in equations (37) and (38), and are copied here:

$$\{\varepsilon_i\} = \begin{Bmatrix} u_{i,x} \\ v_{i,y} \\ u_{i,y} + v_{i,x} \end{Bmatrix} \quad \{\kappa_i\} = - \begin{Bmatrix} w_{i,xx} \\ w_{i,yy} \\ 2w_{i,xy} \end{Bmatrix} \quad (81)$$

Using equations (81), the mid-surface strain and curvature fields can be evaluated and expressed using separation of variables:

$$\{\varepsilon_i\} = \begin{Bmatrix} \bar{\varepsilon}_{x_i}(y) \sin m\pi x/L \\ \bar{\varepsilon}_{y_i}(y) \sin m\pi x/L \\ \bar{\gamma}_{xy_i}(y) \cos m\pi x/L \end{Bmatrix} \quad \{\kappa_i\} = \begin{Bmatrix} \bar{\kappa}_{x_i}(y) \sin m\pi x/L \\ \bar{\kappa}_{y_i}(y) \sin m\pi x/L \\ \bar{\kappa}_{xy_i}(y) \cos m\pi x/L \end{Bmatrix} \quad (82)$$

where

$$\begin{aligned}
\bar{\varepsilon}_{x_i} &= -m \frac{\pi}{L} \xi_i & \bar{\kappa}_{x_i} &= m^2 \left(\frac{\pi}{L} \right)^2 \phi_i \\
\bar{\varepsilon}_{y_i} &= \eta_i' & \bar{\kappa}_{y_i} &= -\phi_i'' \\
\bar{\gamma}_{xy_i} &= \xi_i' + m \frac{\pi}{L} \eta_i & \bar{\kappa}_{xy_i} &= -2m \frac{\pi}{L} \phi_i'
\end{aligned} \tag{83}$$

Now the first-order stress resultant fields can be expressed using separation of variables:

$$\{N_i\} = \left\{ \begin{array}{l} \bar{N}_{x_i}(y) \sin m\pi x/L \\ \bar{N}_{y_i}(y) \sin m\pi x/L \\ \bar{N}_{xy_i}(y) \cos m\pi x/L \end{array} \right\} \quad \{M_i\} = \left\{ \begin{array}{l} \bar{M}_{x_i}(y) \sin m\pi x/L \\ \bar{M}_{y_i}(y) \sin m\pi x/L \\ \bar{M}_{xy_i}(y) \cos m\pi x/L \end{array} \right\} \tag{84}$$

where the y -dependent contributions to the stress resultants depend on the y -dependent portions of the strain fields:

$$\{\bar{N}_i\} = [A]\{\bar{\varepsilon}_i\} \quad \{\bar{M}_i\} = [D]\{\bar{\kappa}_i\} \tag{85}$$

where the plate stiffness matrices $[A]$ and $[D]$ are given in equations (15).

3.5.2 Second-Order Fields in terms of Separated Variables

By substituting the separated form of the unknown functions $\{u_{ij}\}$ from equation (78) and the known eigenfunctions $\{u_i\}$ from equation (80) into the second-order mid-surface strain and curvature shape-functions (repeated here from equations (37) and (38)),

$$\{\varepsilon_{ij}\} = \left\{ \begin{array}{l} u_{ij,x} + 1/2(v_{i,x}v_{j,x} + w_{i,x}w_{j,x}) \\ v_{ij,y} + 1/2(u_{i,y}u_{j,y} + w_{i,y}w_{j,y}) \\ u_{ij,y} + v_{ij,x} + 1/2(w_{i,x}w_{j,y} + w_{i,y}w_{j,x}) \end{array} \right\} \quad \{\kappa_{ij}\} = - \left\{ \begin{array}{l} w_{ij,xx} \\ w_{ij,yy} \\ 2w_{ij,xy} \end{array} \right\} \tag{86}$$

and applying the following trigonometric identities,

$$\begin{aligned}
\sin m\zeta \sin n\zeta &= 1/2 \sum_{\alpha=1}^2 -s_{\alpha} \cos \hat{m}\zeta & \sin m\zeta \cos n\zeta &= 1/2 \sum_{\alpha=1}^2 \sin \hat{m}\zeta \\
\cos m\zeta \cos n\zeta &= 1/2 \sum_{\alpha=1}^2 \cos \hat{m}\zeta & \cos m\zeta \sin n\zeta &= 1/2 \sum_{\alpha=1}^2 s_{\alpha} \sin \hat{m}\zeta
\end{aligned} \tag{87}$$

where s_{α} is given by

$$s_{\alpha} = \begin{cases} 1 & \text{if } \alpha = 1 \\ -1 & \text{if } \alpha = 2 \end{cases} \tag{88}$$

the strain and curvature functions can be expressed in terms of separated variables as follows:

$$\{\varepsilon_{ij}\} = \sum_{\alpha=1}^2 \begin{Bmatrix} \bar{\varepsilon}_{x\alpha_{ij}}(y) \cos \hat{m}\pi x/L \\ \bar{\varepsilon}_{y\alpha_{ij}}(y) \cos \hat{m}\pi x/L \\ \bar{\gamma}_{xy\alpha_{ij}}(y) \sin \hat{m}\pi x/L \end{Bmatrix} \quad \{\kappa_{ij}\} = \sum_{\alpha=1}^2 \begin{Bmatrix} \bar{\kappa}_{x\alpha_{ij}}(y) \cos \hat{m}\pi x/L \\ \bar{\kappa}_{y\alpha_{ij}}(y) \cos \hat{m}\pi x/L \\ \bar{\kappa}_{xy\alpha_{ij}}(y) \sin \hat{m}\pi x/L \end{Bmatrix} \tag{89}$$

where the y -dependent portions are given by

$$\begin{aligned}
\bar{\varepsilon}_{x\alpha_{ij}} &= \hat{m} \frac{\pi}{L} \xi_{\alpha_{ij}} + \frac{1}{4} mn \left(\frac{\pi}{L} \right)^2 (\eta_i \eta_j + \phi_i \phi_j) & \bar{\kappa}_{x\alpha_{ij}} &= \hat{m}^2 \left(\frac{\pi}{L} \right)^2 \phi_{\alpha_{ij}} \\
\bar{\varepsilon}_{y\alpha_{ij}} &= \eta_{\alpha_{ij}}' + \frac{1}{4} (\xi_i' \xi_j' - s_{\alpha} \phi_i' \phi_j') & \bar{\kappa}_{y\alpha_{ij}} &= -\phi_{\alpha_{ij}}'' \\
\bar{\gamma}_{xy\alpha_{ij}} &= \xi_{\alpha_{ij}}' - \hat{m} \frac{\pi}{L} \eta_{\alpha_{ij}} + \frac{1}{4} s_{\alpha} \frac{\pi}{L} (m\phi_i \phi_j' + s_{\alpha} n\phi_i' \phi_j) & \bar{\kappa}_{xy\alpha_{ij}} &= 2\hat{m} \frac{\pi}{L} \phi_{\alpha_{ij}}'
\end{aligned} \tag{90}$$

Now the second-order stress resultant fields can be expressed using separation of variables:

$$\{N_{ij}\} = \sum_{\alpha=1}^2 \begin{Bmatrix} \bar{N}_{x\alpha_{ij}}(y) \cos \hat{m}\pi x/L \\ \bar{N}_{y\alpha_{ij}}(y) \cos \hat{m}\pi x/L \\ \bar{N}_{xy\alpha_{ij}}(y) \sin \hat{m}\pi x/L \end{Bmatrix} \quad \{M_{ij}\} = \sum_{\alpha=1}^2 \begin{Bmatrix} \bar{M}_{x\alpha_{ij}}(y) \cos \hat{m}\pi x/L \\ \bar{M}_{y\alpha_{ij}}(y) \cos \hat{m}\pi x/L \\ \bar{M}_{xy\alpha_{ij}}(y) \sin \hat{m}\pi x/L \end{Bmatrix} \tag{91}$$

where the y -dependent contributions to the stress resultants depend on the y -dependent portions of the strain fields:

$$\{\bar{N}_{\alpha_{ij}}\} = [A]\{\bar{\varepsilon}_{\alpha_{ij}}\} \quad \{\bar{M}_{\alpha_{ij}}\} = [D]\{\bar{\kappa}_{\alpha_{ij}}\} \quad (92)$$

where the matrices $[A]$ and $[D]$ are given in equations (15).

3.5.3 Governing Equations in terms of Separated Variables

The displacement and stress resultant shape-functions appearing in the partial differential equations (77) are now replaced with the corresponding expressions given in equations (78), (80), (84), and (91). Through use of the trigonometric identities of equations (87), the partial differential equations can be expressed in terms of separated variables:

$$\sum_{\alpha=1}^2 \left\{ -\hat{m} \frac{\pi}{L} \bar{N}_{x\alpha_{ij}} + \bar{N}_{xy\alpha_{ij}}' + \frac{1}{4} [s_{\alpha}(\bar{N}_{y_j} \xi_i') + (\bar{N}_{y_j} \xi_i')] \right\} \sin \hat{m}\pi x/L = 0 \quad (93)$$

$$\sum_{\alpha=1}^2 \left\{ \hat{m} \frac{\pi}{L} \bar{N}_{xy\alpha_{ij}} + \bar{N}_{y\alpha_{ij}}' - \lambda_b N_{x_L} \hat{m}^2 \left(\frac{\pi}{L} \right)^2 \eta_{\alpha_{ij}} + \frac{1}{4} \left(\frac{\pi}{L} \right)^2 [m(n + s_{\alpha} m) \bar{N}_{x_j} \eta_i + n(m + s_{\alpha} n) \bar{N}_{x_j} \eta_j] \right\} \cos \hat{m}\pi x/L = 0 \quad (94)$$

$$\sum_{\alpha=1}^2 \left\{ -\hat{m}^2 \left(\frac{\pi}{L} \right)^2 \bar{M}_{x\alpha_{ij}} + 2\hat{m} \frac{\pi}{L} \bar{M}_{xy\alpha_{ij}}' + \bar{M}_{y\alpha_{ij}}'' + \lambda_b \left[-N_{x_L} \hat{m}^2 \left(\frac{\pi}{L} \right)^2 \phi_{\alpha_{ij}} + N_{y_L} \phi_{\alpha_{ij}}'' \right] + \frac{1}{4} \left[m(s_{\alpha} m + n) \left(\frac{\pi}{L} \right)^2 \bar{N}_{x_j} \phi_i + (2m + s_{\alpha} n) \frac{\pi}{L} \bar{N}_{xy_j} \phi_i' + m \frac{\pi}{L} \bar{N}_{xy_j}' \phi_i - s_{\alpha} (\bar{N}_{y_j} \phi_i')' + n(m + s_{\alpha} n) \left(\frac{\pi}{L} \right)^2 \bar{N}_{x_j} \phi_j + (s_{\alpha} m + 2n) \frac{\pi}{L} \bar{N}_{xy_j} \phi_j' + n \frac{\pi}{L} \bar{N}_{xy_j}' \phi_j - s_{\alpha} (\bar{N}_{y_j} \phi_j')' \right] \right\} \times \cos \hat{m}\pi x/L = 0 \quad (95)$$

In each of the three equations above, the two x -dependent trigonometric functions that correspond to $\alpha=1$ and $\alpha=2$, respectively, vary independently and are in general nonzero. Thus the two y -dependent portions of each equation, corresponding to $\alpha = 1$ and $\alpha = 2$, respectively, are independently set equal to zero. This provides six ordinary differential equations in the variable y for each index pair (ij). (The one exception occurs when $m = n$ making $\hat{m} = 0$ when $\alpha = 2$, so that $\sin \hat{m}\pi x/L \equiv 0$ for $\alpha = 2$ in equation (93). In this case there are only five equations obtained.)

To get the final working form of the six equations, the stress resultant terms in equations (93)-(95) are expressed in terms of $\{\xi_i\}$ and $\{\xi_{\alpha ij}\}$ using the equations developed in this section. This provides two uncoupled trios of equations governing the functions $\{\xi_{\alpha ij}\}$ ($\alpha = 1, 2$). The equations are linear, nonhomogeneous ordinary differential equations with constant coefficients, having the following form, where the ij subscripts are omitted:

$$C_{1\alpha}\xi_{\alpha}'' + C_{2\alpha}\xi_{\alpha} + C_{3\alpha}\eta_{\alpha}' = F_{\alpha}(y) \quad (96a)$$

$$D_{1\alpha}\xi_{\alpha}' + D_{2\alpha}\eta_{\alpha}'' + D_{3\alpha}\eta_{\alpha} = G_{\alpha}(y) \quad \alpha = 1, 2 \quad (96b)$$

$$E_{1\alpha}\phi_{\alpha}'''' + E_{2\alpha}\phi_{\alpha}'' + E_{3\alpha}\phi_{\alpha} = H_{\alpha}(y) \quad (96c)$$

where the constant coefficients are given by

$$\begin{aligned} C_{1\alpha} &= A_{66} & C_{3\alpha} &= -\hat{m} \frac{\pi}{L} (A_{12} + A_{66}) \\ D_{1\alpha} &= \hat{m} \frac{\pi}{L} (A_{12} + A_{66}) & D_{3\alpha} &= -\hat{m}^2 \left(\frac{\pi}{L}\right)^2 (A_{66} + \lambda_b N_{x_L}) \\ E_{1\alpha} &= -D_{22} & E_{3\alpha} &= -\hat{m}^4 \left(\frac{\pi}{L}\right)^4 D_{11} - \lambda_b \hat{m}^2 \left(\frac{\pi}{L}\right)^2 N_{x_L} \\ C_{2\alpha} &= -\hat{m}^2 \left(\frac{\pi}{L}\right)^2 A_{11} & & \\ D_{2\alpha} &= A_{22} & & \\ E_{2\alpha} &= 2\hat{m}^2 \left(\frac{\pi}{L}\right)^2 (D_{12} + 2D_{66}) + \lambda_b N_{y_L} & & \end{aligned} \quad (97)$$

and the right-hand-side functions are given by

$$\begin{aligned}
F_\alpha(y) &= F_\alpha(\{\xi_i(y)\}, \{\xi_j(y)\}) \\
&= \frac{1}{4} \left\{ mn\hat{m} \left(\frac{\pi}{L} \right)^3 A_{11}(\eta_i\eta_j + \phi_i\phi_j) + \hat{m} \frac{\pi}{L} A_{12}(\xi_i'\xi_j' - s_\alpha\phi_i'\phi_j') \right. \\
&\quad \left. - s_\alpha \frac{\pi}{L} A_{66}[(m + s_\alpha n)\phi_i'\phi_j' + m\phi_i\phi_j'' + s_\alpha n\phi_i''\phi_j] + (m + s_\alpha n) \frac{\pi}{L} A_{12}\xi_i'\xi_j' \right. \\
&\quad \left. + \frac{\pi}{L} A_{12}(m\xi_i\xi_j'' + s_\alpha n\xi_i''\xi_j) - A_{22}[(\eta_i''\xi_j' + \eta_i'\xi_j'') + s_\alpha(\xi_i''\eta_j' + \xi_i'\eta_j'')] \right\} \quad (98)
\end{aligned}$$

$$\begin{aligned}
G_\alpha(y) &= G_\alpha(\{\xi_i(y)\}, \{\xi_j(y)\}) \\
&= \frac{1}{4} \left\{ -s_\alpha\hat{m} \left(\frac{\pi}{L} \right)^2 A_{66}(m\phi_i\phi_j' + s_\alpha n\phi_i'\phi_j) - mn \left(\frac{\pi}{L} \right)^2 A_{12}(\eta_i'\eta_j + \eta_i\eta_j' + \phi_i'\phi_j + \phi_i\phi_j') \right. \\
&\quad \left. - A_{22}[(\xi_i''\xi_j' + \xi_i'\xi_j'') - s_\alpha(\phi_i''\phi_j' + \phi_i'\phi_j'')] \right. \\
&\quad \left. + mn \left(\frac{\pi}{L} \right)^3 A_{11}(m\xi_i\eta_j + n\eta_i\xi_j) - mn \left(\frac{\pi}{L} \right)^2 A_{12}(\eta_i'\eta_j + \eta_i\eta_j') \right. \\
&\quad \left. + s_\alpha mn \left(\frac{\pi}{L} \right)^3 A_{11}(n\xi_i\eta_j + m\eta_i\xi_j) - s_\alpha \left(\frac{\pi}{L} \right)^2 A_{12}(n^2\eta_i'\eta_j + m^2\eta_i\eta_j') \right\} \quad (99)
\end{aligned}$$

$$\begin{aligned}
H_\alpha(y) &= H_\alpha(\{\xi_i(y)\}, \{\xi_j(y)\}) \\
&= -\frac{1}{4} \left\{ n(m + s_\alpha n) \left(\frac{\pi}{L} \right)^2 \left(-m \frac{\pi}{L} A_{11}\xi_i\phi_j + A_{12}\eta_i'\phi_j \right) \right. \\
&\quad \left. + (s_\alpha m + 2n) \frac{\pi}{L} A_{66}(\xi_i'\phi_j' + m \frac{\pi}{L} \eta_i\phi_j') + n \frac{\pi}{L} A_{66}(\xi_i''\phi_j + m \frac{\pi}{L} \eta_i'\phi_j) \right. \\
&\quad \left. + s_\alpha m \frac{\pi}{L} A_{12}(\xi_i'\phi_j' + \xi_i\phi_j'') - s_\alpha A_{22}(\eta_i''\phi_j' + \eta_i'\phi_j'') \right. \\
&\quad \left. + m(s_\alpha m + n) \left(\frac{\pi}{L} \right)^2 \left(-n \frac{\pi}{L} A_{11}\phi_i\xi_j + A_{12}\phi_i\eta_j' \right) \right. \\
&\quad \left. + (2m + s_\alpha n) \frac{\pi}{L} A_{66}(\phi_i'\xi_j' + n \frac{\pi}{L} \phi_i'\eta_j) + m \frac{\pi}{L} A_{66}(\phi_i\xi_j'' + n \frac{\pi}{L} \phi_i\eta_j') \right. \\
&\quad \left. + s_\alpha n \frac{\pi}{L} A_{12}(\phi_i'\xi_j' + \phi_i''\xi_j) - s_\alpha A_{22}(\phi_i'\eta_j'' + \phi_i''\eta_j') \right\} \quad (100)
\end{aligned}$$

In equations (97)-(100) both \hat{m} and s_α depend on the value of α . For the special case where $m = n$ and $\alpha = 2$, equation (96a) is omitted and $\xi_{*ij} \equiv 0$.

3.5.4 Generalized Displacements and Generalized Force-Resultants

Along Boundaries:

Expressions must be developed for the generalized edge force-resultants associated with the second-order displacement fields, to facilitate specification of the boundary conditions which accompany the differential equations (96). The portions of the generalized force-resultants at the side edges of a plate strip ($\{f_e\}$ of equation (13)) associated with the second-order displacement fields are given by

$$\begin{aligned}
 f_{x_{ij}^e} &= (-1)^e \left[N_{xy_{ij}} + \frac{1}{2} (N_{y_j} u_{i,y} + N_{y_i} u_{j,y}) \right] \Big|_{y_e} \\
 f_{y_{ij}^e} &= (-1)^e N_{y_{ij}} \Big|_{y_e} \\
 f_{z_{ij}^e} &= (-1)^e \left[2M_{xy_{ij},x} + M_{y_{ij},y} + \lambda_b N_{y_i} w_{ij,y} + \frac{1}{2} (N_{xy_j} w_{i,x} + N_{y_j} w_{i,y} + N_{xy_i} w_{j,x} + N_{y_i} w_{j,y}) \right] \Big|_{y_e} \\
 m_{ij}^e &= -(-1)^e M_{y_{ij}} \Big|_{y_e} \\
 e &= 1, 2
 \end{aligned} \tag{101}$$

The above equations can be expressed in terms of separated variables by substituting in for the stress resultant and displacement terms the separated-variable expressions presented earlier in this section, and applying the trigonometric identities given in equations (87). Equations (101) can thus be converted to the following form:

$$\{f_{ij}^e(x)\} = \sum_{\alpha=1}^2 \left\{ \begin{array}{l} \dot{f}_{x\alpha_{ij}^e} \sin \hat{m}\pi x/L \\ \dot{f}_{y\alpha_{ij}^e} \cos \hat{m}\pi x/L \\ \dot{f}_{z\alpha_{ij}^e} \cos \hat{m}\pi x/L \\ \dot{m}_{\alpha_{ij}^e} \cos \hat{m}\pi x/L \end{array} \right\} \tag{102}$$

where the scalar amplitudes introduced above are given by

$$\begin{aligned}
\dot{i}_{x\alpha_{ij}e} &= (-1)^e \left[\bar{N}_{xy\alpha_{ij}} + \frac{1}{4} (s_\alpha \bar{N}_{y_j} \xi_i' + \bar{N}_{y_i} \xi_j') \right] \Big|_{y_e} \\
\dot{i}_{y\alpha_{ij}e} &= (-1)^e \bar{N}_{y\alpha_{ij}} \Big|_{y_e} \\
\dot{i}_{z\alpha_{ij}e} &= (-1)^e \left\{ 2\hat{m} \frac{\pi}{L} \bar{M}_{xy\alpha_{ij}} + \bar{M}_{y\alpha_{ij}}' + \lambda_b N_{y_L} \phi_{\alpha_{ij}}' \right. \\
&\quad \left. + \frac{1}{4} \left[\frac{\pi}{L} (m \bar{N}_{xy_j} \phi_i + n \bar{N}_{xy_i} \phi_j) - s_\alpha (\bar{N}_{y_j} \phi_i' + \bar{N}_{y_i} \phi_j') \right] \right\} \Big|_{y_e} \\
\dot{m}_{\alpha_{ij}e} &= -(-1)^e \bar{M}_{y\alpha_{ij}} \Big|_{y_e}
\end{aligned} \tag{103}$$

To get the final working form for the above equations, the stress resultant terms are expressed in terms of $\{\xi_i\}$ and $\{\xi_{\alpha ij}\}$ using the equations developed in this section. Omitting the ij subscripts, the equations have the form

$$\begin{aligned}
\dot{i}_{x\alpha e} &= (-1)^e [\bar{C}_{1\alpha} \xi_\alpha' + \bar{C}_{2\alpha} \eta_\alpha + \bar{F}_\alpha(y)] \Big|_{y_e} \\
\dot{i}_{y\alpha e} &= (-1)^e [\bar{D}_{1\alpha} \xi_\alpha + \bar{D}_{2\alpha} \eta_\alpha' + \bar{G}_\alpha(y)] \Big|_{y_e} \\
\dot{i}_{z\alpha e} &= (-1)^e [\bar{E}_{1\alpha} \phi_\alpha''' + \bar{E}_{2\alpha} \phi_\alpha' + \bar{H}_\alpha(y)] \Big|_{y_e} \\
\dot{m}_{\alpha e} &= -(-1)^e [\bar{E}_{3\alpha} \phi_\alpha'' + \bar{E}_{4\alpha} \phi] \Big|_{y_e}
\end{aligned} \quad \alpha = 1, 2 \tag{104}$$

where the constant coefficients are given by

$$\begin{aligned}
\bar{C}_{1\alpha} &= A_{66} & \bar{C}_{2\alpha} &= -\hat{m} \frac{\pi}{L} A_{66} \\
\bar{D}_{1\alpha} &= \hat{m} \frac{\pi}{L} A_{12} & \bar{D}_{2\alpha} &= A_{22} \\
\bar{E}_{1\alpha} &= -D_{22} & \bar{E}_{2\alpha} &= \hat{m}^2 \left(\frac{\pi}{L} \right)^2 (D_{12} + 4D_{66}) + \lambda_b N_{y_L} \\
\bar{E}_{3\alpha} &= -D_{22} & \bar{E}_{4\alpha} &= \hat{m}^2 \left(\frac{\pi}{L} \right)^2 D_{12}
\end{aligned} \tag{105}$$

and the functions of y are given by

$$\begin{aligned}
\bar{F}_\alpha(y) &= \bar{F}_\alpha(\{\xi_i(y)\}, \{\xi_j(y)\}) \\
&= \frac{1}{4} \left[s_\alpha \frac{\pi}{L} A_{66}(m\phi_i\phi_j' + s_\alpha n\phi_i'\phi_j) - \frac{\pi}{L} A_{12}(m\xi_i\xi_j' + s_\alpha n\xi_i'\xi_j) + A_{22}(\eta_i'\xi_j' + s_\alpha\xi_i'\eta_j') \right] \\
\bar{G}_\alpha(y) &= \bar{G}_\alpha(\{\xi_i(y)\}, \{\xi_j(y)\}) \\
&= \frac{1}{4} \left[mn \left(\frac{\pi}{L} \right)^2 A_{12}(\eta_i\eta_j + \phi_i\phi_j) + A_{22}(\xi_i'\xi_j' - s_\alpha\phi_i'\phi_j') \right] \\
\bar{H}_\alpha(y) &= \bar{H}_\alpha(\{\xi_i(y)\}, \{\xi_j(y)\}) \\
&= \frac{1}{4} \left[\frac{\pi}{L} A_{66}(n\xi_i'\phi_j + m\phi_i\xi_j') + mn \left(\frac{\pi}{L} \right)^2 A_{66}(\eta_i\phi_j + \phi_i\eta_j) \right. \\
&\quad \left. + s_\alpha \frac{\pi}{L} A_{12}(m\xi_i\phi_j' + n\phi_i'\xi_j) - s_\alpha A_{22}(\eta_i'\phi_j' + \phi_i'\eta_j') \right]
\end{aligned} \tag{106}$$

For the second-order displacement fields, the four components of the associated generalized displacements and generalized force-resultants along the plate side-edges and the node lines follow a consistent pattern with regard to x-dependence, shown in the following equation, where ij subscripts are omitted:

$$\begin{aligned}
\{u_e \ U^n \ f_e \ f^n \ F^n\} &= \sum_{\alpha=1}^2 \left\{ \begin{aligned} &(\dot{\xi}_{e\alpha} \ \dot{U}_\alpha^n \ \dot{f}_{x\alpha e} \ \dot{f}_{x\alpha}^n \ \dot{F}_{x\alpha}^n) \sin \hat{m}\pi x/L \\ &(\dot{\eta}_{e\alpha} \ \dot{V}_\alpha^n \ \dot{f}_{y\alpha e} \ \dot{f}_{y\alpha}^n \ \dot{F}_{y\alpha}^n) \cos \hat{m}\pi x/L \\ &(\dot{\phi}_{e\alpha} \ \dot{W}_\alpha^n \ \dot{f}_{z\alpha e} \ \dot{f}_{z\alpha}^n \ \dot{F}_{z\alpha}^n) \cos \hat{m}\pi x/L \\ &(\dot{\psi}_{e\alpha} \ \dot{\Psi}_\alpha^n \ \dot{m}_{e\alpha} \ \dot{m}_\alpha^n \ \dot{M}_\alpha^n) \cos \hat{m}\pi x/L \end{aligned} \right\}
\end{aligned} \tag{107}$$

where the superscript n denotes the number for the node line corresponding to side-edge number e of the plate strip under consideration, and $(\dot{\quad})$ denotes scalar values. By applying the transformation equations (19) and (20) in the same manner as was done for the first-order displacement fields (the buckling eigenfunctions), the rotation and eccentricity transformations can be expressed as matrix operations involving the scalar amplitudes appearing in the right-hand side of equation (107). For specific values of i, j , and α , the transformation of generalized displacements has the form

$$\{\dot{\xi}_e\} = [T_{ecc}]_e [T_r] \{\dot{U}^n\} \quad e = 1, 2 \tag{108}$$

where the subscript α is now also omitted, the rotation-transformation matrix $[T_r]$ is given in equation (72), and the eccentricity transformation matrix is given by

$$[T_{ecc}]_e = \begin{bmatrix} 1 - \hat{m} \frac{\pi}{L} e_{ye} - \hat{m} \frac{\pi}{L} e_{ze} & 0 & 0 & 0 \\ 0 & 1 & 0 & e_{ze} \\ 0 & 0 & 1 & -e_{ye} \\ 0 & 0 & 0 & 1 \end{bmatrix} \quad (109)$$

where e_{ye} and e_{ze} are the eccentricity measures (defined in Figure 4) for edge e of the plate-strip edge under consideration. Because of the presence of \hat{m} in equation (109), the eccentricity-transformation matrix depends on the value of α . The matrix is different in form from the corresponding matrix which applies to the buckling eigenfunctions (equation (73)).

Using the same approach as was used in Section 3.4 for the buckling eigensolutions, the generalized edge force-resultants are transformed from the side-edge of a plate to the associated node line and global coordinate axes by using the following equation:

$$\{\dot{f}^n\} = [T_r]^T [T_{ecc}]_e^T \{\dot{f}_e\} \quad (110)$$

The amplitude of the generalized node-line force-resultants, $\{\dot{F}^n\}$, is the sum of the contributions $\{\dot{f}^n\}$ due to the plate strips terminating at the node line (see equation (21)).

3.5.5 Boundary Conditions Along the Node Lines

Along nonboundary node lines it is required, consistent with equation (24), that $\{F_{ij}^n\} = 0$. This is enforced by imposing the condition $\{\dot{F}_{ij}^n\} = 0$ ($\alpha = 1, 2$), where $\{\dot{F}_{ij}^n\}$ was defined in the preceding paragraph. Along boundary node-lines, it is required to satisfy the homogeneous form of the boundary conditions which have been selected from Table 1 on page 42, with the exception of the third boundary condition option for displacement component V^n . For this op-

tion it is required that $V_{ij,\alpha} = 0$ and $\bar{F}_{y_{ij}}^n = 0$. It can be shown that these conditions will be satisfied by requiring

$$\left. \begin{aligned} \dot{V}_{\alpha_{ij}}^n &= 0 && \text{if } \alpha = 1 \\ \dot{V}_{\alpha_{ij}}^n &= 0 && \text{if } m \neq n \\ \dot{F}_{y_{ij}}^n &= 0 && \text{if } m = n \end{aligned} \right\} \alpha = 2 \quad (111)$$

3.5.6 Solution of the Boundary Value Problem for $\{\xi_{\alpha ij}(y)\}$

Because of the complexity of the expressions found in $[F_{\alpha ij}(y) G_{\alpha ij}(y) H_{\alpha ij}(y)]$ of equations (98)-(100), it was opted to perform a finite difference analysis to obtain values of the functions $\{\xi_{\alpha ij}(y)\}$ at a finite number of evenly spaced y -stations on each plate strip. The finite-difference analysis procedure is presented in detail in Appendix C.

3.5.7 Symmetry of Second-Order Displacement Fields with respect to i and j

The boundary-value problem for the displacement fields $\{u_{ij}\}$, $i, j = 1, 2, \dots$, has been posed so that $\{u_{ij}\}$ is symmetric in i and j , or expressed symbolically,

$$\{u_{ij}\} = \{u_{ji}\} \quad (112)$$

This raises the question of how the functions $\{\xi_{\alpha ij}\}$ and $\{\xi_{\alpha ji}\}$ relate. The expression for $\{u_{ij}\}$ of equation (78) can be used to re-express equation (112):

$$\sum_{\alpha=1}^2 \left\{ \begin{array}{l} \xi_{\alpha_{ij}}(y) \sin(m + s_{\alpha}n)\pi x/L \\ \eta_{\alpha_{ij}}(y) \cos(m + s_{\alpha}n)\pi x/L \\ \phi_{\alpha_{ij}}(y) \cos(m + s_{\alpha}n)\pi x/L \end{array} \right\} = \sum_{\alpha=1}^2 \left\{ \begin{array}{l} \xi_{\alpha_{ji}}(y) \sin(n + s_{\alpha}m)\pi x/L \\ \eta_{\alpha_{ji}}(y) \cos(n + s_{\alpha}m)\pi x/L \\ \phi_{\alpha_{ji}}(y) \cos(n + s_{\alpha}m)\pi x/L \end{array} \right\} \quad (113)$$

where the following substitution has been made, based on equations (79) and (88):

$$\hat{m} = (m + s_{\alpha}n) \quad (114)$$

It is noted that

$$(m + s_{\alpha}n) = s_{\alpha}(n + s_{\alpha}m) \quad (115)$$

and that

$$\begin{aligned} \sin[s_{\alpha}(n + s_{\alpha}m)\pi x/L] &= s_{\alpha} \sin[(n + s_{\alpha}m)\pi x/L] \\ \cos[s_{\alpha}(n + s_{\alpha}m)\pi x/L] &= \cos[(n + s_{\alpha}m)\pi x/L] \end{aligned} \quad (116)$$

Using equations (115) and (116) in conjunction with equation (113), it is easily shown that

$$\begin{aligned} \xi_{\alpha_{ji}}(y) &= \xi_{\alpha_{ij}}(y) & \alpha &= 1 \\ \xi_{\alpha_{ji}}(y) &= -\xi_{\alpha_{ij}}(y) & \alpha &= 2 \\ \left. \begin{array}{l} \eta_{\alpha_{ji}}(y) = \eta_{\alpha_{ij}}(y) \\ \phi_{\alpha_{ji}}(y) = \phi_{\alpha_{ij}}(y) \end{array} \right\} & \alpha &= 1, 2 \end{aligned} \quad (117)$$

Computational efficiency is gained by avoiding redundant computation of $\{u_{ji}\}$ if $\{u_{ij}\}$ is known.

For example, to get the full set of required functions, compute $\{u_{ji}\}$ only if $j \geq i$.

3.5.8 Discussion of the Load-Dependence of the Second-Order Fields:

Three special cases are identified which effect the load-dependence of the second-order displacement fields. The first case is for an unstiffened panel configuration which buckles out-of-plane. In this case, the only nonzero eigenfunction component is w_i . This causes $H_a(y)$ of equations (96c) and (100) to be identically zero, making the differential equation (96c) homogeneous and accepting of the solution $\phi_{a ij}(y) \equiv 0$. Furthermore, the conventional von Karman nonlinear plate equations can be assumed to apply, with the consequence that the coefficient D_{3a} of equation (97) lacks the term containing the load parameter, and the equations governing $\xi_{a ij}$ and $\eta_{a ij}$ become load-independent.

The second case is a stiffened panel undergoing local postbuckling, such that in the buckling eigenfunction only the component w_i will be nonzero on each plate strip. In-plane rotations of each plate strip will be small, making the von Karman nonlinear plate equations acceptable. As was the case for unstiffened panels, discussed above, the differential equations governing $\xi_{a ij}$ and $\eta_{a ij}$ (equations (96a) and (96b)) are load-independent, and the differential equation governing $\phi_{a ij}$ (equation (96c)) is now homogeneous. However, unlike the case of the unstiffened panel, the three equations (96) are coupled through the displacement compatibility and equilibrium conditions at the joints between noncoplanar plate strips. Thus, the second-order fields have three nonzero components, and because the reference load parameter λ_b appears with equation (96c), the second-order fields are load-dependent. However, if the "classical assumptions" for local postbuckling analysis (see Section 2.2.2.3) are invoked, then the coupling of equations (96a) and (96b) with equation (96c) is removed, and the second-order displacement fields become load-independent, with component $\phi_{a ij}$ equal to zero. The "classical assumptions" referred to are not incorporated in the analytical results presented in this document, but as will be discussed in Chapter 4, when performing local postbuckling analysis, the assumption is made that the second-order displacement fields are load-independent.

The third case is when $\hat{m} = 0$, which occurs when $m = n$ and $\alpha = 2$ (see equation (79)). In this situation, as stated earlier, $\xi_{\alpha ij} \equiv 0$. Furthermore, equations (96b) and (96c) reduce to

$$\left. \begin{aligned} A_{22}\eta_{\alpha ij}'' &= G_{\alpha}(y) \\ -D_{22}\phi_{\alpha ij}'''' + \lambda_b N_{yL} &= H_{\alpha}(y) \end{aligned} \right\} \alpha = 2 \quad (118)$$

and thus, if N_{yL} is zero (uniaxial rather than biaxial loading) then the displacement contributions $\eta_{\alpha ij}$ and $\phi_{\alpha ij}$ are load-independent.

3.6 Enforcement of the Load Ratio

This discussion applies to cases in which the structural configuration admits biaxial loading and the unit global load \hat{N}_{yG} is specified. For this situation the ratio of the global load components is to be maintained at a constant ratio, as specified in equations (23) and repeated here:

$$N_{yG}/N_{xG} = \hat{R} = \hat{N}_{yG}/\hat{N}_{xG} \quad (119)$$

In the linear regime of response of the perfect structure, the equilibrium solution which also satisfies equation (119) is obtained by setting the load parameter A and the modal amplitudes q_i ($i = 1, 2, \dots$) to zero in the expression for displacements of equation (33). In the regime of nonlinear response, however, the load parameter A is needed to assure that equation (119) is satisfied.

Assume for the simplicity of this discussion that the panel skin terminates as a simple plate edge at the two boundaries node-lines, so that the normal force-resultant at a side-edge of the panel is simply $f_y = n_y N_y$, evaluated at the appropriate location. Global force resultant N_{yG} is evaluated at a boundary node line, and it has the definition

$$N_{yG} = \frac{1}{L} \int_0^L N_y|_{n_1} dx \quad (120)$$

where n_1 is the node-line index number of a boundary node-line. Global force resultant N_{xG} is evaluated at $x = 0$, and it has the definition

$$N_{xG} = \frac{1}{B} \sum_{p=1}^P \left(\int_0^b N_x|_{x=0} dy \right)_p \quad (121)$$

where b is the width of the p^{th} plate strip, B is the reference width for the panel, p is the plate-strip index number (not intended as an exponent), and P is the total number of plate strips.

By expressing N_x and N_y , appearing in equation (121) and equation (120), respectively, with the expansions given in equation (39), the global loads N_{xG} and N_{yG} can be expressed in expanded form:

$$\begin{aligned} \begin{Bmatrix} N_{xG} \\ N_{yG} \end{Bmatrix} &= \lambda \begin{Bmatrix} \hat{N}_{xG} \\ \hat{N}_{yG} \end{Bmatrix} + (A - A^0) \begin{Bmatrix} N_{xG}^A \\ \hat{N}_{yG}^A \end{Bmatrix} + (q_i - q_i^0) \begin{Bmatrix} N_{xG_i} \\ N_{yG_i} \end{Bmatrix} + (q_i q_j - q_i^0 q_j^0) \begin{Bmatrix} N_{xG_{ij}} \\ N_{yG_{ij}} \end{Bmatrix} \\ &+ (q_i q_j q_k - q_i^0 q_j^0 q_k^0) \begin{Bmatrix} N_{xG_{ijk}} \\ N_{yG_{ijk}} \end{Bmatrix} + (q_i q_j q_k q_\ell - q_i^0 q_j^0 q_k^0 q_\ell^0) \begin{Bmatrix} N_{xG_{ijk\ell}} \\ N_{yG_{ijk\ell}} \end{Bmatrix} \end{aligned} \quad (122)$$

where \hat{N}_{xG} , \hat{N}_{yG} , and \hat{N}_{zG} are all specified unit loads, N_{xG}^A is known from an earlier analysis (Section 3.3), and

$$\begin{bmatrix} N_{xG_i} \\ N_{xG_{ij}} \\ N_{xG_{ijk}} \\ N_{xG_{ijk\ell}} \end{bmatrix} = \frac{1}{B} \sum_{p=1}^P \left(\int_0^b \begin{bmatrix} N_{x_i} \\ N_{x_{ij}} \\ N_{x_{ijk}} \\ N_{x_{ijk\ell}} \end{bmatrix} \Big|_{x=0} dy \right)_p \quad (123)$$

$$\begin{bmatrix} N_{yG_i} \\ N_{yG_{ij}} \\ N_{yG_{ijk}} \\ N_{yG_{ijk\ell}} \end{bmatrix} = \frac{1}{L} \int_0^L \begin{bmatrix} N_{y_i} \\ N_{y_{ij}} \\ N_{y_{ijk}} \\ N_{y_{ijk\ell}} \end{bmatrix} \Big|_{n_1} dx \quad (124)$$

It is found upon evaluation of equations (123) that because of the form of the harmonic x-dependence of the stress resultants,

$$N_{xG_i} \equiv 0 \quad i = 1, 2, 3, \dots \quad (125)$$

$$N_{xG_{ijk}} \equiv 0 \quad i, j, k = 1, 2, 3, \dots \quad (126)$$

The expanded expressions for the global force-resultants of equation (122) are now used to express constancy of the load ratio (equation (119)) to get

$$\begin{aligned} & \lambda(\hat{N}_{yG} - \hat{R}\hat{N}_{xG}) + (A - A^0)(\hat{N}_{yG}^A - \hat{R}\hat{N}_{xG}^A) + (q_i - q_i^0)N_{yG_i} + (q_i q_j - q_i^0 q_j^0)(N_{yG_{ij}} - \hat{R}N_{xG_{ij}}) \\ & + (q_i q_j q_k - q_i^0 q_j^0 q_k^0)N_{yG_{ijk}} + (q_i q_j q_k q_\ell - q_i^0 q_j^0 q_k^0 q_\ell^0)(N_{yG_{ijk\ell}} - \hat{R}N_{xG_{ijk\ell}}) = 0 \end{aligned} \quad (127)$$

The above equation will be satisfied if A is taken to be

$$A = q_i A_i + q_i q_j A_{ij} + q_i q_j q_k A_{ijk} + q_i q_j q_k q_\ell A_{ijk\ell} \quad i, j, k, \ell = 1, 2, 3, \dots \quad (128)$$

where

$$\begin{aligned} A_i &= - \left[\frac{N_{yG_i}}{\hat{N}_{yG}^A - \hat{R}\hat{N}_{xG}^A} \right] & A_{ij} &= - \left[\frac{N_{yG_{ij}} - \hat{R}N_{xG_{ij}}}{\hat{N}_{yG}^A - \hat{R}\hat{N}_{xG}^A} \right] \\ A_{ijk} &= - \left[\frac{N_{yG_{ijk}}}{\hat{N}_{yG}^A - \hat{R}\hat{N}_{xG}^A} \right] & A_{ijk\ell} &= - \left[\frac{N_{yG_{ijk\ell}} - \hat{R}N_{xG_{ijk\ell}}}{\hat{N}_{yG}^A - \hat{R}\hat{N}_{xG}^A} \right] \end{aligned} \quad i, j, k, \ell = 1, 2, 3, \dots \quad (129)$$

Now the variable parameter A can be replaced wherever it appears, using the form given in equation (128).

One unanticipated use for the parameter A was discovered through applications to test cases. It was originally believed that the need for the parameter was limited to cases for which a nonzero secondary load component N_{yG} is present [62]. This belief was based on the fact that the shape functions $\{u_L\}$ satisfy the boundary conditions, and the shape functions $\{u_i\}$ and $\{u_{ij}\}$ each satisfy the homogeneous forms of the boundary conditions for their respective boundary value problems. However, the boundary-value problem governing the eigensolutions $\{u_i\}$ actually governs the buckling of an infinitely long structure having periodic supports, rather than finite-length panels which may be of interest. Consider a wide (relative to the supported length) flat panel, stiffened on one side with blade stiffeners. During global buckling of an infinite-length, periodically supported panel, the skin will have an incremental longitudinal strain which alternates between positive and negative values in sequential bays along the loading axis, due to the eccentricity of the skin relative to the neutral bending axis. Away from the side-edges of the panel, this alternating longitudinal strain induces a normal stress resultant N_y , which alternates between positive and negative values in sequential bays along the loading axis. Such a panel would typically be represented in an analysis by a single stiffener attached to skin which extends to either side the distance of one half of the stiffener spacing, with symmetry conditions imposed at the two side-edges. The global buckling mode for this model exhibits nonzero normal stress resultants at each side boundary, which provide zero net side loading on each boundary when integrated over an even number of bay lengths in the longitudinal direction, but which provides a nonzero side load when integrated over only a single bay length. Using the current method to analyze this representative width of a finite-length panel, the parameter A , of equation (129) is nonzero, acting to modify the buckling mode-shape to ensure that the average load \bar{N}_y over the length of the the single panel bay is zero.

3.7 Final Determination of Equilibrium Solutions

With the shape functions determined as described in the previous sections, it remains to determine final, approximate equilibrium solutions. The originally planned method for accomplishing this was unsatisfactory, and it is of some interest to note the sources of detrimental error in the original approach. For this reason, the original approach will be discussed briefly, followed by a discussion of the final approach used in obtaining results.

3.7.1 Original Approach

In the original approach to obtaining final equilibrium solutions, M eigensolutions are first selected to establish finite basis for the expression of displacements (see equation (33)), strains, stress resultants, and so forth. The next step is to form a set of M nonlinear algebraic equations through use of the following weighted-residual expressions:

$$\sum_{p=1}^P \left[\left\{ [N_{x,x} + N_{xy,y} + (N_y u_{,y})_{,y}] u_i + [N_{xy,x} + N_{y,y} + (N_x v_{,x})_{,x}] v_i + [M_{x,xx} + 2M_{xy,xy} + M_{y,yy} + (N_x w_{,x} + N_{xy} w_{,y})_{,x} + (N_{xy} w_{,x} + N_y w_{,y})_{,y}] w_i \right\} dA \right]_p \quad (130)$$

$$= 0, \quad i = 1, 2, \dots, M$$

where the bracketed expressions now represent the residuals associated with the finite-basis expression of the three Euler equations (10). The weight functions are seen to be the three components of the buckling eigenfunctions. For a simple plate problem, equation (130) degenerates to an application of the Galerkin weighted-residuals method, and is suitable for determining exact series solutions. This is not the case for linked-plate configurations. By comparing the above expression to the second expression of the virtual work principle, given in equation (28), the source of errors can be illuminated.

First, a proper expression for the components of $\{\delta u\}$ appearing in equation (28) would be

$$\{\delta u\} = \sum_{i=1}^M \delta q_i \left(\{u_i\} + \sum_{j=1}^M 2q_j \{u_{ij}\} \right) \quad (131)$$

whereas the use of equation (130) neglects the contribution of the second term in the parenthesis above. A second approach was investigated in which the three eigenfunction components used as weight functions in equation (30) were replaced with the corresponding components of the expressions inside the parentheses in equations (131). However this approach was still unsatisfactory for some problems.

The second source of error comes in neglecting the boundary integrals present in equation (28). In solving the boundary value problems governing the linear, buckling, and second-order displacement solutions, respectively, the associated force-related boundary conditions were satisfied exactly. However, in computing higher-order contributions to force resultants at the panel boundaries and internal node-lines, there are finite errors in the satisfaction of force-related boundary conditions of equations (30) and (31), such that the errors must be accounted for in expressing equation (28) in order to avoid gross errors in the final solutions. The above-mentioned sources of error were both discovered and confirmed through application to a variety of test cases.

3.7.2 Final Approach

The final approach used to obtain approximate equilibrium solutions involves a direct application of the virtual work statement given in equation (32). A set of M eigensolutions is selected to establish a finite basis for the expression of displacements, generalized strains, stress resultants, and so forth. Some strategies for selecting the set of M eigenfunctions are

discussed in the Chapter 4. The virtual work statement of equation (32) is evaluated with the expanded forms for the generalized strains and stress resultants which have been developed, and expressed in the following form:

$$\delta W = \sum_{i=1}^M K_i \delta q_i = 0 \quad (132)$$

where K_i is the expression forming the coefficient for δq_i . Because of the independence of the M virtual modal amplitudes δq_i , M independent equations are obtained from equation (132):

$$K_i = 0, \quad i = 1, 2, \dots, M \quad (133)$$

The set of M equations (133) can be expressed as a set of nonlinear algebraic equations in the following form:

$$\begin{aligned} & \left[\lambda C_i^\lambda - \sum_{j=1}^M q_j^\circ C_i^j - \sum_{j=1}^M \sum_{k=1}^M q_j^\circ q_k^\circ C_i^{jk} - \sum_{j=1}^M \sum_{k=1}^M \sum_{\ell=1}^M q_j^\circ q_k^\circ q_\ell^\circ C_i^{jke} \right] \\ & + \sum_{j=1}^M q_j \left[C_{ij} + \lambda C_{ij}^\lambda - \sum_{k=1}^M q_k^\circ C_{ij}^k - \sum_{k=1}^M \sum_{\ell=1}^M q_k^\circ q_\ell^\circ C_{ij}^{ke} \right] \\ & + \sum_{j=1}^M \sum_{k=1}^M q_j q_k \left[C_{ijk} + \lambda C_{ijk}^\lambda - \sum_{\ell=1}^M q_\ell^\circ C_{ijk}^\ell \right] \\ & + \sum_{j=1}^M \sum_{k=1}^M \sum_{\ell=1}^M q_j q_k q_\ell [C_{ijk\ell} + \lambda C_{ijk\ell}^\lambda] + O(q_j^4) = 0, \quad i = 1, 2, \dots, M \end{aligned} \quad (134)$$

where the sub- and super-scripted coefficients C are constants. Before giving the expressions which define the constant coefficients, some shorthand notation is introduced. First, it is noted that, because $\{u_{ij}\} = \{u_{ji}\}$, the definition of the strain shape-functions given in equations (37) assures the following subscript reversibility:

$$\begin{aligned}
\{\varepsilon_{ij}\} &= \{\varepsilon_{ji}\} \\
\{\varepsilon_{ijk}\} &= \{\varepsilon_{ikj}\} \\
\{\varepsilon_{ijk\ell}\} &= \{\varepsilon_{ik\ell j}\} = \{\varepsilon_{k\ell ij}\}
\end{aligned}
\tag{135}$$

The same subscript reversibility applies to $\{\kappa_{ij}\}$ of equation (38), $\{N_{ij}\}$, $\{N_{ijk}\}$, and $\{N_{ijk\ell}\}$ of equation (39), $\{M_{ij}\}$ of equation (40), and to A_{ij} , A_{ijk} , and $A_{ijk\ell}$ of equation (128). A tilde over certain variables is used to denote the following abbreviations:

$$\begin{aligned}
\{\tilde{N}_i\} &= \{N_i\} + A_i\{N_L^A\} \\
\{\tilde{N}_{ij}\} &= \{N_{ij}\} + A_{ij}\{N_L^A\} \\
\{\tilde{N}_{ijk}\} &= \{N_{ijk}\} + A_{ijk}\{N_L^A\}
\end{aligned}
\tag{136}$$

$$\begin{aligned}
\{\tilde{\varepsilon}_i\} &= \{\varepsilon_i\} + A_i\{\varepsilon_L^A\} \\
\{\tilde{\varepsilon}_{ij}\} &= \{\varepsilon_{ij}\} + A_{ij}\{\varepsilon_L^A\} \\
3\{\tilde{\varepsilon}_{ijk}\} &= (\{\varepsilon_{ijk}\} + A_{ijk}\{\varepsilon_L^A\}) + 2(\{\varepsilon_{kij}\} + A_{kij}\{\varepsilon_L^A\}) \\
4\{\tilde{\varepsilon}_{ijk\ell}\} &= 2(\{\varepsilon_{ijk\ell}\} + A_{ijk\ell}\{\varepsilon_L^A\}) + 2(\{\varepsilon_{k\ell ij}\} + A_{k\ell ij}\{\varepsilon_L^A\})
\end{aligned}
\tag{137}$$

$$\begin{aligned}
\tilde{V}_i^n &= V_i^n + A_i V_L^{A^n} \\
\tilde{V}_{ij}^n &= V_{ij}^n + A_{ij} V_L^{A^n}
\end{aligned}
\tag{138}$$

$$\begin{aligned}
3\tilde{A}_{ijk} &= A_{ijk} + 2A_{kij} \\
4\tilde{A}_{ijk\ell} &= 2A_{ijk\ell} + 2A_{k\ell ij}
\end{aligned}
\tag{139}$$

$$\begin{aligned}
\tilde{N}_{y_{G_i}} &= N_{y_{G_i}} + A_i \hat{N}_{y_G}^A \\
\tilde{N}_{y_{G_{ij}}} &= N_{y_{G_{ij}}} + A_{ij} \hat{N}_{y_G}^A \\
\tilde{N}_{y_{G_{ijk}}} &= N_{y_{G_{ijk}}} + A_{ijk} \hat{N}_{y_G}^A
\end{aligned}
\tag{140}$$

In the above equations, $\{\varepsilon_L^A\}$ is defined in equation (37), $\{N_L^A\}$ represents the corresponding stress resultants, $\hat{N}_{y_G}^A$ is a unit global load discussed in the Section 3.3, $N_{y_{G_i}}$, $N_{y_{G_{ij}}}$, and $N_{y_{G_{ijk}}}$ are

from equation (124), and V_L^n , V_p^n , and V_{ij}^n are the shape functions of expanded expressions for node-line displacement component V^n .

Using the abbreviated notation given above, the constant coefficients of equations (134) can be expressed in the following form:

$$\begin{aligned}
 C_i^\lambda &= \sum_{p=1}^P \left[\int_A \{N_L\}^T \{\tilde{\varepsilon}_i\} dA \right]_p - \int_0^L \hat{N}_{y_G} \tilde{V}_i^n \Big|_{n_1}^{n_2} dx \\
 C_i^j &= \sum_{p=1}^P \left[\int_A (\{\tilde{N}_j\}^T \{\tilde{\varepsilon}_i\} + \{\tilde{M}_j\}^T \{\tilde{\kappa}_i\}) dA \right]_p - \int_0^L \tilde{N}_{y_{G_j}} \tilde{V}_i^n \Big|_{n_1}^{n_2} dx \\
 C_{ij} &= C_i^j \\
 C_{ij}^\lambda &= \sum_{p=1}^P \left[\int_A 2\{N_L\}^T \{\tilde{\varepsilon}_{ij}\} dA \right]_p - \int_0^L 2\hat{N}_{y_G} \tilde{V}_{ij}^n \Big|_{n_1}^{n_2} dx \\
 C_{ij}^k &= \sum_{p=1}^P \left[\int_A 2(\{\tilde{N}_k\}^T \{\tilde{\varepsilon}_{ij}\} + \{\tilde{M}_k\}^T \{\tilde{\kappa}_{ij}\}) dA \right]_p - \int_0^L 2\tilde{N}_{y_{G_k}} \tilde{V}_{ij}^n \Big|_{n_1}^{n_2} dx \\
 C_i^{jk} &= \sum_{p=1}^P \left[\int_A (\{\tilde{N}_{jk}\}^T \{\tilde{\varepsilon}_i\} + \{\tilde{M}_{jk}\}^T \{\tilde{\kappa}_i\}) dA \right]_p - \int_0^L \tilde{N}_{y_{G_{jk}}} \tilde{V}_i^n \Big|_{n_1}^{n_2} dx \\
 C_{ijk} &= C_{ij}^k + C_i^{jk} \\
 C_{ijk}^\lambda &= \sum_{p=1}^P \left[\int_A 3\{N_L\}^T \{\tilde{\varepsilon}_{ijk}\} dA \right]_p - \int_0^L 3\hat{N}_{y_G} \tilde{A}_{ijk} V_L^{A^n} \Big|_{n_1}^{n_2} dx \\
 C_{ijk}^\ell &= \sum_{p=1}^P \left[\int_A 3\{\tilde{N}_\ell\}^T \{\tilde{\varepsilon}_{ijk}\} dA \right]_p - \int_0^L 3\tilde{N}_{y_{G_\ell}} \tilde{A}_{ijk} V_L^{A^n} \Big|_{n_1}^{n_2} dx \\
 C_{ij}^{k\ell} &= \sum_{p=1}^P \left[\int_A 2(\{\tilde{N}_{k\ell}\}^T \{\tilde{\varepsilon}_{ij}\} + \{\tilde{M}_{k\ell}\}^T \{\tilde{\kappa}_{ij}\}) dA \right]_p - \int_0^L 2\tilde{N}_{y_{G_{k\ell}}} \tilde{V}_{ij}^n \Big|_{n_1}^{n_2} dx \\
 C_i^{jke} &= \sum_{p=1}^P \left[\int_A \{\tilde{N}_{jke}\}^T \{\tilde{\varepsilon}_i\} dA \right]_p - \int_0^L \tilde{N}_{y_{G_{jke}}} \tilde{V}_i^n \Big|_{n_1}^{n_2} dx \\
 C_{ijk\ell} &= C_{ijk}^\ell + C_{ij}^{k\ell} + C_i^{jke} \\
 C_{ijk\ell}^\lambda &= \sum_{p=1}^P \left[\int_A 4\{N_L\}^T \{\tilde{\varepsilon}_{ijk\ell}\} dA \right]_p - \int_0^L 4\hat{N}_{y_G} \tilde{A}_{ijk\ell} V_L^{A^n} \Big|_{n_1}^{n_2} dx
 \end{aligned} \tag{141}$$

In the above equations, n_1 and n_2 are the node-line numbers for the two boundary node-lines having edge-normal vectors in the negative and positive global y -directions, respectively. To perform the integration indicated in the above equations, each integrand is first expressed in terms of separated variables. The x -dependent terms in the integrands involve only known trigonometric functions, and thus are integrated analytically. The y -dependent terms in the integrands are evaluated at the discrete points in the y -domain of each plate strip where finite-difference solutions were obtained for the second-order displacement fields (see Appendix C). One-dimensional numerical integration is then performed using Simpson's rule [63].

In the nonlinear algebraic equations (134), terms were retained through $O(q_i^3)$, with terms of equal order in the modal imperfection amplitudes q_i^0 . This approach is helpful in determining the form of the coefficients presented above, but it is expected that in the regime of nonlinear response the modal amplitudes will exceed the modal imperfection amplitudes by perhaps one or two orders of magnitude. Assume now that

$$O((q_i^0)) = O((q_i)^2) \quad (142)$$

With this assumption, equation (134) can be simplified:

$$\begin{aligned} & \left(\lambda C_i^\lambda - \sum_{j=1}^M q_j^0 C_i^j \right) + \sum_{j=1}^M q_j \left(C_{ij} + \lambda C_{ij}^\lambda - \sum_{k=1}^M q_k^0 C_{ij}^k \right) \\ & + \sum_{j=1}^M \sum_{k=1}^M q_j q_k (C_{ijk} + \lambda C_{ijk}^\lambda) + \sum_{j=1}^M \sum_{k=1}^M \sum_{\ell=1}^M q_j q_k q_\ell (C_{ijk\ell} + \lambda C_{ijk\ell}^\lambda) + O(q_j^4) \\ & = 0, \quad i = 1, 2, \dots, M \end{aligned} \quad (143)$$

In applying equations (143), the $O(q_i^4)$ contributions are neglected.

Load-dependence of the algebraic equations: It was noted Section 3.5 that in determining the second-order displacement fields, a reference value must be specified for the load parameter; the reference value is labeled λ_b . If λ_b is taken to be λ , which is implied by some

researchers to be the correct approach [38], then the second-order fields and the coefficients of equations (141) must be computed at every load value investigated. This is undesirable from the standpoint of economy, and also introduces the complication that the coefficient equations used to determine the second-order displacement fields become singular at certain load values, an occurrence which is apparently a mathematical artifact not necessarily correlating to any behavior of the structure [38]. Nonetheless, for the local/Euler mode-interaction problems investigated in the following chapter, two different methods are used; in the first method, λ_b is set to zero, whereas in the second method, λ_b is set to λ . Results are compared for the two approaches.

Solution of the nonlinear algebraic equations: As discussed in the review of literature, there are methods developed for following a nonlinear load-response path through limit points [30] and bifurcation points [31,32], and these methods provide an important capability for a general method of nonlinear analysis. For the test cases discussed in Chapter 4, simple Newton-Raphson iteration, when used with end-shortening control, has proven to be adequate as a solution technique. While cases were investigated which show limit-load behavior, it was found that limit loads are traversed in a regime in which the iterative procedure still performs satisfactorily using controlled end-shortening. Thus, the results presented herein were generated using the Newton-Raphson iterative procedure. The implementation of this procedure is now outlined.

For a specified set of modal imperfection amplitudes $\{q^o\}$ and specified load level λ , equation (143) can be expressed in terms of a new set of constant coefficients:

$$D_i + \sum_{j=1}^M q_j D_{ij} + \sum_{j=1}^M \sum_{k=1}^M q_j q_k D_{ijk} + \sum_{j=1}^M \sum_{k=1}^M \sum_{\ell=1}^M q_j q_k q_\ell D_{ijk\ell} = 0, \quad i = 1, 2, \dots, M \quad (144)$$

where

$$\begin{aligned}
D_i &= \lambda C_i^\lambda - \sum_{j=1}^M q_j^\circ C_i^j \\
D_{ij} &= C_{ij} + \lambda C_{ij}^\lambda - \sum_{k=1}^M q_k^\circ C_{ij}^k \\
D_{ijk} &= C_{ijk} + \lambda C_{ijk}^\lambda \\
D_{ijk\ell} &= C_{ijk\ell} + \lambda C_{ijk\ell}^\lambda
\end{aligned} \tag{145}$$

Given an approximate known solution, $\{q^r\}$, representing the r^{th} solution obtained in an iterative procedure (or the starting solution, if $r = 0$), define the associated residual vector, $\{R^r\}$, to be

$$R_i^r = D_i + \sum_{j=1}^M q_j^r D_{ij} + \sum_{j=1}^M \sum_{k=1}^M q_j^r q_k^r D_{ijk} + \sum_{j=1}^M \sum_{k=1}^M \sum_{\ell=1}^M q_j^r q_k^r q_\ell^r D_{ijk\ell} \quad i = 1, 2, \dots, M \tag{146}$$

The residual vector of the exact solution, $\{0\}$, is expressed as a Taylor series expansion about the approximate, known solution:

$$R_i|_{\{q\}} = 0 = R_i^r + \sum_{j=1}^M \left[\frac{\partial R_i}{\partial q_j} \Big|_{\{q^r\}} (q_j - q_j^r) \right] + O((q_j - q_j^r)^2) \quad i = 1, 2, \dots, M \tag{147}$$

The difference $(q_i - q_i^r)$ is assumed to be small so that the square of the difference can be ignored in establishing an iterative procedure. Equation (147) can then be rearranged to get

$$\{q\} - \{q^r\} \approx -[K^r]^{-1} \{R\}^r \tag{148}$$

where the tangent stiffness matrix, $[K^r]$, is defined by

$$K_{ij}^r = \frac{\partial R_i}{\partial q_j} \Big|_{\{q^r\}} \tag{149}$$

The Newton-Raphson iterative procedure is established using equation (148), by calling $\{q\}$ the $(r + 1)^{\text{st}}$ solution vector:

$$\{q^{r+1}\} = \{q^r\} - [K^r]^{-1} \{R\}^r \quad (150)$$

Equation (149), when evaluated using the expression in equation (146), provides the following expression for the tangent stiffness matrix:

$$K_{ij}^r = D_{ij} + \sum_{k=1}^M q_k^r \left[(D_{ij k} + D_{i k j}) + \sum_{\ell=1}^M q_\ell^r (D_{ij k \ell} + D_{i k j \ell} + D_{i k \ell j}) \right] \quad i, j = 1, 2, \dots, M \quad (151)$$

Convergence of the iteration procedure is assumed to occur when the following criterion is met:

$$\sqrt{\left(\frac{\sum_{i=1}^M (q_i^{r+1} - q_i^r)^2}{\sum_{i=1}^M (q_i^{r+1})^2} \right)} < \varepsilon \quad (152)$$

where ε is a small positive number much less than one.

4.0 Results and Discussion

In this chapter, four sets of results are presented and discussed. In the first set, the postbuckling response of several square unstiffened panels is investigated. NLPAN predictions are compared with theoretical results from the literature. In the second set, the predictions of NLPAN are compared with test data for the postbuckling behavior of an unstiffened rectangular quasi-isotropic composite panel. Next, NLPAN is used to predict the local postbuckling response of a blade-stiffened panel of isotropic material, having three bays across the width. The results are compared with finite element predictions. Finally, NLPAN is used to predict modal interaction and imperfection sensitivity in several wide, blade stiffened panels, for which experimental results are available in the literature. A few comments are made concerning the computational cost of running NLPAN.

4.1 *Postbuckling of Square Unstiffened Panels*

4.1.1 **Isotropic Plates with Simple Edge Support**

As discussed in Section 2.1.2, exact series solution procedures have been developed for simply supported rectangular isotropic plates subjected to uniaxial loading in the form of imposed end shortening. Levy [13] obtained results for perfect square plates where the unloaded edges are constrained to remain straight while carrying no net edge-normal load. Coan [14]

obtained results for perfect and imperfect square plates for which the unloaded edges are uniformly free of edge-normal force resultants. In both of the mentioned works, the value used for Poisson's ratio was $\nu = 0.316$.

Predictions for end load versus center deflection computed using NLPAN are compared with the results of Levy and Coan in Figure 5. The end load, \bar{N}_x , is the mean value of N_x over the width of the panel, and the center deflection is denoted w_c . The eigenfunctions used in applying NLPAN were those deemed important in [13] and [14] (four modes for Levy's results and three modes for Coan's results). Thirty finite-difference intervals were used in NLPAN for computing the second-order displacement fields. For simple plates such as these, the method of NLPAN degenerates to the solution approach used by Levy and Coan. The buckling eigenfunctions involve only $w_i(x, y)$, and the second-order displacement fields involve only $u_{ij}(x, y)$ and $v_{ij}(x, y)$, as can be seen in equation (2). Consequently, the results of NLPAN agree nearly exactly with the results of both Levy and Coan, for perfect plates and for imperfect plates. The slight differences in results at higher load levels are most likely due to numerical errors associated with the finite-difference procedure used in NLPAN for determining the second-order displacement fields (Levy and Coan both used analytical solutions for the second-order displacement fields). It is interesting to note that the differences between the two sets of boundary conditions modelled do not affect the initial buckling problem, but do significantly affect the postbuckling response.

Convergence with respect to finite-difference discretization: A convergence study was performed to investigate the effect of the number of finite-difference intervals, l , used in computing the second-order displacement fields. The plate reported in [13] and the imperfect plate reported in [14] (see Figure 5) were both modelled. The procedure used was to specify an end-shortening value, Δu , compute the end load \bar{N}_x using NLPAN for a range of values of l , and compare \bar{N}_x with the values provided in [13] or [14], as appropriate. The results are presented in Figure 6. Two postbuckling load ratios were investigated: $\bar{N}_x/N_{xcr} \simeq 2$, indicated by open symbols, and $\bar{N}_x/N_{xcr} \simeq 4$, indicated by closed symbols, where N_{xcr} is the critical buckling load. Results for Levy's boundary conditions (straight unloaded edges) are indicated with

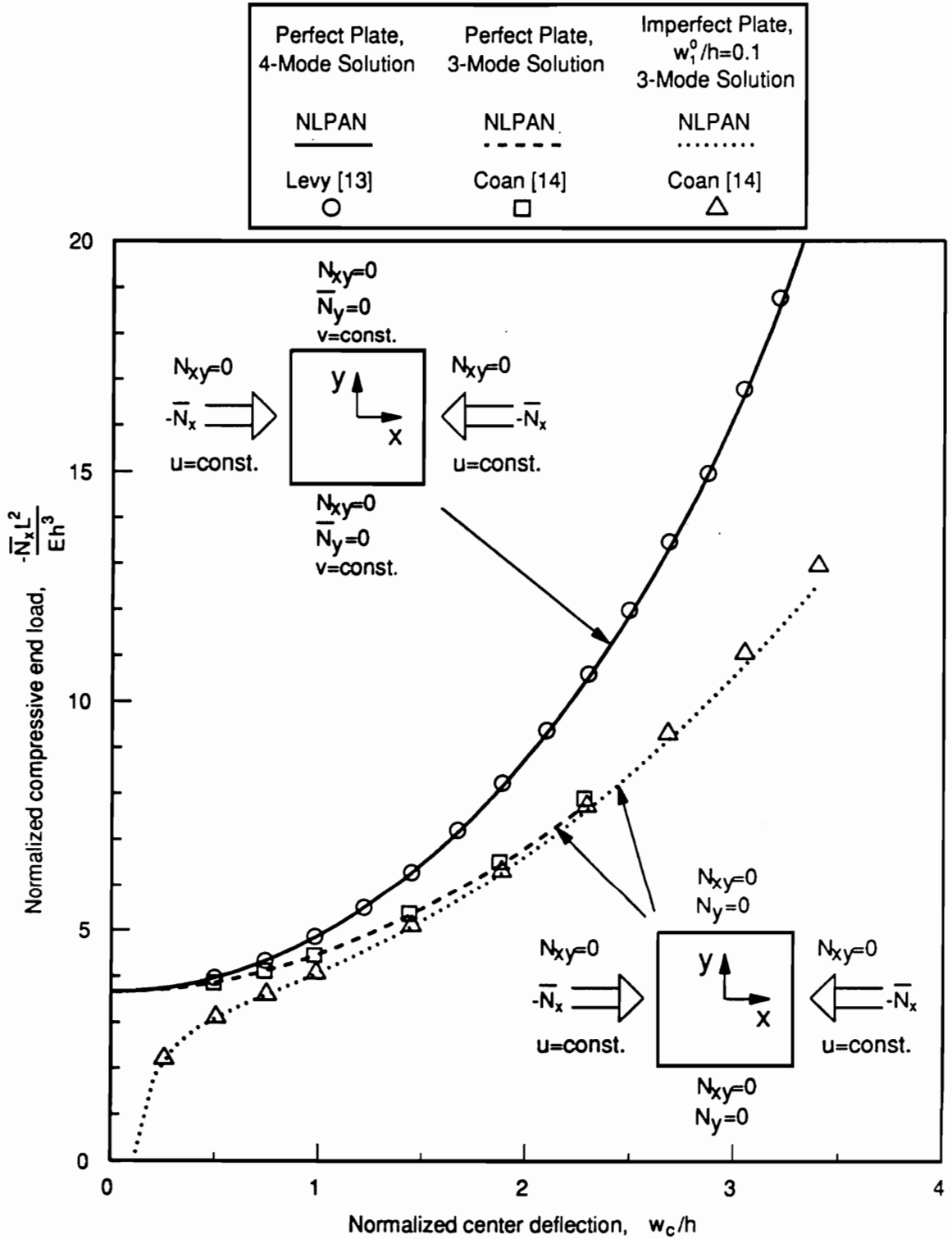


Figure 5. End load versus center deflection for simply supported square plates: Isotropic material, $\nu = 0.316$.

circles, and results for Coan's boundary conditions (unloaded edges free of edge-normal loads) are indicated with squares.

Two observations can readily be made. First, the numerical error increases as the postbuckling load ratio increases. This is reasonable, since the second-order fields which contain the numerical error become increasingly active as the postbuckling load increases. The second observation is that the NLPAN results for the plate with straight unloaded edges exhibit much less numerical error than the NLPAN results for the plate with unloaded edges which are uniformly free of edge-normal force resultants. At a load of four times the critical value, the results for the straight-edge plate have an error of about 1.5% when ten finite-difference intervals are used, whereas to get the same accuracy for the other plate requires the use of about thirty intervals. A qualitative explanation is offered for the great difference in the error for the two plates. Gradients of the in-plane displacements are used in the analysis to express the force boundary conditions at the side edges. The displacement gradients are expressed in terms of approximate finite-difference relationships, making them subject to numerical error. The plate with side edges free of load N_y experiences larger in-plane displacement gradients than the plate with straight edges, and thus suffers more from numerical error.

4.1.2 Composite Panel with Simple Edge Support

Shin [64] analyzed the postbuckling response of several rectangular unstiffened composite panels with simply supported edges. The approach was essentially the same as that used by Levy [13] (see Section 2.1.2). For simple plate problems, the method of NLPAN degenerates to the solution method of [13], and thus, NLPAN should provide results in agreement with those given in [64]. A single configuration is considered here. The panel is square with dimensions $L = b = 20$ inches, and $h = 0.12$ inches. The laminate configuration is $[\pm 30]_n$, where n is sufficiently large so that the laminate elastic constants D_{16} and D_{26} can

B. C. On Unloaded Edge	$\frac{\Delta u}{\Delta u_{cr}}$	$\frac{\bar{N}_x}{N_{x_{cr}}}$
○ $\bar{N}_y=0, v=const.$	3.015	~ 2
● $\bar{N}_y=0, v=const.$	8.137	~ 4
□ $N_y=0$	4.261	~ 2
■ $N_y=0$	11.28	~ 4

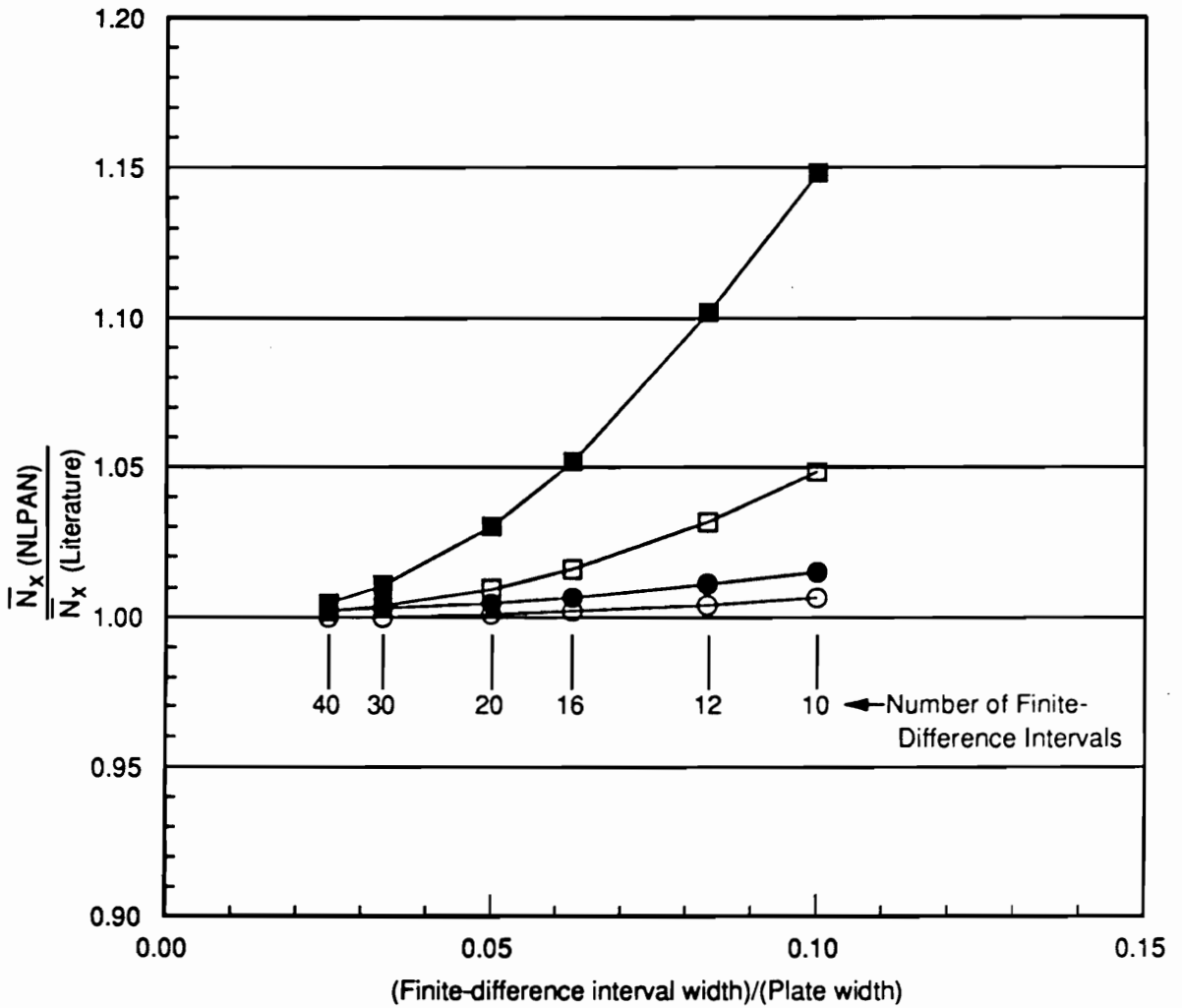


Figure 6. Convergence of results with respect to the finite-difference interval width: End shortening is specified, end load is computed, literature results from [13] and [14].

be assumed to be zero. The lamina properties are shown in Table 2. A uniform end shortening, Δu , is imposed, and the y -normal edges are restrained against edge-normal displacements, i.e. $v = 0$. Complete details of the in-plane boundary conditions are shown in Figure 7.

Table 2. Graphite/Epoxy Lamina Properties [64]

Longitudinal Young's Modulus	19.01×10^6 psi
Transverse Young's Modulus	1.89×10^6 psi
Shear Modulus	0.93×10^6 psi
Major Poisson's Ratio	0.38

In both the analysis used in [64] and the analysis of NLPAN, the out-of-plane displacements can be expressed as $w = \sum_m \sum_n w_{mn} \sin(m\pi x/L) \sin(n\pi y/b)$. Six modes were used in [64], corresponding to the coefficients w_{11} , w_{13} , w_{31} , w_{33} , w_{51} , and w_{15} . Five modes were incorporated in the NLPAN analysis, matching those used in [64] except for the exclusion of the mode corresponding to coefficient w_{51} . Results presented in [13] suggest that the excluded mode is of negligible importance compared to the other five modes. Twenty finite-difference intervals across the width were used in the NLPAN analysis for computation of the second-order displacement fields.

The results for normalized end shortening versus normalized center deflection are shown in Figure 7. The critical buckling point corresponds to $\epsilon_x = -0.00725\%$ ($N_x = -103.9$ lb/in.). As expected, the agreement between the two analyses is essentially exact. The NLPAN analysis predicted that the mean load \bar{N}_y , acting on the y -normal edges is compressive for end shortening values up to about $\Delta u = 10\Delta u_{cr}$ ($\bar{N}_x \approx 3.1N_{xcr}$), beyond which \bar{N}_y acts in tension.

4.1.3 Square Isotropic Plates with Various Boundary Conditions

A number of the general methods of nonlinear analysis discussed in Section 2.2.2.5 apply only to wide stiffened panels with evenly spaced stiffeners; side boundaries are not modelled. NLPAN is capable of modelling a variety of boundary conditions at the side (y -normal)

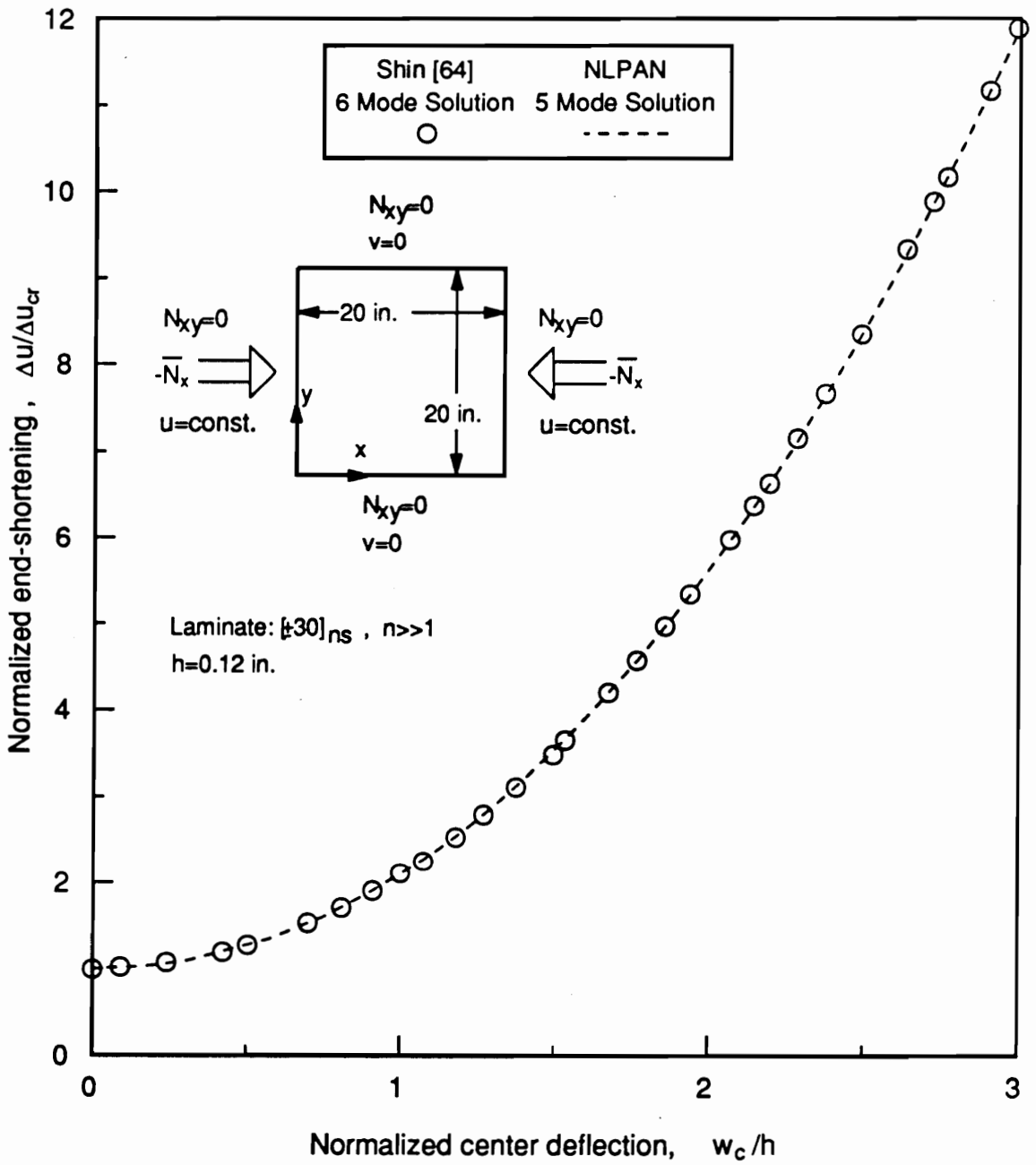


Figure 7. End shortening versus center deflection for a simply supported square unstiffened graphite/epoxy composite panel.

boundaries of a structure, as discussed in Section 3.1.2.4 . As a demonstration of this flexibility, single mode analyses were performed for square plates using six different sets of boundary conditions. The exact sets of boundary conditions used are documented in Figure 8. Briefly described, the side-edge boundary conditions for the six sets are (listed in order of decreasing constraint): i) clamped, ii) simply supported (Levy's boundary conditions), iii) simply supported (Coan's boundary conditions), iv) one edge simply supported, one edge free, v) infinite width (symmetry conditions), and vi) free edges. The normalized results are presented in in Figure 9 and Figure 10. Results for the end load versus the center deflection are presented in Figure 9, and results for the end load versus the end shortening are presented in Figure 10. While the first four sets of boundary conditions produce plates with postbuckling strength, the last two sets result in plates which are (approximately) neutral in postbuckling.

4.2 Postbuckling of a Rectangular Unstiffened Composite Panel

NLPAN was used to predict the postbuckling response of a uniaxially loaded flat unstiffened composite panel, for which experimental results are presented in [9]. The test specimen (specimen C17 of [9]) was a sixteen ply quasi-isotropic graphite/epoxy laminate with the stacking sequence $[\pm 45/0/90]_{2s}$. The lamina properties used in the NLPAN analysis are given in Table 3. The mean ply thickness given in Table 3 is based on the measured thickness of the laminate rather than the nominal ply thickness reported in [9]. The ratio of specimen length to width (L/B) was 3.64, and the ratio of width to thickness (B/h) was 70. The loaded ends of the panel were loosely clamped, and knife-edge fixtures were used to provide simple support slightly inboard of the two unloaded side edges. Additional details of the ex-

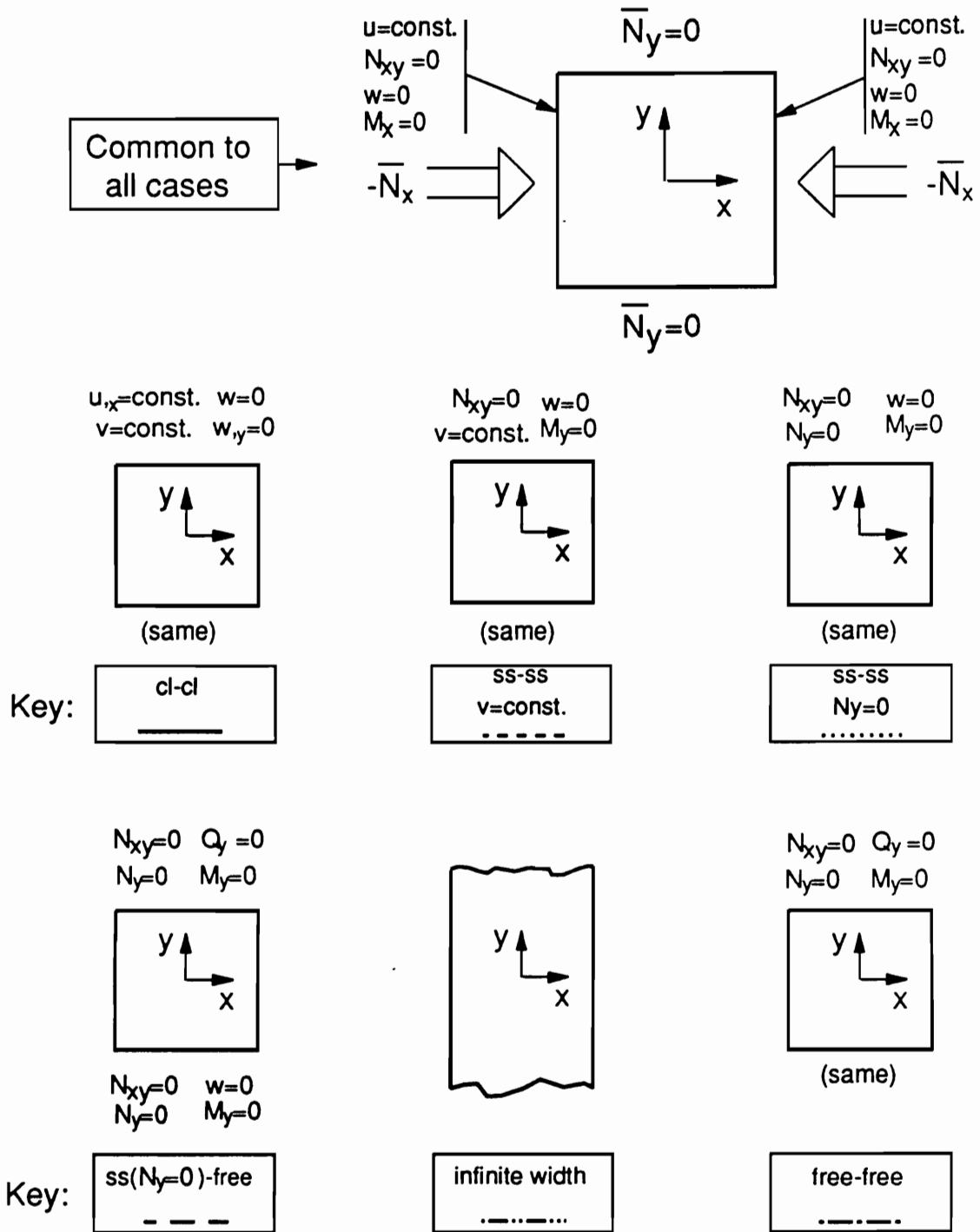


Figure 8. Labeling key for the boundary conditions considered for square isotropic plates with uniaxial loading.

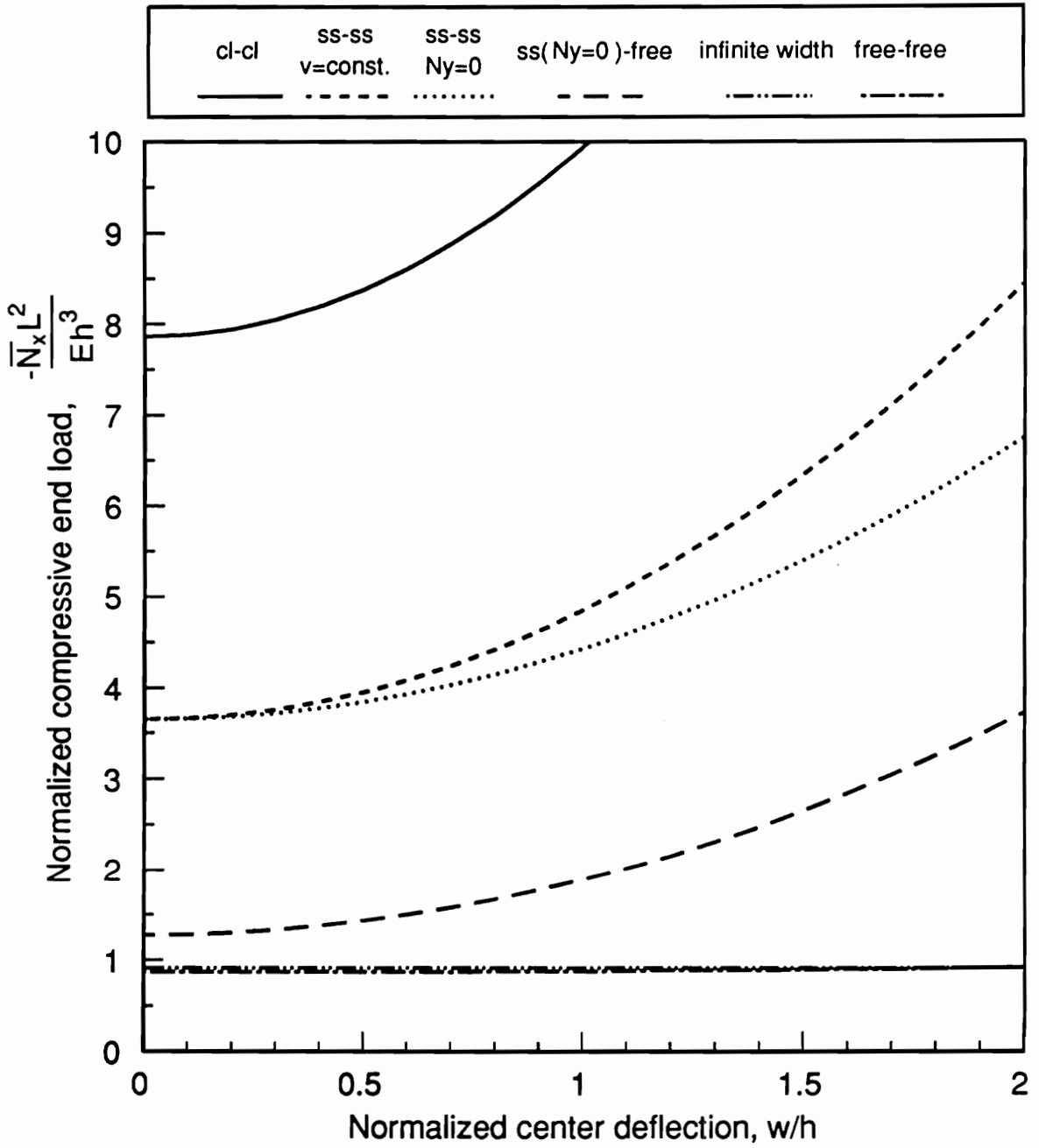


Figure 9. End load versus center deflection for square plates having a variety of boundary conditions on the unloaded edges: Isotropic material, $\nu = 0.316$, single mode solutions (see key in Figure 8 for boundary conditions).

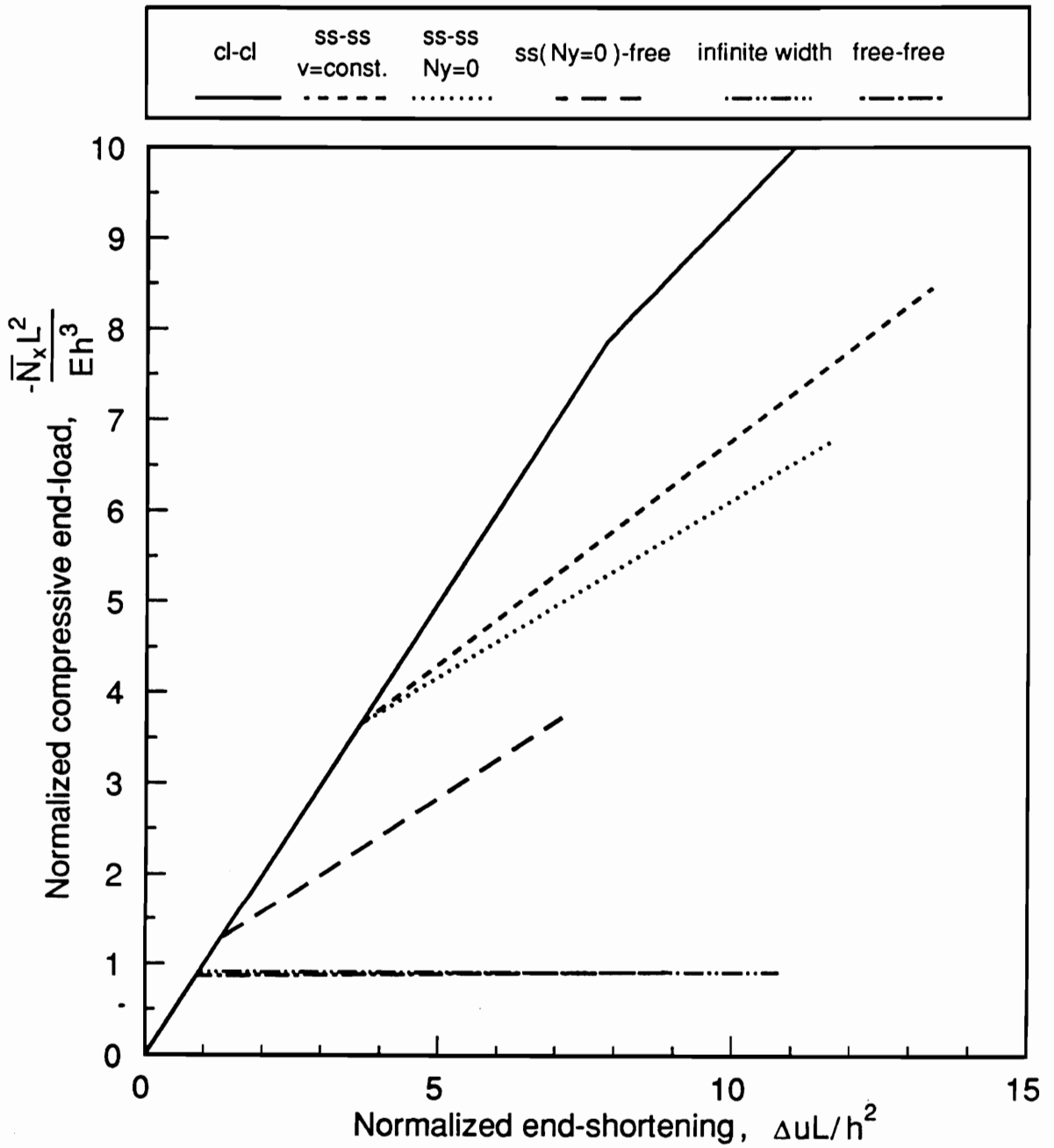


Figure 10. End load versus end shortening for square plates having a variety of boundary conditions on the unloaded edges: Isotropic material, $\nu = 0.316$, single mode solutions (see key in Figure 8 for boundary conditions).

perimental configuration are shown in Figure 11(a). The test specimen was observed to buckle with five halfwaves over the length. Despite the fact that NLPAN cannot model the clamped end condition used in testing, it was felt that five was a sufficient number of buckling halfwaves to assure that NLPAN could accurately predict the postbuckling response at points away from the panel ends.

Table 3. Graphite/Epoxy Lamina Properties [9]

Longitudinal Young's Modulus	$131.0 \times 10^5 \text{ N/cm}^2$
Transverse Young's Modulus	$13.0 \times 10^5 \text{ N/cm}^2$
Shear Modulus	$6.4 \times 10^5 \text{ N/cm}^2$
Major Poisson's Ratio	0.38
Mean Ply Thickness	0.0125 cm (0.00492 in.)

The details of the test boundary conditions which are shown in Figure 11(a) are not all described in [9]. Particular omissions include the grip length over which the panel ends were clamped and the width of the margins between the knife-edge supports and the side edges of the panel. Thus, in the initial NLPAN model it was assumed that the test specimen was simply supported around its outer edges. The boundary conditions are given in Figure 11(b), and the model is referred to as Model 1. NLPAN results obtained using Model 1 showed poor agreement with the test data. Subsequent conversations with Marshal Rouse, co-author of [9], revealed additional details of the test boundary conditions which are reflected in Figure 11(a). A second NLPAN model, referred to as Model 2 and depicted in in Figure 11(c), was used to more accurately represent the test boundary conditions. Model 2 incorporates three plate strips, two of which are narrow strips which model the unsupported panel edges outside of the knife-edge supports. While Model 1 simulates the full specimen length, Model 2 simulates only the unsupported length of the specimen. Using Model 2, NLPAN gives greatly improved agreement with the experimental results (as will be presented shortly), and thus, except where noted otherwise, NLPAN results presented here were produced using Model 2. In the results presented for NLPAN Model 2, a correction is applied to the imposed end shortening value, which only applies to the unsupported length of the panel. The end segments of the panel, which are loosely clamped, are assumed to shorten as a function of the axial stiffness

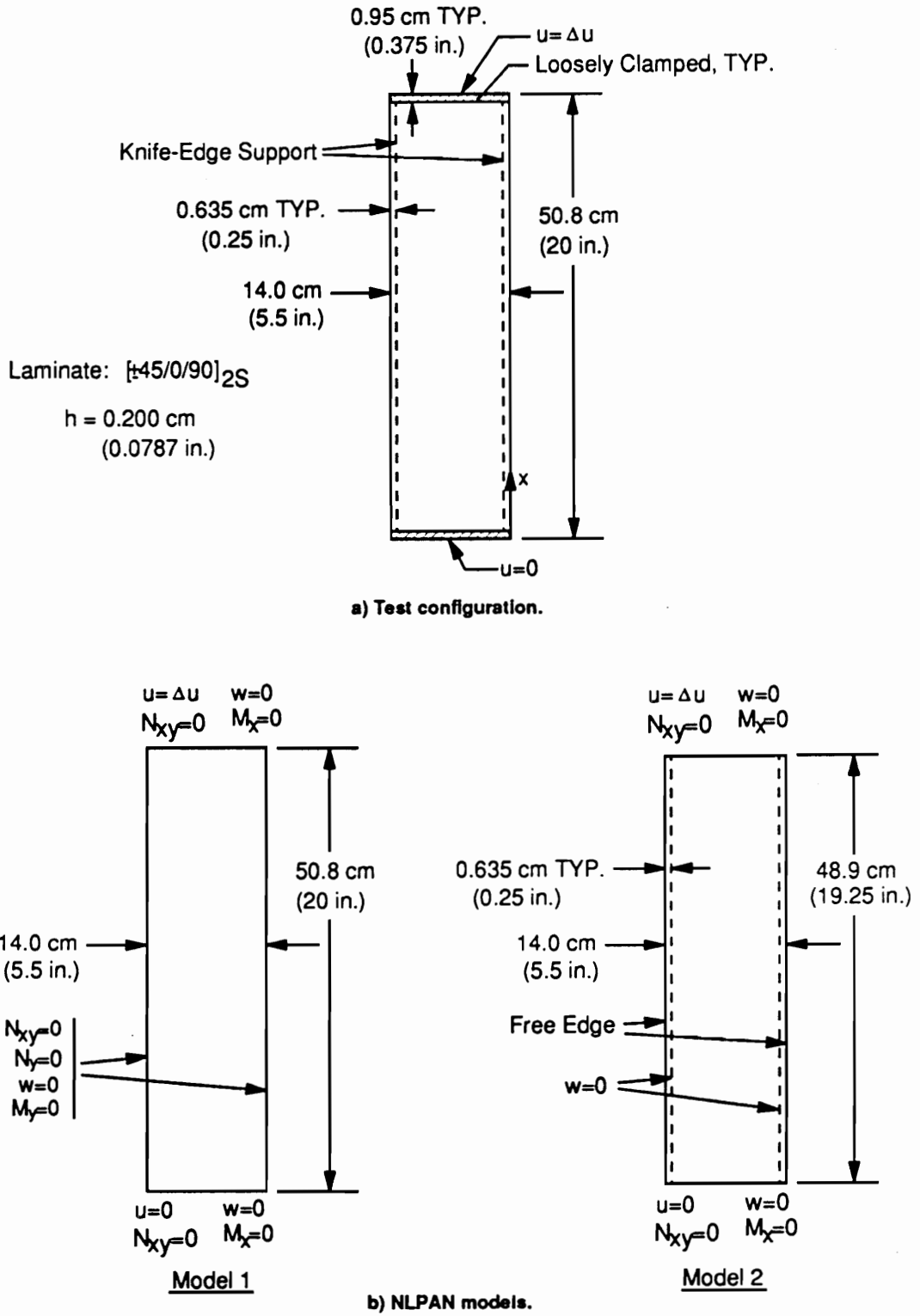


Figure 11. Unstiffened quasi-isotropic composite panel with uniaxial loading: Test description in [9].

of the unbuckled panel and the mean axial force resultant \bar{N}_x , as if the stress resultant in the clamped ends were uniform at a value $N_x = \bar{N}_x$.

Some comments are made regarding buckling loads and mode shapes. The buckling eigenvalues computed using PASCO are given in Table 4 for both Models 1 and 2, and for halfwave numbers 3, 4, and 5. For both of the models, the ascending order of eigenvalues corresponds to halfwave numbers 4, 3, and 5, respectively. It is puzzling that the test specimen considered here exhibited five buckling halfwaves, particularly considering that the clamped end conditions would be expected to drive the halfwave number toward a lower value than what would be expected for a panel with simply supported ends. (Test specimen C18 of [9] was nominally identical to specimen C17, but exhibited four buckling halfwaves.) One explanation offered here is that perhaps the true buckling mode had three bulges, but in postbuckling an additional bulge developed at each end due to the propensity of the longitudinal wavelength to decrease with increasing load in postbuckling.

Table 4. PASCO-Computed Buckling Loads for an Unstiffened Composite Panel

	Critical Load, N_{scr} (N/cm)		
	$m = 3$	$m = 4$	$m = 5$
NLPAN Model 1	-880.6	-877.4	-961.6
NLPAN Model 2	-1166	-1129	-1202

In the NLPAN predictions presented here, five buckling modes were incorporated as shape functions. These are the first three symmetric modes having five halfwaves over the length, and the first two symmetric modes having fifteen halfwaves over the length, where fifteen was selected because it is three times the halfwave number of the primary buckling mode. (The analogous modes for a square plate correspond to the coefficients w_{11} , w_{13} , w_{15} , w_{31} , and w_{33} , where $w = \sum w_{mn} \sin(m\pi x/a) \sin(n\pi y/a)$, where a is the length of the sides of the plate. These modes were selected based on the results of Levy's analysis of a postbuckled square plate [13].) In computing the second-order displacement fields, twenty intervals were used for Model 1, whereas for Model 2, sixteen intervals were used between the knife-edge supports and four intervals were used for each of the outboard plate strips. In the NLPAN

analysis geometric shape imperfections were assumed to be present in the shape of the primary buckling mode, at an amplitude of five percent of the panel thickness.

Figure 12 presents the end load versus end shortening for the panel, comparing NLPAN predictions for both Models 1 and 2 with the test data from [9]. As can be seen, Model 2 results fall much closer to the test data than Model 1 results. The large difference between the results for the two NLPAN models shows the importance of what may appear to be minor differences in boundary conditions. The Model 2 results are in close agreement with the test data in the middle of the postbuckled range considered, but fall slightly high in the early and advanced postbuckling ranges. In the early postbuckling range, the test data, reported in Figure 4(d) of [9], may be slightly in error, since it appears that the plotted data were forced to go through a theoretical bifurcation buckling load which this author believes was too low. In the advanced postbuckling range, the test specimen has contracted in the width direction to compensate for large out-of-plane deflections, so that the knife-edges support the panel closer to the edges than in the early postbuckling regime. The effective shifting of the support toward the panel edges is not accounted for in the NLPAN analysis, and may be responsible for the reduced extensional stiffness observed in the test relative to the NLPAN predictions. A second possible explanation for the disagreement in the advanced postbuckling regime is that the effects of transverse shear deformation, not accounted for in NLPAN, may be significant.

Comparisons of longitudinal surface strains predicted by NLPAN with those measured experimentally using strain gauges are presented in Figure 13. Figure 13(a) presents the longitudinal strains on opposing surfaces at the center of the panel, which corresponds to a point of maximum out-of-plane displacement. The agreement between the NLPAN predictions and the test measurements is generally good. There is a small over-prediction of strain levels on the compression side at the higher load levels. At lower load levels, it appears that the agreement would be even better if a smaller imperfection amplitude were used in the NLPAN analysis (the amplitude used was five percent of the panel thickness).

The distribution of longitudinal surface strains across the width of the panel at the panel mid-length are presented in Figure 13(b). for a fixed load level. The test data were recorded

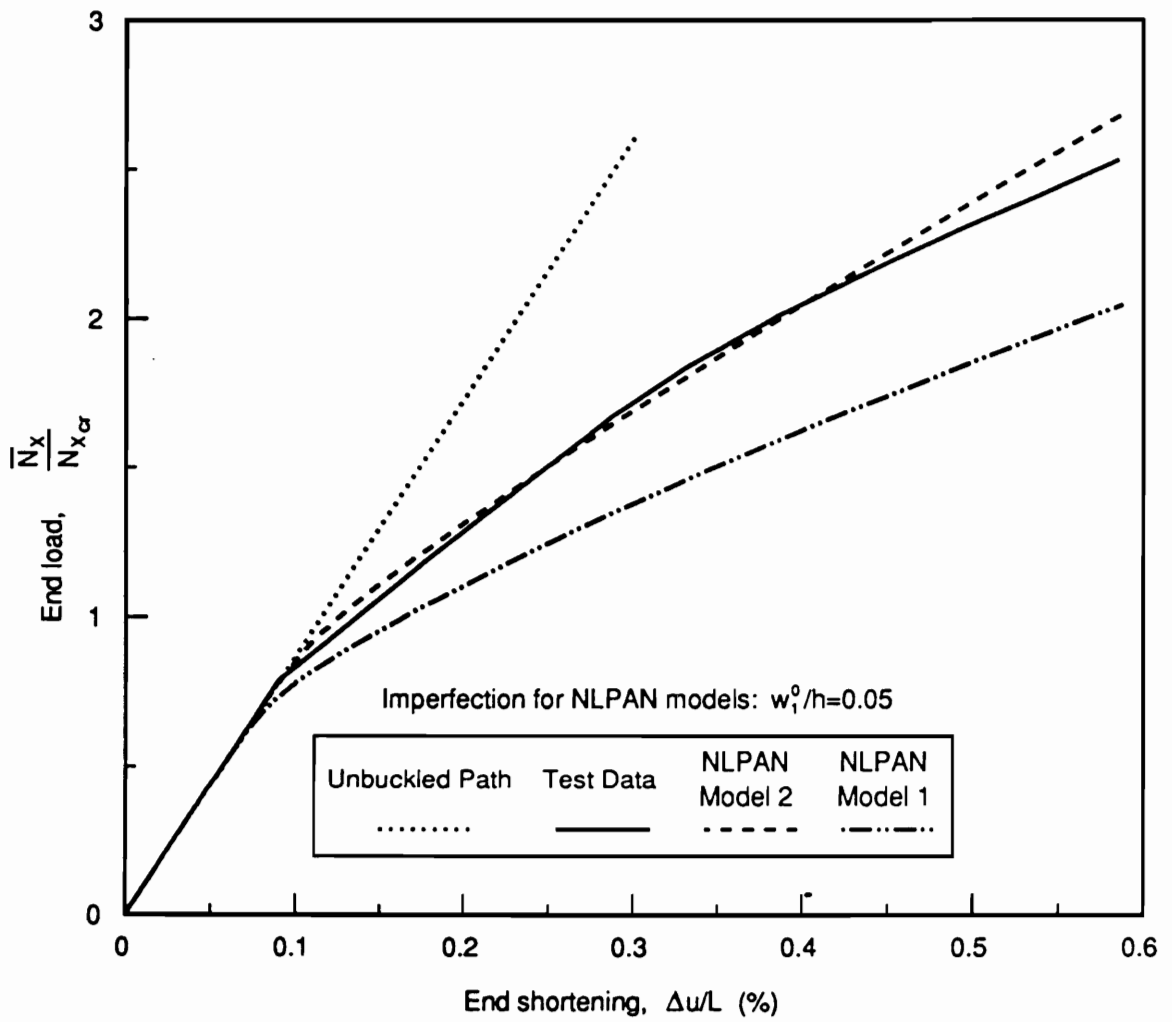
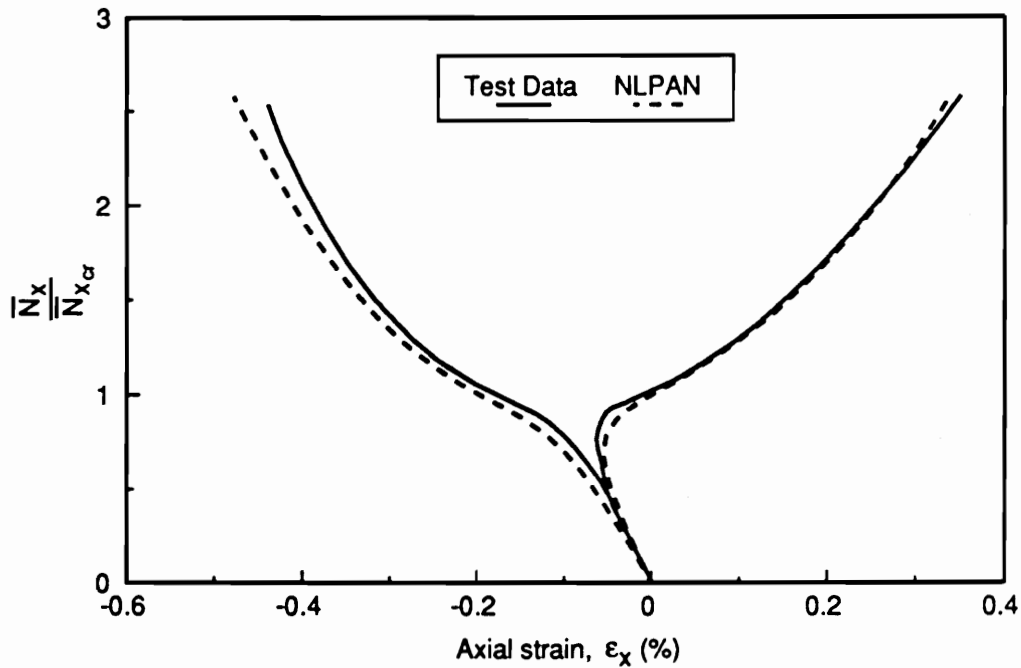


Figure 12. End load versus end shortening for a uniaxially loaded quasi-isotropic composite panel: Test data from [9].

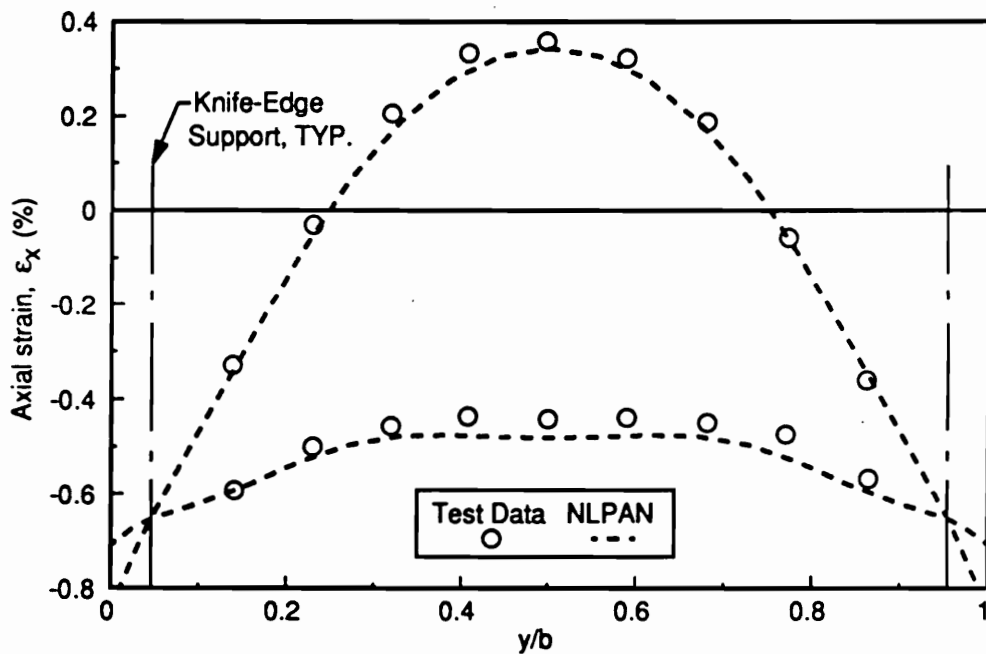
at 3.26 times the theoretical buckling load as computed in [9]. However the theoretical buckling load used in [9] was reported with poor accuracy ($\pm 4\%$), so for purposes here it was assumed that the theoretical buckling load in question was the value computed by PASCO for Model 1 for five halfwaves, which is provided in Table 4 on page 105. (This value was within the possible range for the theoretical buckling load given in [9], whereas the corresponding value for Model 2 was not.) A factor of 3.26 times the critical load for Model 1 (for $m = 5$) translates to a factor of 2.61 times the critical load for Model 2 (for $m = 5$). In view of the uncertainty in the load level of the test data, the NLPAN predictions are in good agreement. The subtleties of the shape of the strain distribution on the compression side of the skin are captured quite well by NLPAN. Note that NLPAN predicts that the highest compressive strains occur in the portions of the panel skin falling outboard of the knife-edge supports.

4.3 Postbuckling of a Three Bay Blade-Stiffened Panel

Results from the finite-element analysis of the postbuckling behavior of a uniaxially loaded blade-stiffened panel are presented in [4]. The panel, depicted in Figure 14(a), has four stiffeners which delineate three bays of equal dimension across the width of the panel. The stiffeners are nearly three times as thick as the skin, and the panel has the approximate elastic properties of aluminum, given in Figure 14(a). The STAGSC-1 computer code [28,29] was used for the finite-element analysis; as discussed in the review of literature, this code is considered to be a robust method for the analysis of complicated nonlinear structural response. In the finite-element analysis, the panel is supported only at its longitudinal ends, where a clamped support condition is modelled. Uniform end-shortening is imposed. The early postbuckling response (through about 4 1/2 times the critical buckling load) is dominated by a local buckling of deflection pattern with five halfwaves in the longitudinal direction (see Figure 14(b)). Despite the difference in boundary conditions between the finite-element anal-



a) Strains at the panel center.



b) Distribution of strains across the panel width at $x=L/2$ for $\bar{N}_x / \bar{N}_{x_{cr}} = 2.61$.

Figure 13. Longitudinal strains at the surface of a uniaxially loaded quasi-isotropic composite panel: Test data from [9].

ysis (clamped) and an NLPAN analysis (simply supported), it was felt that five was a sufficient number of halfwaves so that the finite-element results would provide a good gauge of the performance of NLPAN in analyzing the local postbuckling response.

Two different NLPAN representations are used to analyze the three bay panel. The first is a complete (symmetric) representation, whereas the second uses a representative strip of panel skin centered around a single stiffener. In Section 4.3.1, results from the full panel representation will be discussed. In Section 4.3.2, results obtained using the two representations will be compared.

4.3.1 Full (Symmetric) Representation of the Panel

An NLPAN model was developed to analyze the response of the three bay panel. The response was assumed to be symmetric about the panel mid-width, so that only half of the panel was modelled and symmetry conditions were imposed at the centerline. For the primary buckling load values computed by STAGSC-1 and PASCO were $N_{xcr} = -336.0$ lb/in. and $N_{xcr} = -344.4$ lb/in., respectively, where the load \bar{N}_x is the total end load divided by the panel width. (\bar{N}_x here replaces N_{xG} of Chapter 3.) All loads reported here are normalized by the PASCO-computed critical load.

In computing the second order fields in NLPAN, ten finite-difference intervals were used across each 4 inch skin width, and four intervals were used across each 1.5 inch stiffener width. A convergence study showed this level of discretization to provide solutions within one percent of converged values for all of the measures reported, through the highest load level reported. Full compatibility of displacements and equilibrium are enforced at the joints between plate strips when computing the second-order displacement fields $\{u_{ij}\}$. As discussed in Section 3.5.8, this causes the second-order fields to be dependant on the reference value of the load parameter, λ_b . It was also noted in the Section 3.5.8 that by invoking the "classical assumptions" of local postbuckling analysis (described in Section 2.2.2.3) the second-order

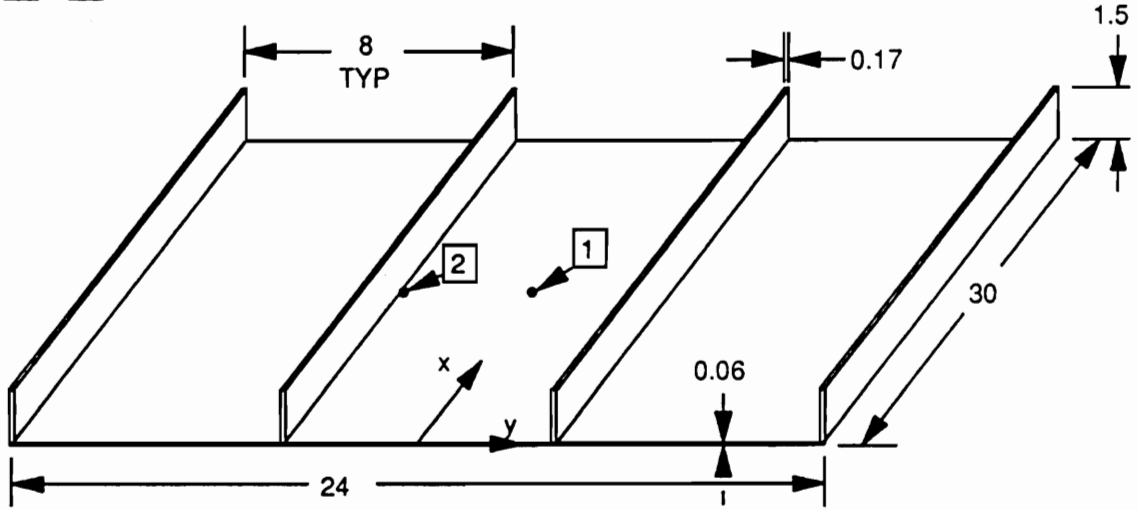
Dimensions: Inches

Homogeneous, isotropic material, $E=10^7 \text{ #/in}^2$, $\nu=0.3$

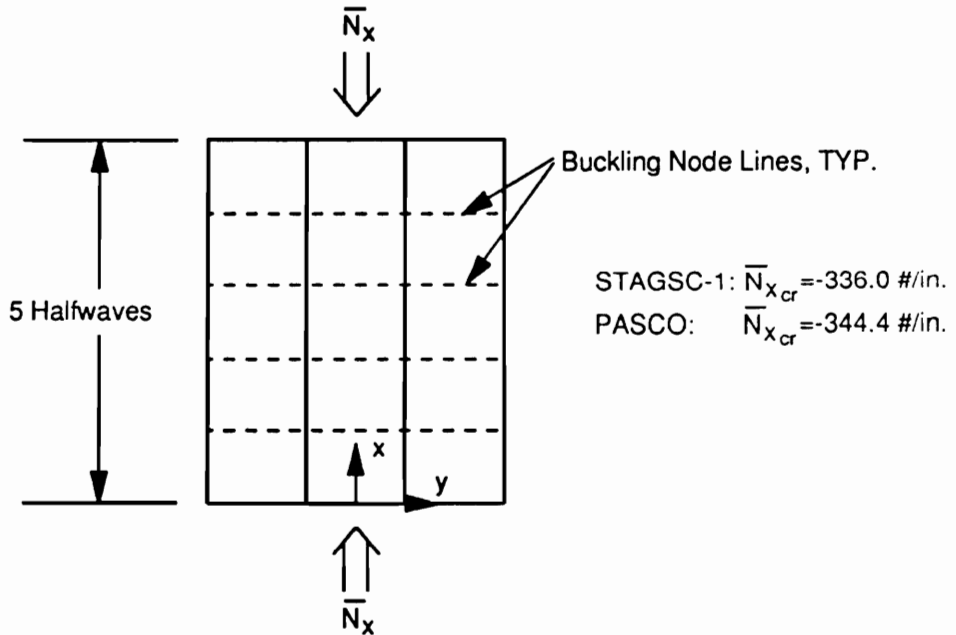
Uniaxial loading, $\bar{N}_x = (\text{Axial Load})/(24 \text{ in.})$

STAGSC-1 Boundary Conditions: Clamped ends with imposed end shortening

1, 2 - Locations of reported skin deflection and surface strains



a) Configuration details.



b) Planform view of primary buckling mode-shape.

Figure 14. Three bay blade-stiffened panel configuration used for the study of local-postbuckling behavior: STAGSC-1 results from [4].

displacement fields became load-independent. Accepting that the classical assumptions provide accurate solutions for local postbuckling, the second-order displacement fields were assumed to be load-independent, and were computed with λ_b set to zero.

Selection of buckling modes: The first issue to be taken up regards the selection of buckling modes for inclusion in the nonlinear analysis. Figure 15 depicts the transverse profiles of the first five symmetric buckling modes having five halfwaves in the longitudinal direction. The primary buckling mode is dominated by skin buckling, with only a small amount of stiffener participation. Note that in the primary buckling mode the displacement amplitude in the center bay of the panel is about forty percent greater than the displacement amplitude in the outer bays. The following approach was used to select the buckling modes to be used in the NLPAN analysis. First, a series of NLPAN analyses was performed, each of which incorporated the primary buckling mode and one of the four additional modes shown in Figure 15. The second and fourth modes were found to interact most strongly with the primary mode, and were thus selected for use. Three additional modes were then selected for use, those being the first, second, and fourth modes having fifteen longitudinal halfwaves. These three additional modes have the same approximate profiles as their counterparts in Figure 15, except that the fourth mode having fifteen halfwaves displays much less stiffener participation than the fourth mode of Figure 15. The selection of secondary modes with a halfwave number three times that of the primary mode follows the pattern suggested by results for the analysis of simply supported square plates [13,14].

Second-order field displacements at the longitudinal ends of the panel: In computing the second-order displacement fields for this NLPAN model in the manner described in Section 3.5, a problem arises with regard to the satisfaction of the boundary conditions at the ends of the panel. The boundary conditions given in equation (29) require that at the panel ends ($x=0, L$) the displacements v and w must be zero, neglecting the contributions of the unbuckled solution. For the second-order fields, however, shape functions v_{ij} and w_{ij} have contributions with an x -dependence of $\cos(\hat{m}\pi x/L)$, where \hat{m} is an integer (possibly zero). Thus, v_{ij} and w_{ij} do not automatically satisfy the boundary conditions at the panel ends. The

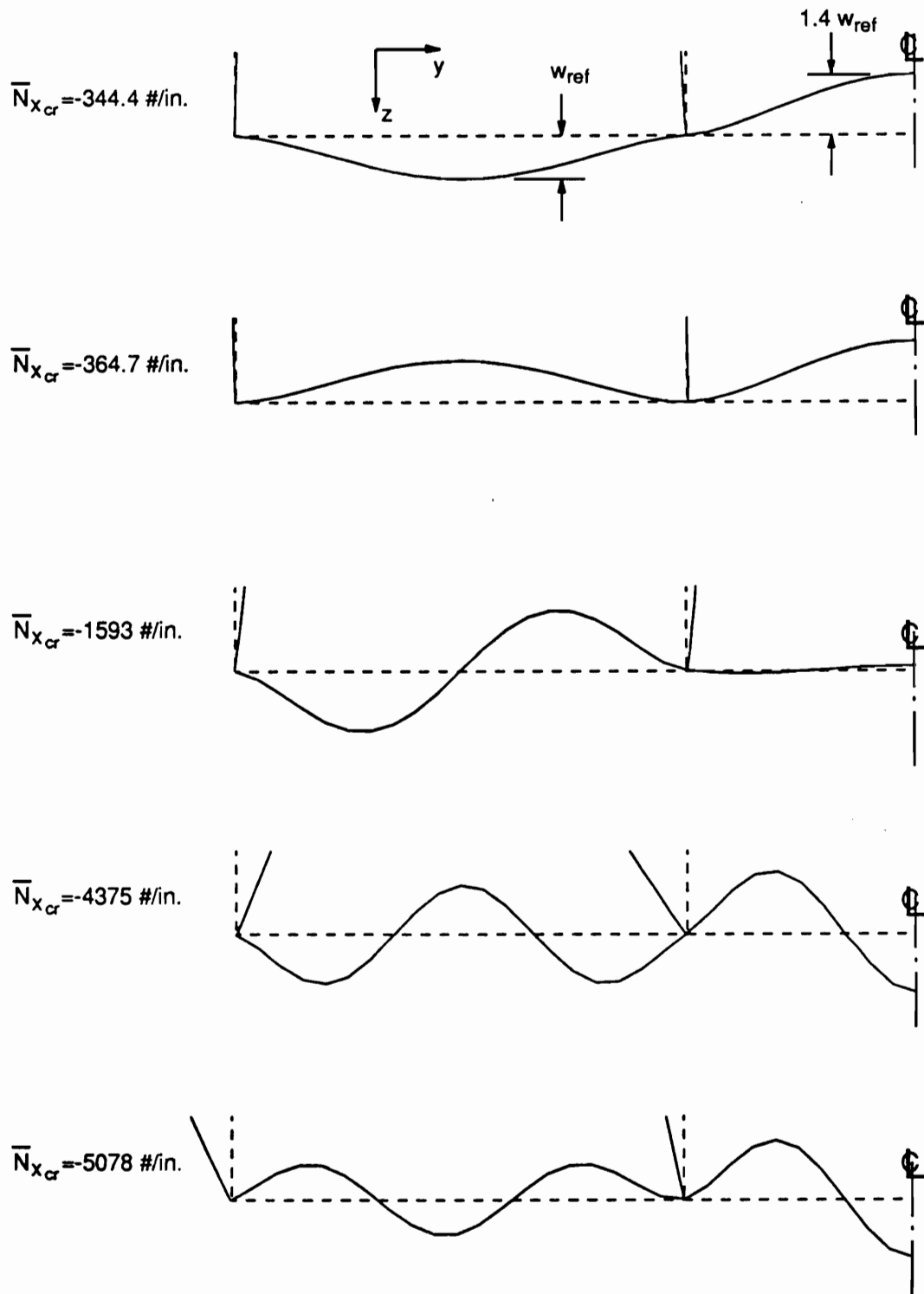


Figure 15. Transverse profiles for the first five symmetric buckling modes having five longitudinal halfwaves.

characteristics of selected second-order fields computed for the three bay panel are examined below in order to investigate this potential discrepancy.

The profile of the primary buckling eigenfunction ($m=5$) is depicted in Figure 16, along with the profiles of the two contributions to its associated second-order displacement field. The two contributions ($\alpha = 1, 2$) have values for \hat{m} of 10 and 0, respectively. Scale bars show the approximate relative amplitudes of the two contributions to the second-order displacement field. For $\alpha=1$, the profile is dominated by in-plane displacements and their gradients on each plate strip (a fact which is not obvious from the figure) whereas for $\alpha=2$ (where the x -dependence is constant) large out-of-plane displacements are present, clearly violating the simple support condition for the plate strips at the ends of the panel. The profiles of the first two buckling eigenfunctions having $m=5$ are depicted in Figure 17, along with the profiles of the two contributions to the associated mixed second-order field. The comments made above regarding the second-order displacement field of Figure 16 also apply to the mixed second-order field of Figure 17. The first buckling eigenfunction for each of the halfwave numbers $m = 5$ and $m = 15$ are depicted in Figure 18, along with the two contributions to their associated mixed second-order field. The two contributions have values for \hat{m} of 20 and 10, respectively. In contrast to the two preceding cases, both profiles are dominated by in-plane displacement gradients (not completely apparent from the figure) and any violation of the boundary conditions at the panel ends is minimal.

The perturbation approach used in deriving the equations governing the second-order fields accounted for the plate Euler equations, but the boundary conditions at the longitudinal ends of the structure were ignored. Obviously if the panel stiffeners were supported at their ends, then the displacement contributions depicted for $\alpha=2$ in Figure 16 and Figure 17 would be greatly altered. While a more elegant solution to this discrepancy is desirable, the simple fix used here to produce more physically permissible second-order fields was to impose a two-point constraint to all fields which are constant in the x -direction ($\hat{m} = 0$). Figure 19 depicts these constraints and their effects in modifying the profile given for $\alpha=2$ in Figure 16. In Figure 19, the constraints can be seen to greatly reduce the out-of-plane displacements on

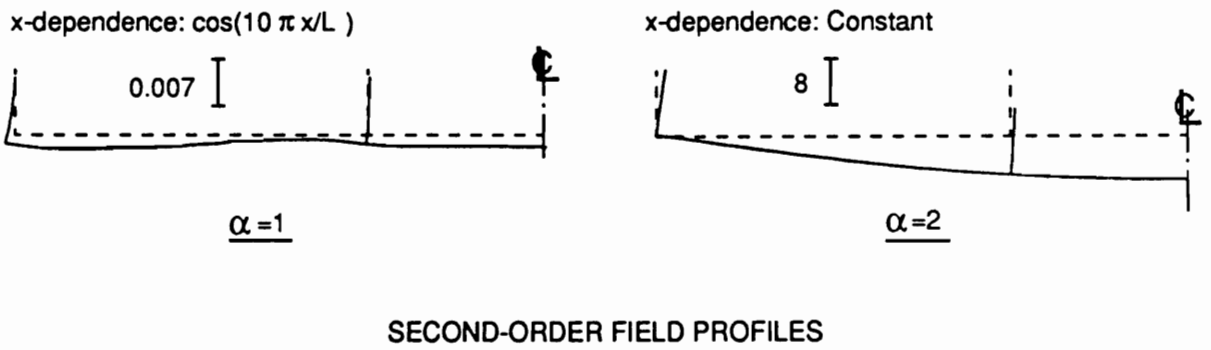
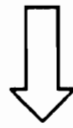
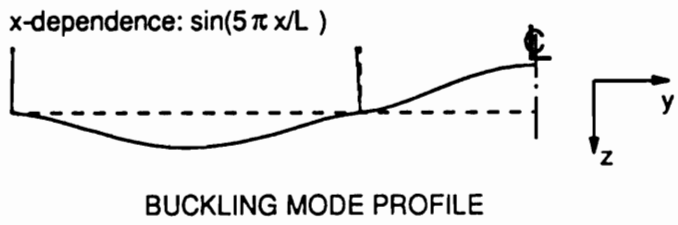


Figure 16. Profiles of the contributions to a second-order displacement field $\{u_{ii}\}$.

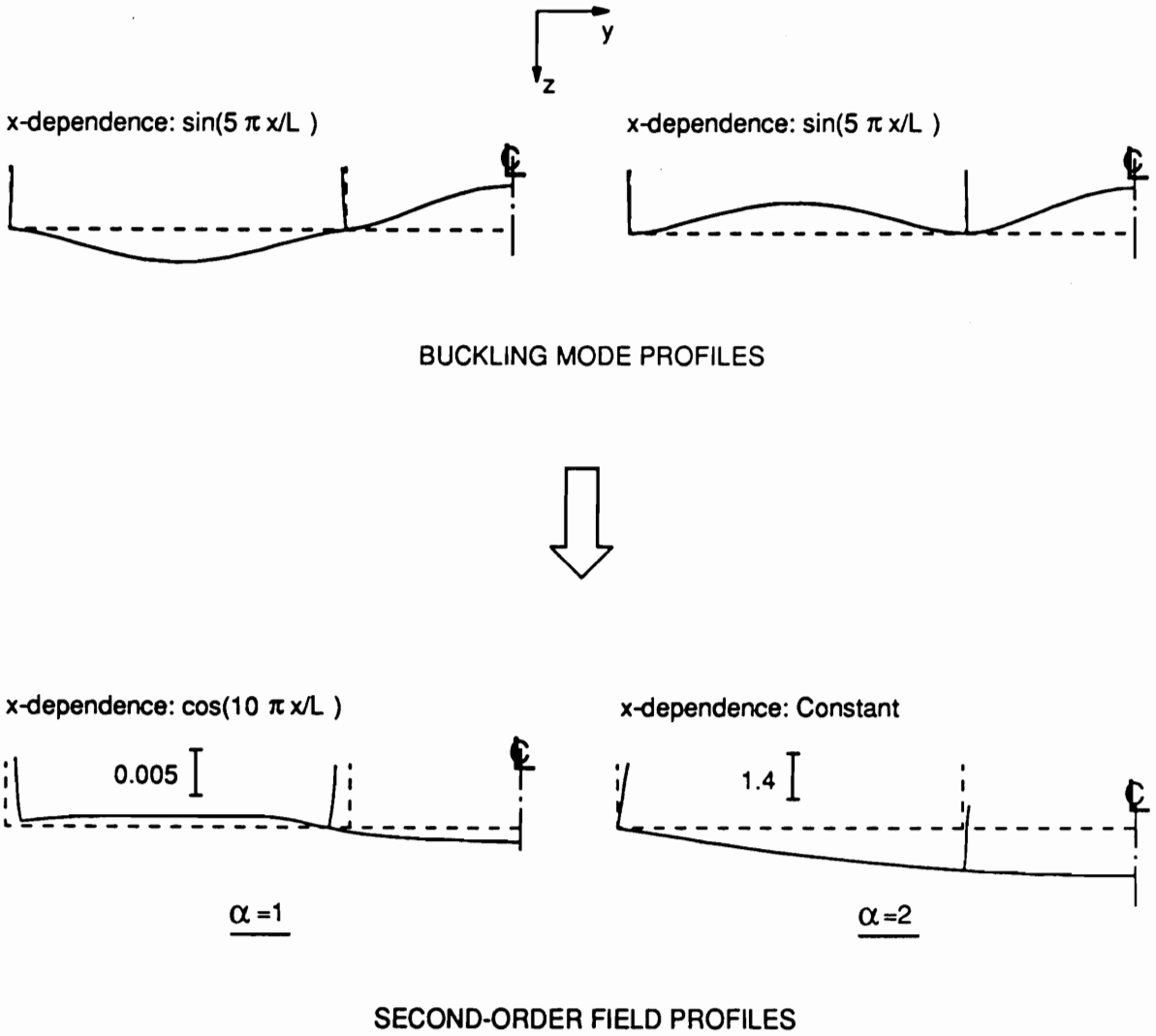


Figure 17. Profiles of the contributions to a second-order displacement field $\{u_{ij}\}$: For $\{u_i\}$ and $\{u_j\}$ with identical halfwave numbers ($m = n$).

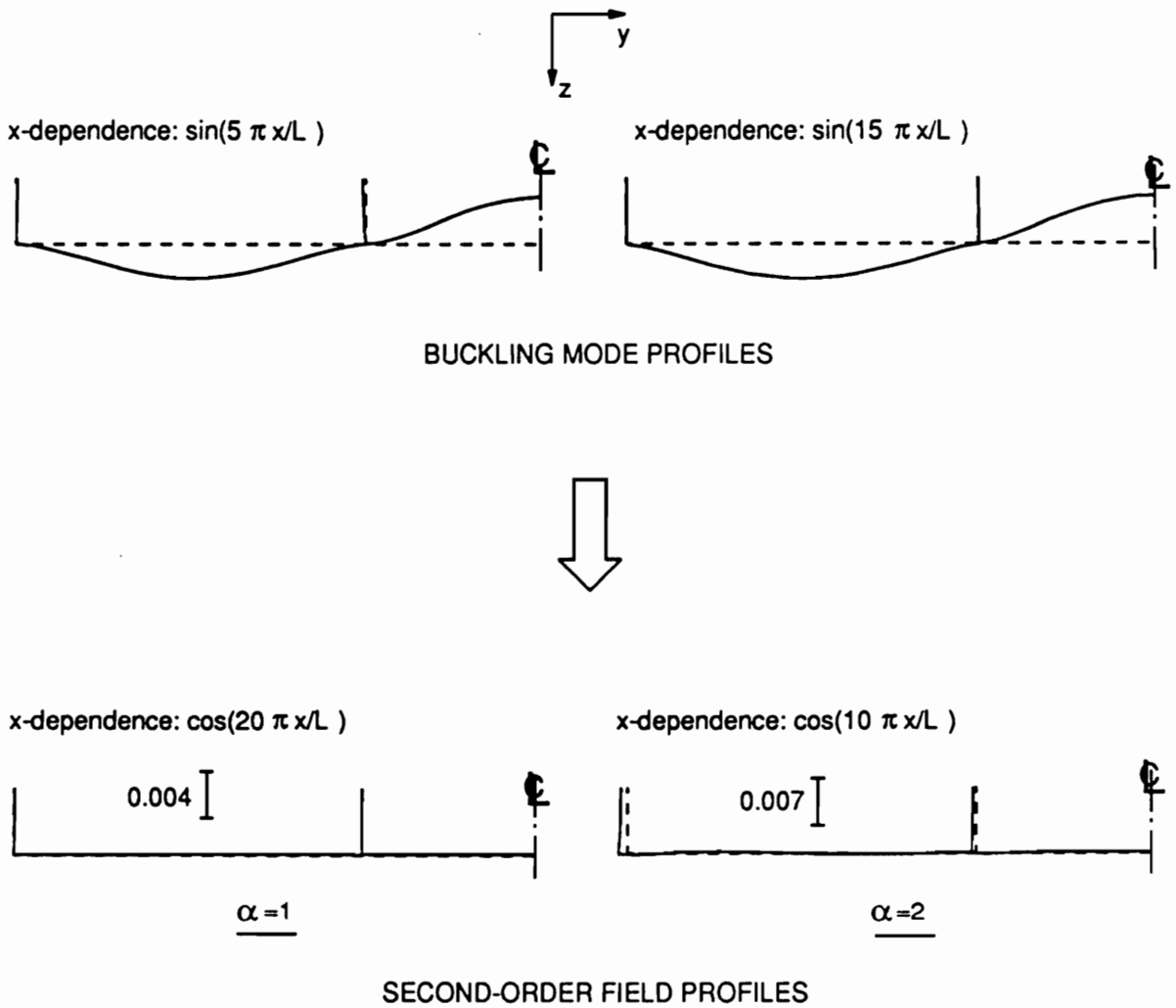


Figure 18. Profiles of the contributions to a second order-displacement field $\{u_{ij}\}$: For $\{u_i\}$ and $\{u_j\}$ with different halfwave numbers ($m \neq n$).

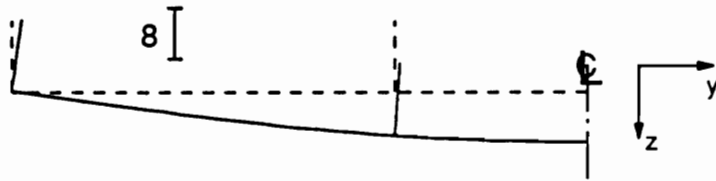
each plate strip, so that the profile in Figure 19(b) is now dominated by in-plane displacements and their gradients on each plate strip. It is not apparent in Figure 19, but the in-plane displacement gradients on each plate strip are essentially unaffected by the addition of the constraints to the field.

A few words are offered here to put into perspective the suppression of out-of-plane displacements discussed above. As was discussed in Section 2.2.2.3, there is justification for the use of the so-called classical assumptions of local postbuckling analysis [41,42]. When these assumptions are invoked, one consequence is that w_{ij} is identically zero on each plate strip. The modification to the displacement field depicted in Figure 19 accomplishes essentially the same thing, because the residual displacements w_{ij} contribute negligibly to strains compared to u_{ij} and v_{ij} .

Results for the full (symmetric) panel representation: A comparison of NLPAN results with STAGSC-1 results for the three-bay panel is presented in Figure 20. For all results presented, the normalizing load used is the PASCO-predicted buckling load. NLPAN results are presented for a single mode analysis in addition to the six mode analysis. The single mode analysis was performed because it represents the most economical possibility for postbuckling analysis using NLPAN. For both load versus end shortening (Figure 20(a)) and load versus center deflection (Figure 20(b)), the six mode NLPAN solutions agree fairly well with the STAGSC-1 solutions, whereas the single mode solutions exhibit a significant deviation from the STAGSC-1 solutions.

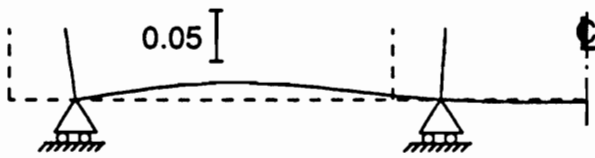
The axial surface strains (ϵ_x) at the center of the panel (location 1 in Figure 14) are plotted as a function of the end load in Figure 20(c). The results are for a bulge at the center directed away from the stiffener side of the panel. In the postbuckling regime the single mode NLPAN solutions are skewed relative to the results of STAGSC-1, reflecting an excessive prediction of extensional membrane strain. The following explanation is offered. The primary buckling mode exhibits deflections in the center bay which are 40% greater than the deflections in the outer bays, whereas in the finite element analysis the deflection amplitudes in the three bays were approximately equal in the early postbuckling regime [4]. The second buckling mode

x-dependence: Constant



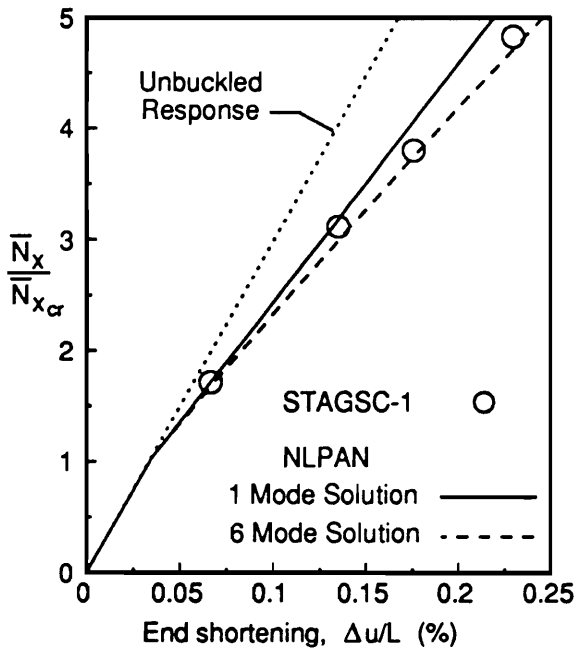
a) Profile of original second-order field.

x-dependence: Constant

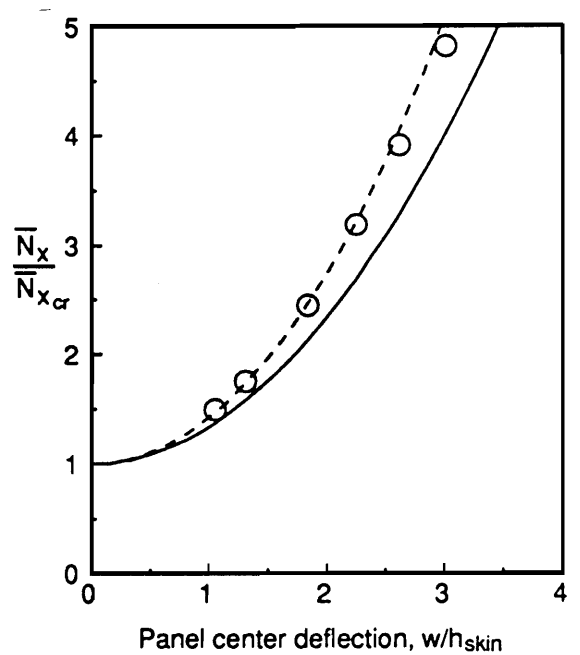


b) Profile of modified second-order field.

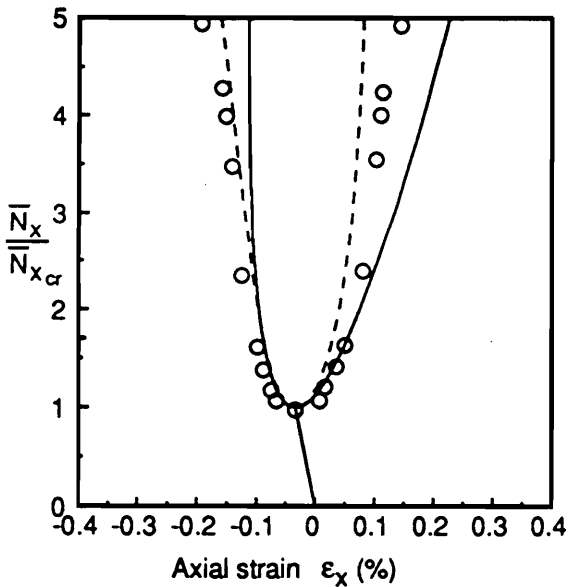
Figure 19. Example of the modification used for x-independent contributions to the second-order displacement fields.



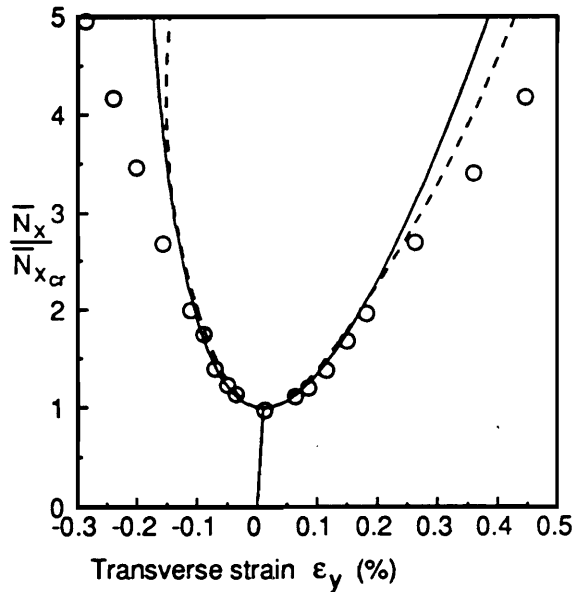
a) End load versus end shortening.



b) End load versus center deflection of skin.



c) Axial surface strains at center of panel skin (location 1).



d) Transverse surface strains of the skin adjoining a stiffener (location 2).

Figure 20. Analytical results for the local-postbuckling response of a three-bay blade-stiffened panel: STAGSC-1 results from [4].

shown in Figure 15 is predicted by NLPAN to be relatively active in the postbuckling regime, and serves to equalize the deflections in the center bay. The excessive deflections in the center bay predicted using a single mode analysis induce the excessive extensional strains detected at the center of the panel. The six mode NLPAN solutions do not exhibit the skewing present in the single mode solutions, and thus give better agreement with the STAGSC-1 results. However, the predicted strain levels are somewhat low for both the compression and tension sides of the skin, apparently reflecting a slightly low predicted magnitude for the bending curvature κ_x .

Results for the transverse strains (ϵ_y) in the skin next to a stiffener at the mid-length of the panel (location 2 in Figure 14) are presented in Figure 20(d). Both the single mode solutions and the six mode solutions show good agreement with the STAGSC-1 results up to a load of about twice the critical load, above which both the compressive and tensile strains are under-predicted. The disparity between the various predictions for transverse strains at higher load levels is discussed more in a following section.

4.3.2 Panel Representation Using a Stiffener-Unit

The three bay panel under study here was modelled using the PANDA2 computer code in [4]. However in the PANDA2 analysis, the panel was modeled using a repeating unit of skin with an attached stiffener, referred to here as a "stiffener-unit." Since the side boundaries of the panel are not modelled in this representation, then an exact analysis of the finite-width panel is precluded, but the approach has the benefit of minimizing the complexity of the structural model, thus minimizing the computational expense of performing the analysis. An NLPAN analysis was performed using a stiffener-unit representation of the panel. This additional analysis was performed for two reasons. The first reason was to investigate the performance of the simplified, more economical model in predicting the response of the three bay panel. The second reason was to help assess the NLPAN results obtained using the complete

(symmetric) panel representation. It is a straightforward matter to select the appropriate modes for use with the stiffener-unit model on an intuitive basis, and thus it was felt that the NLPAN results computed using the stiffener-unit model should serve as a check of the set of modes used with the complete (symmetric) representation of the panel.

The stiffener-unit used with NLPAN is depicted in Figure 21(a). Symmetry conditions are imposed at each side boundary of the stiffener-unit. The load \bar{N}_x^u is defined as the total end load carried by the stiffener-unit divided by the 8 inch width. While a series of three stiffener-units has the same width as the three bay panel, the three-unit series has less cross-sectional area than the panel, having one less stiffener. An area-compensated force resultant, \bar{N}_x^* is defined:

$$\begin{aligned}\bar{N}_x^* &= \frac{A_{TOTAL}}{3A_{UNIT}} \bar{N}_x^u \\ &= 1.116 \bar{N}_x^u\end{aligned}\tag{153}$$

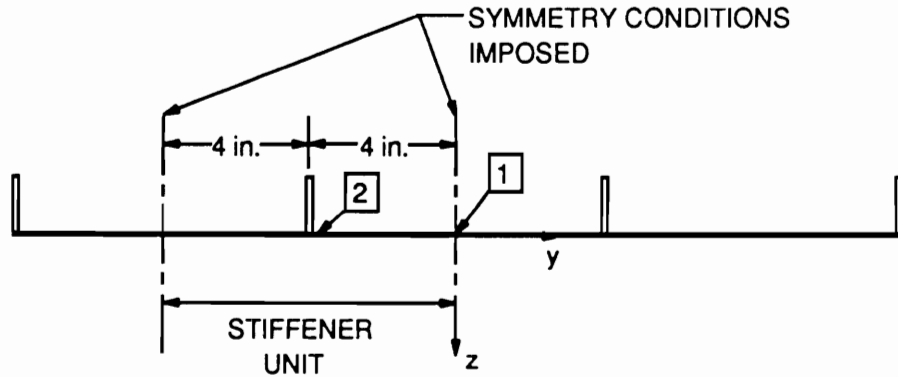
where A_{TOTAL} is the cross-sectional area of the complete three bay panel, and A_{UNIT} is the cross-sectional area of a stiffener-unit. Therefore, in prebuckling response, equal loads \bar{N}_x and \bar{N}_x^* produce equal end shortening values in the three bay panel and the stiffener-unit, respectively. In presenting NLPAN results from this stiffener-unit representation, the load \bar{N}_x^* is used.

Selection of buckling modes: Five buckling modes were incorporated in the NLPAN analysis using the stiffener-unit representation. These were the first three unsymmetric modes having five halfwaves in the x-direction, the profiles of which are shown in Figure 21(b), and the first two unsymmetric modes having fifteen halfwaves in the x-direction. This set of modes is analogous to the five most important modes for an isotropic square plate, as described in [13]. A single mode analysis was also performed with NLPAN, because this represents the most economical possibility for a local postbuckling analysis.

Results for stiffener-unit representation: Results from one and five mode analysis for the stiffener-unit model, compared with the STAGSC-1 results from [4] Figure 22. Figure 22(a)

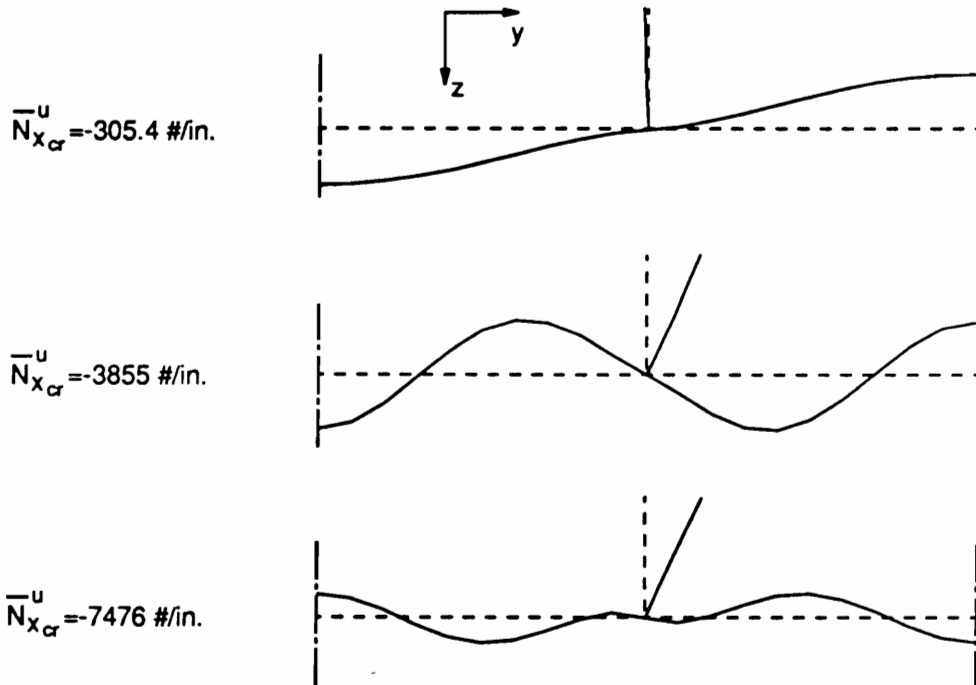
DEFINE: $\bar{N}_x^u = (\text{Axial Load on Stiffener Unit}) / (8 \text{ in.})$

1, 2 - Locations of reported skin deflection and surface strains



PANEL CROSS-SECTION

a) Stiffener unit definition.



b) Transverse profiles of the first three unsymmetric buckling modes for which $m=5$.

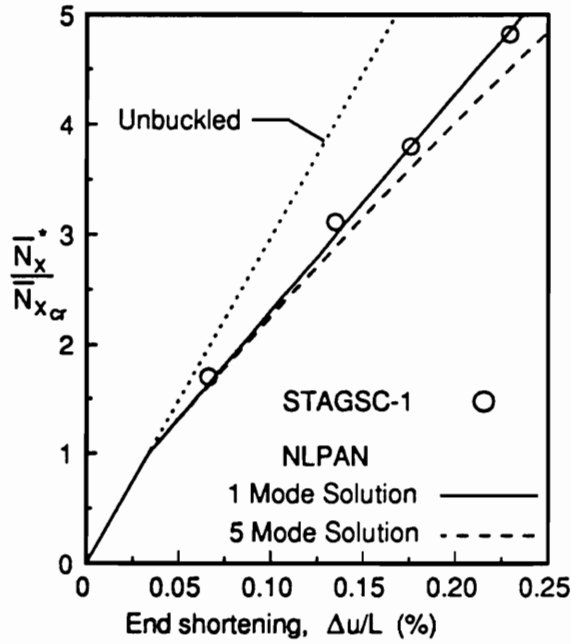
Figure 21. Stiffener-unit representation of a three bay blade-stiffened panel.

presents the end load versus end shortening, and the five mode NLPAN solutions can be seen to slightly under-predict the axial stiffness in postbuckling. Good agreement is obtained for the end load versus skin center deflection, shown in Figure 22(b), though this may be somewhat of a coincidence, since there is no obvious reason why the end-load/skin-deflection results should be better than the end-load/end-shortening results. Similarly, the fact that the single mode analysis seems to provide better results than the five mode analysis for end load versus end shortening is likely only a coincidence of cancelling errors.

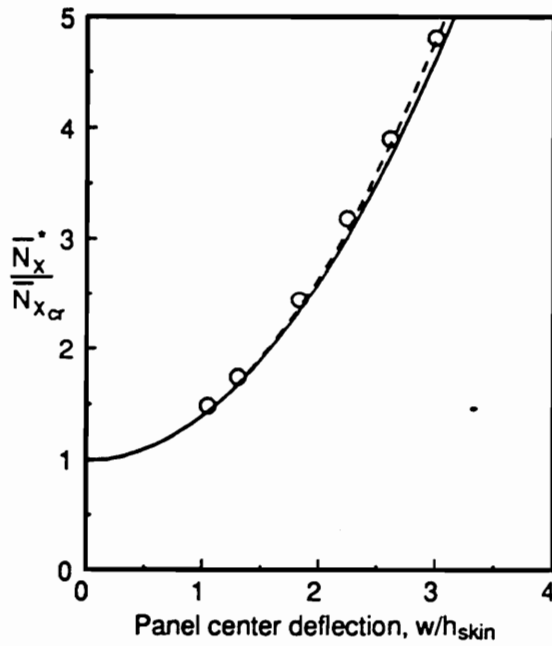
The axial surface strains in the skin at the center of the panel (location 1 of Figure 14 and Figure 22) are presented in Figure 23. NLPAN results obtained using the stiffener-unit representation are compared with those for the full-panel representation. In the single mode solutions, presented in Figure 23(a), the stiffener-unit model gives better results than the full-panel model, because the results for the former model do not exhibit the previously discussed skewing exhibited in the results for the latter model. For the multiple mode solutions, presented in Figure 23(b), the two models give nearly identical results, though both results sets exhibit somewhat lower strain amplitudes than those predicted by STAGSC-1.

The transverse strains in the skin surfaces at the mid-length of the panel next to a stiffener (location 2 in Figure 14 and Figure 21) are presented in Figure 24. NLPAN results obtained using the stiffener-unit representation are compared with those for the full-panel representation. For single mode analyses (Figure 24(a)), the full panel model provides slightly better agreement with the STAGSC-1 results than does the stiffener-unit model, though the results from both NLPAN models diverge from the STAGSC-1 results at the higher load levels. For the for multiple mode analyses, summarized in Figure 24(b), the two NLPAN models provide results which agree well with each other, and which agree with the STAGSC-1 results up to a load level of about twice the critical value, beyond which the strain levels predicted by NLPAN fall below the levels predicted by STAGSC-1.

Judging as a whole the results presented in Figure 22 through Figure 22, the stiffener-unit representation of the three-bay panel is fairly accurate in predicting the characterizing features of the postbuckling response. The good agreement between the multiple-mode strain

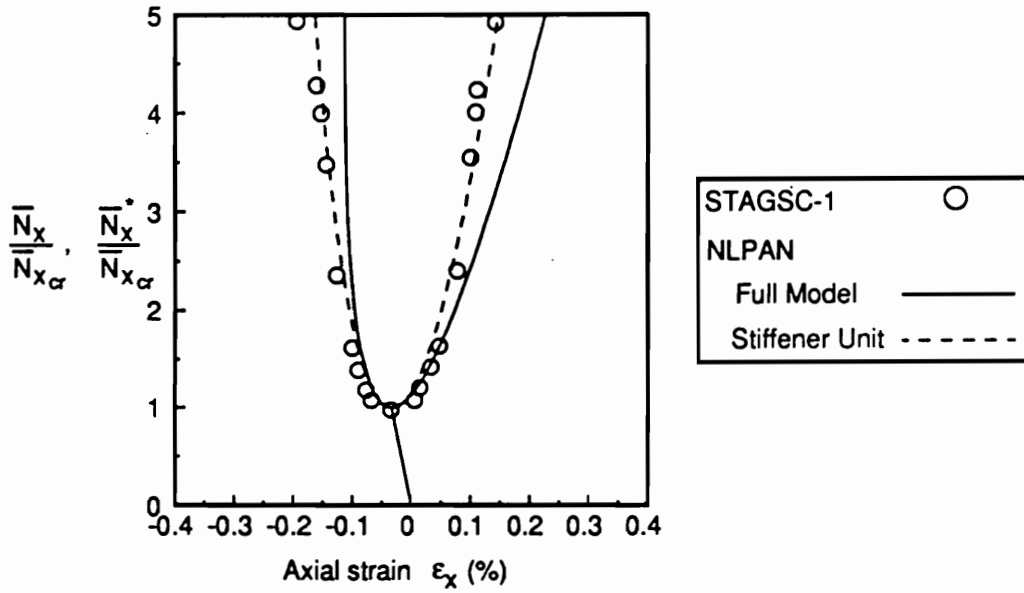


a) End load versus end shortening.

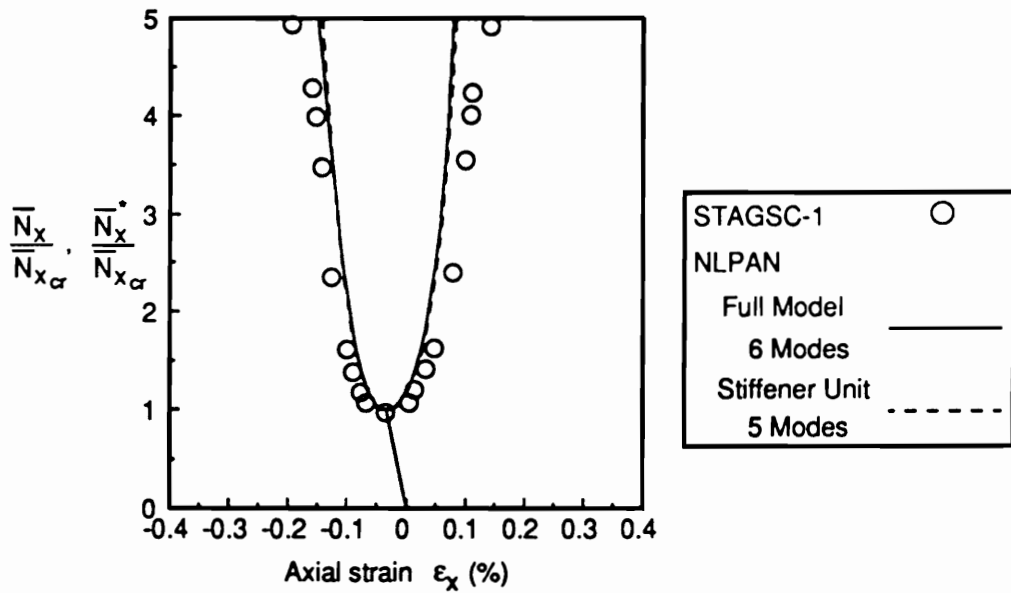


b) End load versus center deflection of skin.

Figure 22. Analytical results from NLPAN using a stiffener-unit representation of a three bay panel: STAGSC-1 results from [4].

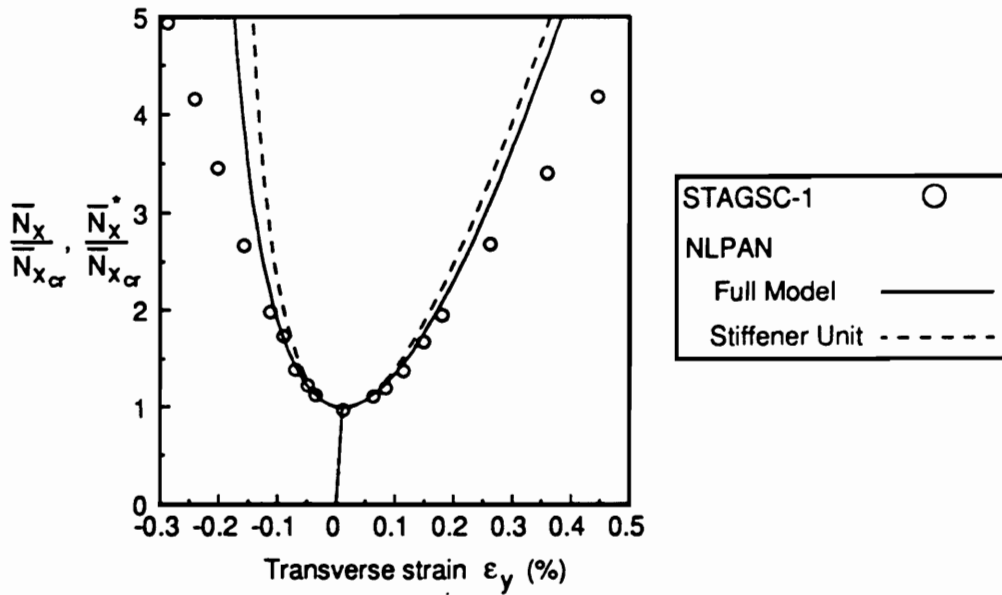


a) Single mode solutions.

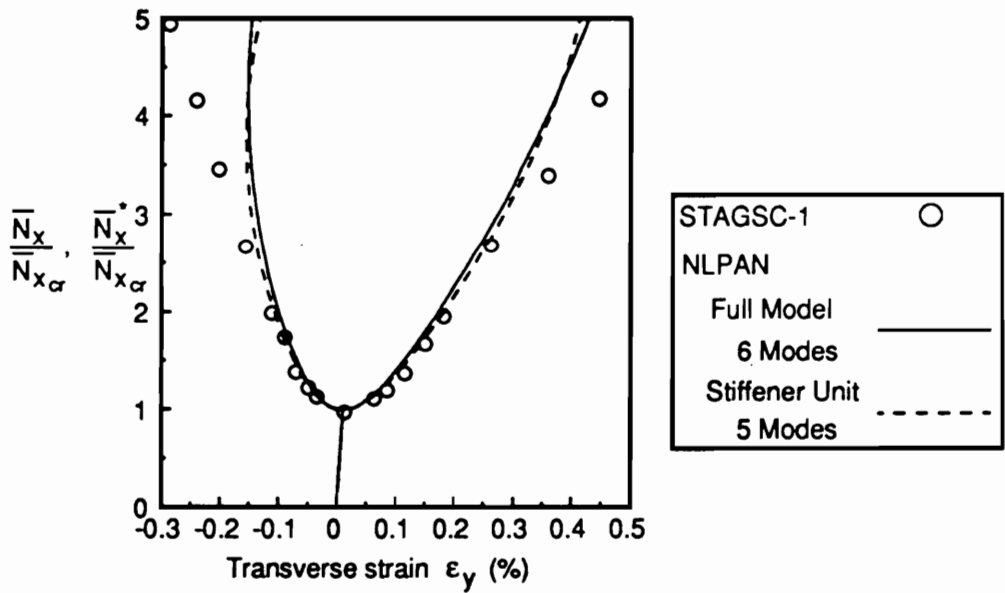


b) Multiple mode solutions.

Figure 23. Longitudinal surface strains in the skin at the center of a three bay panel (location 1): Comparison of two NLPAN representations; STAGSC-1 results from [4].



a) Single mode solutions.



b) Multiple mode solutions.

Figure 24. Transverse surface strains in the skin adjoining a stiffener for a three bay panel (location 2): Comparison of two NLPAN representations; STAGSC-1 results from [4].

predictions for the two NLPAN models (Figure 23(b) and Figure 24(b)) suggests that no important buckling modes were omitted in applying either of the two models. It is unclear why the axial surface strains (Figure 23(b)) are under-predicted using both NLPAN models, even in the early postbuckling regime. The possibility of a reporting error in [4] can not be discounted. A question remains as to why the NLPAN predictions for the transverse surface strains (Figure 24) diverge from the STAGSC-1 results in the upper range of the loads investigated. One possible explanation is offered here. The STAGSC-1 analysis predicted the onset of a secondary instability at a load approaching five times the critical load [4]. Above this load, there are deflections which resemble a global postbuckling response (panel cross-sections translates toward the stiffener side of the panel). It is possible that even before the secondary instability occurs, there is load shifting occurring in the panel which is not predicted by a local-postbuckling analysis, and which thus modifies the deformation state compared to the pure local-postbuckling analysis. No global buckling modes were included in the NLPAN analysis because of the inability of NLPAN to model clamped end conditions.

For the single mode NLPAN analyses performed, the stiffener-unit representation gives better solutions overall than the (symmetric) full panel representation, especially considering the strain predictions shown in Figure 23(a). As discussed before, the reason the full-panel representation performed poorly when a single mode was used is because the primary buckling eigenfunction for the complete panel is a poor representation of the early postbuckling displacements. A clue to this fact is that the second buckling eigenvalue is close to the primary eigenvalue (6% difference), indicating that in this case the second eigenfunction of Figure 21 plays an important role even in the early postbuckling response. This type of modal interaction thus may be anticipated when there is a secondary local buckling mode which has both the same halfwave number as the primary local buckling mode, and has an eigenvalue only slightly above the primary value.

4.4 Modal Interaction in Wide, Blade Stiffened Panels

In this section, NLPAN is applied to wide, blade stiffened panel configurations which were tested experimentally in a study [25] designed to explore the interaction between the local and Euler buckling modes, and the resulting imperfection sensitivity. The problem of analyzing these phenomena in thin-walled columns and stiffened panels has received considerable attention in the literature [38,41,43-56,64]. Several different methods have been used to obtain analytical predictions which are reasonably accurate when compared with test results of the type to be considered here from [25]. Such results are reported in the series of papers [24-27]; the PANDA2 panel design code was used to obtain approximate results in [65]; a method pioneered by Koiter and associates [47,52,53,55], and subsequently refined by Sridharan and associates [38,48,49] appears to give results in excellent agreement with test data [38]. Problems with perturbation approaches have been documented and discussed in the literature [1,38,51,52], and successful approaches noted above have all abandoned the pure perturbation approach. It is the intent in this section to investigate the performance of NLPAN in its current form (as documented in Chapter 3) which uses a perturbation approach; this hints that problems with accuracy may be encountered. Nonetheless, some information from the named references is used in this section to help guide the NLPAN analyses where flexibility in the method exists. In order to help illuminate some of the intuitive concepts involved in the analysis, the displacement shape functions to be used will be examined in detail in the following section.

4.4.1 Test Configurations

In the experimental study of [25], several panels, each having the general configuration shown in Figure 25(a), were tested in uniaxial compression. Panels of two different types were

tested, one type having stocky stiffeners and eight bays across the width, the second type having thin stiffeners and nine bays across the width. The cross-sectional dimensions of the two panel types are shown in Figure 25(b). The panels were fabricated from epoxy resin. The ends of each panel were mounted in protective shoes, and the load end of the shoes featured a series of parallel V-grooves which spanned the width of the panel. A knife-edge supported each end of a panel in one of the V-grooves. The eccentricity of the load relative to the neutral bending axis was varied by selecting from among the parallel V-grooves in each load shoe. Imperfections in the shape of the local buckling modes were introduced by taking advantage of the temperature-dependant viscoelastic properties of the epoxy resin. A local postbuckling deformation shape was maintained by an applied end load while the panel was heated, then cooled, causing a deformation shape to set and thereby take on the role of an imperfection in the nominal shape of the local buckling mode.

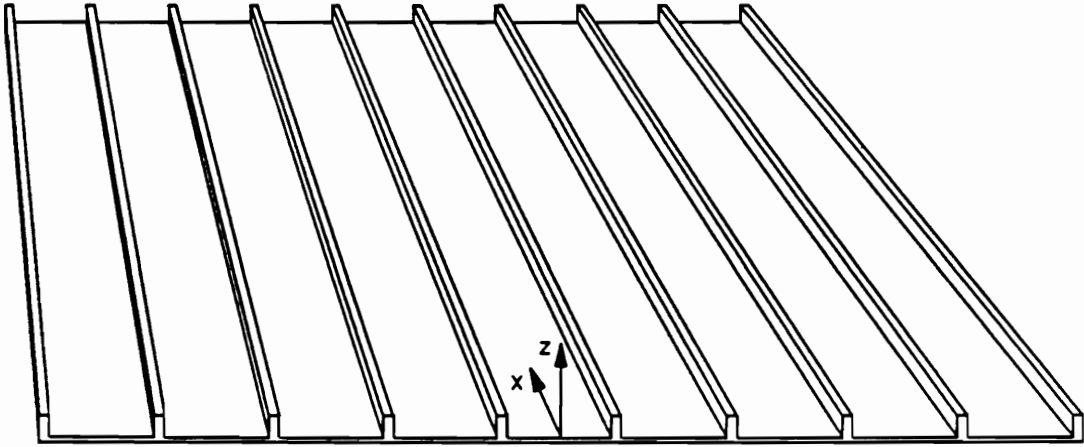
The load eccentricity value, e , is reported in [25] in terms of the effective Euler-mode imperfection amplitude, w^o (the transverse deflection at the mid-length of an unloaded panel). In the absence of any further explanation in [25], the assumption has apparently been made that the two imperfection measures convert directly. In other words, it is apparently assumed in [25] that

$$w^o = e \tag{154}$$

However, the two different types of imperfections have different effects on structural response because an eccentric end load introduces a bending moment at the end of the panel which is not present in a simply supported panel with a bowing eccentricity. An investigation of equivalency relationships for the two types of imperfections is discussed in [39], in which the following relationship is recommended to relate the two measures:

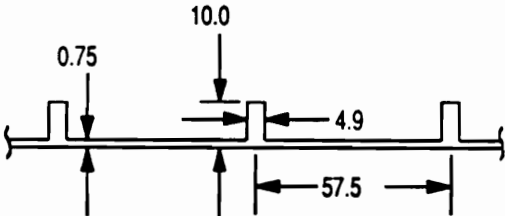
$$w^o = 1.25 e \tag{155}$$

This issue introduces some uncertainty regarding an effective Euler-mode imperfection amplitudes for the test data of [25]. The local mode imperfection amplitudes reported in [25] are



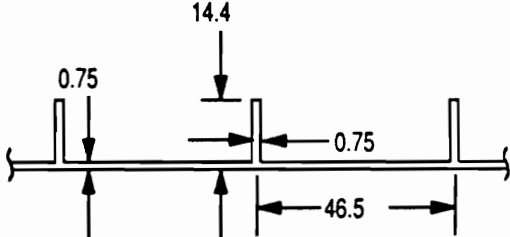
a) General configuration of stiffened panels.

Dimensions: mm



Stocky-Stiffener Panel (8 bays)

Dimensions: mm



Thin-Stiffener Panel (9 bays)

b) Nominal cross-sectional dimensions.

Figure 25. Blade stiffened panel configurations used in experiments investigating modal interaction: Experiments described in [25].

based on measured deflection profiles of the panel skin along the centerline of a panel bay (midway between two stiffeners) of the unloaded panel.

To model the panels using NLPAN, a stiffener-unit representation was used, as was done for the three bay panel in the previous section (see Figure 21(a)). Because of the large number of bays of each panel, no correction was made to the NLPAN results to account for the additional stiffener present in the test panels compared to the equivalent-width representation using stiffener-units. The elastic properties of the panel material were not given in [28]; in the NLPAN analysis, it was assumed that the material was linearly elastic with material properties $E = 34.5 \times 10^3 \text{ N/cm}^2$ ($50 \times 10^3 \text{ #/in.}^2$) and $\nu = 0.35$.

The length L for each test panel was not reported directly in [25]. Instead, the ratio of the theoretical critical loads for local and Euler buckling, P_L/P_E , was reported. P_E is given by the column formula

$$P_E = EI \left(\frac{\pi}{L} \right)^2 \quad (156)$$

where I is the moment of inertia of the panel cross-section, and P_L is based in the critical stress for local buckling σ_L , given by [25]

$$\sigma_L = k \left(\frac{E\pi^2 h^2}{12(1-\nu^2)b^2} \right) \quad (157)$$

where b is the bay width, h is the skin thickness, and $k = 6.96$ for stocky stiffener panels, and $k = 4.0$ for thin-stiffener panels. To determine the length, L , of each stocky stiffener panel for use in NLPAN, the equations (156) and (157) were used along with the reported ratios P_L/P_E given in [25]. Because of differences in the formulae used and the infinite-width representation used for the NLPAN model, the ratios P_L/P_E computed using PASCO (containing the VIPASA analysis) are slightly different than the nominal values reported in [25]. The results for the stocky-stiffener panels are summarized in Table 5, along with the longitudinal halfwave numbers for local buckling, m_L , computed by PASCO.

Table 5. Values of Length Computed for Three Stocky Stiffener Panels

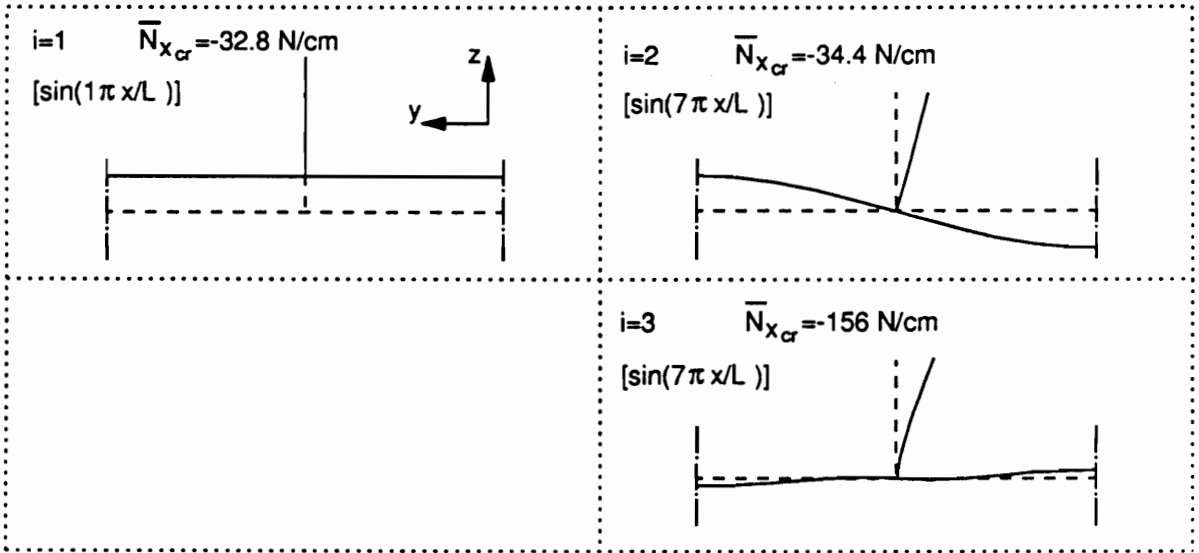
Panel #	P_L/P_E (Nominal)	L (cm)	P_L/P_E (PASCO)	m_L (PASCO)
1	1.50	36.5	1.50	10
2	1.02	30.1	1.04	8
3	0.64	23.8	0.68	6

A different approach was used to select the length for use in representing a thin-stiffener panel with NLPAN. The length L was simply chosen so that the ratio of critical loads predicted by PASCO matched the nominal value reported in [25]. For the single panel considered, the result was $L = 35.6 \text{ cm}$ for $P_L/P_E = 1.05$, with $m_L = 7$. Any discrepancies between the lengths used in model tests and those used with NLPAN should be of little consequence in the reported results, which are presented in a normalized fashion.

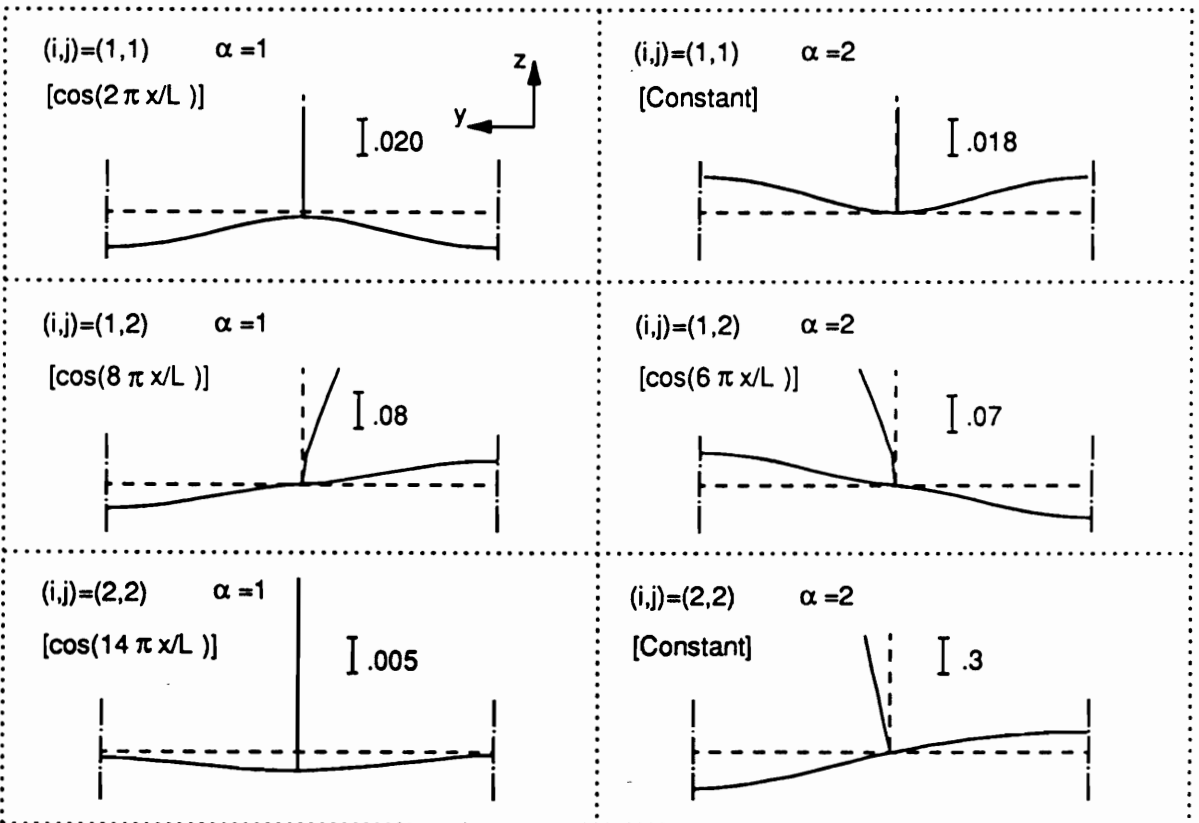
4.4.2 Displacement Shape Functions for the Thin-Stiffener Panel

The profiles of three buckling modes of the thin-stiffener panel are depicted in Figure 26(a). The first mode ($i = 1$) is the Euler-buckling mode ($m = 1$), the second mode ($i = 2$) is the primary local buckling mode, having seven longitudinal halfwaves ($m = 7$), and the third mode ($i = 3$) is a secondary local mode, specifically the second unsymmetric mode having seven longitudinal halfwaves ($m = 7$). The Euler mode can be seen to involve little deformation of the cross-section, and the primary local mode can be seen to involve significant buckling of both the stiffener and the panel skin. The secondary local mode serves a role to be discussed later.

The profiles of the contributions to the second-order displacement fields associated with the first two buckling modes are presented in Figure 26(b). The fields depicted in Figure 26(b) were computed with a reference load parameter value $\lambda_b = 0$ (see equations (77)). The first pair of profiles is associated with the Euler-buckling mode ($[i,j] = [1,1]$). Allowing



a) Buckling modes.



b) Second-order displacement fields, $\lambda_b = 0$.

Figure 26. Profiles of the displacement fields of a thin-stiffener panel: The x-dependence is shown in brackets.

for rigid-body translation in the second ($\alpha = 2$) contribution, it can be seen that the out-of-plane displacements of the two contributions ($\alpha = 1$ and $\alpha = 2$) cancel for the most part at the panel ends, thus closely satisfying the boundary condition $w = 0$ for each plate strip. At the mid-length of the panel, the two contributions reinforce each other to produce sagging or bulging of the skin between the stiffeners, depending on the direction of the Euler buckling.

The third pair of profiles in Figure 26(b) is associated with the primary local mode ($[i,j]=[2,2]$). The first contribution ($\alpha = 1$) is dominated by large in-plane displacements and their gradients, and has comparatively small out-of-plane displacements. The second contribution ($\alpha = 2$), which is constant in the x -direction, exhibits extremely large out-of-plane displacements which grossly violate the requirement $w = 0$ at the longitudinal ends of each plate strip. As discussed in Section 4.3.1, there are grounds for suppressing these large out-of-plane displacements. For the results presented in following sections, constraints were imposed at the node lines when computing the second displacement contribution ($\alpha = 2$), in order to reduce the out-of-plane displacements in the same general manner as was done for the three bay panel (see Figure 19).

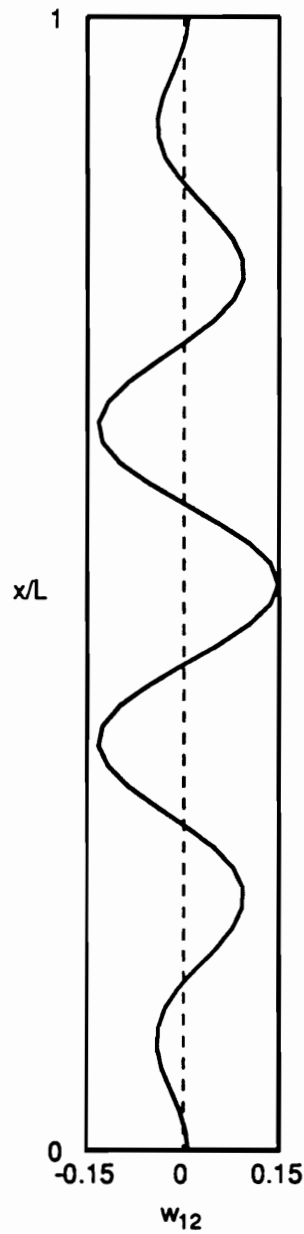
The second pair of displacement profiles depicted in Figure 26(b) form the mixed second-order displacement field ($[i,j]=[1,2]$) associated with the interaction of the local and Euler buckling mode-shapes. Considering the x -dependency associated with the two profiles, it can be seen that the out-of-plane displacements of the two contributions tend to cancel each other at the panel ends (closely satisfying the boundary condition $w = 0$ for each plate strip) and reinforce each other at the panel mid-length. The net result is a deformation pattern with the same halfwave number as the local buckling mode ($m = 7$), but with an amplitude that varies along the length. As an illustration of this amplitude distribution, the function w_{12} along the tip of the stiffener is shown in Figure 27. The cross-sectional profile of the mixed second-order field represents the modification to the local-buckling mode profile due to the imposition of curvature associated with the Euler buckling mode. Because the Euler mode curvature goes to zero at the panel ends, the amplitude of the mixed second-order field also goes to zero. For a positive Euler mode deflection, compression of the skin is increased and

compression near the stiffener tip is decreased, so the mixed second-order field serves to increase the out-of-plane deflections of the skin and decrease those of the stiffeners. For a negative Euler mode deflection, the reverse is true. Structural instability in postbuckling is due to a loss of bending stiffness associated with either skin postbuckling, for a positive Euler mode deflection, or stiffener postbuckling, for a negative Euler mode deflection.

The second-order displacement fields $\{u_{11}\}$ and $\{u_{22}\}$ display a negligibly small dependence on the reference value of the load parameter, λ_b , for the range of interest. In contrast, the mixed second-order field $\{u_{12}\}$, specifically its third component, w_{12} , has a strong dependence on λ_b , exhibiting singular behavior at discrete values of λ_b . The singular behavior is depicted in Figure 28, which shows the maximum amplitudes of $\phi_{\alpha 12}$ ($\alpha = 1, 2$) in the cross-section, as a function of λ_b . The normalizing value λ_1 used in Figure 28 is the critical value of end shortening for the primary buckling mode. Not only is the amplitude of w_{12} dependent on λ_b , but the shape is also. Figure 29 depicts the profiles of the two contributions to w_{12} both for $\lambda_b = 0$, and for $\lambda_b = 0.96\lambda_1$. It can be seen that the bending of the stiffener section, which is pronounced for $\lambda_b = 0$, is still present for $\lambda_b = 0.96\lambda_1$, but is reduced in proportion to the skin displacements. The in-plane displacement contributions u_{12} and v_{12} are small relative to w_{12} , and are virtually unaffected by the value of λ_b .

4.4.3 Displacement Shape Functions for a Stocky-Stiffener Panel

Figure 30(a) depicts the profiles of two buckling modes for the stocky-stiffener panel with the critical load ratio is $P_L/P_E = 1.02$. The first mode ($i = 1$) is the Euler buckling mode ($m = 1$), and the second mode ($i = 2$) is the primary local buckling mode, having eight longitudinal halfwaves ($m = 8$). The Euler buckling mode involves little deformation of the cross-section, and the local buckling mode is limited for the most part to skin buckling with little involvement of the stiffener.



Along the Stiffener Tip: $w_{12} = 0.08 [\cos(8 \pi x/L)] + 0.07 [\cos(6 \pi x/L)]$

Figure 27. The mixed second-order displacement field at the stiffener tip for a thin-stiffener panel ($\lambda_b = 0$).

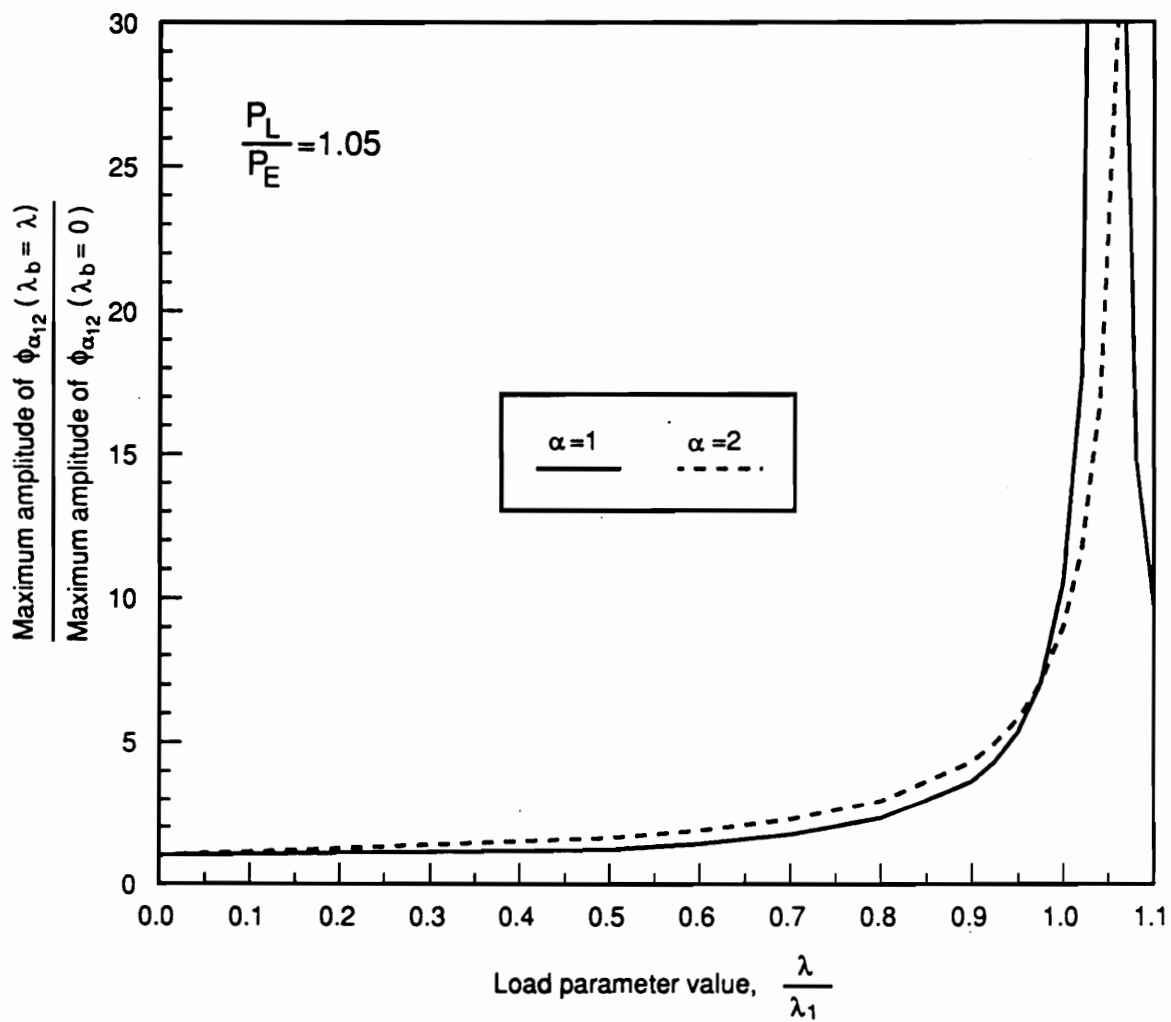


Figure 28. Demonstration of the singularities in the contributions to the mixed second-order displacement field: Thin-stiffener panel.

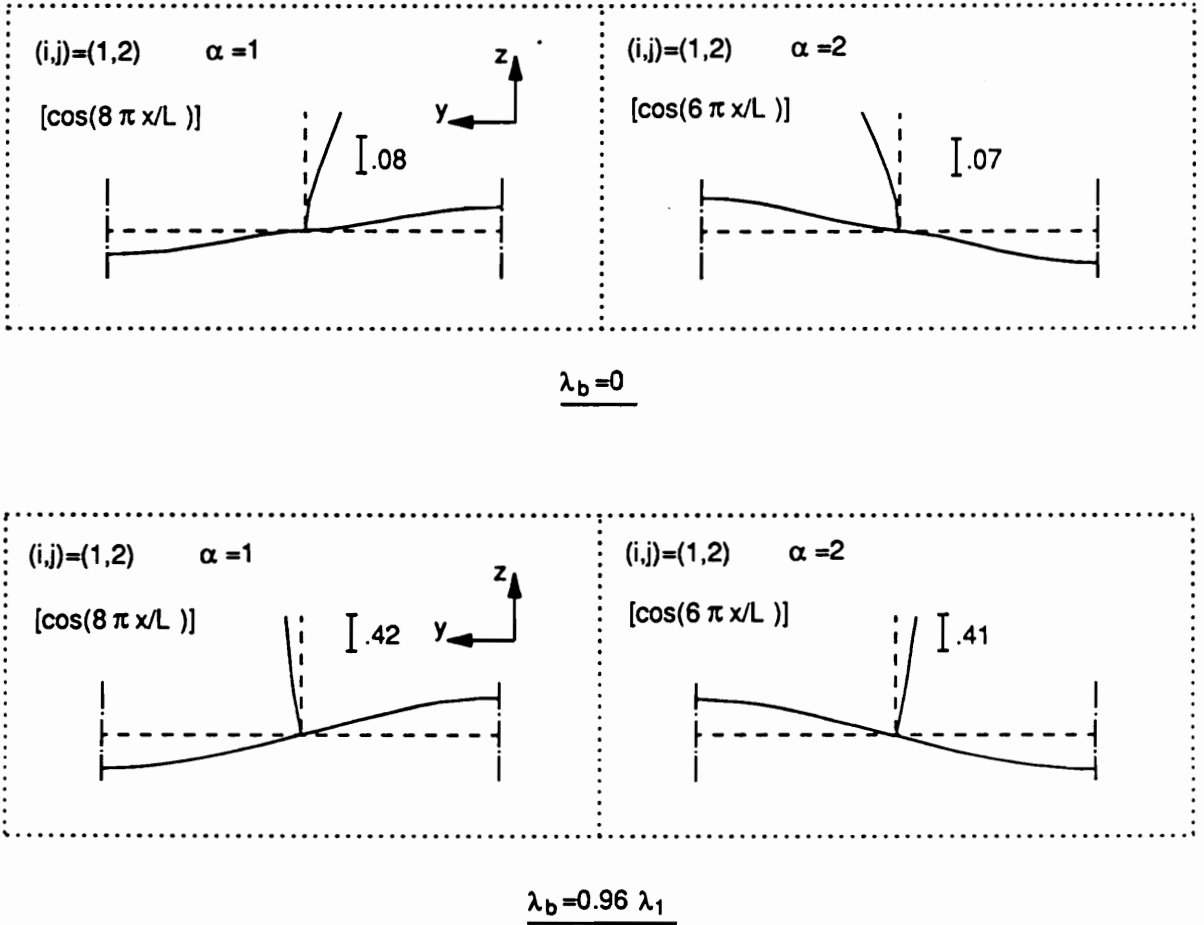
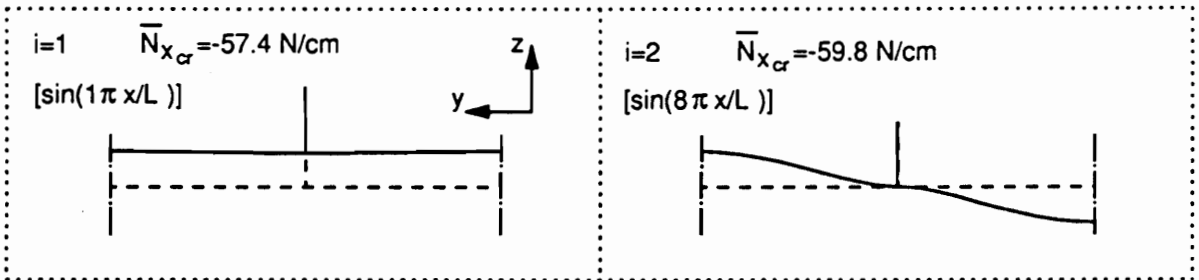
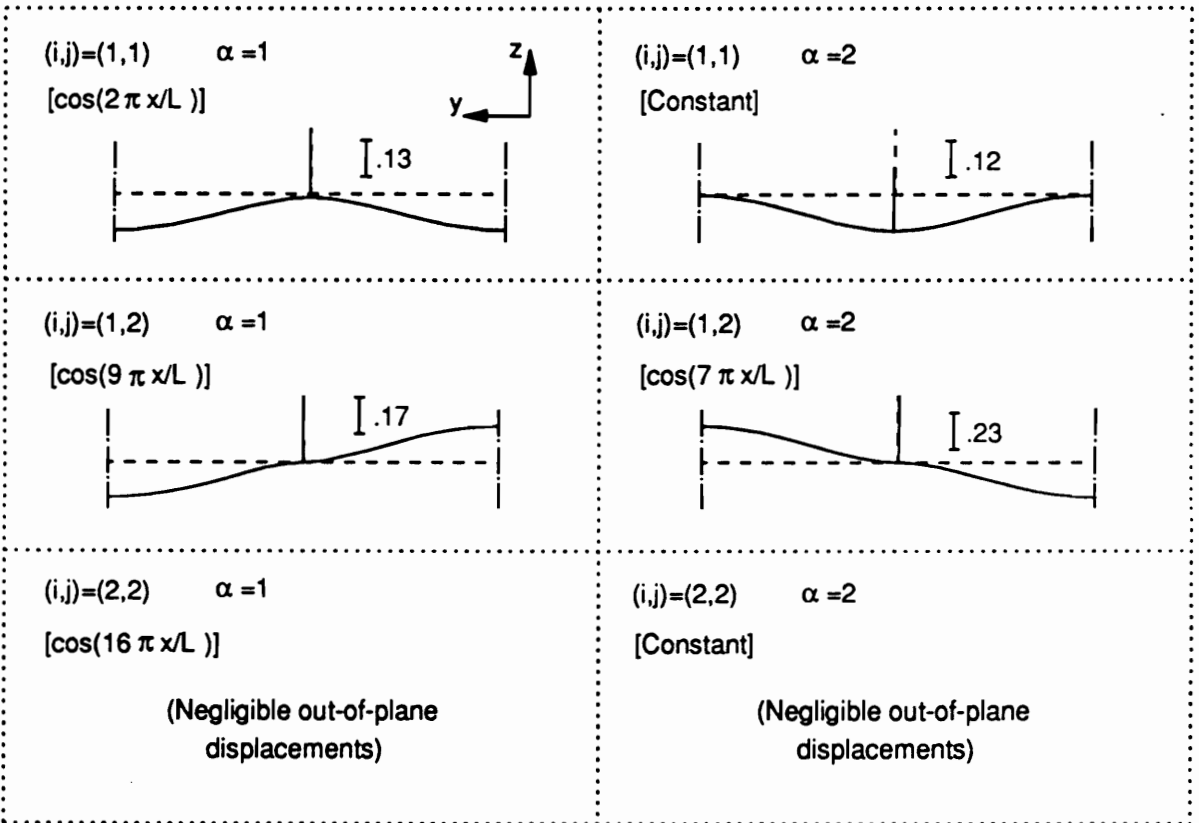


Figure 29. Profiles of the mixed second-order field contributions as affected by the reference value of the load parameter: Thin-stiffener panel.



a) Buckling modes.



b) Second-order displacement fields, $\lambda_b=0$.

Figure 30. Profiles of the displacement fields of stocky-stiffener panel # 2: The x-dependence is shown in brackets.

The profiles of the contributions to the second-order displacement fields associated with the two buckling modes are presented in Figure 30(b), as computed with a reference load parameter value $\lambda_b = 0$. The first pair of profiles is associated with the Euler buckling mode $([i,j]=[1,1])$, and are qualitatively similar to the corresponding profiles for the thin-stiffener panel. Allowing for rigid-body translation of the second ($\alpha = 2$) contribution, the out-of-plane displacements of the two contributions cancel for the most part at the panel ends, thus closely satisfying the boundary condition $w = 0$ for each plate strip. At the mid-length of the panel, the two contributions reinforce each other to produce sagging or bulging of the skin between the stiffeners, depending on the direction of the Euler buckling.

The third pair of profiles, associated with the primary local buckling mode $([i,j]=[2,2])$, are not shown in Figure 30(b), because they involve negligible out-of-plane displacements on each plate strip. This is explained by an inspection of the local buckling mode ($i = 2$) in Figure 30(a). Because of the rigidity of the stocky stiffeners, each skin bay between neighboring stiffeners behaves nearly like a simple plate which is clamped at its side edges. As was discussed in Section 3.5.8, the second-order displacement fields contain only in-plane components for the postbuckling of simple plates.

The second pair of displacement profiles depicted in Figure 30(b) form the mixed second-order displacement field $([i,j]=[1,2])$ associated with the interaction of the local and Euler buckling mode shapes. As was the case with the thin-stiffener panel, the out-of-plane displacements of the two contributions tend to cancel each other at the panel ends, and to reinforce each other at the panel mid-length. The complete displacement field has the same halfwave number as the local buckling mode ($m = 8$), but the wave amplitude varies along the length. Here, as with the thin-stiffener panel, the cross-sectional profile of the mixed second-order field represents the modification to the local buckling mode profile due to the imposition of curvature from the Euler buckling mode. However, in contrast to the case of the thin-stiffener panel, the profile of the mixed second-order field here is essentially the same as that of the primary local buckling mode. For a positive Euler mode deflection, compression of the skin is increased, so the mixed second-order field w_{12} serves to increase the out-of-

plane deflections of the skin. For a negative Euler mode deflection, the compression of the skin is decreased, so the field w_{12} serves to decrease the out-of-plane deflections of the skin. Structural instability in postbuckling is due to a loss of bending stiffness associated with skin postbuckling and a positive Euler mode deflection. A negative Euler mode deflection does not induce a significant postbuckling instability. Thus, imperfection sensitivity is associated with positive Euler mode deflections, as can be seen in the test results of [25] which are repeated here in a following section.

As with the thin-stiffener panel, the second-order displacement fields $\{u_{11}\}$ and $\{u_{22}\}$ of the stocky-stiffener panel display a negligibly small dependence on the reference value of the load parameter, λ_b . Component w_{12} of the mixed second-order field does exhibit a dependence on λ_b , and exhibits singular behavior at discrete values of λ_b , but unlike the situation with the thin-stiffener panel, here the cross-sectional shape of w_{12} keeps its same basic shape. The in-plane displacement contributions u_{12} and v_{12} are small relative to w_{12} , and are virtually unaffected by the selection of λ_b .

4.4.4 Analysis with NLPAN

Sridharan and Peng [38] report analytical predictions which are in close agreement with the test results for the panels considered here, using a method which is highly tailored to the analysis of local/Euler mode interaction in isotropic columns and wide panels. Thus, while the method of analysis used in [38] differs in many ways from the approach of NLPAN, several points from the discussions in [38] are considered here for guidance in designing the NLPAN analyses for these panels.

First, Sridharan and Peng state that the singularities in the mixed local/Euler second-order field are simply artifacts of the perturbation approach which uses modal amplitudes as generalized coordinates. The approach in [38] used to overcome the singularity problem is to include as a participating mode in the analysis a secondary local buckling mode which has

the same number of halfwaves as the primary local buckling mode, and which has a transverse profile similar to that of the mixed second-order displacement field. The profile of the mixed second-order field is then computed while constrained to be orthogonal to the secondary local mode; the singularity problem is eliminated. An example of an appropriate secondary local mode, consider the thin-stiffener panel, for which the profile of the secondary local buckling mode ($i = 3$) in Figure 26(a) is similar to the profile of the mixed second-order field ($[i,j] = [1,2]$) shown in Figure 26(b). In the approach of [38], the thin-stiffener panel is analyzed using all three buckling modes in Figure 26(a), which together can simulate three fundamental types of deformation: i) Euler (overall) buckling deformation, ii) skin postbuckling, iii) stiffener postbuckling. The stocky-stiffener panel, on the other hand, would require only two modes: one producing Euler mode displacements, and one producing local postbuckling of the skin.

Second, Sridharan and Peng use "amplitude modulation functions" (see Section 2.2.2.4) to allow the amplitudes of each of the local buckling modes to vary along the longitudinal coordinate of the panel. Again referring to the thin-stiffener panel, the feature of amplitude modulation applied to the secondary local buckling mode ($i = 3$) of Figure 26(a) would create a displacement field which is similar in both profile and x -dependence (see Figure 27) to the mixed second-order displacement field. It is noted here that the phenomenon of amplitude modulation of a local buckling mode-shape can be simulated using multiple buckling modes having the same approximate transverse profile, but which differ in longitudinal halfwave number m .

NLPAN analyses were performed using two different approaches. In the first approach (Approach 1), the second-order displacement fields were computed once with the reference load parameter value $\lambda_b = 0$. In the second approach (Approach 2), the second-order displacement fields were computed at each load level where a solution was sought, or in other words, by setting $\lambda_b = \lambda$ in equation (77).. Despite the opinion expressed in [38] that the phenomenon of singularities in the computation of the second-order fields has no physical basis, this second approach was investigated to see if the limit point values of the panels are cor-

rectly predicted as the singularity is approached. All four of the panels considered were modelled with both approaches. The thin-stiffener panel was modelled using Approach 1, first with two modes, then with three, to study the importance of including the third mode. The thin-stiffener panel was modelled with Approach 2 using two modes. The three stocky-stiffener panels were modelled using two modes in both of the approaches. While it was mentioned earlier that the use of additional modes in the NLPAN analyses would enable the simulation of the amplitude-modulation phenomenon, it was felt that the important features of the modal interaction problem would still be captured using simple mode shapes.

4.4.5 NLPAN Results for the Thin-Stiffener Panel

Results for the thin-stiffener panel showing the limit load (as a fraction of the Euler buckling load) versus the Euler mode imperfection amplitude are presented in Figure 31 for two different amplitudes of imperfections in the shape of the local buckling mode. Results obtained from NLPAN Approach 1, both for two mode and three mode analyses, are compared with test results from [25]. For positive Euler mode imperfections, both the two and three mode analysis give similar results, whereas for negative Euler mode imperfections, the two mode analysis does not predict any limit load below the Euler buckling load. Apparently, despite the presence of the stiffener buckling type of displacements in the mixed second-order field for the two mode analysis, the three types of displacement shapes are not sufficiently independent to permit the prediction of collapse induced by stiffener-dominated local buckling. Both the two mode and the three mode analyses under-predict the imperfection sensitivity for both positive and negative values of Euler mode imperfection, although the three mode analysis succeeds in predicting both the skin buckling and stiffener buckling modes of global collapse.

Results for the thin-stiffener panel featuring the same test data as Figure 31 are presented in Figure 32, but the NLPAN results presented are for the three-mode Approach 1 analysis and the two-mode Approach 2 analysis. Both NLPAN approaches predict the two

Local-mode imperf. ampl., w_L^o/h	Experiment [25]	NLPAN Approach 1 2 modes	NLPAN Approach 1 3 modes
0.02	○	—	- - - -
0.10	●	—	- - - -

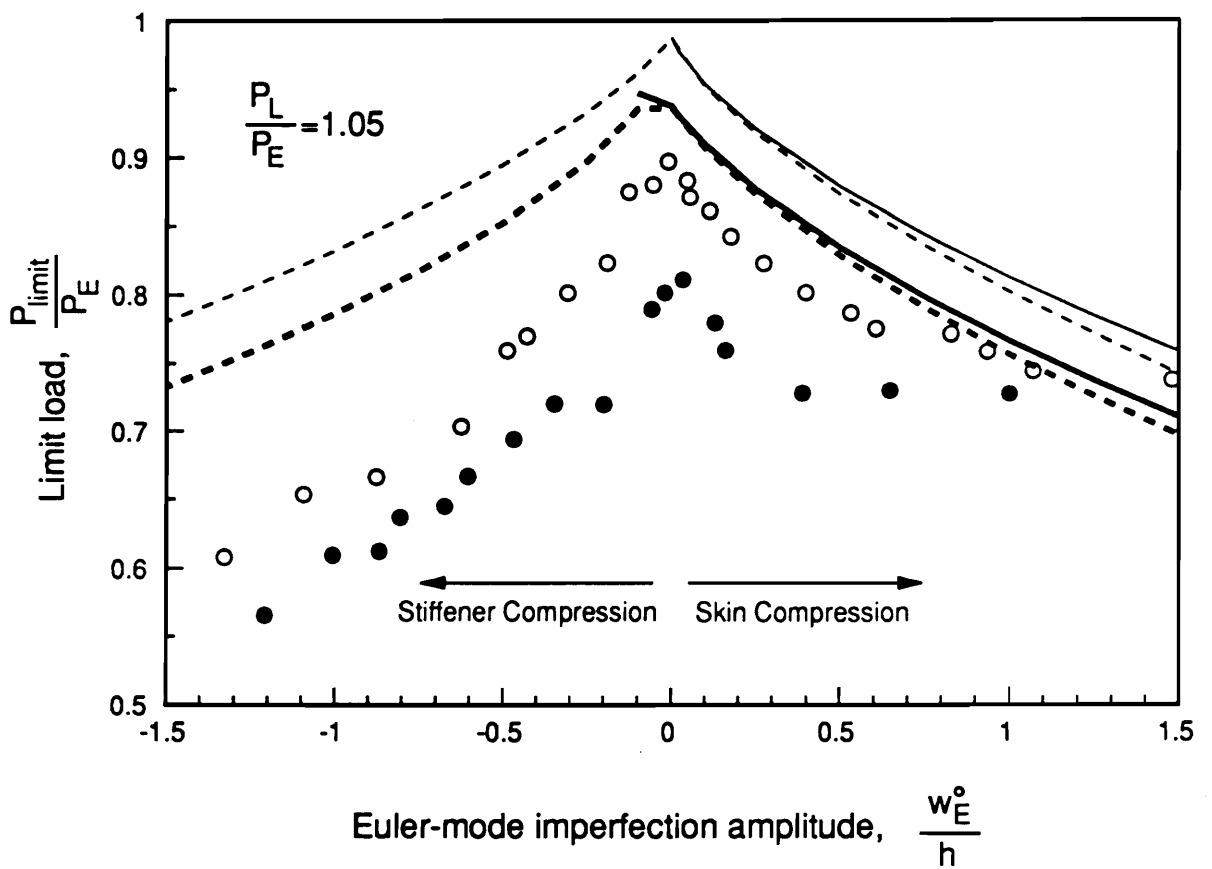


Figure 31. Results for the thin-stiffener panel, NLPAN Approach 1.

modes of collapse (stiffener buckling and skin buckling), but both approaches generally over-predict the limit loads, except for large positive Euler mode imperfections, for which the test results show an asymptotic value of the limit load for an increasing Euler mode imperfection. The asymptotic trend is not exhibited by the NLPAN results. In general, the analytical results from Approach 2 fall closer to the test data than those from Approach 1, but considering that the Approach 2 analysis is at least an order of magnitude more expensive than the Approach 1 analysis, it can hardly be concluded that Approach 2 is superior. There is irregular behavior of the Approach 2 results for the greater of the two local mode imperfection values, at negative Euler mode imperfection values (see Figure 32). This reflects numerical difficulty in computing the limit load when in the proximity of the singularities of the mixed second-order displacement fields. Nonetheless, it appears that both the three-mode Approach 1 analysis and the two-mode Approach 2 analysis are successful in representing the primary physical phenomena which produce imperfection sensitivity.

As mentioned earlier, the local mode imperfection amplitudes reported in [25] were based on measurements of the panel skin deformation. However, there is no guarantee that the local deformations had the same transverse profile as the primary local buckling mode of Figure 26(a). Indeed, analytical results obtained [38] which show excellent agreement with the test results of [25] were obtained by taking the local mode imperfections to be in the shape of the secondary local buckling mode ($j = 3$) shown in Figure 26(a), rather than in the shape of the primary local buckling mode. That choice significantly amplifies the assumed stiffener deformations. Making the same choice for the NLPAN analyses would result in a significant lowering of the computed limit loads for negative Euler mode imperfections, thus improving the agreement with the test data; there is, however, no information on which to base the selection of an amplitude for an imperfection in the shape of the secondary local buckling mode.

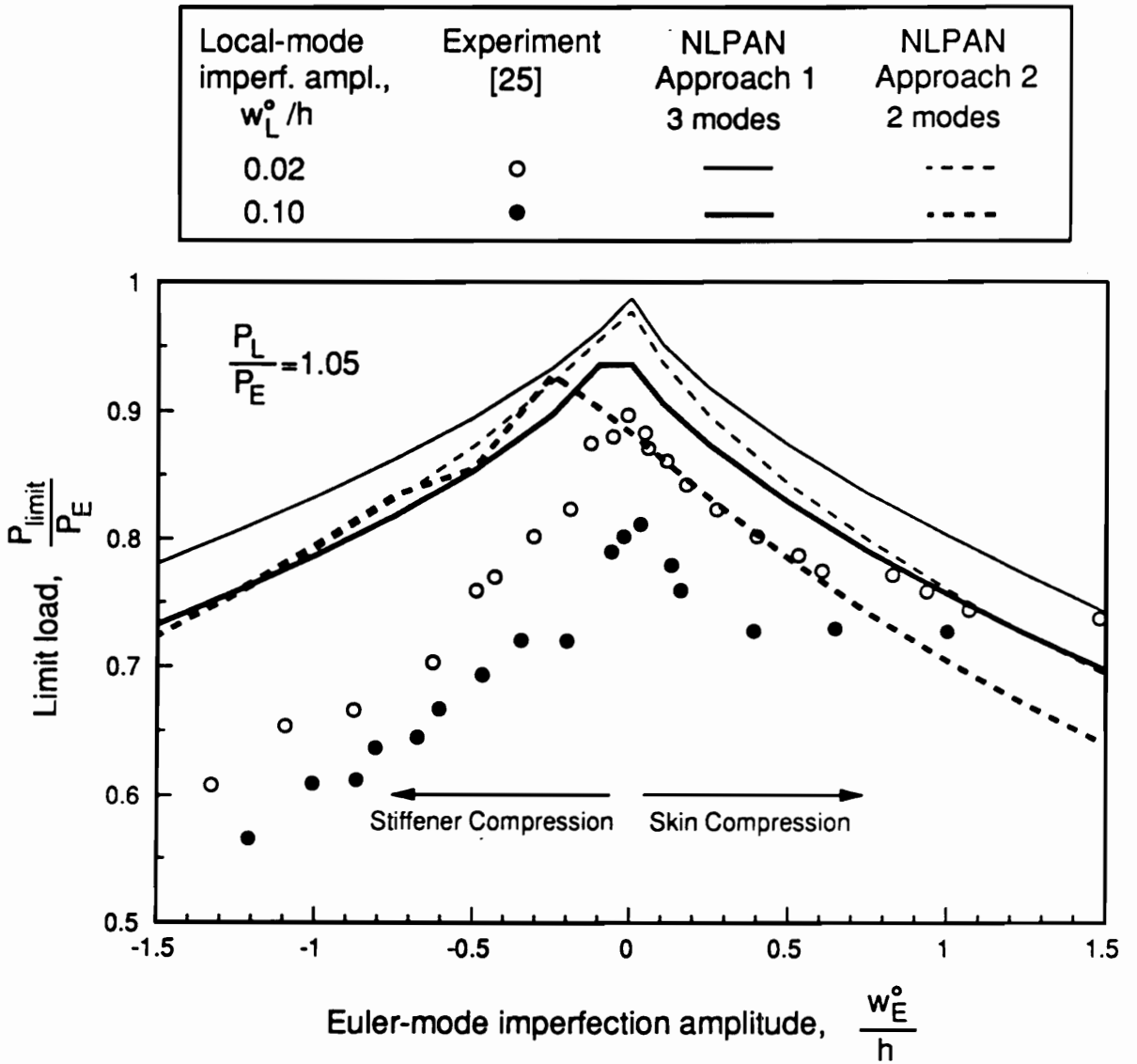


Figure 32. Results for the thin-stiffener panel comparing NLPAN Approaches 1 and 2.

4.4.6 NLPAN Results for the Stocky-Stiffener Panels

Results for the three stocky-stiffener panels (see Table 5 on page 133) are presented in Figure 33 through Figure 35. Results from two mode analyses, using both Approach 1 and Approach 2, are compared with the test data from [25]. The panels were each tested at two different local-mode imperfection amplitudes (except for Panel 3 which was tested at a single local-mode imperfection amplitude) over a range of Euler-mode imperfection amplitudes. Results from the two NLPAN approaches agree fairly well with each other, except for Panel 3 for negative values of imperfections in the Euler mode-shape. In this latter case, the irregular results of Approach 2 are apparently due to numerical problems associated with the proximity of singularities in the mixed second-order field. For all three panels, there is fair qualitative agreement between NLPAN predictions and the test data for small amplitudes of the Euler mode imperfection, but the test data for all three panels exhibit an asymptotic value of the limit load for an increasing amplitude of the Euler mode imperfections, and NLPAN fails to predict this phenomenon. The results for the two NLPAN approaches match each other closely enough that the extreme economy of Approach 1 relative to Approach 2 makes the former approach the preferred one.

4.4.7 Additional Comments on the NLPAN Results for Imperfection

Sensitive Panels

There are several factors which bring uncertainty into the attempts to correlate the analytical predictions of NLPAN with the test data of [25]. These factors include the use of linearly elastic material properties to model the epoxy material, the use of bowing imperfections to model load eccentricities, and the use of a single local buckling mode-shape to model the local shape imperfections. In a related concern, Sridharan and Peng [38] reported that in order

Local-mode imperf. ampl., w_L^o/h	Experiment [25]	NLPAN Approach 1 2 modes	NLPAN Approach 2 2 modes
0.01	○	—	- - - -
0.14	●	—	- - - -

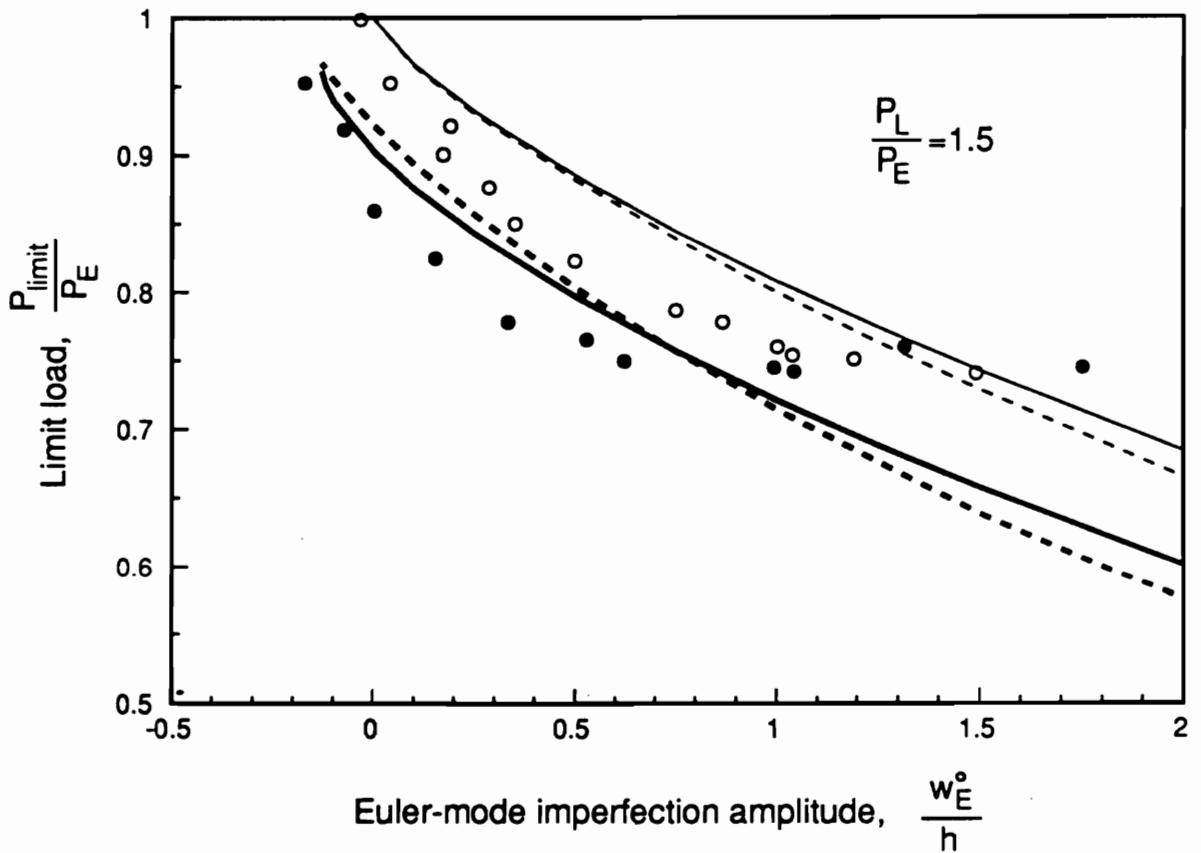


Figure 33. Results for stocky-stiffener panel # 1 comparing NLPAN Approaches 1 and 2.

Local-mode imperf. ampl., w_L°/h	Experiment [25]	NLPAN Approach 1 2 modes	NLPAN Approach 2 2 modes
0.01	○	—	- - - -
0.14	●	—	- - - -

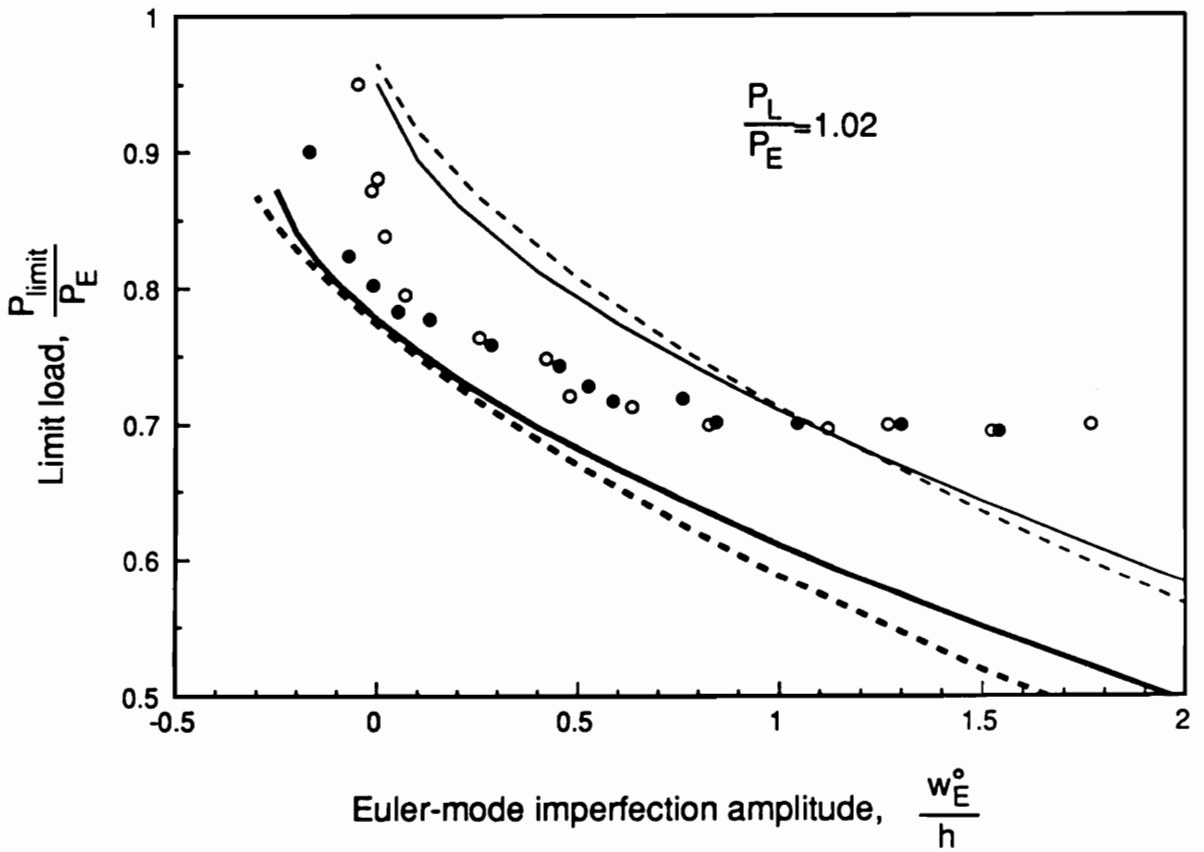


Figure 34. Results for stocky-stiffener panel # 2 comparing NLPAN Approaches 1 and 2.

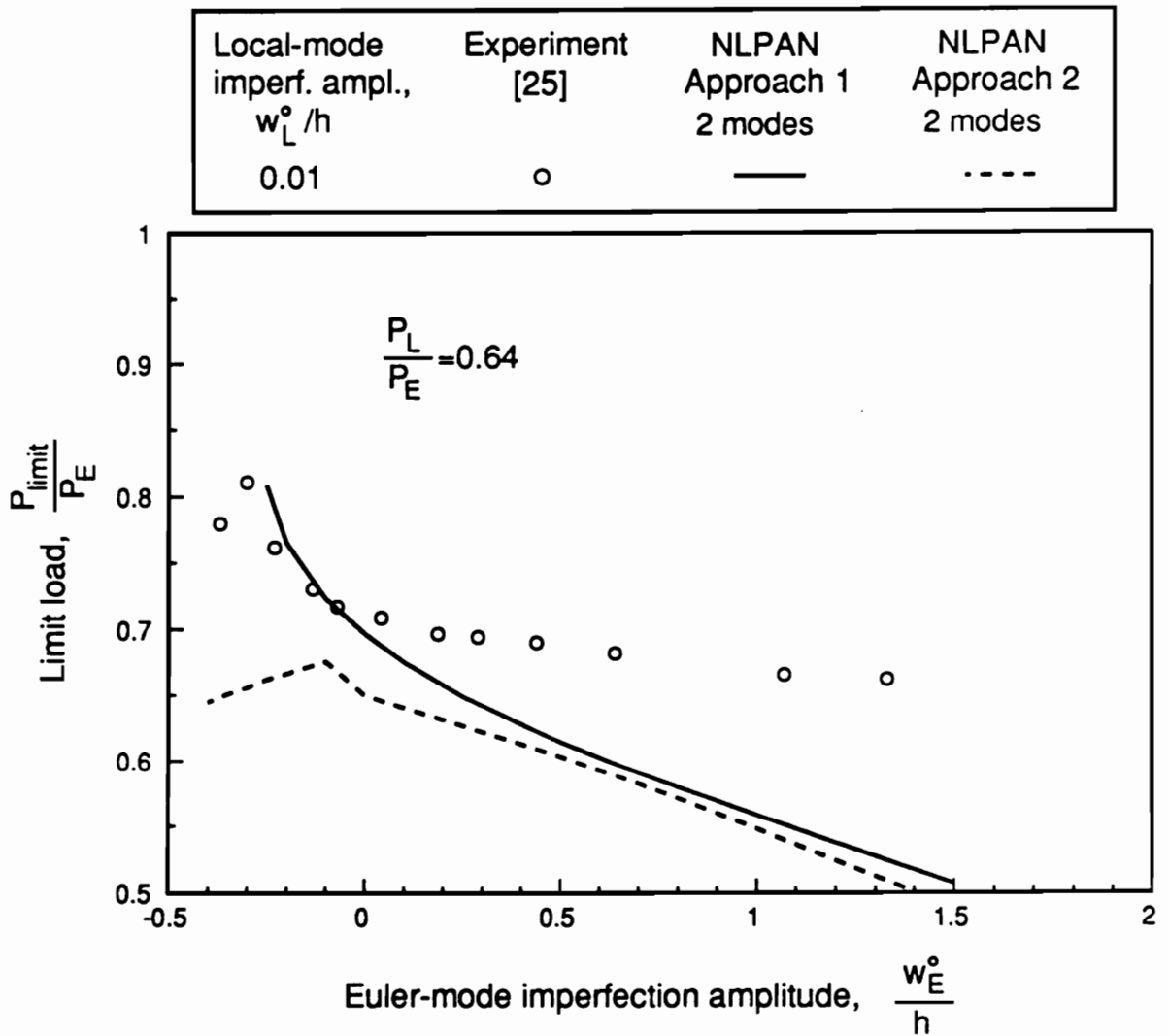


Figure 35. Results for stocky-stiffener panel # 3 comparing NLPAN Approaches 1 and 2.

to get good agreement with the test data for the stocky-stiffener panel with the critical load ratio $P_L/P_E = 0.64$, it was necessary to incorporate an expression for the mid-surface curvature of plate strips, κ_x , which accounts for large rotations associated with the large Euler mode deflections which are encountered. While better accounting for some of these factors might improve the agreement between the present analysis and the experiments, there seems to be a fundamental shortcoming in the NLPAN approach so that the asymptotic behavior of the limit load with respect to increasing Euler mode imperfections is not predicted. (The presence of a lower bound to the limit load observed in the test data for positive Euler mode deflections was also predicted analytically for stocky-stiffener panels by Koiter and Pignataro [52].)

Of the two NLPAN approaches used, Approach 1 is judged to be superior for reasons of economy. However, as seen with the thin-stiffener panel, it is important to select the proper combination of local buckling modes to assure that all dominant type of deformation can vary independently. A theoretical drawback of Approach 2, not discussed earlier, is that the presence of singularities in the the second-order displacement fields at certain critical values of λ produce singular behavior in the predicted structural response as the end shortening λ traverses those critical values. Thus, while Approach 2 produces limit load predictions comparable to those determined from Approach 1, the prediction of continuous structural behavior as the end shortening increases beyond the load-limit point is precluded in Approach 2.

The various methods which provide reasonably accurate results for these imperfection sensitive panels (described in the references listed at the beginning of Section 4.4 all make use of analytical models which place various restrictions on the configuration geometry. These restrictions prohibit the direct incorporation of any of the methods into the general method of NLPAN, because one of the goals here is to retain the configuration flexibility of the buckling analysis in VIPASA. Improved accuracy of the NLPAN method in analyzing local/Euler mode interaction is desirable. Should further attempts to refine the theory behind NLPAN fail to produce the desired improvements in accuracy, then it would be worth considering implementing concepts from some of these other methods into NLPAN for application to the limited classes of configurations to which they apply.

4.5 Computational Expense of NLPAN

The version of NLPAN used to generate the reported results is still in a state of development, and thus, a number of refinements which would improve the computational efficiency have not yet been implemented. Nonetheless, some execution times are given here in order to characterize the computational expense of NLPAN. The times reported are for runs made on an IBM 3090-300 digital computer.

Computational costs will be discussed for the symmetric representation of the three bay blade stiffened panel (see Section 4.3.1), because this model has the most complicated cross-section of any of the configurations investigated. The model features four plate strips and five node lines. A total of 42 discrete y -coordinates were used on the cross-sections of the various plate strips, both for obtaining the finite-difference solution to equations (96), and for performing numerical integration in the y -direction in evaluating the area integrals appearing in equations (141). The central processor unit (CPU) times required by NLPAN to perform 1, 2, 3, 4, 5, and 6 mode analyses were 1.7, 2.8, 5.5, 12, 25, and 48 seconds, respectively, not including the run times for the PASCO (VIPASA) analyses (used to provide the buckling mode shapes), which were small in comparison. Note that the NLPAN run time is approximately doubled each time an addition mode shape is incorporated in the analysis.

To get an indication of the improvements in computational economy which can be realized by implementing the "classical assumptions" for local postbuckling analysis (see Section 2.2.2.3), an additional NLPAN run was made with the following modification: the integrals appearing in equations (141) were simplified by incorporating the assumption that $u_i = v_i = w_{ij} \equiv 0$ ($i, j = 1, 2, \dots, M$). (The indicated displacement contributions are zero as an outcome of imposing the classical assumptions.) For a 6 mode analysis, the modification decreased the CPU time from 48 seconds to 17 seconds. The results of the analysis were essentially unaffected by the modification, supporting the validity of the classical assumptions.

5.0 Conclusions and Recommendations

5.1 Conclusions

A method has been presented for the geometrically nonlinear analysis of compressively loaded prismatic composite structures. The permitted structural loading is uniaxial compression, or for flat panels, biaxial compression. Geometric shape imperfections are permitted, and the longitudinal ends of the structure are assumed to be simply supported (transverse deflections are zero). Structures are modelled as assemblages of flat plate strips which are rigidly joined along mutual longitudinal edges. In order to permit the accurate modelling of various structural sections, small eccentricities can be simulated between the reference edge lines of adjoining plate strips.

The method is semi-analytical in nature, and thus, is computationally economical when compared to finite element methods. Buckling eigenfunctions, determined using the VIPASA computer code (the primary analysis code within the PASCO sizing code for stiffened panels), are used as the primary shape functions for the displacements in the nonlinear analysis. The modal amplitudes associated with the buckling eigenfunctions serve as the generalized coordinates in a nonlinear analysis. Displacement contributions which are of second order in the modal amplitudes are also incorporated. The principle of virtual work is used to obtain an approximate expression for the equilibrium condition, which takes the form of a set of nonlinear algebraic equations involving a finite basis of modal amplitudes.

The method has been implemented on a digital computer in a FORTRAN computer code designated NLPAN. Central processor unit times for the NLPAN runs were found to double

with each addition mode shape incorporated in an analysis. For situations where they are applicable, implementing the "classical assumptions" of local postbuckling analysis into NLPAN would provide large reductions in the computational cost of the method.

While the method is applicable to a wide variety of structural configurations, those investigated here were selected based on the need during the development of the method to start with simple configurations and systematically increase the complexity. The verification test cases include several stiffened and unstiffened panel configurations for which results are available in the literature. NLPAN was demonstrated to provide accurate results for the local postbuckling behavior of unstiffened and stiffened panels through moderately large postbuckling loads.

For blade-stiffened panels exhibiting interaction between local and global buckling modes, NLPAN is successful in predicting sensitivity to geometric imperfections in the shape of the local and/or global buckling modes. However, both theoretical and experimental results in the literature demonstrate that for certain types of stiffened panels the loss of strength associated with a global-mode imperfection has a limiting value for an increasing imperfection amplitude, and this phenomenon is not predicted by NLPAN. This apparently reflects an inherent limitation of the perturbation approach used in the current method.

Two different weighted-residual approaches were explored for obtaining a set of nonlinear algebraic equations governing equilibrium. However, it was discovered that there are unbalanced force- and moment-resultants at the edges of the plate strips and along joint lines, which were not accounted for in the weighted-residual approaches, thus resulting in gross violations of the virtual work statement (for some configurations). It was decided to employ the virtual work statement directly for obtaining the nonlinear algebraic equations.

The assumed functional form for the second-order displacement fields was chosen so as to permit separation of the variables x and y in the differential equations governing the fields. This has the consequence that the boundary condition at the longitudinal ends which requires that the transverse deflections be zero is not automatically satisfied. In applications to the verification test cases, however, it was found that the second-order displacement fields do

closely satisfy the stated boundary condition, except for contributions which are both associated with local postbuckling and are x -independent. The difficulty with this one special case could be eliminated with the adoption of the so-called "classical assumptions" for local postbuckling analysis (see Section 2.2.2.3), the use of which appears to be well justified for the configurations explored.

The equations governing the second-order displacement fields, determined using a perturbation expansion of the plate equilibrium equations, possess a term containing the end-shortening control parameter, suggesting that the second-order displacement fields should be load dependent. However, that is highly undesirable from the standpoint of computational economy. For the analysis of local postbuckling, the use of the "classical assumptions" mentioned above removes the load-dependence of the second-order fields, and thus it was assumed here that for local postbuckling analysis the second-order displacement fields could be considered to be load-independent. For the analysis of local/global model interaction, the second-order fields associated with global buckling were found here to be only slightly load-dependent over the load range of interest. On the other hand, the mixed local/global second-order fields are highly load-dependent, both in amplitude and in shape, and even become unbounded in amplitude for certain values of the load parameter. This singular behavior poses a fundamental problem with the use of load-dependent second-order displacement fields. As reported in the literature, this difficulty has been dealt with and overcome in approaches which consider some special classes of configurations, but whether analogous fixes could be made to the general method presented here is a question which requires further study. The most successful approach attempted here for the analysis of local/global mode interaction was to compute the mixed second-order field at a zero load level, and add as a participating mode a second local buckling mode with the same halfwave number as the primary local mode, but with a transverse profile similar to that of the mixed second-order displacement field. As mentioned previously, there remain accuracy problems with this approach.

Results for locally postbuckled rectangular plates suggest that the primary buckling mode is a good indication of the deflection shape in the early postbuckling regime. Furthermore, the selection of additional modes to be included in an analysis is based on the idea of refining the dominant mode shape while retaining its basic symmetries or anti-symmetries. However the selection of modes for use in the analysis of more complicated structural sections was found here to be less straightforward. In a local postbuckling analysis of a blade-stiffened panel with three bays across the width, it was found that although the primary buckling mode appeared to have the general shape expected for the early postbuckling displacements, a second buckling mode, having the same longitudinal halfwave number as the primary buckling mode, played a significant role in representing the displacements of early postbuckling. The secondary buckling mode mentioned had a critical load only 6% greater than the primary buckling eigenvalue, suggesting that a close proximity of eigenvalues should be taken as a hint of this particular type of modal interaction.

5.2 Recommendations for Future Work

Several recommendations are made here for improvements to and additional assessment of the method of NLPAN. These are:

1. Incorporate the so-called "classical assumptions" of local postbuckling analysis, thereby improving the computational economy and eliminating certain discrepancies in the satisfaction of boundary conditions at the longitudinal ends of the structure.
2. Explore modifications to the theoretical approach which will improve the accuracy of the method in predicting the response of structures exhibiting local/global mode interaction.

3. Investigate the performance of NLPAN in analyzing the response of configurations which are subjected to biaxial loading.
4. Investigate the performance of NLPAN in analyzing the response of shell-like structures, specifically structures featuring plates which join at shallow angles.
5. To improve the computational economy, explore the practicality of replacing certain numerically derived solutions used in NLPAN with analytically-derived solutions. The particular solutions of concern are the solutions for the transverse-dependency of the second-order displacement fields, and the solutions for integrals which are evaluated over the cross-sectional domain of the structure in determining the coefficients of the nonlinear algebraic equations.
6. Implement continuation methods into the solution procedure to permit the negotiation of limit points and secondary bifurcation points.

References

1. Budiansky, B., and Hutchinson, J.W., "Buckling: Progress and Challenge," from *Trends in Solid Mechanics 1979*, ed., J.F. Besseling and A.M.A. van der Heijden, Delft University Press, Sijthoff & Noordhoff Int'l Pub., 1979, pp. 93-116.
2. Stroud, W.J., and Anderson, M.S., "PASCO: Structural Panel Analysis and Sizing Code, Capability and Analytical Foundations," NASA-TM-80181, November, 1981.
3. Dickson, J.N. and Biggers, S.B., "POSTOP: Postbuckled Open-Stiffener Optimum Panels - Theory and Capability," NASA-CR-172259, January 1984.
4. Bushnell, D., "PANDA2 - Program for Minimum Weight Design of Stiffened, Composite, Locally Buckled Panels," *Computers & Structures*, Vol 25, No. 4, 1987, pp. 469-605.
5. Wittrick, W.H., and Williams, F.W., "Buckling and Vibration of Anisotropic or Isotropic Plate Assemblies under Combined Loadings," *Int. J. Mechanical Science*, Vol. 16, 1973, pp. 209-239.
6. Leissa, A.W., "Buckling of Laminated Composite Plates and Shell Panels," AFWAL-TR-85-3069, June, 1985.
7. Tvergaard, V., "Buckling Behavior of Plate and Shell Structures," *Theoretical and Applied Mechanics*, ed., W.T. Koiter, North-Holland Publishing Co., 1976, pp. 233-247.
8. Von Karman, T., Sechler, E.E., and Donnell, L.H., "The Strength of Thin Plates in Compression," *Transactions of the ASME, Applied Mechanics*, APM-54-5, Vol. 54, No. 2, 1932, pp. 53-57.
9. Starnes, J.H. Jr., and Rouse, M., "Postbuckling and Failure Characteristics of Selected Flat Rectangular Graphite-Epoxy Plates Loaded in Compression," AIAA-81-0543, presented at the AIAA 22nd Structures, Structural Dynamics and Materials Conference, Atlanta, Georgia, 1981.
10. Jeffrey, Glenda L., "Postbuckling of Laminated Anisotropic Panels," NASA-TM-100509, October, 1987.
11. Spier, E.E., "Postbuckling Fatigue Behavior of Graphite-Epoxy Stiffeners," AIAA-82-0779, *Proceedings, AIAA 23rd Structures, Structural Dynamics and Materials Conference, New Orleans, LA*, 1982, pp. 511-527.
12. Stein, M., "Postbuckling of Eccentric Open-Section Stiffened Composite Panels," AIAA-88-2215, *Proceedings, AIAA 29th Structures, Structural Dynamics and Materials Conference, Williamsburg, VA*, 1988, pp. 57-61.
13. Levy, S., "Bending of Rectangular Plates with Large Deflections," NACA Rept. 737, 1942.

14. Coan, J.M., "Large-Deflection Theory for Plates with Small Initial Curvature Loaded in Compression," *ASME J. of Applied Mechanics*, June, 1951, pp. 143-151.
15. Chia, C.-Y., *Nonlinear Analysis of Plates*, McGraw-Hill, Inc., New York, 1980.
16. Supple, W.J., "Changes of Waveform of Plates in the Post-Buckling Range," *Int. J. of Solids and Structures*, Vol. 6, 1970, pp. 1243-1258.
17. Minguet, P.J., Dugundji, J., and Lagace, P., "Postbuckling Behavior of Laminated Plates using a Direct Energy-Minimization Technique," *AIAA Journal*, Vol. 27, No. 12, December, 1989, pp. 1785-1792.
18. Thurston, G.A., "Modal Interaction in Postbuckled Plates: Theory," NASA TP-2943, November, 1989.
19. Romeo, Giulio, "Experimental Investigation on Advanced Composite-Stiffened Structures under Uniaxial Compression and Bending," *AIAA Journal*, Vol. 24, No. 11, November, 1986, pp. 1823-1830.
20. Starnes, J.H. Jr., Knight, N.F. Jr., and Rouse, M., "Postbuckling Behavior of Selected Flat Stiffened Graphite-Epoxy Panels Loaded in Compression," *AIAA Journal*, Vol. 23, No. 8, August, 1985, pp.1236-1246.
21. Smith, C.S., and Dow, R.S., "Compressive Strength of Longitudinally Stiffened GRP Panels," in *Composite Structures 3 (Proceedings, Third Int. Conf. on Composite Structures, Paisley College of Technology, 1985)*, ed., I.H. Marshall, Elsevier Applied Science Publishers, London, 1985, pp. 468-490.
22. Spier, E.E., and Klouman, F.L., "Post Buckling Behavior of Graphite/Epoxy Laminated Plates and Channels," *Proceedings, Army Symp. Solid Mechanics, 1976 - Composite Materials: The Influence of Mechanics of Failure on Design*, Army Materials and Mechanics Research Center, Watertown, MA, AMMRC MS 76-2, September, 1976, pp.62-78.
23. Williams, J.G., and Stein, M., "Buckling Behavior and Structural Efficiency of Open-Section Stiffened Composite Compression Panels," *AIAA Journal*, Vol. 14, No. 11, November, 1976, pp. 1618-1626.
24. Tulk, J.D., and Walker, A.C., "Model Studies of the Elastic Buckling of a Stiffened Plate," *J. of Strain Analysis*, Vol. 11, No. 3, 1976, pp. 137-143.
25. Thompson, J.M.T., Tulk, J.D., and Walker, A.C., "An Experimental Study of Imperfection-Sensitivity in the Interactive Buckling of Stiffened Plates," in *Buckling of Structures*, ed., B. Budiansky, Springer-Verlag, Berlin, 1976, pp. 149-159.
26. Fok, W.C., Rhodes, J., and Walker, A.C., "Local Buckling of Outstands in Stiffened Plates," *The Aeronautical Quarterly*, Vol. 27, Part 4, November, 1976, pp. 277-291.
27. Fok, W.C., Walker, A.C., and Rhodes, J., "Buckling of Locally Imperfect Stiffeners in Plates," *J. of the Engineering Mechanics Division, ASCE*, Vol. 103, No. EM5, October, 1977, pp. 895-911.
28. Almroth, B.O., Brogan, F.A., and Stanley, G.M., "User's Manual for STAGS - Volume I: Theory," NASA CR-165670, March, 1978.

29. Almroth, B.O., Brogan, F.A., and Stanley, G.M., "Structural Analysis of General Shells - Volume II: User Instructions for STAGSC-1," LMSC-D633873, Applied Mechanics Lab., Lockheed Palo Alto Research Lab., Palo Alto, CA, December, 1982, updated 1985.
30. Riks, E., "An Incremental Approach to the Solution of Snapping and Buckling Problems," *Int. J. Solids and Structures*, Vol. 15, 1979, pp.529-551.
31. Thurston, G.A., Brogan, F.A., and Stehlin, P., "Postbuckling Analysis Using a General-Purpose Code," *AIAA Journal*, Vol. 24, No. 6, June 1986, pp. 1013-1020.
32. Rankin, C.C., and Brogan, F.A., "Application of the Thurston Bifurcation Solution Strategy to Problems with Modal Interaction," AIAA-88-2286, *Proceedings, 29th Structures, Structural Dynamics and Materials Conference, Williamsburg, VA, 1988*, pp. 590-595.
33. Koiter, W.T., "On The Stability of Elastic Equilibrium," Doctoral Thesis, Polytechnic Institute of Delft, 1945 (English translation: NASA TT F-10,833, March, 1973).
34. Hunt, G.W., "Imperfection-Sensitivity of Semi-Symmetric Branching," *Proc. R. Soc. Lond., Series A*, Vol. 357, 1977, pp. 193-211.
35. Arnold, R.R., and Kedward, K.T., "Stability Critical Stiffened Panels," Chapter 12 of *Handbook of Composites, Vol. 2 - Structures and Design*, ed., C.T. Herakovich, and Y.M. Tarnopol'skii, Elsevier Science Publishers, New York, 1989, pp. 623-665.
36. Arnold, R.R., and Mayers, J., "Buckling, Postbuckling, and Crippling of Materially Nonlinear Laminated Composite Plates," *Int. J. of Solids and Structures*, Vol. 20, No. 9/10, 1984, pp. 863-880.
37. Dawe, D.J., and Craig, T.J., "Buckling and Vibration of Shear Deformable Prismatic Plate Structures by a Complex Finite Strip Method," *Int. J. Mechanical Sciences*, Vol. 30, No. 2, 1988, pp.77-99.
38. Sridharan, S., and Peng, M.-H., "Performance of Axially Compressed Stiffened Panels," *Int. J. Solids and Structures*, Vol. 25, No. 8, 1989, pp. 879-899.
39. Giles, G.L., and Anderson, M.S., "Effects of Eccentricities and Lateral Pressure on the Design of Stiffened Compression Panels," NASA Technical Note D-6784, 1972.
40. Anderson, M.S. and Stroud, W.J., "General Panel Sizing Computer Code and Its Application to Composite Structural Panels," *AIAA Journal*, Vol. 17, No. 8, August, 1979, pp. 892-897.
41. Bijlaard, P.P., and Fisher, G.P., "Column Strength of H-Sections and Square Tubes in Postbuckling Range of Component Plates," NACA TN 2994, August, 1953.
42. Sridharan, S., and Graves-Smith, T.R., "Postbuckling Analysis with Finite Strips," *J. of the Engineering Mechanics Division, ASCE*, Vol. 107, No. EM5, October, 1981, pp. 869-888.
43. van der Neut, A., "The Interaction of Local Buckling and Column Failure of Thin-Walled Compression Members," *Proceedings 12th Int. Congr. Appl. Mech, Stanford University, 1968*, Springer, Berlin, 1969, pp. 389-399.
44. van der Neut, A., "Mode Interaction with Stiffened Panels," *Proceedings, IUTAM Symp. on Buckling of Structures, 1974*, ed., B. Budiansky, Springer-Verlag, Berlin, 1976, pp. 117-132.
45. Crawford, R.F., and Hedgepeth, J.M., "Effects of Initial Waviness on the Strength and Design of Built-up Structures," *AIAA Journal*, Vol. 13, No. 5, May, 1975, pp. 672-675.

46. Graves-Smith, T.R., "The Ultimate Strength of Locally Buckled Columns of Arbitrary Length," *Thin Walled Steel Structures; Their Design and Use in Buildings (Proceedings, 1st International Symposium on Thin Walled Structures, University College of Swansea, 1967)*, Gordon and Breach, New York, 1968, pp. 35-60.
47. Koiter, W.T., and van der Neut, A., "Interaction between Local and Overall Buckling of Stiffened Compression Panels," in *Thinwalled Structures*, ed., J. Rhodes and A.C. Walker, Granada, 1980, pp. 61-85.
48. Sridharan, S., and Ali, M.A., "Interactive Buckling in Thin-Walled Beam-Columns," *J. Engineering Mechanics, (ASCE)*, Vol. 111, No. 12, December, 1985, pp. 1470-1486.
49. Ali, M.A., and Sridharan, S., "A Versatile Model for Interactive Buckling of Columns and Beam-Columns," *Int. J. Solids and Structures*, Vol. 24, No. 5, 1988, pp. 481-496.
50. Tvergaard, Viggo, "Imperfection-Sensitivity of a Wide Integrally Stiffened Panel under Compression," *Int. J. Solids and Structures*, Vol. 9, 1973, pp. 177-192.
51. Tvergaard, Viggo, "Influence of Post-Buckling Behavior on Optimum Design of Stiffened Panels," *Int. J. of Solids and Structures*, Vol. 9, 1973, pp. 1519-1534.
52. Koiter, W.T., and Pignaturo, M., "An Alternative Approach to the Interaction between Local and Overall Buckling in Stiffened Panels," in *Proceedings, IUTAM Symp. on Buckling of Structures, 1974*, ed., B. Budiansky, Springer-Verlag, 1976, pp. 133-148.
53. Koiter, W.T., and Pignataro, M., "A General Theory for the Interaction Between Local and Overall Buckling of Stiffened Panels," Delft U. of Tech., Dept. Mech. Eng., Rept WTHD-83, 1976.
54. Benito, R., and Sridharan, S., "Mode Interaction in Thin-Walled Structural Members," *J. Structural Mechanics*, Vol. 12, No. 4, 1984-85, pp. 517-542.
55. Koiter, W.T. and Kuikan, G.D.C., "The Interaction Between Local Buckling and Overall Buckling on the Behavior of Built-up Columns," WTHD Report 23, Delft University of Technology, 1971.
56. Sridharan, S., "Doubly Symmetric Interactive Buckling of Plate Structures," *Int. J. of Solids and Structures*, Vol. 19, No. 7, 1983, pp. 625-641.
57. Bushnell, D., Truss-Core Sandwich Design via Panda2," AIAA-90-1070-CP, *Proceedings, 31st AIAA Structures, Structural Dynamics and Materials Conference, Long Beach, CA, 1990*, pp.1313-1332.
58. Sheinman, I., and Frostig, Y., "Post-Buckling Analysis of Stiffened Laminated Panel," *ASME J. of Applied Mechanics*, Vol. 55, September 1988, pp. 635-640.
59. Plank, R.J., and Williams, F.W., "Critical Buckling of Some Stiffened Panels in Compression, Shear, and Bending," *Aeronautical Quarterly*, Vol. 25, August, 1974, pp. 165-179.
60. Anderson, M.S., Williams, F.W., and Wright, C.J., "Buckling and Vibration of Any Prismatic Assembly of Shear and Compression Loaded Anisotropic Plates with an Arbitrary Supporting Structure," *Int. J. Mechanical Science*, Vol. 25, No. 8, 1983, pp. 579-584.
61. Jones, R.M., *Mechanics of Composite Materials*, Hemisphere Publishing Corp., New York, 1975.

62. Stoll, F., and Gurdal, Z., "Nonlinear Analysis of Compressively Loaded Linked-Plate Structures," AIAA-90-0968, *Proceedings, 31st AIAA Structures, Structural Dynamics and Materials Conference, Long Beach, CA, 1990*.
63. Hornbeck, R.W., *Numerical Methods*, Prentice-Hall, Inc., Englewood Cliffs, New Jersey, 1975.
64. Shin, D.K., "Minimum-Weight Design of Symmetrically Laminated Composite Plates for Postbuckling Performance under In-plane Compression Loads," PhD dissertation, Engineering Science and Mechanics Department, Virginia Polytechnic Institute and State University, September, 1990.
65. Bushnell, David, "Nonlinear Equilibrium of Imperfect, Locally Deformed Stringer-Stiffened Panels under Combined In-Plane Loads," *Computers and Structures*, Vol. 27, No. 4, 1987, pp. 519-539.
66. Donnell, L.H., *Beams, Plates and Shells*, McGraw-Hill Book Co., New York, 1976, sections 4.2, 4.3.
67. Malvern, L.E., *Introduction to the Mechanics of a Continuous Medium*, Prentice-Hall, Inc., Englewood Cliffs, New Jersey, 1969, p. 161.
68. Reddy, J.N., *Energy and Variational Methods in Applied Mechanics*, John Wiley & Sons, New York, 1984, Sections 2.3.2; Section 4.1.1 .

Appendix A. Nonlinear Plate Theory

The plate theory developed here applies independently to each plate of the linked-plate structure. While large displacements may occur, material strains are assumed to be small (as limited by material failure) and Hooke's law is assumed to govern material response. Plates have elastic properties consistent with the assumptions of classical laminated composite plate theory [61]. The Kirchhoff-Love assumptions are used for specifying the distribution of displacements through the thickness of the plate. Geometrically nonlinear effects are accounted for in a manner consistent with the plate theory of von Karman [66], but with certain modifications required due to the nature of displacement fields experienced by certain component plates in a linked-plate structure. The principle of virtual work is used to derive the boundary value problem governing equilibrium of the plate. A development of the plate theory follows, which includes a consideration of geometric imperfections.

A.1.1 Strain-Displacement Relations

Let $\{u\} = [u(x, y) \ v(x, y) \ w(x, y)]^T$ denote the three displacement components of the plate mid-surface in the x -, y -, and z -directions, respectively, where the x - y plane lies at the mid-surface of the undeformed plate (see Figure 36. For a Lagrangian description of deformation, the finite-strain expressions for the in-plane strain components of the mid-surface are given by [67]

$$\begin{aligned}
\varepsilon_x^c &= u_{,x} + \frac{1}{2} (u_{,x}^2 + v_{,x}^2 + w_{,x}^2) \\
\varepsilon_y^c &= v_{,y} + \frac{1}{2} (u_{,y}^2 + v_{,y}^2 + w_{,y}^2) \\
\gamma_{xy}^c &= u_{,y} + v_{,x} + u_{,x}u_{,y} + v_{,x}v_{,y} + w_{,x}w_{,y}
\end{aligned} \tag{A1}$$

In the plate theory of von Karman, only displacement gradients $w_{,x}$ and $w_{,y}$ are expected to achieve significantly large amplitudes, so of the nonlinear terms in equations (A1), only $w_{,x}^2$, $w_{,y}^2$, and $w_{,x}w_{,y}$ are retained. However, in the present application, gradients of u and v , in addition to gradients of w , may become significantly large due to in-plane rotation of a component plate, as would occur in a stiffener which participates in the global buckling motion of a stiffened panel. Thus, displacement gradients due to in-plane rotations are explored here.

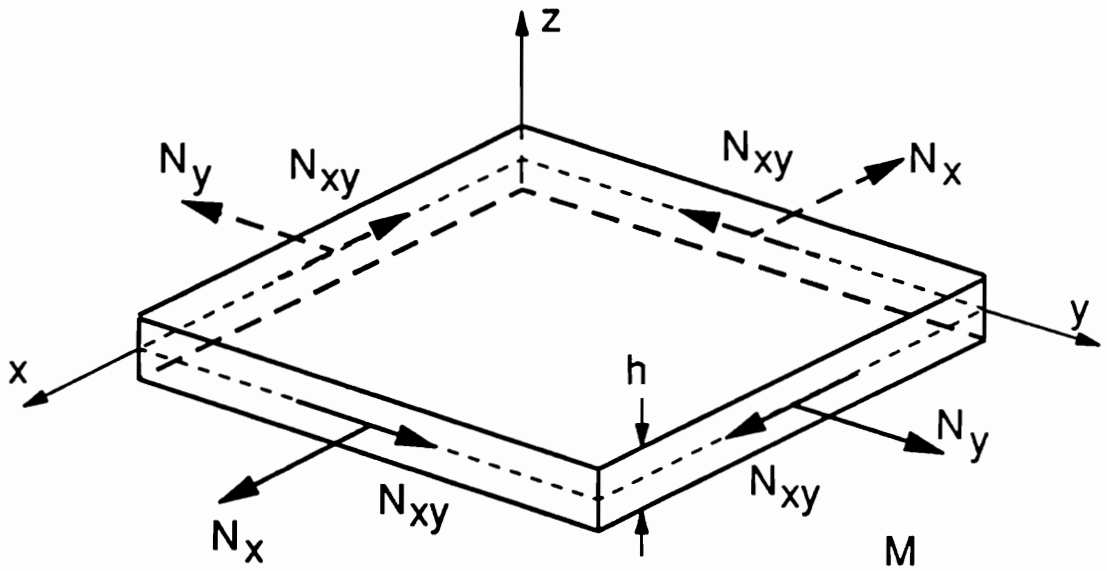
Consider a local rotation with a vector denotation of $\bar{\omega} = \omega \hat{k}$ using the right hand rule, where ω is the rotation amplitude, and \hat{k} is the unit vector in the z-direction. The in-plane displacement gradients corresponding to this rotation are expressed in terms of Taylor series expansions in ω :

$$\begin{aligned}
u_{,x} = v_{,y} &= -(1 - \cos \omega) = -\frac{\omega^2}{2} + O(\omega^4) \\
-u_{,y} = v_{,x} &= \sin \omega = \omega + O(\omega^3)
\end{aligned} \tag{A2}$$

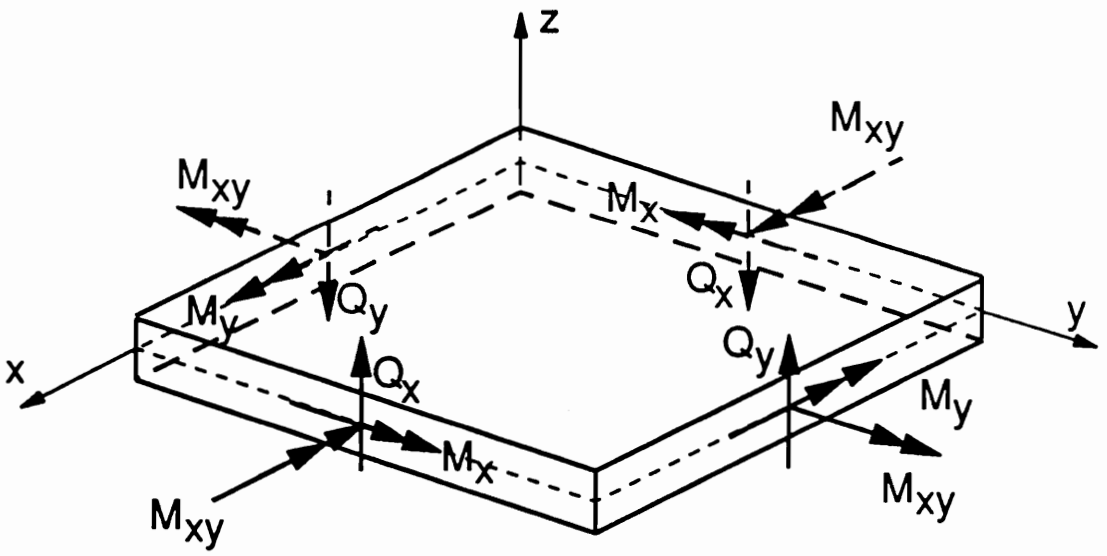
Displacement gradients $u_{,x}$ and $v_{,y}$ are of order ω^2 , whereas $u_{,y}$ and $v_{,x}$ are of order ω . It is assumed that ω is sufficiently small to permit the neglect of terms of order (ω^3) in equations (A1). The following expressions for the mid-surface in-plane strain components are obtained:

$$\begin{aligned}
\varepsilon_x^c &= u_{,x} + \frac{1}{2} (v_{,x}^2 + w_{,x}^2) \\
\varepsilon_y^c &= v_{,y} + \frac{1}{2} (u_{,y}^2 + w_{,y}^2) \\
\gamma_{xy}^c &= u_{,y} + v_{,x} + w_{,x}w_{,y}
\end{aligned} \tag{A3}$$

In the above equations, the terms $v_{,x}^2$ and $u_{,y}^2$ represent contributions not found in the von Karman nonlinear strain expressions.



a) In-plane stress resultants.



b) Bending and shear stress resultants.

Figure 36. Conventions for plate stress-resultants and coordinate axes.

The Kirchhoff-Love assumptions are used to determine the distribution of the in-plane strain components through the thickness of the plate. The assumptions are that material lines perpendicular to the mid-surface of the undeformed plate remain straight, inextensional, and perpendicular to the mid-surface. Donnell [66] derives the following relations for the distribution of strains through the thickness, using the Kirchhoff-Love assumptions:

$$\begin{aligned}
 \varepsilon_x &= u_{,x} + \frac{1}{2}(v_{,x}^2 + w_{,x}^2) + z[-w_{,xx} + u_{,xx}w_{,x} + v_{,xx}w_{,y} + u_{,x}w_{,xx}] \\
 \varepsilon_y &= v_{,y} + \frac{1}{2}(u_{,y}^2 + w_{,y}^2) + z[-w_{,yy} + u_{,yy}w_{,x} + v_{,yy}w_{,y} + v_{,y}w_{,yy}] \\
 \gamma_{xy} &= u_{,y} + v_{,x} + w_{,x}w_{,y} - u_{,x}v_{,x} - u_{,y}v_{,y} \\
 &\quad + z[-2w_{,xy} + 2u_{,xy}w_{,x} + 2v_{,xy}w_{,y} + 2(u_{,x} + v_{,y})w_{,xy} + (u_{,y} + v_{,x})(w_{,xx} + w_{,yy})]
 \end{aligned} \tag{A4}$$

where terms of higher order and terms nonlinear in z have been neglected. If terms in equations (A4) which are independent of z (the mid-surface strains) are retained or discarded using the same assumptions as used in deriving equations (A3), then the mid-surface strains of equations (A4) reduce to equations (A3). It is further assumed that the plate thickness and the displacement derivatives are all sufficiently small so that only the lowest order z -dependent contributions need to be retained. The resulting z -dependence is the same as that of classical linear plate theory. The final expression for the distribution of in-plane strains in the plate is given by

$$\begin{aligned}
 \varepsilon_x(x, y, z) &= \varepsilon_x^c(x, y) + z\kappa_x^c(x, y) \\
 \varepsilon_y(x, y, z) &= \varepsilon_y^c(x, y) + z\kappa_y^c(x, y) \\
 \gamma_{xy}(x, y, z) &= \gamma_{xy}^c(x, y) + z\kappa_{xy}^c(x, y)
 \end{aligned} \tag{A5}$$

where the mid-surface strains are given in equations (A3), and where the mid-surface curvatures are given by

$$\begin{aligned}
 \kappa_x^c &= -w_{,xx} \\
 \kappa_y^c &= -w_{,yy} \\
 \kappa_{xy}^c &= -2w_{,xy}
 \end{aligned} \tag{A6}$$

In the presence of geometric shape imperfections, it is assumed that when the imperfect plate is unloaded and free of stress resultants, the displacement variables describe the imperfection shape: $\{u\} = \{u^0\} = [u^0 \ v^0 \ w^0]^T$. In order to establish the "mechanical strain," meaning the change in strain due to the application of structural loading, express the mid-surface strains and curvatures, $\{\varepsilon^c\} = [\varepsilon_x^c \ \varepsilon_y^c \ \gamma_{xy}^c]^T$ and $\{\kappa^c\} = [\kappa_x^c \ \kappa_y^c \ \kappa_{xy}^c]^T$, respectively, as functions of the displacement components:

$$\begin{aligned} \{\varepsilon^c\} &= \{\varepsilon^c(\{u\})\} \\ \{\kappa^c\} &= \{\kappa^c(w)\} \end{aligned} \quad (A7)$$

where the functional relations are given in equations (A3) and (A6). The mid-surface mechanical strains and curvatures, $\{\varepsilon^m\}$ and $\{\kappa^m\}$, respectively, are given by the difference between the apparent strains and curvatures (those based on $\{u\}$) and the initial strains and curvatures (those based on $\{u^0\}$):

$$\{\varepsilon^m\} = \{\varepsilon^c(\{u\})\} - \{\varepsilon^c(\{u^0\})\} = \begin{Bmatrix} [u_{,x} + .5(v_{,x}^2 + w_{,x}^2)] - [u_{,x}^0 + .5(v_{,x}^{0^2} + w_{,x}^{0^2})] \\ [v_{,y} + .5(u_{,y}^2 + w_{,y}^2)] - [v_{,y}^0 + .5(u_{,y}^{0^2} + w_{,y}^{0^2})] \\ [u_{,y} + v_{,x} + w_{,x}w_{,y}] - [u_{,y}^0 + v_{,x}^0 + w_{,x}^0w_{,y}^0] \end{Bmatrix} \quad (A8)$$

$$\{\kappa^m\} = \{\kappa^c(w)\} - \{\kappa^c(w^0)\} = - \begin{Bmatrix} w_{,xx} - w_{,xx}^0 \\ w_{,yy} - w_{,yy}^0 \\ 2w_{,xy} - 2w_{,xy}^0 \end{Bmatrix} \quad (A9)$$

The other three stress/strain components are considered briefly for later use. The Kirchhoff-Love assumptions imply zero transverse shear strain, and this condition is expressed as

$$\gamma_{xz} = \gamma_{yz} \equiv 0 \quad (A10)$$

Transverse normal stress is assumed to be negligible compared to in-plane stresses, so the assumption is made that

$$\sigma_z \equiv 0 \quad (A11)$$

where σ_z is the normal stress perpendicular to the plate mid-surface.

A.1.2 Equilibrium Equations in Terms of Stress Resultants:

Consider a linearly elastic body in the absence of body forces, undergoing large displacements but small strains. The principle of virtual work (equivalent, for this conservative system, to the principle of minimum total potential energy) provides the following equilibrium condition [68], where tensor notation is used:

$$\int_V \sigma_{ij} \delta \varepsilon_{ij} dV - \int_{S_2} \hat{t}_i \delta u_i dS = 0 \quad i, j = 1, 2, 3 \quad (A12)$$

where summation on i and j is implied, and where S_2 is the portion of the boundary surface on which tractions, \hat{t}_i are specified, $\delta \varepsilon_{ij}$ is any kinematically admissible virtual strain field within the domain of the body, and δu_i is any kinematically admissible virtual displacement field for the boundary surface. On portions of the boundary surface where tractions are not specified, displacements are assumed to be specified.

For application to plates, integration over the volume is replaced by successive integrations over the plate area, A (in the x - y plane), and through the plate thickness, h (in the z -direction). Integration over the boundary surface is replaced by successive integrations along the tangential edge coordinate, s , and through the plate thickness, h , where it is assumed here that all non-zero boundary tractions are applied at the plate edges. The stress and strain tensor components are converted to the symbols preferred here:

$$\begin{aligned} [\sigma_{11}, \sigma_{22}, \sigma_{33}, \sigma_{23}, \sigma_{13}, \sigma_{12}] &= [\sigma_x, \sigma_y, \sigma_z, \tau_{yz}, \tau_{xz}, \tau_{xy}] \\ [\varepsilon_{11}, \varepsilon_{22}, \varepsilon_{33}, 2\varepsilon_{23}, 2\varepsilon_{13}, 2\varepsilon_{12}] &= [\varepsilon_x, \varepsilon_y, \varepsilon_z, \gamma_{yz}, \gamma_{xz}, \gamma_{xy}] \end{aligned} \quad (A13)$$

where it is recognized that the stress and strain tensors are symmetric. Accounting for the zero stress and strain components specified in equations (A10) and (A11), the virtual work expression can then be written

$$\int_A \int_{-\frac{h}{2}}^{\frac{h}{2}} (\sigma_x \delta \varepsilon_x + \sigma_y \delta \varepsilon_y + \tau_{xy} \delta \gamma_{xy}) dz dA - \int_{S_2} \int_{-\frac{h}{2}}^{\frac{h}{2}} \hat{t}_i \delta u_i dz ds = 0 \quad i = 1, 2, 3 \quad (A14)$$

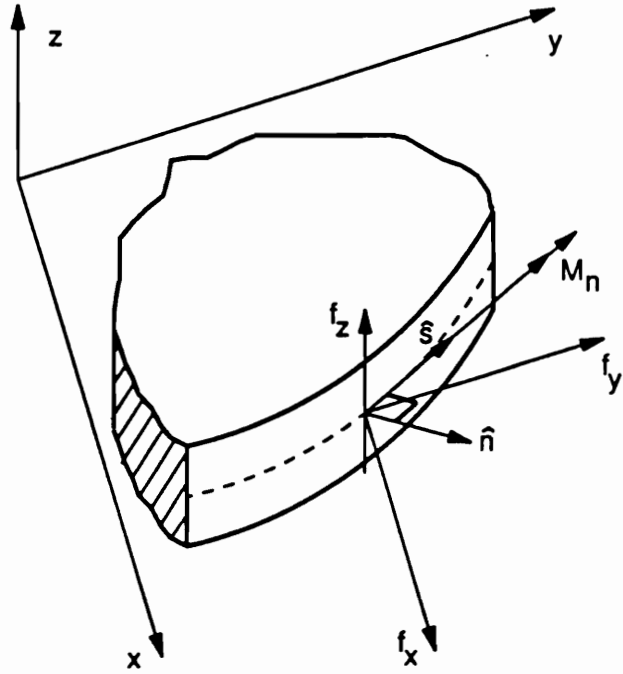
where S_2 is the portion of the edge coordinate along which tractions are specified on the edge surface.

Now define generalized force resultants on the boundary, f_x , f_y , f_z , and M_n , which are depicted in Figure 37(a). Resultants f_x , f_y , and f_z are edge forces per unit tangential length directed parallel to the coordinate axes. Resultant M_n is the edge bending-moment per unit tangential length, and its line of action follows the plate edge during deformation, so that the vector direction of the moment is not constant. The edge twisting moment M_s , shown in Figure 37(b), is not included in the above group of stress resultants, because f_z is assumed to contain the Kirchhoff equivalent shear force due to the edge twisting moment.

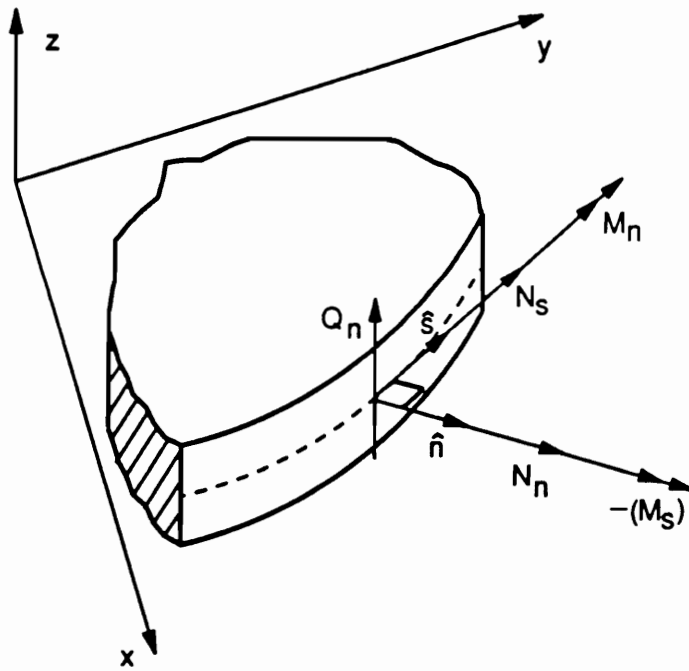
The previous definition of S_2 is refined here. Assume that prescribed boundary tractions are specified in terms of the four generalized force-resultant values \hat{f}_x , \hat{f}_y , \hat{f}_z , and \hat{M}_n , each of which acts on a specific portion of the boundary. Denote these four different portions as C_1 , C_2 , C_3 , and C_4 , where these portions may overlap or coincide. When the strain forms of equations (A5) are substituted into the virtual work expression (equation (A14)) and the integral through the thickness is evaluated, the resulting expression is

$$\begin{aligned} & \int_A (N_x \delta \varepsilon_x^c + N_y \delta \varepsilon_y^c + N_{xy} \delta \gamma_{xy}^c + M_x \delta \kappa_{x,xx}^c + M_y \delta \kappa_{y,yy}^c + M_{xy} \delta \kappa_{xy,xy}^c) dA \\ & - \int_{C_1} \hat{f}_x \delta u ds - \int_{C_2} \hat{f}_y \delta v ds - \int_{C_3} \hat{f}_z \delta w ds + \int_{C_4} \hat{M}_n \delta w_{,n} ds \\ & = 0 \end{aligned} \quad (A15)$$

where the stress resultants are defined by



a) Generalized edge force-resultants used in the nonlinear plate theory.



b) Stress resultants at a plate edge.

Figure 37. Measures of the loads acting on a plate edge.

$$\begin{Bmatrix} N_x \\ N_y \\ N_{xy} \end{Bmatrix} = \int_{-\frac{h}{2}}^{\frac{h}{2}} \begin{Bmatrix} \sigma_x \\ \sigma_y \\ \tau_{xy} \end{Bmatrix} dz \quad (\text{A16})$$

$$\begin{Bmatrix} M_x \\ M_y \\ M_{xy} \end{Bmatrix} = \int_{-\frac{h}{2}}^{\frac{h}{2}} \begin{Bmatrix} \sigma_x \\ \sigma_y \\ \tau_{xy} \end{Bmatrix} z dz$$

The stress resultants are depicted in Figure 36.

Substituting the expressions for mid-surface strains and curvatures of equations (A3) and (A6) into equation (A15) and applying the two-dimensional form of Green's Theorem, the area integral of equation (A15) can be converted into the following expression:

$$\begin{aligned} & - \int_A \{ [N_{x,x} + N_{xy,y} + (N_y u_{,y})_{,y}] \delta u + [N_{xy,x} + N_{y,y} + (N_x v_{,x})_{,x}] \delta v \\ & \quad + [M_{x,xx} + 2M_{xy,xy} + M_{y,yy} + (N_x w_{,x} + N_{xy} w_{,y})_{,x} + (N_{xy} w_{,x} + N_y w_{,y})_{,y}] \delta w \} dA \\ & + \int_S \{ [n_x N_x + n_y (N_{xy} + N_y u_{,x})] \delta u + [n_x (N_{xy} + N_x v_{,x}) + n_y N_y] \delta v \\ & \quad + [n_x (M_{x,x} + M_{xy,y} + N_x w_{,x} + N_{xy} w_{,y}) + n_y (M_{xy,x} + M_{y,y} + N_{xy} w_{,x} + N_y w_{,y})] \delta w \\ & \quad - (n_x M_x + n_y M_{xy}) \delta w_{,x} - (n_x M_{xy} + n_y M_y) \delta w_{,y} \} ds \end{aligned} \quad (\text{A17})$$

where n_x and n_y are the components of the unit normal vector of the undeformed plate edge, defined by

$$\hat{n} = n_x \hat{i} + n_y \hat{j} \quad (\text{A18})$$

It is convenient at this point to refer certain terms to a natural edge coordinate system ($n s$), where n and s are directed along unit vectors \hat{n} and \hat{s} , respectively. Vector \hat{n} is defined in equation (A18) and \hat{s} is defined by

$$\hat{s} = -n_y \hat{i} + n_x \hat{j} \quad (\text{A19})$$

These unit vectors are depicted in Figure 37(a). Derivatives in x and y can be expressed in terms of the natural edge coordinates:

$$\begin{aligned}\frac{\partial}{\partial x} &= n_x \frac{\partial}{\partial n} - n_y \frac{\partial}{\partial s} \\ \frac{\partial}{\partial y} &= n_y \frac{\partial}{\partial n} + n_x \frac{\partial}{\partial s}\end{aligned}\tag{A20}$$

Using these relationships, the last three terms in expression (A17) can be converted as follows:

$$\begin{aligned}& \int_S \{ [n_x(M_{x,x} + M_{xy,y} + N_x w_{,x} + N_{xy} w_{,y}) + n_y(M_{xy,x} + M_{y,y} + N_{xy} w_{,x} + N_y w_{,y})] \delta w \\ & \quad - (n_x M_x + n_y M_{xy}) \delta w_{,x} - (n_x M_{xy} + n_y M_y) \delta w_{,y} \} ds \\ &= \int_S \{ (Q_n + N_n w_{,n} + N_s w_{,s}) \delta w - M_n \delta w_{,n} - M_s \delta w_{,s} \} ds\end{aligned}\tag{A21}$$

where the newly introduced stress-resultants are given by the following expressions [68]:

$$\begin{aligned}Q_n &= (M_{x,x} + M_{xy,y})n_x + (M_{xy,x} + M_{y,y})n_y \\ N_n &= N_x n_x^2 + N_y n_y^2 + 2n_x n_y N_{xy} \\ N_s &= (N_y - N_x)n_x n_y + N_{xy}(n_x^2 - n_y^2) \\ M_n &= M_x n_x^2 + M_y n_y^2 + 2n_x n_y M_{xy} \\ M_s &= (M_y - M_x)n_x n_y + M_{xy}(n_x^2 - n_y^2)\end{aligned}\tag{A22}$$

The stress resultants defined above are depicted in Figure 37(b). The last term in equation (A22) is now manipulated to establish the Kirchhoff equivalent shear force contribution of M_s . If we require that the edge-tangent vector \hat{s} varies continuously with s except at coordinates s_1, s_2, \dots, s_N , then applying Green's Theorem it can be shown that

$$\int_S -M_s \delta w_{,s} ds = \int_S M_{s,s} \delta w ds + \left(M_s \delta w \Big|_{s_1^-}^{s_1^+} + M_s \delta w \Big|_{s_2^-}^{s_2^+} + \dots + M_s \delta w \Big|_{s_N^-}^{s_N^+} \right)\tag{A23}$$

The terms in parentheses represent the virtual work due to concentrated forces at s_1, s_2, \dots, s_N , which are usually neglected in applications of plate theory, as they will be here.

The equilibrium condition is now reassembled using the substitutions developed above. It is noted that for edge coordinates not lying on the respective boundary portions $C_1, C_2, C_3,$ and $C_4,$ the corresponding virtual displacements $\delta u, \delta v, \delta w,$ and $\delta w_{,n},$ are zero. Thus, the virtual work statement (equation (A15)) can be written as

$$\begin{aligned}
& - \int_A \{ [N_{x,x} + N_{xy,y} + (N_y u_{,y})_{,y}] \delta u + [N_{xy,x} + N_{y,y} + (N_x v_{,x})_{,x}] \delta v \\
& \quad + [M_{x,xx} + 2M_{xy,xy} + M_{y,yy} + (N_x w_{,x} + N_{xy} w_{,y})_{,x} + (N_{xy} w_{,x} + N_y w_{,y})_{,y}] \delta w \} dA \\
& + \int_{C_1} [n_x N_x + n_y (N_{xy} + N_y u_{,y}) - \hat{f}_x] \delta u ds + \int_{C_2} [n_x (N_{xy} + N_x v_{,x}) + n_y N_y - \hat{f}_y] \delta v ds \quad (A24) \\
& + \int_{C_3} [Q_n + M_{s,s} + N_n w_{,n} + N_s w_{,s} - \hat{f}_z] \delta w ds - \int_{C_4} [M_n \delta w_{,n} - \hat{M}_n] \delta w_{,n} ds \\
& = 0
\end{aligned}$$

By the fundamental lemma of the calculus of variations, $\delta u, \delta v,$ and δw may vary independently, and may vary within the domain independently of the values at the boundaries. This supplies the Euler equations by requiring that the bracketed expressions in the area integrals of equation (A24) be identically zero over the domain of the plate:

$$\begin{aligned}
N_{x,x} + N_{xy,y} + (N_y u_{,y})_{,y} &= 0 \\
N_{xy,x} + N_{y,y} + (N_x v_{,x})_{,x} &= 0 \\
M_{x,xx} + 2M_{xy,xy} + M_{y,yy} + (N_x w_{,x} + N_{xy} w_{,y})_{,x} + (N_{xy} w_{,x} + N_y w_{,y})_{,y} &= 0
\end{aligned} \quad (A25)$$

The boundary conditions are obtained by requiring that each boundary integral of equation (A24) be zero. One possible set of boundary conditions is obtained by requiring that the following force or displacement boundary conditions must be satisfied at all points of the boundary (plate edge):

$$\begin{aligned}
f_x &= \hat{f}_x \quad \text{or} \quad u = \hat{u} \\
f_y &= \hat{f}_y \quad \text{or} \quad v = \hat{v} \\
f_z &= \hat{f}_z \quad \text{or} \quad w = \hat{w} \\
M_n &= \hat{M}_n \quad \text{or} \quad w_{,n} = \hat{w}_{,n}
\end{aligned} \quad (A26)$$

where expressions for edge force-resultants f_x , f_y , and f_z are extracted from equations (A24):

$$\begin{aligned}
 f_x &= n_x N_x + n_y (N_{xy} + N_y u_{,y}) \\
 f_y &= n_x (N_{xy} + N_x v_{,x}) + n_y N_y \\
 f_z &= Q_n + M_{s,s} + N_n w_{,n} + N_s w_{,s}
 \end{aligned}
 \tag{A27}$$

Edge force-resultants f_x and f_y are not expressed in terms of the stress resultants defined in equations (A22) because of the complicated, counter-intuitive form which results.

In the current application, all plate strips are rectangular in shape, so that all plate edges can either be classified as x-normal ($\hat{n} = \pm \hat{i}$) or y-normal ($\hat{n} = \pm \hat{j}$). Equations (A26) and (A22) can be evaluated to obtain, for an x-normal edge,

$$\begin{aligned}
 f_x &= n_x N_x \\
 f_y &= n_x (N_{xy} + N_x v_{,x}) \\
 f_z &= n_x (M_{x,x} + 2M_{xy,y} + N_x w_{,x} + N_{xy} w_{,y}) \\
 M_n &= M_x
 \end{aligned}
 \tag{A28}$$

and for a y-normal edge,

$$\begin{aligned}
 f_x &= n_y (N_{xy} + N_y u_{,y}) \\
 f_y &= n_y N_y \\
 f_z &= n_y (2M_{xy,x} + M_{y,y} + N_{xy} w_{,x} + N_y w_{,y}) \\
 M_n &= M_y
 \end{aligned}
 \tag{A29}$$

A.1.3 Plate Constitutive Equations:

In the conventional notation of laminated composite plate theory [61] the stress resultants and the mechanical strains and curvatures at the mid-surface have the following relationship:

$$\begin{Bmatrix} N_x \\ N_y \\ N_{xy} \\ M_x \\ M_y \\ M_{xy} \end{Bmatrix} = \begin{bmatrix} A_{11} & A_{12} & A_{16} & B_{11} & B_{12} & B_{16} \\ A_{12} & A_{22} & A_{26} & B_{12} & B_{22} & B_{26} \\ A_{16} & A_{26} & A_{66} & B_{16} & B_{26} & B_{66} \\ B_{11} & B_{12} & B_{16} & D_{11} & D_{12} & D_{16} \\ B_{12} & B_{22} & B_{26} & D_{12} & D_{22} & D_{26} \\ B_{16} & B_{26} & B_{66} & D_{16} & D_{26} & D_{66} \end{bmatrix} \begin{Bmatrix} \varepsilon_x^m \\ \varepsilon_y^m \\ \gamma_{xy}^m \\ \kappa_x^m \\ \kappa_y^m \\ \kappa_{xy}^m \end{Bmatrix} \quad (A30)$$

where the square matrix is the stiffness matrix of the laminate. All elements of the stiffness matrix are constant for a given laminate, and follow conventional definitions given in, for example, reference [61].

Appendix B. Y-Dependence of Buckling

Eigensolutions

In this appendix, the functional forms for the buckling eigenfunctions are developed. The basis for the development presented here is the development provided in [5] pertaining to the VIPASA computer code. Much of the notation used here follows that of [5], though some changes were made to accommodate notation preferred in the current development. Aspects of the development in [5] which are related to vibration or to loading and plate anisotropic constants not being treated by the current method, are omitted here. The focus in [5] was on obtaining stiffness matrices for plate strips, so the functional forms for buckling eigensolutions were not provided. Thus, the functional forms are derived here.

B.1.1 Complex Representation

Variables x and y describe the mid-surface coordinates of a plate strip, where x lies in the interval $[0, L]$, and y lies in the interval $[0, b]$. The integer m denotes the number of halfwaves over the length L corresponding to the buckling eigenfunction under consideration, and dimensionless variables X and Y are introduced, defined by the expressions

$$X = \frac{m\pi x}{L} \quad Y = \frac{m\pi y}{L} \quad (B1)$$

A buckling eigenfunction, here denoted as $[u \ v \ w]$, is represented using complex functions of X and Y . The following form is assumed in VIPASA, for the special case when the plate elastic constants D_{16} and D_{26} are zero:

$$\begin{Bmatrix} u(x, y) \\ v(x, y) \\ w(x, y) \end{Bmatrix} = \text{Re} \left[\begin{Bmatrix} U(Y) \\ V(Y) \\ W(Y) \end{Bmatrix} e^{iX} \right] \quad (\text{B2})$$

where $i = \sqrt{-1}$, the functions U , V , and W are in general complex, and Re signifies the real portion of the complex expression in the brackets. For the current application, a phase shift is applied to the assumed form of equation (B2), by taking as the displacements the imaginary, rather than real, portions of the complex functions. This is done to locate the x -domain of the structure in the interval $[0, L]$. The new expression is

$$\begin{Bmatrix} u(x, y) \\ v(x, y) \\ w(x, y) \end{Bmatrix} = \text{Im} \left[\begin{Bmatrix} U(Y) \\ V(Y) \\ W(Y) \end{Bmatrix} e^{iX} \right] \quad (\text{B3})$$

The complex functions $[U \ V \ W]$ are represented in terms of two sets of real functions, $[U_R \ V_R \ W_R]$ and $[U_I \ V_I \ W_I]$, as shown:

$$\begin{Bmatrix} U(Y) \\ V(Y) \\ W(Y) \end{Bmatrix} = \begin{Bmatrix} U_R(Y) \\ V_R(Y) \\ W_R(Y) \end{Bmatrix} + i \begin{Bmatrix} U_I(Y) \\ V_I(Y) \\ W_I(Y) \end{Bmatrix} \quad (\text{B4})$$

In the current application the applied shear loading and the elastic constants D_{16} and D_{26} are all zero within each plate strip, with the consequence that

$$U_R = V_I = W_I \equiv 0 \quad (\text{B5})$$

so equation (B4) becomes

$$\begin{Bmatrix} U(Y) \\ V(Y) \\ W(Y) \end{Bmatrix} = \begin{Bmatrix} U_i(Y) \\ V_R(Y) \\ W_R(Y) \end{Bmatrix} \quad (B6)$$

and the eigenfunctions (B3) can now be written in the form

$$\begin{Bmatrix} u(x, y) \\ v(x, y) \\ w(x, y) \end{Bmatrix} = \begin{Bmatrix} U_i(Y) \cos X \\ V_R(Y) \sin X \\ W_R(Y) \sin X \end{Bmatrix} \quad (B7)$$

In the following sections, the functions $U_i(Y)$, $V_R(Y)$, and $W_R(Y)$ are determined using the differential equations governing buckling. Symbols U , V , and W will be used henceforth to denote the functions U_i , V_R , and W_R , respectively.

B.1.2 Out-of-Plane Displacements

The out-of-plane portion of the buckling eigensolution is governed by the following differential equation, taken from the body of the text:

$$M_{x_i,xx} + 2M_{xy_i,xy} + M_{y_i,yy} + \lambda_i(N_{x_L}w_{i,xx} + N_{y_L}w_{i,yy}) = 0 \quad (B8)$$

where unit loads N_{x_L} and N_{y_L} are known constants on a given plate strip, and the subscript i , which denotes the eigensolution index number, will henceforth be omitted. As shown in [5], through use of the assumed form for $w(x, y)$ (equation (B7)) and the definitions for the strains and stress resultants, the partial differential equation (B8) is converted to the following linear, homogeneous ordinary differential equation:

$$W'''' - 2TW''' + (T^2 - L)W = 0 \quad (B9)$$

where primes denote differentiation with respect to Y , and parameters T and L are given by

$$T = \frac{1}{D_{22}} \left(D_{12} + 2D_{66} + \lambda \frac{L^2 N_{yL}}{2m^2 \pi^2} \right) \quad L = \frac{1}{D_{22}} \left(-\lambda \frac{L^2 N_{xL}}{m^2 \pi^2} + T^2 - D_{11} \right) \quad (B10)$$

The general solution for equation (B9) has the form

$$W = Ce^{pY} \quad (B11)$$

where C is an arbitrary constant, and p is a constant governed by the characteristic equation

$$p^4 - 2Tp^2 + (T^2 - L) = 0 \quad (B12)$$

or

$$p^2 = T \pm \sqrt{L} \quad (B13)$$

The exact nature of the roots p depends on the relative amplitudes of the parameters T and L , but the following common form will be used to express the function $W(Y)$:

$$W(Y) = \sum_{j=1}^4 C_j \bar{f}_j(Y) \quad (B14)$$

where the constants C_j are determined by the boundary conditions at the side edges of the plate strip. In [5], four cases are identified for characterizing the form of the function $W(Y)$, but the first case corresponds to conditions which are not considered here. The remaining three cases (Case (b) through Case (d)) are considered independently below.

VIPASA Out-of-Plane Case b) $L > 0$: Two non-negative, real roots are identified, consistent with equations (B13):

$$\alpha^2 = -\hat{\alpha}^2 = T + \sqrt{L} \quad \gamma^2 = -\hat{\gamma}^2 = T - \sqrt{L} \quad (B15)$$

where either α or $\hat{\alpha}$ is real, and either γ or $\hat{\gamma}$ is real. Note that if γ is real then α must be real, and that if $\hat{\alpha}$ is real then $\hat{\gamma}$ must be real. Four roots p are then given by $p = \pm \alpha$ or $p = \pm i\hat{\alpha}$,

and $p = \pm \gamma$ or $p = \pm i\hat{\gamma}$. The four roots p establish four contributions to $W(Y)$, each having the form given in equation (B11), where it is understood that only the real portions of complex contributions are retained. The four contributions are combined and regrouped in such a way that the four functions \bar{f}_j of equation (B14) take the forms given in the following table:

Table 6. Functional Forms Used for VIPASA Out-of-Plane Case (b)

	$\alpha^2 \geq 0$	$\hat{\alpha}^2 > 0$		$\gamma^2 \geq 0$	$\hat{\gamma}^2 > 0$	
$\bar{f}_1(Y)$	$\cosh(\alpha Y)$	$\cos(\hat{\alpha} Y)$		$\bar{f}_3(Y)$	$\cosh(\gamma Y)$	$\cos(\hat{\gamma} Y)$
$\bar{f}_2(Y)$	$\sinh(\alpha Y)$	$\sin(\hat{\alpha} Y)$		$\bar{f}_4(Y)$	$\sinh(\gamma Y)$	$\sin(\hat{\gamma} Y)$

VIPASA Out-of-Plane Case c) $L < 0$: Here the roots of equation (B13) are complex, and two positive real constants α and β are sought which satisfy

$$p^2 = (\alpha + i\beta)^2 = T \pm i\sqrt{-L} \quad (B16)$$

The values α and β are found to satisfy

$$\alpha^2 = \frac{1}{2}(T + \sqrt{T^2 - L}) > 0 \quad \beta^2 = \frac{1}{2}(-T + \sqrt{T^2 - L}) > 0 \quad (B17)$$

Four roots p are then given by $p = \pm(\alpha \pm i\beta)$. The four roots p establish four contributions to $W(Y)$, each of the form given in equation (B11), where it is understood that only the real portions of complex contributions are retained. The four contributions are combined and regrouped in such a way that the four functions \bar{f}_j of equation (B14) are given in the following table:

Table 7. Functional Forms Used for VIPASA Out-of-Plane Case (c)

$\bar{f}_1(Y)$	$\cosh(\alpha Y) \cos(\beta Y)$
$\bar{f}_2(Y)$	$\sinh(\alpha Y) \cos(\beta Y)$
$\bar{f}_3(Y)$	$\cosh(\alpha Y) \sin(\beta Y)$
$\bar{f}_4(Y)$	$\sinh(\alpha Y) \sin(\beta Y)$

VIPASA Out-of-Plane Case d) $L = 0$: A single non-negative real value μ or $\hat{\mu}$ is sought, defined by the equation

$$\mu^2 = -\hat{\mu}^2 = T \quad (B18)$$

There are only two distinct roots, $p_1 = \mu$ and $p_2 = -\mu$, or $p_1 = i\hat{\mu}$ and $p_2 = -i\hat{\mu}$, so the form of the solution for $W(Y)$ is given by

$$W(Y) = \bar{C}_1 e^{\rho_1 Y} + \bar{C}_2 e^{-\rho_1 Y} + \bar{C}_3 Y e^{\rho_1 Y} + \bar{C}_4 Y e^{-\rho_1 Y} \quad (B19)$$

where only the real portions of complex contributions are retained. The four contributions are combined and regrouped in such a way that the four functions \bar{f}_i of equation (B14) take the forms given in the following table:

Table 8. Functional Forms Used for VIPASA Out-of-Plane Case (d)

	$\mu^2 \geq 0$	$\hat{\mu}^2 > 0$
$\bar{f}_1(Y)$	$\cosh(\mu Y)$	$\cos(\hat{\mu} Y)$
$\bar{f}_2(Y)$	$\sinh(\mu Y)$	$Y \cos(\hat{\mu} Y)$
$\bar{f}_3(Y)$	$Y \cosh(\mu Y)$	$\sin(\hat{\mu} Y)$
$\bar{f}_4(Y)$	$Y \sinh(\mu Y)$	$Y \sin(\hat{\mu} Y)$

B.1.3 In-Plane Displacements

The in-plane portion of the buckling eigensolution is governed by the following equations, taken from the body of the text:

$$\begin{aligned} N_{x_i, x} + N_{xy_i, y} &= 0 \\ N_{xy_i, x} + N_{y_i, y} + \lambda_i N_{x_L} v_{i, xx} &= 0 \end{aligned} \quad (B20)$$

where the third term originally present in the first of these two equations has been omitted, consistent with the discussion in the main text, and the unit load N_{x_L} is known based on the prebuckling analysis. The subscript i , which denotes the eigensolution index number, will henceforth be omitted. Through use of the assumed forms for $u(x, y)$ and $v(x, y)$ of equations

(B7) and the definitions for the stress resultants, the partial differential equations (B20) can be converted to the following two coupled, linear, homogeneous, ordinary differential equations [5]:

$$\begin{aligned} A_{66}U'' - L_1U + A_0V' &= 0 \\ -A_0U' + A_{22}V'' - L_3V &= 0 \end{aligned} \quad (B21)$$

where the newly introduced constants are defined by

$$\begin{aligned} A_0 &= A_{12} + A_{66} \\ L_1 &= A_{11} \\ L_3 &= A_{66} + \lambda N_{xL} \end{aligned} \quad (B22)$$

Equations (B21) can be manipulated through differentiation and elimination of variables, with the result that both U and V must satisfy the same fourth-order differential equation:

$$\begin{aligned} U'''' - 2BU'' + CU &= 0 \\ V'''' - 2BV'' + CV &= 0 \end{aligned} \quad (B23)$$

where constants B and C are given by

$$B = \frac{A_{66}L_3 + A_{22}L_1 - A_0^2}{2A_{22}A_{66}} \quad C = \frac{L_1L_3}{A_{22}A_{66}} \quad (B24)$$

While $U(Y)$ and $V(Y)$ must individually satisfy their respective governing equations (B23), there is, in addition, a compatibility condition relating the two functions which can be determined using either of the equations (B21).

The general form of the solutions for U and V are given by

$$U(Y) = Ee^{pY} \quad V(Y) = Ge^{pY} \quad (B25)$$

where E and G are arbitrary constants, and p is a constant governed by the characteristic equation

$$p^4 - 2Bp^2 + C = 0 \quad (B26)$$

or

$$p^2 = B \pm \sqrt{B^2 - C} \quad (B27)$$

The exact nature of the roots p depends on the relative amplitudes of the parameters B and C , but the following common form will be used to express the functions $U(Y)$ and $V(Y)$:

$$U(Y) = \sum_{j=1}^4 E_j \bar{g}_j(Y) \quad (B28)$$

$$V(Y) = \sum_{j=1}^4 G_j \bar{g}_j(Y)$$

The compatibility condition can be expressed as

$$E_j = \sum_{k=1}^4 R_{jk} G_k \quad j = 1, 2, 3, 4 \quad (B29)$$

where the values R_{jk} are constants. The constants E_j and G_j of equations (B28) are determined by the boundary conditions at the side edges of the plate strip. In [5], two cases are identified for characterizing the form of the four functions $\bar{g}_j(Y)$. These cases are considered independently below.

VIPASA In-Plane Case a) $B^2 > C$: Two non-negative, real roots are identified, defined by the following equations:

$$\theta^2 = -\hat{\theta}^2 = B + \sqrt{B^2 - C} \quad \phi^2 = -\hat{\phi}^2 = B - \sqrt{B^2 - C} \quad (B30)$$

where either θ or $\hat{\theta}$ is real, and either ϕ or $\hat{\phi}$ is real. Note that if ϕ is real then θ is real, and similarly, if $\hat{\theta}$ is real, then $\hat{\phi}$ is real. Four roots p are given by $p = \pm \theta$ or $p = \pm i\hat{\theta}$, and $p = \pm \phi$ or $p = \pm i\hat{\phi}$. The four roots p establish four contributions to each of the functions

$U(Y)$ and $V(Y)$, consistent with the forms given in equations (B25), where it is understood that only the real portions of complex contributions are retained. The four contributions to each function are combined and regrouped into expressions having the form of equations (B28), and the compatibility constants R_{jk} of equation (B29) are determined by substituting equations (B28) into either of the differential equations (B21). The four functions \bar{g}_j and the non-zero constants R_{jk} are given in the following table:

Table 9. Functional Forms Used for VIPASA In-Plane Case (a)

	$\theta^2 \geq 0^*$	$\hat{\theta}^2 > 0$			$\phi^2 \geq 0^*$	$\hat{\phi}^2 > 0$
$\bar{g}_1(Y)$	$\cosh(\theta Y)$	$\cos(\hat{\theta} Y)$		$\bar{g}_3(Y)$	$\cosh(\phi Y)$	$\cos(\hat{\phi} Y)$
$\bar{g}_2(Y)$	$\sinh(\theta Y)$	$\sin(\hat{\theta} Y)$		$\bar{g}_4(Y)$	$\sinh(\phi Y)$	$\sin(\hat{\phi} Y)$
R_{12}	R	\bar{R}		R_{34}	S	\bar{S}
R_{21}	R	$-\bar{R}$		R_{43}	S	$-\bar{S}$
<p>* If $\theta = 0$: $E_1 = E_2 = G_1 = G_2 \equiv 0$ If $\phi = 0$: $E_3 = E_4 = G_3 = G_4 \equiv 0$</p>						

The constants R , \bar{R} , S , and \bar{S} introduced in the table above are given by

$$R = -\frac{A_o\theta}{A_{66}\theta^2 - L_1} = \frac{A_{22}\theta^2 - L_3}{A_o\theta} \quad \bar{R} = -\frac{A_o\hat{\theta}}{A_{66}\hat{\theta}^2 + L_1} = \frac{A_{22}\hat{\theta}^2 + L_3}{A_o\hat{\theta}} \quad (B31)$$

$$S = -\frac{A_o\phi}{A_{66}\phi^2 - L_1} = \frac{A_{22}\phi^2 - L_3}{A_o\phi} \quad \bar{S} = \frac{A_o\hat{\phi}}{A_{66}\hat{\phi}^2 + L_1} = \frac{A_{22}\hat{\phi}^2 + L_3}{A_o\hat{\phi}} \quad (B32)$$

The two expressions given for each parameter above arise through separate applications of the first and second equilibrium equations (B21); the alternate forms can be shown to be equivalent.

VIPASA In-Plane Case b) $B^2 \leq C$: Here the roots p of equations (B27) are complex, and two non-negative real constants, ϕ_1 and ϕ_2 , are sought which satisfy

$$p^2 = (\phi_1 + i\phi_2)^2 = B \pm i\sqrt{C - B^2} \quad (B33)$$

The values ϕ_1 and ϕ_2 are found to satisfy the equations

$$\phi_1^2 = \frac{1}{2}(\sqrt{C} + B) \geq 0 \quad \phi_2^2 = \frac{1}{2}(\sqrt{C} - B) \geq 0 \quad (B34)$$

Four roots p are then given by $p = \pm(\phi_1 \pm i\phi_2)$. The four roots p establish four contributions to each of the functions $U(Y)$ and $V(Y)$, consistent with the forms given in equations (B25), where it is understood that only the real portions of complex contributions are retained. The four contributions to each function are combined and regrouped into expressions consistent with equations (B28), and the compatibility constants R_{jk} are determined in the same manner as for In-plane Case (a). The four functions \bar{g}_j and the non-zero constants R_{jk} are given in the following table:

Table 10. Functional Forms Used for VIPASA In-Plane Case (b)

	$B^2 < C$	$B = \sqrt{C} \quad (\phi_2 = 0)$	$B = - \sqrt{C} \quad (\phi_1 = 0)$
$\bar{g}_1(Y)$	$\cosh(\phi_1 Y) \cos(\phi_2 Y)$	$\cosh(\phi_1 Y)$	$\cos(\phi_2 Y)$
$\bar{g}_2(Y)$	$\sinh(\phi_1 Y) \cos(\phi_2 Y)$	$\sinh(\phi_1 Y)$	$Y \cos(\phi_2 Y)$
$\bar{g}_3(Y)$	$\cosh(\phi_1 Y) \sin(\phi_2 Y)$	$Y \cosh(\phi_1 Y)$	$\sin(\phi_2 Y)$
$\bar{g}_4(Y)$	$\sinh(\phi_1 Y) \sin(\phi_2 Y)$	$Y \sinh(\phi_1 Y)$	$Y \sin(\phi_2 Y)$
R_{12}, R_{34}	P	P	\bar{P}
R_{21}, R_{43}	P	P	0
R_{13}, R_{24}	Q	\bar{Q}	Q
R_{31}, R_{42}	$-Q$	0	$-Q$

The constants P , \bar{P} , Q , and \bar{Q} are given by the following expressions:

$$P = -\frac{A_0 \phi_1 (A_{66} \sqrt{C} - L_1)}{(A_{66}^2 C - 2A_{66} L_1 B + L_1^2)} = \frac{\phi_1 (A_{22} \sqrt{C} - L_3)}{A_0 \sqrt{C}} \quad (B35)$$

$$\bar{P} = -\frac{A_0 (A_{66} \sqrt{C} - L_1)}{(A_{66} \sqrt{C} + L_1)^2} = \frac{A_{22} \sqrt{C} - L_3}{A_0 \sqrt{C}}$$

$$\begin{aligned}
Q &= \frac{A_o \phi_2 (A_{66} \sqrt{C} + L_1)}{(A_{66}^2 C - 2A_{66} L_1 B + L_1^2)} = \frac{\phi_2 (A_{22} \sqrt{C} + L_3)}{A_o \sqrt{C}} \\
\bar{Q} &= \frac{A_o (A_{66} \sqrt{C} + L_1)}{(A_{66} \sqrt{C} - L_1)^2} = \frac{A_{22} \sqrt{C} + L_3}{A_o \sqrt{C}}
\end{aligned} \tag{B36}$$

The two expressions given for each parameter above arise through separate applications of the first and second equilibrium equations (B21); the alternate forms can be shown to be equivalent.

B.1.4 Final Expression of the Eigensolutions

It is desired to express the buckling eigensolutions in the form

$$\begin{Bmatrix} u(x, y) \\ v(x, y) \\ w(x, y) \end{Bmatrix} = \begin{Bmatrix} \xi(y) \cos(m\pi x/L) \\ \eta(y) \sin(m\pi x/L) \\ \phi(y) \sin(m\pi x/L) \end{Bmatrix} \tag{B37}$$

where the subscript denoting the eigensolution index number is omitted, and ξ , η , and ϕ are given by

$$\begin{Bmatrix} \xi(y) \\ \eta(y) \\ \phi(y) \end{Bmatrix} = \sum_{j=1}^4 \begin{Bmatrix} E_j g_j(y) \\ G_j g_j(y) \\ C_j f_j(y) \end{Bmatrix} \tag{B38}$$

The barred and unbarred functions in equations (B14), (B28), and (B38) have the following relationship:

$$\begin{Bmatrix} f_j(y) \\ g_j(y) \end{Bmatrix} = \begin{Bmatrix} \bar{f}_j(\gamma) \\ \bar{g}_j(\gamma) \end{Bmatrix} = \begin{Bmatrix} \bar{f}_j(m\pi y/L) \\ \bar{g}_j(m\pi y/L) \end{Bmatrix} \quad j = 1, 2, 3, 4 \tag{B39}$$

Thus, in using the expressions for $\bar{f}_i(Y)$ and $\bar{g}_i(Y)$ presented in the appendix to express derivatives of the functions $\xi_i(y)$, $\eta_i(y)$, and $\phi_i(y)$, an appropriate constant must be incorporated, as shown in this example:

$$\frac{d\xi(y)}{dy} = \sum_{j=1}^4 E_j \frac{df_j(y)}{dy} = \frac{m\pi}{L} \sum_{j=1}^4 E_j \frac{d\bar{f}_j(Y)}{dY} \quad (B40)$$

Appendix C. Finite-Difference Solution for the Second-Order Displacement Fields

In this appendix, a procedure is established for determining an approximate finite-difference solution for the functions which provide the y -dependence of the second-order displacement fields. These functions are denoted as $\{\xi_{\alpha ij}(y)\} = [\xi_{\alpha ij}(y) \ \eta_{\alpha ij}(y) \ \phi_{\alpha ij}(y)]^T$, $\alpha = 1, 2$, and $i, j = 1, 2, \dots$. The solution procedure is performed once for each combination of α , i , and j (except for case ji when case ij has already been solved). With this understood, the subscripts α , i , and j will be omitted for the remainder of this discussion, except where needed for clarity. First, finite-difference approximations for derivatives are used to determine finite-difference expressions of the governing differential equations and the side-edge stress resultant contributions on a plate strip. A linear system of equations is formed in terms of the unknowns in the discretized y -domain of the plate strip, and then the appropriate transformations are introduced which allow the assembly of a system of linear equations applying to the complete configuration. Boundary conditions are applied to the global system of equations.

C.1.1 Finite-Difference Expressions for the Governing Equations

On each plate strip, the functions $\{\xi\}$ are governed by differential equations of the following form:

$$\begin{aligned}
C_1 \xi'' + C_2 \xi + C_3 \eta' &= F(y) \\
D_1 \xi' + D_2 \eta'' + D_3 \eta &= G(y) \\
E_1 \phi'''' + E_2 \phi'' + E_3 \phi &= H(y)
\end{aligned} \tag{C1}$$

The associated generalized edge force-resultant amplitudes, used in expressing boundary conditions, depend on the functions $\{\xi\}$ as shown in the following equations:

$$\begin{aligned}
\dot{i}_{x_e} &= (-1)^e [\bar{C}_1 \xi' + \bar{C}_2 \eta + \bar{F}(y)] \Big|_{y_e} \\
\dot{i}_{y_e} &= (-1)^e [\bar{D}_1 \xi + \bar{D}_2 \eta' + \bar{G}(y)] \Big|_{y_e} \\
\dot{i}_{z_e} &= (-1)^e [\bar{E}_1 \phi'''' + \bar{E}_2 \phi' + \bar{H}(y)] \Big|_{y_e} \\
\dot{m}_e &= -(-1)^e [\bar{E}_3 \phi'' + \bar{E}_4 \phi] \Big|_{y_e}
\end{aligned} \quad e = 1, 2 \tag{C2}$$

The y -domain of the plate strip is discretized into l intervals, defining $l + 1$ discrete y -stations. The functional values at these discrete stations will be denoted by, for example, $\xi_1, \xi_2, \dots, \xi_l, \xi_{l+1}$, where

$$\xi_j = \xi(y_j) \tag{C3}$$

where the station y_j is defined by

$$y_j = (j - 1) \frac{b}{l} \tag{C4}$$

where b is the width of the plate strip.

Derivatives of the functions $\{\xi\}$ at the discrete stations are expressed using finite-difference approximations. The formulae used are central-difference representations with truncation errors of order (h^2) , where h is the interval width, given by

$$h = \frac{b}{l} \tag{C5}$$

The finite-difference formulae are [63]:

$$\begin{aligned}
 f'(y)|_{y_j} &= \frac{1}{2h} (-f_{j-1} + f_{j+1}) \\
 f''(y)|_{y_j} &= \frac{1}{h^2} (f_{j-1} - 2f_j + f_{j+1}) \\
 f'''(y)|_{y_j} &= \frac{1}{2h^3} (-f_{j-2} + 2f_{j-1} - 2f_{j+1} + f_{j+2}) \\
 f''''(y)|_{y_j} &= \frac{1}{h^4} (f_{j-2} - 4f_{j-1} + 6f_j - 4f_{j+1} + f_{j+2})
 \end{aligned} \tag{C6}$$

Using the above formulae for derivatives to express the differential equations (C1) at $y = y_j$, the following finite difference equations are obtained:

$$\begin{aligned}
 k_{11}\xi_{j-1} + k_{12}\xi_j + k_{13}\xi_{j+1} + k_{14}\eta_{j-1} + k_{15}\eta_{j+1} &= F_j \\
 k_{21}\xi_{j-1} + k_{22}\xi_{j+1} + k_{23}\eta_{j-1} + k_{24}\eta_j + k_{25}\eta_{j+1} &= G_j \quad j = 1, 2, \dots, l, l+1 \\
 k_{31}\phi_{j-2} + k_{32}\phi_{j-1} + k_{33}\phi_j + k_{34}\phi_{j+1} + k_{35}\phi_{j+2} &= H_j
 \end{aligned} \tag{C7}$$

where the constant coefficients are given by

$$\begin{aligned}
 k_{11} &= \frac{C_1}{h^2} & k_{12} &= -\frac{2C_1}{h^2} + C_2 & k_{13} &= \frac{C_1}{h^2} & k_{14} &= -\frac{C_3}{2h} & k_{15} &= \frac{C_3}{2h} \\
 k_{21} &= -\frac{D_1}{2h} & k_{22} &= \frac{D_1}{2h} & k_{23} &= \frac{D_2}{h^2} & k_{24} &= -\frac{2D_2}{h^2} + D_3 & k_{25} &= \frac{D_2}{h^2} \\
 k_{31} &= \frac{E_1}{h^4} & k_{32} &= -\frac{4E_1}{h^4} + \frac{E_2}{h^2} & k_{33} &= \frac{6E_1}{h^4} - \frac{2E_2}{h^2} + E_3 & k_{34} &= -\frac{4E_1}{h^4} + \frac{E_2}{h^2} & k_{35} &= \frac{E_1}{h^4}
 \end{aligned} \tag{C8}$$

and the right-hand-side functions are given by

$$F_j = F(y_j) \quad G_j = G(y_j) \quad H_j = H(y_j) \tag{C9}$$

It is helpful to express equations (C7) in terms of matrices and vectors. Introduce the notation $\{\xi_j\} = [\xi_j \eta_j \phi_j]^T$ and $\{F_j\} = [F_j G_j H_j]^T$, and now equations (C7) can be written as

$$[K^{-2}]\{\xi_{j-2}\} + [K^{-1}]\{\xi_{j-1}\} + [K^0]\{\xi_j\} + [K^{+1}]\{\xi_{j+1}\} + [K^{+2}]\{\xi_{j+2}\} = \{F_j\} \tag{C10}$$

where

$$[K^{-1}] = \begin{bmatrix} k_{11} & k_{14} & 0 \\ k_{21} & k_{23} & 0 \\ 0 & 0 & k_{32} \end{bmatrix} \quad [K^0] = \begin{bmatrix} k_{12} & 0 & 0 \\ 0 & k_{24} & 0 \\ 0 & 0 & k_{33} \end{bmatrix} \quad [K^{+1}] = \begin{bmatrix} k_{13} & k_{15} & 0 \\ k_{22} & k_{25} & 0 \\ 0 & 0 & k_{34} \end{bmatrix} \quad (C11)$$

and where the only nonzero elements of $[K^{-2}]$ and $[K^{+2}]$ are given by

$$\begin{aligned} K_{33}^{-2} &= k_{31} \\ K_{33}^{+2} &= k_{35} \end{aligned} \quad (C12)$$

C.1.2 Finite-Difference Expressions for the Generalized Edge

Force-Resultants

As with the governing equations, the edge stress-resultant amplitudes are expressed in terms of discrete values of the displacement variables by applying the finite-difference formulae of equations (C5) to equations (C2). The following expressions are obtained:

$$\begin{aligned} \dot{i}_{\xi_1} &= \frac{\bar{C}_1}{2h} \xi_0 - \frac{\bar{C}_1}{2h} \xi_2 - \bar{C}_2 \eta_1 - \bar{F}(0) \\ \dot{i}_{\eta_1} &= -\bar{D}_1 \xi_1 + \frac{\bar{D}_2}{2h} \eta_0 - \frac{\bar{D}_2}{2h} \eta_2 - \bar{G}(0) \\ \dot{i}_{\phi_1} &= \frac{\bar{E}_1}{2h^3} \phi_{-1} + \left(-\frac{\bar{E}_1}{h^3} + \frac{\bar{E}_2}{2h} \right) \phi_0 + \left(\frac{\bar{E}_1}{h^3} - \frac{\bar{E}_2}{2h} \right) \phi_2 - \frac{\bar{E}_1}{2h^3} \phi_3 - \bar{H}(0) \\ \dot{m}_{\phi_1} &= \frac{\bar{E}_3}{h^2} \phi_0 + \left(-\frac{2\bar{E}_3}{h^2} + \bar{E}_4 \right) \phi_1 + \frac{\bar{E}_3}{h^2} \phi_2 \end{aligned} \quad (C13)$$

$$\begin{aligned}
\dot{f}_{xe_2} &= -\frac{\bar{C}_1}{2h} \xi_l + \frac{\bar{C}_1}{2h} \xi_{l+2} + \bar{C}_2 \eta_{l+1} + \bar{F}(b) \\
\dot{f}_{ye_2} &= \bar{D}_1 \xi_{l+1} - \frac{\bar{D}_2}{2h} \eta_l + \frac{\bar{D}_2}{2h} \eta_{l+2} + \bar{G}(b) \\
\dot{f}_{ze_2} &= -\frac{\bar{E}_1}{2h^3} \phi_{l-1} + \left(\frac{\bar{E}_1}{h^3} - \frac{\bar{E}_2}{2h} \right) \phi_l + \left(-\frac{\bar{E}_1}{h^3} + \frac{\bar{E}_2}{2h} \right) \phi_{l+2} + \frac{\bar{E}_1}{2h^3} \phi_{l+3} + \bar{H}(b) \\
\dot{m}_{e_2} &= -\frac{\bar{E}_3}{h^2} \phi_l + \left(\frac{2\bar{E}_3}{h^2} - \bar{E}_4 \right) \phi_{l+1} - \frac{\bar{E}_3}{h^2} \phi_{l+2}
\end{aligned} \tag{C14}$$

where e_1 implies $e = 1$, and e_2 implies $e = 2$.

Inspection of equations (C7), (C13), and (C14) reveals that eight nonexistent function values have been introduced, corresponding to stations outside of the y -domain. These are denoted as ϕ_{-1} , ξ_o , η_o , and ϕ_o , associated with values of y less than zero, and ξ_{l+2} , η_{l+2} , ϕ_{l+2} , and ϕ_{l+3} , associated with values of y greater than b . It is necessary to replace these nonexistent values with expressions involving existent function values. The first step in doing this is to add an edge-rotation variable to each end of the y -domain, denoted $\dot{\psi}_o$, and defined by

$$\dot{\psi}_o = \phi'(y)|_{y_o} \quad e = 1, 2 \tag{C15}$$

This establishes $3(l+1) + 2$ discrete unknowns across the width of the plate strip. Recalling that $\{\dot{\xi}_o\} = [\dot{\xi}_o \ \dot{\eta}_o \ \dot{\phi}_o \ \dot{\phi}_o]^T$ ($e = 1, 2$) and introducing the notation $\{d\} = [\xi_2 \ \eta_2 \ \phi_2 \ \xi_3 \ \eta_3 \ \phi_3 \ \dots \ \xi_l \ \eta_l \ \phi_l]^T$, the vector of unknowns is given by

$$\begin{pmatrix} \{\dot{\xi}_{e_1}\} \\ \{d\} \\ \{\dot{\xi}_{e_2}\} \end{pmatrix} \tag{C16}$$

Express $\dot{\psi}_o$ in terms of finite-difference approximations to get

$$\dot{\psi}_{e_1} = -\frac{1}{2h} \phi_o + \frac{1}{2h} \phi_2 \quad \dot{\psi}_{e_2} = -\frac{1}{2h} \phi_l + \frac{1}{2h} \phi_{l+2} \tag{C17}$$

By rearranging equations (C17), the following expressions for ϕ_o and ϕ_{l+2} can be obtained:

$$\phi_o = -2h\dot{\psi}_{e_1} + \phi_2 \quad \phi_{l+2} = 2h\dot{\psi}_{e_2} + \phi_l \quad (C18)$$

Equations (C18) are also written another way for later use:

$$\phi_o = c_1\dot{\psi}_1 + c_2\phi_2 \quad \phi_{l+2} = \bar{c}_1\dot{\psi}_2 + \bar{c}_2\phi_l \quad (C19)$$

where the constant coefficients are given by

$$\begin{aligned} c_1 &= -2h & c_2 &= 1 \\ \bar{c}_1 &= 2h & \bar{c}_2 &= 1 \end{aligned} \quad (C20)$$

The six remaining nonexistent function values can be expressed in terms of existent values by rearranging equations (C13) and (C14), and making substitutions using equations (C18) where appropriate. The following expressions can be obtained:

$$\begin{aligned} \xi_o &= a_1\dot{f}_{xe_1} + a_2\xi_2 + a_3\eta_1 + a_4 & \xi_{l+2} &= \bar{a}_1\dot{f}_{xe_2} + \bar{a}_2\xi_l + \bar{a}_3\eta_{l+1} + \bar{a}_4 \\ \eta_o &= b_1\dot{f}_{ye_1} + b_2\xi_1 + b_3\eta_2 + b_4 & \eta_{l+2} &= \bar{b}_1\dot{f}_{ye_2} + \bar{b}_2\xi_{l+1} + \bar{b}_3\eta_l + \bar{b}_4 \\ \phi_{-1} &= d_1\dot{f}_{ze_1} + d_2\dot{\psi}_{e_1} + d_3\phi_3 + d_4 & \phi_{l+3} &= \bar{d}_1\dot{f}_{ze_2} + \bar{d}_2\dot{\psi}_{e_2} + \bar{d}_3\phi_{l-1} + \bar{d}_4 \end{aligned} \quad (C21)$$

where

$$\begin{aligned} a_1 &= \frac{2h}{C_1} & a_2 &= 1 & a_3 &= 2h \frac{\bar{C}_2}{C_1} & a_4 &= 2h \frac{\bar{F}(0)}{C_1} \\ b_1 &= \frac{2h}{D_2} & b_2 &= 2h \frac{\bar{D}_1}{D_2} & b_3 &= 1 & b_4 &= 2h \frac{\bar{G}(0)}{D_2} \\ d_1 &= \frac{2h^3}{\bar{E}_1} & d_2 &= -4h + \frac{2h^3\bar{E}_2}{\bar{E}_1} & d_3 &= 1 & d_4 &= 2h^3 \frac{\bar{H}(0)}{\bar{E}_1} \end{aligned} \quad (C22)$$

$$\begin{aligned}
\bar{a}_1 &= \frac{2h}{\bar{C}_1} & \bar{a}_2 &= 1 & \bar{a}_3 &= -2h \frac{\bar{C}_2}{\bar{C}_1} & \bar{a}_4 &= -2h \frac{\bar{F}(b)}{\bar{C}_1} \\
\bar{b}_1 &= \frac{2h}{\bar{D}_2} & \bar{b}_2 &= -2h \frac{\bar{D}_1}{\bar{D}_2} & \bar{b}_3 &= 1 & \bar{b}_4 &= -2h \frac{\bar{G}(b)}{\bar{D}_2} \\
\bar{d}_1 &= \frac{2h^3}{\bar{E}_1} & \bar{d}_2 &= 4h - \frac{2h^3 \bar{E}_2}{\bar{E}_1} & \bar{d}_3 &= 1 & \bar{d}_4 &= -2h^3 \frac{\bar{H}(b)}{\bar{E}_1}
\end{aligned} \tag{C23}$$

The edge moments of equations (C13) and (C14) were not required in determining the expressions of equations (C21), but they will be required in order to add two additional equations corresponding to the two edge-rotation amplitudes which have been added as unknowns. For this purpose, the edge moments of equations (C13) and (C14) are expressed in the following way:

$$\dot{m}_{e_1} = g_1 \dot{\psi}_{e_1} + g_2 \phi_1 + g_3 \phi_2 \qquad \dot{m}_{e_2} = \bar{g}_1 \dot{\psi}_{e_2} + \bar{g}_2 \phi_1 + \bar{g}_3 \phi_{1+1} \tag{C24}$$

where

$$\begin{aligned}
g_1 &= -\frac{2\bar{E}_3}{h} & g_2 &= -\frac{2\bar{E}_3}{h^2} + \bar{E}_4 & g_3 &= \frac{2\bar{E}_3}{h^2} \\
\bar{g}_1 &= -\frac{2\bar{E}_3}{h} & \bar{g}_2 &= -\frac{2\bar{E}_3}{h^2} & \bar{g}_3 &= \frac{2\bar{E}_3}{h^2} - \bar{E}_4
\end{aligned} \tag{C25}$$

Some new notation is introduced in order to facilitate expression of equations (C19) and (C21) in terms of vectors and matrices. Define the vectors $\{\dot{\xi}_e\}$ and $\{\dot{f}_e^*\}$ ($e = 1, 2$):

$$\{\dot{\xi}_e\} = \begin{Bmatrix} \dot{\xi}_e \\ \dot{\eta}_e \\ \dot{\phi}_e \\ \dot{\psi}_e \end{Bmatrix} = \begin{Bmatrix} \xi(y_e) \\ \eta(y_e) \\ \phi(y_e) \\ \psi_e \end{Bmatrix} \qquad \{\dot{f}_e^*\} = \begin{Bmatrix} \dot{f}_{x_e} \\ \dot{f}_{y_e} \\ \dot{f}_{z_e} \end{Bmatrix} \tag{C26}$$

Expressing $\{\dot{\xi}_e\}$ ($e = 1, 2$) in terms of finite-difference unknowns and ψ_e , we can say that

$$\begin{array}{ccc}
 \xi_1 & & \xi_{l+1} \\
 \{\dot{\xi}_{e_1}\} = \begin{Bmatrix} \eta_1 \\ \phi_1 \end{Bmatrix} & & \{\dot{\xi}_{e_2}\} = \begin{Bmatrix} \eta_{l+1} \\ \phi_{l+1} \end{Bmatrix} \\
 \dot{\psi}_{e_1} & & \dot{\psi}_{e_2}
 \end{array} \tag{C27}$$

Now equations (C19) and (C21) can be expressed using matrix notation:

$$\begin{aligned}
 \{\xi_0\} &= [A^0]\{\dot{f}_{e_1}^*\} + [A^1]\{\dot{\xi}_{e_1}\} + [A^2]\{\xi_2\} + \{A^4\} \\
 \{\xi_{-1}\} &= [B^0]\{\dot{f}_{e_1}^*\} + [B^1]\{\dot{\xi}_{e_1}\} + [B^3]\{\xi_3\} + \{B^4\}
 \end{aligned} \tag{C28}$$

$$\begin{aligned}
 \{\xi_{l+2}\} &= [\bar{A}^0]\{\dot{f}_{e_2}^*\} + [\bar{A}^1]\{\dot{\xi}_{e_2}\} + [\bar{A}^2]\{\xi_l\} + \{\bar{A}^4\} \\
 \{\xi_{l+3}\} &= [\bar{B}^0]\{\dot{f}_{e_2}^*\} + [\bar{B}^1]\{\dot{\xi}_{e_2}\} + [\bar{B}^3]\{\xi_{l-1}\} + \{\bar{B}^4\}
 \end{aligned} \tag{C29}$$

The nonzero elements of the matrices introduced in equations (C28) are given by

$$\begin{array}{llll}
 A_{11}^0 = a_1 & A_{22}^0 = b_1 & & B_{33}^0 = d_1 \\
 A_{12}^1 = a_3 & A_{21}^1 = b_2 & A_{34}^1 = c_1 & B_{34}^1 = d_2 \\
 A_{11}^2 = a_2 & A_{22}^2 = b_3 & A_{33}^2 = c_2 & B_{33}^3 = d_3 \\
 A_1^4 = a_4 & A_2^4 = b_4 & & B_3^4 = d_4
 \end{array} \tag{C30}$$

The nonzero elements of the matrices in equations (C29) are given by the same expressions as in the equations above, except that the unsubscripted constants a , b , and d are replaced by the subscripted constants \bar{a} , \bar{b} , and \bar{d} . Now all the elements are in place for assembly of the system of finite-difference equations which apply to a single plate strip.

C.1.3 System of Equations for a Plate Strip

Equations at $y = y_1$: To obtain the first three equations, consider the finite-difference equations (C10) for the case $j = 1$ ($y = 0$):

$$[K^{-2}]\{\xi_{-1}\} + [K^{-1}]\{\xi_0\} + [\tilde{K}^0]\{\dot{\xi}_{e_1}\} + [K^{+1}]\{\xi_2\} + [K^{+2}]\{\xi_3\} = \{F_1\} \quad (C31)$$

where $\{\dot{\xi}_{e_1}\}$ of equation (C26) has replaced $\{\xi_1\}$, and one coefficient matrix was modified to account for the added degree of freedom:

$$[\tilde{K}^0] = \left[\begin{array}{c|c} [K^0] & \begin{matrix} | 0 \\ | 0 \\ | 0 \end{matrix} \end{array} \right] \quad (C32)$$

The vectors $\{\xi_{-1}\}$ and $\{\xi_0\}$ appearing in equations (C31) are replaced by the expressions given in equations (C28); equations (C31) can then be expressed in the form

$$[\tilde{K}]\{\dot{\xi}_{e_1}\} + [\tilde{L}]\{\xi_2\} + [\tilde{M}]\{\xi_3\} = [\tilde{J}]\{\dot{e}_1\} + \{\tilde{F}_1\} \quad (C33)$$

where the newly introduced matrices and vector are given symbolically, and in evaluated form, by

$$[\tilde{K}] = [\tilde{K}^0] + [K^{-1}][A^1] + [K^{-2}][B^1] = \left[\begin{array}{cccc} (k_{12} + k_{14}b_2) & k_{11}a_3 & 0 & 0 \\ k_{23}b_2 & (k_{24} + k_{21}a_3) & 0 & 0 \\ 0 & 0 & k_{33} & (k_{32}c_1 + k_{31}d_2) \end{array} \right] \quad (C34)$$

$$[\tilde{L}] = [K^{+1}] + [K^{-1}][A^2] = \left[\begin{array}{cc} (k_{13} + k_{11}a_2)(k_{15} + k_{14}b_3) & 0 \\ (k_{22} + k_{21}a_2)(k_{25} + k_{23}b_3) & 0 \\ 0 & 0 & (k_{34} + k_{32}c_2) \end{array} \right] \quad (C35)$$

$$[\tilde{J}] = - ([K^{-1}][A^0] + [K^{-2}][B^0]) = - \begin{bmatrix} k_{11}a_1 & k_{14}b_1 & 0 \\ k_{21}a_1 & k_{23}b_1 & 0 \\ 0 & 0 & k_{31}d_1 \end{bmatrix} \quad (C36)$$

$$\{\tilde{F}_1\} = \{F_1\} - ([K^{-1}]\{A^4\} + [K^{-2}]\{B^4\}) = \begin{cases} F_1 - (k_{11}a_4 + k_{14}b_4) \\ G_1 - (k_{21}a_4 + k_{23}b_4) \\ H_1 - k_{31}d_4 \end{cases} \quad (C37)$$

and where $[\tilde{M}]$ has only one nonzero element:

$$[\tilde{M}] = [K^{+2}] + [K^{-2}][B^3], \quad \tilde{M}_{33} = (k_{35} + k_{31}d_3) \quad (C38)$$

Finally, isolate $\{\dot{f}_{e_1}^*\}$ by premultiplying equation (C33) by $[\tilde{J}]^{-1}$:

$$[\bar{K}]\{\dot{\xi}_{e_1}\} + [\bar{L}]\{\xi_2\} + [\bar{M}]\{\xi_3\} = \{\dot{f}_{e_1}^*\} + \{\bar{F}_1\} \quad (C39)$$

where

$$([\bar{K}], [\bar{L}], [\bar{M}], \{\bar{F}_1\}) = [\tilde{J}]^{-1}([\tilde{K}], [\tilde{L}], [\tilde{M}], \{\tilde{F}_1\}) \quad (C40)$$

The three linear equations (C39) correspond to the first three unknowns, $\dot{\xi}_{e_1}$, $\dot{\eta}_{e_1}$, and $\dot{\phi}_{e_1}$, of the vector in equation (C16).

The fourth equation, corresponding to the unknown $\dot{\psi}_{e_1}$, is the first of equations (C24). Rewriting the equation in notation compatible with equations (C39),

$$[0 \ 0 \ g_2 \ g_1]\{\dot{\xi}_1\} + [0 \ 0 \ g_3]\{\xi_2\} = \dot{m}_{e_1} \quad (C41)$$

Equations at $y = y_2$: To obtain the fifth through seventh equations, corresponding to unknowns ξ_2 , η_2 , and ϕ_2 of the vector in equation (C16), consider the finite-difference equations (C10) for the case $j = 2$:

$$[K^{-2}]\{\xi_0\} + [\tilde{K}^{-1}]\{\dot{\xi}_{e_1}\} + [K^0]\{\xi_2\} + [K^{+1}]\{\xi_3\} + [K^{+2}]\{\xi_4\} = \{F_2\} \quad (C42)$$

where $\{\dot{\xi}_{e_1}\}$ of equation (C26) has replaced $\{\xi_1\}$, and one coefficient matrix was modified to accommodate the added degree of freedom:

$$[\tilde{K}^{-1}] = \left[\begin{array}{c|c} & 0 \\ [K^{-1}] & 0 \\ & 0 \end{array} \right] \quad (C43)$$

The vector $\{\xi_0\}$ appearing in equations (C42) is replaced by the expression given in equations (C28). Equations (C42) can then be expressed in the following form, which is suitable for direct incorporation into the system of equations for the plate strip as a whole:

$$[\bar{K}^{-1}]\{\dot{\xi}_{e_1}\} + [\bar{K}^0]\{\xi_2\} + [K^{+1}]\{\xi_3\} + [K^{+2}]\{\xi_4\} = \{F_2\} \quad (C44)$$

where the newly introduced matrices and vector are given symbolically, and in evaluated form, by

$$[\bar{K}^{-1}] = [\tilde{K}^{-1}] + [K^{-2}][A^1] = \begin{bmatrix} k_{11} & k_{14} & 0 & 0 \\ k_{21} & k_{23} & 0 & 0 \\ 0 & 0 & k_{32} & k_{31}c_1 \end{bmatrix} \quad (C45)$$

$$[\bar{K}^0] = [K^0] + [K^{-2}][A^2] = \begin{bmatrix} k_{12} & 0 & 0 \\ 0 & k_{24} & 0 \\ 0 & 0 & (k_{33} + k_{31}c_2) \end{bmatrix} \quad (C46)$$

and where it is noted in addition that some expected matrix terms do not appear in equations (C44) because certain matrix products vanish:

$$[K^{-2}][A^0] = \{0\} \quad [K^{-2}]\{A^4\} = \{0\} \quad (C47)$$

Equations at $y = y_l$: The three equations evaluated at y_l require the same special consideration as those evaluated at y_2 . Consider the finite-difference equations (C10) for the case $j = l$:

$$[K^{-2}]\{\xi_{l-2}\} + [K^{-1}]\{\xi_{l-1}\} + [K^0]\{\xi_l\} + [\tilde{K}^{+1}]\{\dot{\xi}_{e_2}\} + [K^{+2}]\{\xi_{l+2}\} = \{F_2\} \quad (C48)$$

where $\{\dot{\xi}_{e_2}\}$ of equation (C26) has replaced $\{\xi_{l+1}\}$, and one coefficient matrix was modified to accommodate the added degree of freedom:

$$[\tilde{K}^{+1}] = \left[\begin{array}{c|c} & 0 \\ [K^{+1}] & 0 \\ & 0 \end{array} \right] \quad (C49)$$

The vector $\{\xi_{l+2}\}$ appearing in equations (C48) is replaced by the expression given in equations (C29). Equations (C48) can then be expressed in the following form, which is suitable for direct incorporation into the system of equations for the plate strip as a whole:

$$[K^{-2}]\{\xi_{l-2}\} + [K^{-1}]\{\xi_{l-1}\} + [\bar{K}^0]\{\xi_l\} + [\bar{K}^{+1}]\{\dot{\xi}_{e_2}\} = \{F_l\} \quad (C50)$$

where

$$[\bar{K}^0] = [K^0] + [K^{+2}][\bar{A}^2] = \begin{bmatrix} k_{12} & 0 & 0 \\ 0 & k_{24} & 0 \\ 0 & 0 & (k_{33} + k_{35}\bar{c}_2) \end{bmatrix} \quad (C51)$$

$$[\bar{K}^{+1}] = [\tilde{K}^{+1}] + [K^{+2}][A^1] = \begin{bmatrix} k_{13} & k_{15} & 0 & 0 \\ k_{22} & k_{25} & 0 & 0 \\ 0 & 0 & k_{34} & k_{35}\bar{c}_1 \end{bmatrix} \quad (C52)$$

and where it is noted in addition that some expected matrix terms do not appear in equations (C50) because certain matrix products vanish:

$$[K^{+2}][\bar{A}^0] = \{0\} \quad [K^{+2}][\bar{A}^4] = \{0\} \quad (C53)$$

Equations at $y = y_{l+1}$: The three equilibrium equations evaluated at y_{l+1} require the same special consideration as those evaluated at y_l . Consider the finite-difference equations (C10) for the case $j = l + 1$ ($y = b$):

$$[K^{-2}]\{\xi_{l-1}\} + [K^{-1}]\{\xi_l\} + [\tilde{K}^0]\{\dot{\xi}_{e_2}\} + [K^{+1}]\{\xi_{l+2}\} + [K^{+2}]\{\xi_{l+3}\} = \{F_{l+1}\} \quad (C54)$$

where $\{\dot{\xi}_{e_2}\}$ of equation (C26) has replaced $\{\xi_{l+1}\}$, and the modified coefficient matrix $[\tilde{K}^0]$ is given by equation (C33). The vectors $\{\xi_{l+2}\}$ and $\{\xi_{l+3}\}$ appearing in equations (C54) are replaced by the expressions given in equations (C30); equations (C54) can then be expressed in the form

$$[\tilde{M}]\{\xi_{l-1}\} + [\tilde{L}]\{\xi_l\} + [\tilde{K}]\{\dot{\xi}_{e_2}\} = [\tilde{J}]\{\dot{f}_{e_2}^*\} + \{\tilde{F}_2\} \quad (C55)$$

where the newly introduced matrices and vector are given symbolically, and in evaluated form, by

$$[\tilde{K}] = [\tilde{K}^0] + [K^{+1}][\bar{A}^1] + [K^{+2}][\bar{B}^1] = \begin{bmatrix} (k_{12} + k_{15}\bar{b}_2) & k_{13}\bar{a}_3 & 0 & 0 \\ k_{25}\bar{b}_2 & (k_{24} + k_{22}\bar{a}_3) & 0 & 0 \\ 0 & 0 & k_{33} & (k_{34}\bar{c}_1 + k_{35}\bar{d}_2) \end{bmatrix} \quad (C56)$$

$$[\tilde{L}] = [K^{-1}] + [K^{+1}][\bar{A}^2] = \begin{bmatrix} (k_{11} + k_{13}\bar{a}_2)(k_{14} + k_{15}\bar{b}_3) & 0 \\ (k_{21} + k_{22}\bar{a}_2)(k_{23} + k_{25}\bar{b}_3) & 0 \\ 0 & 0 & (k_{32} + k_{34}\bar{c}_2) \end{bmatrix} \quad (C57)$$

$$[\tilde{J}] = -([K^{+1}][\bar{A}^0] + [K^{+2}][\bar{B}^0]) = - \begin{bmatrix} k_{13}\bar{a}_1 & k_{15}\bar{b}_1 & 0 \\ k_{22}\bar{a}_1 & k_{25}\bar{b}_1 & 0 \\ 0 & 0 & k_{35}\bar{d}_1 \end{bmatrix} \quad (C58)$$

$$\{\tilde{F}_{l+1}\} = \{F_{l+1}\} - ([K^1]\{\bar{A}^4\} + [K^2]\{\bar{B}^4\}) = \begin{cases} F_{l+1} - (k_{13}\bar{a}_4 + k_{15}\bar{b}_4) \\ G_{l+1} - (k_{22}\bar{a}_4 + k_{25}\bar{b}_4) \\ H_{l+1} - k_{35}\bar{d}_4 \end{cases} \quad (C59)$$

and where $[\tilde{M}]$ has only one nonzero element:

$$[\tilde{M}] = [K^{-2}] + [K^{+2}][\bar{B}^3], \quad \tilde{M}_{33} = (k_{31} + k_{35}\bar{d}_3) \quad (C60)$$

Finally, isolate $\{\dot{f}_{e_2}^*\}$ by premultiplying equation (C55) by $[\tilde{J}]^{-1}$:

$$[\bar{M}]\{\xi_{l-1}\} + [\bar{L}]\{\xi_j\} + [\bar{K}]\{\dot{\xi}_{e_2}\} = \{\dot{f}_{e_2}^*\} + \{\bar{F}_{l+1}\} \quad (C61)$$

where

$$([\bar{K}], [\bar{L}], [\bar{M}], \{\bar{F}\}) = [\tilde{J}]^{-1}([\tilde{K}], [\tilde{L}], [\tilde{M}], \{\tilde{F}\}) \quad (C62)$$

The three linear equations (C61) correspond to the unknowns $\dot{\xi}_{e_2}$, $\dot{\eta}_{e_2}$, and $\dot{\phi}_{e_2}$

The equation corresponding to the unknown $\dot{\psi}_{e_2}$ is the second of equations (C24). Rewriting the equation in notation compatible with equations (C61),

$$[0 \ 0 \ \bar{g}_2]\{\xi_j\} + [0 \ 0 \ \bar{g}_3 \ \bar{g}_1]\{\dot{\xi}_{e_2}\} = \dot{m}_{e_2} \quad (C63)$$

Equations at $y = y_3, y_4, \dots, y_{l-1}$: For the y -stations corresponding to $j = 3, 4, \dots, l-1$, the application of equation (C10) in assembling the stiffness matrix for the plate strip is straightforward, with the one clarification that for $j = 3$ and $j = l-1$, the vectors $\{\xi_1\}$ and $\{\xi_{l+1}\}$ which appear are expressed in terms of the vectors $\{\dot{\xi}_{e_1}\}$ and $\{\dot{\xi}_{e_2}\}$, respectively (see equation (C27)).

Note regarding the preceding derivations: Close inspection of the development in this section, beginning with equation (C31), will reveal that the matrix operations as used were unnecessarily cumbersome, because the third of the governing equations (C7) remains un-

coupled from the first two throughout the derivations. Nonetheless, the development is correct as presented.

Final expression of the equations for a plate strip: Now a system of linear equations has been assembled which applies to the plate strip. Introducing the notation $\{F\} = [F_2 G_2 H_2 F_3 G_3 H_3 \dots F_l G_l H_l]^T$, and recalling the notation for the displacement unknowns given in equation (C16), the system of equations can be expressed in the following way:

$$\begin{bmatrix} K_{11} & | & K_{12} & | & 0 \\ \hline & & & & \\ K_{21} & | & K_{22} & | & K_{23} \\ \hline & & & & \\ 0 & | & K_{32} & | & K_{33} \end{bmatrix} \begin{Bmatrix} \{\dot{\xi}_{e_1}\} \\ \{\dot{f}_{e_1}\} \\ \{\bar{F}_1\} \\ \{\dot{\xi}_{e_2}\} \\ \{\dot{f}_{e_2}\} \\ \{\bar{F}_2\} \end{Bmatrix} = \{0\} + \{F\} \quad (C64)$$

where certain sub-matrices are zero as indicated, assuming l is greater than or equal to four.

In order to assemble the systems of equations for the individual plate strips into a global system of equations for the entire panel, the vectors for generalized edge displacements and generalized edge force-resultants, $\{\dot{\xi}_e\}$ and $\{\dot{f}_e\}$, respectively, must be transformed into the equivalent values referred to the appropriate node-line and the global coordinate axes. The transformations are effected through the following equations:

$$\{\dot{\xi}_e\} = [T_{ecc}]_e [T_r] \{\dot{U}^{n_e}\} \quad e = 1, 2 \quad (C65)$$

$$\{\dot{f}^{n_e}\} = [T_r]^T [T_{ecc}]_e^T \{\dot{f}_e\} \quad e = 1, 2 \quad (C66)$$

where the transformation matrices are given in the main text. To incorporate the transformations into the system of equations, replace $\{\dot{\xi}_e\}$ ($e = 1, 2$) with the appropriate expressions given in equation (C65), premultiply the first four equations of (C64) by $[T_r]^T [T_{ecc}]_{e_1}^T$, and premultiply the last four equations of (C64) by $[T_r]^T [T_{ecc}]_{e_2}^T$. Now the system of equations has the form

$$\begin{bmatrix} \hat{K}_{11} & \hat{K}_{12} & 0 \\ \hat{K}_{21} & \hat{K}_{22} & \hat{K}_{23} \\ 0 & \hat{K}_{32} & \hat{K}_{33} \end{bmatrix} \begin{Bmatrix} \dot{U}^{n_1} & \dot{f}^{n_1} & \hat{F}_1 \\ d & & \\ \dot{U}^{n_2} & \dot{f}^{n_2} & \hat{F}_2 \end{Bmatrix} = \{0\} + \{F\} \quad (C67)$$

where

$$\begin{aligned} [\hat{K}_{11}] &= [T_r]^T [T_{ecc}]_{e_1}^T [K_{11}] [T_{ecc}]_{e_1} [T_r] \\ [\hat{K}_{12}] &= [T_r]^T [T_{ecc}]_{e_1}^T [K_{12}] \\ [\hat{K}_{21}] &= [K_{21}] [T_{ecc}]_{e_1} [T_r] \\ [\hat{K}_{23}] &= [K_{23}] [T_{ecc}]_{e_2} [T_r] \\ [\hat{K}_{32}] &= [T_r]^T [T_{ecc}]_{e_2}^T [K_{32}] \\ [\hat{K}_{33}] &= [T_r]^T [T_{ecc}]_{e_2}^T [K_{33}] [T_{ecc}]_{e_2} [T_r] \\ \{\hat{F}_1\} &= [T_r]^T [T_{ecc}]_{e_1}^T \{\bar{F}_1\} \\ \{\hat{F}_2\} &= [T_r]^T [T_{ecc}]_{e_2}^T \{\bar{F}_2\} \end{aligned} \quad (C68)$$

C.1.4 Global System of Equations

The global system of equations, applying to the entire panel, has as unknowns the four components of $\{\dot{U}^n\}$ for each node line, and the $3(l-1)$ values in $\{d\}$ for each plate strip. When the system of equations applying to each plate strip (equations (C67)) has been assembled into the global system of equations, the sum of the vectors $\{\dot{f}^n\}$ for all plate edges terminating at a given node line is simply the vector of generalized force-resultant amplitudes for the node line, $\{\dot{F}^n\}$. Along nonboundary node lines, these values must be zero. Along boundary node lines, the homogeneous form of the selected options for boundary conditions are applied, so that each component of $\{\dot{F}^n\}$ either is zero or has its corresponding generalized displacement component set to zero, removing from consideration the equation containing the generalized force-resultant amplitude. Thus, the final system of equations to be solved after application

of boundary conditions has a form analogous to that of equation (C67), but without the presence of the first right-hand-side vector. The stiffness matrix will in general be banded, and this fact is used to select an efficient numerical procedure for solution of the system of equations.

Solution of the global system of equations provides the values values $\{\dot{U}^n\}$ for each node line, and the $3(l - 1)$ values in $\{d\}$ for each plate strip. Using the transformation relationship of equation (C65), the vectors $\{\dot{\xi}_e\}$ can be determined for each edge of each plate strip, and that completes the set of discrete values for $\{\xi(y)\}$ on the plate strip. Also needed for later use are first and second derivatives of $\xi(y)$ and $\eta(y)$, and first through fourth derivatives of $\phi(y)$. In order to determine these derivatives, the following sequence of operations is performed:

1. Apply equations (C39) and (C61) to solve for vectors $\{\dot{f}_e^*\}$ ($e = 1, 2$).
2. Apply equations (C28) and (C29) to determine the nonexistent function values $\{\xi_{-1}\}$, $\{\xi_0\}$, $\{\xi_{l+2}\}$, and $\{\xi_{l+3}\}$.
3. Use equations (C6) to determine finite-difference approximations for the derivatives at the end points of the y -domain.

Vita

Frederick Stoll was born in Oxnard, California on January 19, 1954. During his undergraduate studies at the University of Michigan, he participated in a cooperative education program with NASA Dryden Flight Research Center. He received the degree Bachelor of Science in Aerospace Engineering magna cum laude in 1979, after which he worked for four years as a research engineer with the Low-Speed Aircraft Research Branch of NASA Ames Research Center. He worked briefly for ultralight aircraft companies in Connecticut and Florida before attending the University of Florida, where he earned the degree Master of Science in Aerospace Engineering in 1986. He began his doctoral studies in 1986 at Virginia Polytechnic Institute and State University, where he was also a participant in the NASA-Virginia Tech Composites Program.

A handwritten signature in black ink that reads "Frederick Stoll". The signature is written in a cursive style with a large, sweeping initial 'F' and a distinct 'S'.